# Exploration of the role of diffusion-controlled dislocation climb in high temperature deformation of magnesium alloys - Recovery alone or key strain accommodation mechanism?

---

A

Dissertation

Presented to

the faculty of the School of Engineering and Applied Science

University of Virginia

---

in partial fulfillment

of the requirements for the degree

Doctor of Philosophy

by

Michael Albert Ritzo

December 2023

# APPROVAL SHEET

This

Dissertation

is submitted in partial fulfillment of the requirements
for the degree of

Doctor of Philosophy

Author: Michael Albert Ritzo

This Dissertation has been read and approved by the examining committee

Advisor: Dr. Sean Agnew

Advisor:

Committee Member: Dr. Jerrold Floro

Committee Member: Dr. James Burns

Committee Member: Dr. Jason Kerrigan

Committee Member: Dr. Tao Sun

Committee Member:

Committee Member:

Accepted for the School of Engineering and Applied Science:

Jennifer L. West, School of Engineering and Applied Science

December 2023

# Contents

Abstract ..... ii

Acknowledgements ..... iv

Dedication ..... v

List of Tables ..... vi

List of Figures ..... viii

Abbreviations and Symbols ..... xii

Introduction ..... 1

Chapter 1: Accounting for the effect of dislocation climb-mediated flow on the anisotropy and texture evolution of Mg alloy, AZ31B ..... 11

Chapter 2: Investigating the transition between ambient temperature and power law regime deformation using VPSC-CLIMB simulations optimized by genetic algorithm ..... 43

Chapter 3: Exploration of texture and alloy chemistry on the generality of significant dislocation climb using Mg alloy ZK10 ..... 95

Chapter 4: Analyzing the plausibility of significant climb activity through dislocation density measurements ..... 126

Chapter 5: Practical application of a climb-enabled Visco-Plastic Self Consistent crystal plasticity model through forming limit curve predictions ..... 150

Chapter 6: Conclusions and future works ..... 178

Chapter 7: References ..... 181

# Abstract

Conventional models of power law creep assume that deformation is accommodated by the activation of dislocation glide and climb, where climb operates as a recovery mechanism that facilitates the continued glide of dislocations past obstacles. The current work explores the utility of a model in which climb can accommodate significant strain independently of glide and may explain changes in the constitutive behavior, such as texture evolution, strain anisotropy, activation energy, and strain rate sensitivity. Specifically, strain accommodation via the climb of <a> dislocations within hexagonal close-packed (HCP) alloys of Mg was modeled using a climb incorporating viscoplastic self-consistent model (VPSC-CLIMB). The parameters governing the simulation results of this model were optimized to experimental texture and strain anisotropy measurements of as-rolled and annealed Mg alloy AZ31B deformed in tension along the sheet rolling direction (RD) and the in-plane transverse direction (TD) (at temperatures ranging from 20 to 350°C and strain rate ranging from $10^{-5}$ to $10^{-1}$ 1/s) by genetic algorithm (GA). Broadening the experimental and computational (VPSC-CLIMB) study to another alloy revealed that climb was also an important strain accommodation mechanism in the dilute Mg alloy ZK10; however, the climb of both <a> and <c> dislocations was necessary to match the experimental strain anisotropy. X-ray Line Profile Analysis (XLPA) was performed to estimate the mobile dislocation densities for <a> climb in AZ31B and <a> and <c> climb in ZK10, and it is suggested that both alloy chemistry and texture may play a role in determining which climb modes are active.

Simulations performed in intermediate temperatures also suggest that strain accommodation via climb may explain the evolution in texture evolution and strain anisotropy observed experimentally, though the role of <c+a> slip in these temperatures is currently unknown as the loading conditions selected could not excite its activation. The assumption of independent climb and glide was investigated using predictions of the rate sensitivity and activation energy could be compared with experimentally obtained values. The agreement was acceptable over a wide range of conditions and was especially good in the power law regime. Obviously, as more climb occurs, the simulations become more rate sensitive than those that only include glide. This generally enables the model to describe the transition from thermally activated plasticity at low temperatures and higher strain rates to power law climb and glide at higher temperatures and lower strain rates. The practical utility of the model was explored in the context of forming limit diagram (FLD) prediction, which is a rather rigorous test given the fact that model parameterization was performed solely on the basis of uniaxial in-plane tensile testing, whereas FLDs explore different straining conditions (e.g., plane strain, equibiaxial stretching). The fundamental hypothesis being explored was whether or not the transition from thermally activated plasticity to climb accommodated flow might explain the transition in formability exhibited by Mg alloys, from very limited cold formability to highly formable at moderately elevated temperatures (200 - 250°C) by predicting forming limit diagrams using the aforementioned VPSC-CLIMB model within the context of the Marciniak and Kuczyński (M-K) forming limit prediction. First, it had to be admitted that the initial experimental data set was inadequate to constrain the parameter (especially that governing the slip of <c+a> slip) selection over the entire range of straining paths required for forming limit prediction. Experimental forming data was used to further refine the model

parameters. Second, in the conditions explored (200 to 250°C and strain rates of ~$10^{-3}$ - $10^{-2}$ 1/s) climb was found to be active only at low rates (~$10^{-3}$ 1/s) or higher temperatures (250°C). At lower temperatures (150 °C), <c+a> slip accommodated significant amounts of strain, suggesting that a transition between a regime where <c+a> slip accommodates significant strain at lower temperatures and a regime where <a> climb begins to accommodate strain at higher temperatures exists. When climb was active, particularly during uniaxial straining, there was a concomitant increase in formability. Third, analysis of forming limit simulations provides a new, though retrospectively obvious, insight regarding the onset of plastic instability within materials undergoing flow by multiple deformation mechanisms. The onset of plastic instability was found to occur when either 1) texture evolution deactivates a major slip mode due to Schmid effects or 2) increases in the defect strain rate causes the deactivation of more rate sensitive mechanisms (i.e., climb).

# Acknowledgements

There are far too many people I have to thank for their encouragement and support in my life to list in this thesis. I fear that if I attempted to do so, it would easily double the length of this document. That being said, there are some people that deserve special recognition. I would first like to thank my teachers who have inspired my love of learning and teaching, especially Mr. Rodgers ($5^{th}$ grade), Mr. Peel ($6^{th}$ grade history) and Mrs. Meyer (AP chemistry). I would then like to thank my family for putting up with my antics for over a year as I wrote my thesis. There were many times that I wanted to give up on this thesis, but they convinced me to see it through to the end. In the same vein, I would also like to thank the members of the Swing Club at UVA , SwingCville in Charlottesville, Virginia who gave me a sense of community away from home in addition to GottaSwing in Woodbridge, Virginia for giving me my favorite release (swing dancing).

On a more serious note, I would like to thank the staff of Nano Materials Characterization Facility (NMCF), specifically Richard White and Diane Dickie who kept the SEM and XRD running, respectively. I would like to thank all members of the Agnew group, past and present, who have contributed to this thesis. Though this document bears my name, the work would not have been possible without them. In particular, I would like to acknowledge Professor Sean Agnew for his guidance which has kept me from spinning off course during this project, Dr. Jishnu Bhattacharyya for his technical expertise in crystal plasticity modeling and Mark Wischhusen for his assistance with electron backscatter diffraction. Finally, I would like to thank Juhyun Lee of the Daegu Institute of Science and Technology (DGIST) (South Korea) for his help with the mechanical testing of ZK10 during his summer internship in the Agnew Group.

# Dedication

This thesis is dedicated to any students, current or future, struggling under the pressures of research, life or academics. You should know that the pain you are feeling is temporary, but giving up on your dreams will last much longer. All too often, the pain we isolate from others isolates us from them. I am glad that I had people like those acknowledged above to share in my burdens.

# List of Tables

Chapter 1

Table 1: Voce hardening parameters for low and high temperature simulations ..... 30

Table 2: Densities of mobile, climbing <a> dislocations for each elevated temperature condition tested ..... 39

Chapter 2

Table 1: Common obstacle types and associated arrangements ..... 50

Table 2: Experimental values of the athermal stress for each slip mode ..... 51

Table 3: Corrected <c+a> slip CRSS ..... 52

Table 4: Optimized RSS values for climb incorporating after GA optimization and rescaled to experimental flow stresses in intermediate temperatures ..... 57

Table 5: Glide mode CRSSs and climb threshold stresses for climb incorporating simulations after bounding nonbasal slip ..... 57

Table B1: Optimized CRSS values for climb incorporating and glide only simulations after GA optimization and rescale to experimental yield stress ..... 76

Table B2: Glide mode CRSSs and climb threshold stresses for climb incorporating and glide only simulations after bounding nonbasal slip and adjusting basal slip ..... 77

Table B3: Fit parameters for glide CRSSs and hardening in climb incorporating and glide only simulations ..... 78

Table B4: Fit parameters for predicting the mobile dislocation density for climb ..... 78

Table D1: Orientation factors for each slip mode using an initial rolled and annealed texture for AZ31B ..... 93

Chapter 3

Table 1: Optimized Voce hardening parameters for low and high temperature simulations for ZK10 ..... 103

Table 2: Glide mode CRSS and hardening parameters for ZK10 ..... 103

Table 3: Climb stress parameters for ZK10 ..... 103

Table 4: Voce parameters for best fit, climb-excluding VPSC simulations ..... 108

Table 5: MTS paramerters of glide only simulations in ZK10 ..... 108

Table 6: Taylor and mobile dislocation densities and the required fraction for dislocations to climb for ZK10 ..... 115

Chapter 4

Table 1: Slip systems involved in XLPA of Mg alloys ..... 12929

Table 2: Total dislocation densities reported by Burgers vector in AZ31B and ZK10 ..... 135

Table 3: Samples compared in the current study ..... 138

Table 4: Determining the role of static recovery in ZK10 ..... 144

Table 5: Determining the role of static recovery in AZ31B of <a> dislocations ..... 145

Chapter 5

Table 1: Average strain rates for each limiting height dome test ..... 156

# List of Figures

Introduction
Figure 1: Diagram of a rectangular rod under a bending load. ..... 1
Figure 2: Common slip systems in HCP crystals. ..... 3
Figure 3: A schematic of the climb and glide creep model compared to independent climb and glide ..... 5
Figure 4: Idealized model of a heterogeneously distributed dislocation microstructure. ..... 6
Figure 5: Forming limit diagram of AZ31B at 300 °C. ..... 7
Figure 6: Initial as-deformed textures of as-rolled and as-extruded AZ31B ..... 9
Figure 7: As-rolled and annealed texture of ZK10 ..... 9

Chapter 1
Figure 1: Constitutive data of AZ31B at a range of temperatures and strain rates ..... 16
Figure 2: The ODF of as-rolled AZ31B presented as slices of Euler space. ..... 19
Figure 3: Coordinate system for considering the forces on dislocations within viscoplastic self consistent simulations that incorporate climb (VPSC-CLIMB) ..... 20
Figure 4: Schematic illustration of the distortions imparted by the glide and climb of various slip systems in Mg ..... 21
Figure 5: Experimental mechanical test data and Ashby map with flow stress data overlaid. ..... 26
Figure 6: Flow stress and strain anisotropy (r-values) as a function of testing conditions ..... 28
Figure 7: The importance of the prismatic slip of <a> dislocations during room temperature tensile testing as indicated by a node-like component in the texture and higher r-values ..... 29
Figure 8: Experimental deformation textures observed after straining to various strain levels in the power law regime ..... 31
Figure 9: The importance of the climb of <a> dislocations during tensile deformation within the low temperature creep regime ..... 32
Figure 10: The influence of strain rate on isothermal tensile testing at 350 °C ..... 33
Figure 11: Experimental and simulated stress strain curves at different temperatures and rates . 34
Figure 12: Experimental and simulated stress strain curves at 350 °C and different rates ..... 35
Figure 13: The importance of the character of the climbing dislocations on high temperature simulations ..... 35

Chapter 2
Figure 1: The determination of slip mode hardening parameters via the mechanical threshold stress (MTS) model ..... 51

Figure 2: Comparison of the experimental texture evolution and r-values with predictions in intermediate temperatures ..... 58

Figure 3: Relative strain accommodation for a range of temperature and strain rates in the intermediate temperature regime ..... 83

Figure 4: Temperature and rate dependencies of a) basal slip, b) prism slip, c) <c+a> slip RSSs and d) climb stress against the Zener Hollomon parameter ..... 61

Figure 5: a) Predicted flow stress and b) strain anisotropy measurements against experimental values obtained in Chapter 1 ..... 62

Figure 6: Strain rate sensitivity predictions with and without climb ..... 63

Figure 7: Predicted activation energies with and without climb incorporation ..... 64

Figure 8: Texture evolution of as-extruded AZ31B samples with geometries to replicate uniaxial straining and equibiaxial stretching ..... 65

Figure 10: Schematic of the slip modes available in FCC and HCP metals ..... 68

Figure 11: Evolution of rate sensitivity and activation energy for each investigated slip mode in AZ31B at an applied strain rate of 0.001 1/s ..... 71

Figure B1: Fitted hardening parameters to experimental flow curves. ..... 79

Figure B2: a) Predicted flow stress and b) strain anisotropy measurements against experimental values obtained in Chapter 1. ..... 79

Figure B3: a) Predicted texture and strain anisotropy evolution for a range of temperatures and strain rates for the TD condition ..... 82

Figure B4: Relative strain accommodation for a range of temperature and strain rates ..... 83

Figure B5: Texture evolution and strain anisotropy predictions without strain hardening responses ..... 84

Figure B6: Relative slip activity plots of 250 and 350 °C simulations without hardening ..... 85

Figure D1: Interpolation of fractions accommodated by each glide mode. ..... 94

Chapter 3

Figure 1: The initial texture of the rolled ZK10 sheet measured in this study using 3 pole figures and a 2-D ($\varphi_2 = 0°$) section of the ODF (Bunge Euler angle convention ($\varphi_1$, $\Phi$, $\varphi_2$)). ..... 98

Figure 2: Constitutive behavior of ZK10 ..... 100

Figure 3: Evolution of the flow stress at 10% true plastic strain with a Garafalo-Sellars-Tegart fit and strain anisotropy ..... 101

Figure 4: Texture evolution after deformation under various temperatures and strain rates ..... 102

Figure 5: Experimental flow stresses when pulled along the transverse direction are compared against VPSC predictions. ..... 104

Figure 6: Optimized simulations for ZK10 using VPSC-CLIMB at elevated temperatures ..... 105

Figure 7: RSA plots for VPSC simulations modeling the presently studied conditions ..... 106
Figure 8: Comparison of the experimental and predicted flow stress and strain anisotropy of ZK10 ..... 106
Figure 9: Texture evolution and r-values using the MTS and climb stress predictions ..... 107
Figure 10: Optimized simulations for ZK10 when climb is excluded..... 109
Figure 11: Comparison of experimental flow stress and strain anisotropy with glide only predictions..... 110
Figure 12: Relative slip activity plots for climb excluded VPSC simulations ..... 110
Figure 13: VPSC simulations of ZK10 using AZ31B parameters..... 112
Figure 14: RSA of VPSC simulations using AZ31B parameters ..... 113
Figure 15: Orientation relationship of a matrix and twinned grain after extension twinning.... 116
Figure 16: Fractional abundance of grain boundary misorientations of AZ31B and ZK10..... 117
Figure 17: Band contrast image of as-rolled and annealed AZ31B..... 118
Figure 18: Band contrast image of as-rolled and annealed ZK10 ..... 119
Figure A1: Inverse pole figure maps of as-rolled and annealed AZ31B and ZK10..... 122
Figure A2: Pole figures of as-rolled and annealed AZ31B and ZK10 ..... 123
Figure A3: Energy Dispersive Spectroscopy (EDS) results of as-rolled and annealed AZ31B. 124
Figure A4: EDS results of as-rolled and annealed ZK10 ..... 125

Chapter 4
Figure 1: Initial textures for AZ31B and ZK10..... 134
Figure 2: The total, <a>, <c> and <c+a> dislocation densities for AZ31B and ZK10..... 136
Figure 3: A comparison between the experimentally observed total and <a> dislocation densities with the predicted mobile density..... 137
Figure 4: Total dislocation densities of pure Mg, AZ31B and ZK10 and the fractions of each type present..... 139
Figure 5: Climb directions of the most well aligned dislocations of the: <a> <c> and <c+a> type under in-plane tension..... 143
Figure 6: The effect of dislocation density on the ratio of pipe diffusion and lattice diffusion-controlled climb in Mg..... 147
Figure 7: Required average dislocation densities needed to accommodate the deformation attributed to climb assuming a heterogeneous dislocation distribution at 250 °C and 350 °C... 148

Chapter 5

Figure 1: Diagram of the M-K method describing the deformation of the bulk material and defect material when subjected to a biaxial strain path ..... 153

Figure 2: Experimental initial as-rolled and extruded textures used during FLD prediction along with the textures used in the following simulations..... 155

Figure 3: Experimental observations along with FLD-VPSC predictions with and without climb ..... 158

Figure 4: Bulk texture evolution for glide-only and climb-incorporating simulations..... 160

Figure 5: Experimental texture measurements of rolled AZ31B tested under various temperatures, strain rates and loading conditions ..... 161

Figure 6: RSA plots for glide-only and climb-incorporating simulations of the bulk..... 162

Figure 7: Defect texture evolution for glide-only and climb-incorporating simulations..... 164

Figure 8: RSA plots for glide-only and climb-incorporating simulations of the defect ..... 167

Figure 9: The RSA plots and forming limits where texture evolution is present, absent in the defect, absent in both the bulk and defect..... 169

Figure 10: The active slip modes when the bulk and defect are strongly textured and randomly textured. ..... 170

Figure 11: Formability comparison between experimental measurements [1] and predictions. 175

Figure 12: Predicted texture evolution in the bulk and defect regions of FLC predictions at 150 °C and a rate of 0.001 1/s..... 175

Figure 13: Relative slip activity plots in the bulk and defect regions of the FLC predictions at 150 °C for a) uniaxial straining, b) plane strain and c) equibiaxial stretching. ..... 175

Figure 14: Predicted and experimental texture evolution of previous models incorporating dynamic recrystallization (DRX)..... 175

Figure 15: A comparison of DRX – incorporating [1] and climb – incorporating simulations against experimental measurements ..... 175176

# Abbreviations and Symbols

Introduction

$a_c$ = dislocation core cross sectional area
$b$ = Burgers vector length
$C_1$ = clamping constant
$D_{eff}$ = effective diffusion coefficient
$D_l$ = lattice diffusion coefficient for vacancies
$D_p$ = pipe diffusion coefficient for vacancies
$d$ = atomic interplanar spacing
$E$ = Young's modulus
$L$ = component length
$M$ = the applied bending moment on a component
$m$ = Schmid factor
$m_t$ = total component mass
$S^*$ = design specified stiffness
$\lambda$ = The angle between the loading direction and slip direction
$\mu$ = shear modulus
$\nu$ = Poisson's ratio
$\rho$ = material density
$\sigma$ = applied stress
$\sigma_y$ = yield strength
$\tau$ = resolved shear stress
$\tau_{PN}$ = Peierls Nabarro stress
$\phi$ = The angle between the loading direction and slip plane normal

Chapter 1

$\left|r_{sim} - r_{exp}\right|_{RD}$ = absolute value of the strain anisotropy difference between simulated and experimental conditions for the rolling direction case
$\left|r_{sim} - r_{exp}\right|_{TD}$ = absolute value of the strain anisotropy difference between simulated and experimental conditions for the transverse direction case
$A$ = Garafalo Sellars Tegart prefactor
$b$ = Burgers vector direction
$c_v$ = vacancy concentration at the dislocation core
$c_v^{th}$ = thermal vacancy concentration at equilibrium
$D_l$ = lattice diffusion coefficient for vacancies
$f$ = Peach Koehler force
$f_0$ = total error for genetic algorithm simulation

$f_c$ = the climb component of the Peach – Koehler force
$f^s_{chemical}$ = chemical force resisting the motion of climbing dislocations
$f_{exp}(g)$ = orientation distribution function for experimental texture
$f_g$ = glide component of the Peach – Koehler force
$f_{sim}(g)$ = orientation distribution function for simulated texture
$I$ = identity tensor
$k_B$ = Boltzmann's constant
$k^{d,s}_{ij}$ = deviatoric component of the Hartley tensor for each slip system
$m$ = macroscopic, power law regime rate sensitivity
$m_c$ = rate sensitivity of climb
$m_g$ = rate sensitivity of glide modes
$m^s_{ij}$ = Schmid tensor for each slip system
$\hat{n}$ = slip plane normal direction
$p$ = hydrostatic pressure
$Q$ = macroscopic activation energy
$q^s_{ij}$ = skew symmetric portion of the Schmid tensor for each slip system
$R$ = ideal gas constant
$R_{cutoff}$ = the dislocation core cutoff radius
$r$ = strain anisotropy
$r^s_{ij}$ = skew symmetric portion of the Hartley tensor for each slip system
$r_{RD\_exp}$ = experimental strain anisotropy when deformed along the rolling direction
$r_{TD\_exp}$ = experimental strain anisotropy when deformed along the transverse direction
$T$ = temperature
$TexErr$ = texture error between the experimental and predicted texture evolutions
$TexErr_{RD}$ = texture error for a sample deformed along the rolling direction
$TexErr_{TD}$ = texture error for a sample deformed along the transverse direction
$t$ = line direction
$\bar{v}_c$ = average climb velocity
$w_r$ = strain anisotropy weighting fraction
$w_{tex}$ = texture weighting fraction
$Z$ = Zener Hollomon parameter
$z_v$ = vacancy capture efficiency

$\alpha$ = Garafalo Sellars Tegart constant that determines the onset of power law breakdown
$\dot{\beta}^s$ = resolved strain rate due to climb on each slip system
$\Gamma$ = accumulated shear in a grain
$\dot{\gamma}^{g,s}$ = shear strain rate for each glide slip system
$\dot{\gamma}_0$ = reference shear rate
$\varepsilon_t$ = thickness strain
$\varepsilon_w$ = width strain
$\dot{\varepsilon}$ = applied strain rate

$\dot{\varepsilon}_{ij}^{c}$ = climb component of the viscoplastic strain rate tensor
$\dot{\varepsilon}_{ij}^{g}$ = glide component of the viscoplastic strain rate tensor
$\dot{\varepsilon}_{ij}^{vp}$ = total viscoplastic strain rate tensor
$\theta_0^s$ = the initial hardening rate
$\xi$ = the cross product of the Burgers vector and slip plane normal directions
$\rho_c^s$ = mobile dislocation density for climbing
$\sigma$ = resolved normal stress
$\sigma'$ = deviatoric component of the applied stress
$\sigma^{c,s}$ = climb threshold stress
$\tau$ = resolved shear stress
$\tau^{g,s}$ = critical resolved shear stress
$\tau_0^s$ = initial critical resolved shear stress with no slip mode hardening
$\tau_0^s + \tau_1^s$ = back – extrapolated critical resolved shear stress
$\Phi$ = angle associated with the rotation around the Z axis in the Bunge convention
$\phi_1$ = angle associated with the first rotation around the X axis in the Bunge convention
$\phi_2$ = angle associated with the second rotation around the X axis in the Bunge convention
$\chi$ = the climb plane normal direction
$\psi$ = angle between the Burgers vector and line directions that determines dislocation character
$\Omega$ = atomic volume
$\dot{\omega}_{ij}^{c}$ = rotation of rotation tensor for climb
$\dot{\omega}_{ij}^{g}$ = rate of rotation tensor for each glide mode

Chapter 2
$A$ = fraction of the total dislocations needed to climb at 0 K and 0 1/s
$A_{DC}$ = pre-power law factor for diffusional creep
$A_{GBS}$ = pre-power law factor for grain boundary sliding
$a_c$ = cross sectional area of the dislocation core
$B$ = temperature dependence on the fraction of total dislocations needed to climb
$b$ = Burgers vector
$C$ = strain dependence on the fraction of total dislocations needed to climb
$C_1$ = interaction parameter
$C_2$ = experimental constant for power law creep
$C_l$ = fitted constant for the intermediate stress regime of the multiscale bowout model
$C_p$ = fitted constant for the low stress regime of the multiscale bowout model
$c_s$ = solute concentration
$D^s$ = drag stress for the $s^{th}$ slip mode
$D_0$ = rate at which the shear modulus decreases with temperature
$D_l$ = lattice diffusion coefficient for vacancies
$D_p$ = pipe diffusion coefficient for vacancies
$D_{sd}$ = self diffusion coefficient
$e$ = total energy changes associated with solutes entering and leaving the dislocation core

$f_c$ = fraction of strain accommodated by <a> climb
$f_i$ = fraction of strain accommodated by the i$^{th}$ slip mode
$g$ = grain size dependence in grain boundary sliding
$g_{ss}$ = normalized, stress – independent activation energy
$H_{dk}^{o}$ = enthalpy of double kink formation
$\bar{k}$ = Hartley factor averaged over every grain
$k_B$ = Boltzmann's constant
$k_1^s$ = material constant related to dislocation storage
$k_2^s$ = temperature and strain rate dependent constant related to dynamic recovery
$m$ = strain rate sensitivity
$\bar{m}_i$ = average Schmid factor for the $i^{th}$ slip mode
$N$ = number of slip modes available
$n$ = stress exponent
$n_c$ = stress exponent of the climb mode
$n_{g,i}$ = stress exponent of the i$^{th}$ glide mode
$P_{dk}$ = softening parameter
$p$ and $q$ = constants that describe the arrangement of dominant obstacles
$Q$ = activation energy
$R$ = ideal gas constant
$S$ = number of sites that can be occupied in the kink by solute
$S_c$ = number of unique core energies
$s_i$ = functional form of the temperature dependence for the resistance due to impurity particles
$s_p$ = functional form of the temperature dependence for the lattice resistance (Peierls)
$s_\varepsilon$ = functional form of the temperature dependence for the resistance due to the stored dislocation density
$T$ = temperature
$T_0$ = reference temperature
$\bar{v}_c$ = average climb velocity
$z_v$ = vacancy capture efficiency

$\alpha$ = mobile and forest dislocation interaction constant
$\alpha_1$ = stress exponent for power law creep
$\dot{\bar{\beta}}$ = resolved strain rate averaged over all grains
Γ = accumulated shear in a grain
$\dot{\bar{\gamma}}$ = shear rate of the $i^{th}$ slip mode averaged over all grains
$\dot{\gamma}_0$ = reference shear rate
$\Delta E_b$ = characteristic energy barrier for the multiscale bowout method
$\overline{\Delta E}$ = mean energy of the possible sites within the screw dislocation core
$\Delta F$ = intrinsic obstacle strength
$\Delta G$ = activation barrier for glide
$\delta E$ = standard deviation of the possible sites
$\varepsilon$ = applied strain rate

$\dot{\varepsilon}_0$ = reference strain rate
$\dot{\varepsilon}_{ij}^c$ = climb component of the viscoplastic strain rate tensor
$\dot{\varepsilon}_{ij}^g$ = glide component of the viscoplastic strain rate tensor
$\theta_0^s$ = the initial hardening rate
$\theta_{II}$ = the steady state work hardening rate
$\kappa$ = constant related to slip mode hardening in the mechanical threshold stress model
$\mu$ = shear modulus
$\mu_0$ = shear modulus at 0K
$\rho$ = total dislocation density
$\tilde{\rho}$ = dislocation fraction needed to climb to accommodate the fraction of strain attributed to climb
$\rho_m^c$ = mobile climbing dislocation density
$\sigma$ = applied stress
$\sigma_c$ = climb stress
$\tau$ = resolved shear stress
$\hat{\tau}$ = critical stress to activate glide at 0K
$\tau^\bigstar$ = Peierls stress for the prismatic plane
$\tau^o$ = cross slip stress
$\tau_0^s$ = initial critical resolved shear stress with no slip mode hardening
$\tau_0^s + \tau_1^s$ = back – extrapolated critical resolved shear stress
$\tau_a$ = athermal stress
$\hat{\tau}_i$ = stress needed to overcome resistance caused by impurity atoms at 0K
$\hat{\tau}_p$ = stress needed to overcome lattice resistance at 0K
$\hat{\tau}_\varepsilon$ = stress needed to overcome dislocation – dislocation interactions at 0K
$\hat{\tau}_{\varepsilon s}$ = saturation stress for work hardening
$\tau_{sat}^s$ = saturation stress for the s$^{th}$ slip mode
$\tau_{y0}$ = yield stress at 0K
$\phi$ = fitted exponent for the low stress regime of the multiscale bowout model
$\Omega$ = atomic volume

Chapter 3
$A$ = Garafalo Sellars Tegart prefactor
$a_c$ = cross sectional area of the dislocation core
$a$ and $b$ = fitted parameters for the climb stress
$b_i$ = Burgers vector of type i
$C_l$ = interaction parameter
$c_v$ = equilibrium vacancy concentration
$D$ = drag stress
$D_{sd}$ = self diffusion coefficient
$D_0$ = diffusivity preexponential
$D_{eff}$ = effective vacancy diffusion
$D_l$ = lattice diffusion coefficient for vacancies
$D_p$ = pipe diffusion coefficient for vacancies

$g_{0,i}$ = stress normalized activation energy for the i$^{th}$ slip mode
$g_{ss}$ = normalized, stress – independent activation energy for slip mode hardening
$\bar{k}$ = average Hartley factor
$k_1^s$ = material constant related to dislocation multiplication
$k_2^s$ = temperature related constant related to recovery (dislocation annihilation)
$k_B$ = Boltzmann's constant
$l$ = dislocation line length
$N$ = number of slip modes
$n$ = stress exponent
$p$ and $q$ = constants that describe the arrangement of the dominant obstacles
$Q$ = macroscopic activation energy
$r$ = strain anisotropy
$T$ = temperature
$t$ = texture error between the experimental and simulated texture evolution
$\bar{v}_c$ = average climb velocity
$Z$ = Zener Hollomon parameter

$\alpha$ = Garafalo Sellars Tegart constant that determines the onset of power law breakdown
$\bar{\alpha}$ = average interaction parameter between mobile and forest dislocations
$\dot{\beta}$ = resolved strain rate
$\gamma$ = stacking fault energy
$\dot{\gamma}$ = applied shear rate
$\dot{\gamma}_0$ = reference strain rate
$\theta_0$ = initial hardening rate
$\mu$ = shear modulus
$\tilde{\rho}$ = fraction of the Taylor density that must climb
$\rho_m^c$ = mobile, climbing dislocation density
$\rho_T$= Taylor dislocation density
$\sigma$ = applied stress
$\sigma'$ = applied deviatoric stress
$\sigma_c$ = climb stress
$\sigma_{crit}$ = critical stress for power law breakdown
$\tau_i$ = critical resolved shear stress of slip mode i
$\tau_{a,i}$ = athermal stress of i$^{th}$ slip mode
$\tau_0^s + \tau_1^s$ = back – extrapolated critical resolved shear stress
$\frac{\hat{\tau}_i}{\mu_0}$ = temperature hardening factor
$\Phi$ = angle associated with the rotation around the Z axis in the Bunge convention
$\phi_1$ = angle associated with the first rotation around the X axis in the Bunge convention
$\phi_2$ = angle associated with the second rotation around the X axis in the Bunge convention
$\Omega$ = atomic volume

Chapter 4

$< \varepsilon_{g,L}^2 >$ = mean square strain

$A_L$ = Fourier coefficients of the diffraction profile

$A_L^D$ = Fourier coefficients of the diffraction profile due to strain effects

$A_L^S$ = Fourier coefficients of the diffraction profile due to size effects

$a$ = lattice parameter

$b$ = Burgers vector

$\bar{C}^i$ = average contrast factor of the i$^{th}$ dislocation type

$\bar{C}_{hk.0}$ = average contrast factors for each (hk.0) reflection

$\bar{C}_{hk.l}$ = average contrast factors for each (hk.l) reflection

$c$ = the length of the <c> axis (5.21 Å in Mg)

$D_0$ = rate at which the shear modulus decreases with temperature

$D_l^{sd}$ = self diffusion coefficient through the lattice

$D_l$ = lattice diffusion coefficient

$D_p$ = pipe diffusion coefficient

$d$ = height of the jog

$d_{hk.l}$ = interplanar spacing

$E_0$ = energy required to form the kink

$f_w$ = fraction of the grain comprised of dislocation cell walls

$g$ = diffraction vector

$h$ = time step for forward difference method

$h_i$ = fraction of total dislocation density of the i$^{th}$ type

$I^D$ = intensity broadening due to strain effects (i.e., dislocations)

$I^P$ = peak intensity

$I^S$ = intensity broadening due to size effects of the crystallites

$k$ = Hartley tensor

$k_1^i$ = material constant controlling the storage of dislocations

$k_2^i$ = temperature and strain rate dependent constant defining the dynamic recovery of dislocations

$k_B$ = Boltzmann's constant

$L$ = Fourier length

$P$ = normalization factor representing the averaged (hk.0) contrast factors weighted by their Burgers vectors

$q_1$ and $q_2$ = elastic property dependent parameters used to calculate the average contrast factors

$R_e$ = cutoff radius

$r_i$ = recovery rate of dislocation type i

$T_0$ = reference temperature

$U_j$ = jog formation energy

$U_{jp}^c$ = critical jog pair formation energy

$v_l$ = climb velocity controlled by lattice diffusion

$v_p$ = climb velocity controlled by pipe diffusion

$X$ = mean free path of a jog nucleating from a pair
$x$ = jog separation distance

$\dot{\beta}$ = resolved strain rate
$\gamma$ = shear strain
$\Delta E$ = energy needed for the dislocation to climb between low energy sites
$\Delta x$ = mean free path for vacancy diffusion
$\Delta U_{sd}^{(v,p)}$ = energy difference between lattice and pipe self diffusion
$\kappa_1$ and $\kappa_2$ = constants related to the static recovery of dislocations
$\mu$ = shear modulus
$\mu_0$ = shear modulus at 0 K
$\rho_i$ = dislocation density of interior region of the grain
$\rho_0$ = initial dislocation density
$\rho_c$ = current dislocation density
$\rho_w$ = dislocation density of wall region of the grain
$\rho_{GND}$ = density of geometrical necessary dislocations
$\rho$ = dislocation density
$\sigma$ = applied stress tensor
$\sigma_c$ = climb stress

Chapter 5
$f$ = ratio of the defect to the bulk thickness
$\bar{k}_{<a>}$ = average Hartley factor for <a> dislocation climb
$m$ = rate sensitivity
$\bar{m}_i$ = average Schmid factor for the i$^{th}$ glide mode

$\Delta\varepsilon$ = strain increment under uniaxial straining conditions
$\Delta\varepsilon'$ = strain increment under non uniaxial straining conditions
$\varepsilon_{eq}$ = von Mises equivalent strain
$\varepsilon_f$ = strain at failure as defined by plastic instability
$\dot{\varepsilon}_{ij}^a$ = bulk strain rate boundary conditions
$\dot{\varepsilon}_{ij}^b$ = defect strain rate boundary conditions
$\nu$ = Poisson's ratio
$\sigma_{ij}^a$ = stress boundary conditions in the bulk material
$\sigma_{ij}^b$ = stress boundary conditions in the defect material
$\tau_0^s$ = initial critical resolved shear stress for s$^{th}$ mode
$\tau_0^s + \tau_1^s$ = back extrapolated critical resolved shear stress for s$^{th}$ mode
$\rho$ = ratio of the minor straining direction to the major straining direction
$\phi$ = angle of inclination between the major straining direction and the defect
$\phi_0$ = initial orientation of the defect

# Introduction

Magnesium has an abundance of potential applications owing to its status as the lightest structural metal (its density is 66% of that of Al and 40% of that of Ti). It is an attractive choice for the aerospace and automotive industries [2] in select applications which are not specific strength limited (i.e., in bending) to promote weight savings and, as a result, fuel efficiency. Under a bending load, there is a gradient in the stress state from compressive on one side to tensile on the other (Figure 1). This requires that the stress be zero at the center of the rod (known as the neutral axis), making material in the center of the component less efficient at carrying load.

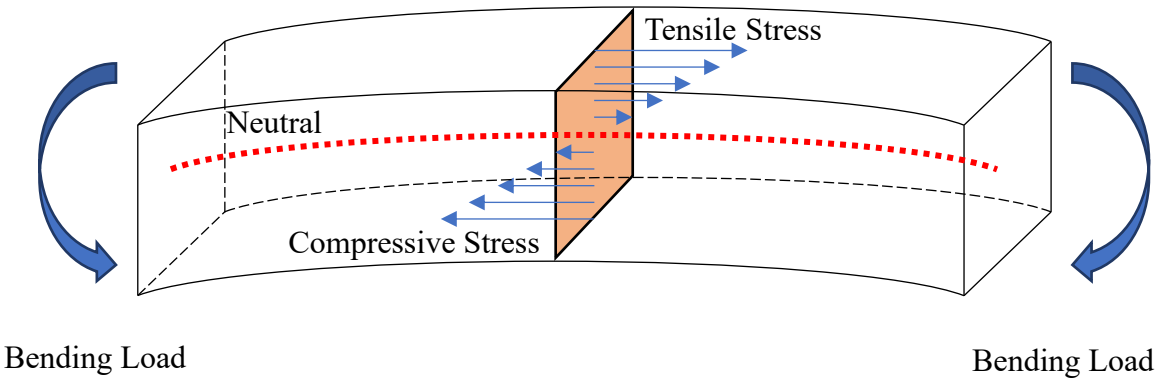


Figure 1: Diagram of a rectangular rod under a bending load. Note that material farther from the neutral axis is carrying more stress.

This creates two avenues to make lightweight components: changing the geometry of the part to move material away from the neutral axis or making a larger component out of a less dense material. The former solution is a geometric problem; the latter is a matter of material selection. This is reflected in the formal definitions for stiffness-limited and strength-limited design criteria of lightweight beams are given in Equations 1 and 2, respectively [3]

$$m_t = \sqrt{\frac{12S^*L^3}{C_1}} L \left(\frac{\rho}{\sqrt{E}}\right) \qquad Equation\ 1$$

$$m_t = (6M)^{\frac{2}{3}} L \left(\frac{\rho}{\sqrt[3]{\sigma_y^2}}\right) \qquad Equation\ 2$$

where $m_t$ is the total mass of the component, $S^*$is the component stiffness required by the design, $L$ is the length of the component, $C_1$is a constant determined by how the component is clamped, $\rho$ is the material density, $E$ is the Young's Modulus, $M$ is the bending moment and $\sigma_y$ is the yield strength. The minimization of material parameter combinations ($\rho/\sqrt{E}$ or $\rho/\sqrt[3]{\sigma_y^2}$ ) minimizes the weight of the component that satisfies the design requirements. Magnesium

compare favorably to other common materials such as Al, Ti and steel under these conditions, suggesting that its alloys could be used for many future applications.

Materials to be adopted by industry must be easily processed (e.g., forming, welding, rolling, etc.) Currently, most applications for Mg parts are die cast [4], although interest for wrought Mg parts (extrusions, rolled sheet, etc.) has been growing since the mid-1990s [5]. Wrought parts have several advantages over the as-cast condition such as finer grain sizes [6] and altered morphologies of secondary phases [7], which lead to better mechanical properties. The difficulty of forming a material is predicted by the Von Mises criterion ([8], [9]), which requires 5 independent slip systems to accommodate an arbitrary load. In most common engineering materials (e.g., Al, Cu), the large quantity of easy $\{111\}$ slip systems in cubic metals allow them to easily meet the Von Mises criterion and are more likely to delay necking and failure to higher strain levels. In contrast, HCP materials, such as Mg and its alloys, have relative few active slip systems at room temperature and do not meet this criterion easily. For these materials, processing must be done at elevated temperatures (> 100 °C) to avoid premature cracking by activating additional slip modes (collections of slip systems using the same family of planes and slip directions). In addition, secondary phases present in Mg alloys also limit the processing rate [10], which makes the processing of Mg components currently less cost effective than other, more common engineering materials. Substantial effort has been put into improving the ductility of Mg via alloying with Li [11], [12] and Y [12], [13] and understanding the deformation of its alloys at elevated temperatures [14] to take advantage of their appealing properties for specific applications with varying degrees of success.

## 1- A mechanistic picture of dislocation glide in HCP Mg

Deformation at room temperature is achieved mainly through the motion of dislocations on closed packed planes along close packed directions. The basal plane ($\{0001\}$) is the closed packed plane in Mg and easy slip occurs along the <a> directions ($< 11\bar{2}0 >$), of which there are two independent directions (two independent slip systems) (Figure 2). Prism slip is also known to operate at room temperature and provides two additional independent slip systems [15]. The last slip mode observed in Mg is the motion of <c+a> ($< 2\bar{1}\bar{1}\bar{3} >$) dislocations on pyramidal planes ($\{\bar{1}10\bar{1}\}$ - first order or $\{2\bar{1}\bar{1}2\}$ - second order) [16], but it is more difficult to activate at room temperature due to its high Peierls-Nabarro stress (Equation 3).

$$\tau_{PN} = \frac{2\mu}{1-\nu} e^{-\frac{2\pi d}{(1-\nu)b}} \qquad Equation\ 3$$

$\tau_{PN}$ is the Peierls-Nabarro stress, $\mu$ is the shear modulus, $\nu$ is Poisson's ratio, $d$ is the interplanar spacing and $b$ is the Burgers vector. <c+a> dislocations have a Burgers vector length of 6.11 Å, compared to 3.21 Å in <a> dislocations.

However, it has been found to operate during room temperature deformation of Mg due to the addition of grain compatibility stresses [17] or in specific alloys (Mg-Li [11], [12] and Mg-Y [12], [13]). In addition to dislocation glide, room temperature deformation of Mg alloys

can be accommodated by crystallographic twinning. In contrast to dislocation glide, twinning involves a radical reorientation of lattice with respect to the matrix material and is a polar mechanism (i.e., each twinning mode can only occur in either tension or compression). The most common mechanisms in Mg are extension and compression twinning, which most likely occur when the crystal is compressed along the <c> axis [18]; however, twinning mechanisms have limited strain carrying capacity and can only occur in untwinned regions of material. Typically, the greatest impact that twinning has on deformation is grain reorientation, which can activate other slip modes.

Each slip mode has a critical resolved shear stress (CRSS) needed to overcome obstacles, such as lattice friction or the stress fields of other defects. In addition to differences in the relative CRSSs, the applied stress must be resolved onto the slip plane and in the direction of slip, denoted by the Schmid factor (Equation 4)

$$\tau = m\sigma = \sigma \cos(\phi) \cos(\lambda) \qquad Equation\ 4$$

where m is the Schmid factor and $\sigma$ is the applied stress. Straining due to glide becomes significant when $\tau$ is comparable to the CRSS.

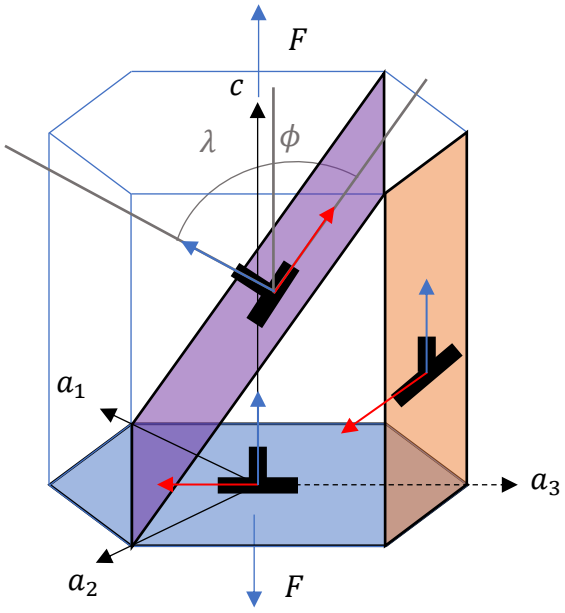


Figure 2: Common slip systems in HCP crystals: basal <a> ($\{0001\} < 11\bar{2}0 >$ - blue), prism <a> ($\{10\bar{1}0\} < 11\bar{2}0 >$ - orange) and pyramidal II <c+a> ($\{2\bar{1}\bar{1}2\} < 2\bar{1}\bar{1}\bar{3} >$ - purple). Under <c> axis loading, only pyramidal II <c+a> has a nonzero Schmid factor. Red arrows denote the glide motion of the relevant dislocations; blue arrows represent climb.

From preceding analysis, it becomes clear that basal and prism slip cannot accommodate strains along <c> axis, as their Schmid factors are zero. In addition, Mg does not satisfy the Von Mises criterion with basal and prism slip alone, as this falls short of the 5 independent slip systems required. Thus, it seems apparent that the 5$^{th}$ independent slip must also accommodate strain along the <c> axis. The addition of <c+a> slip has been proposed as a means of meeting the Von Mises criterion. <c+a> slip is a hard slip mode to activate at room temperature, as previously mentioned, and its absence could explain the poor ductility observed in dilute Mg alloys tested at room temperature (AZ31B ([19], [20]), ZK10 [21]). Increasing the temperature may facilitate the activation of <c+a> slip, as it is known to be highly temperature sensitive [16]. Proposed models of the constitutive behavior have suggested that the cross slip of <c+a> dislocations between pyramidal planes is the rate limiting step in the continued deformation [14].

Thus far, only the conservative glide of dislocations has been considered. Dislocations can also climb out of their slip planes under resolved normal stresses (analogous to Equation 4) assisted by vacancy diffusion. Dislocation climb is inactive at room temperature due to the incredibly slow rates of diffusion; therefore, like <c+a> slip, dislocation climb is highly temperature dependent. However, classical creep theories in the literature assume that climb is the rate limiting step due to its reliance on vacancy diffusion and, as a result, only accommodates small amounts of strain. This model of high temperature defomation is known as the "climb and glide" creep model [22], where climb is assumed to be a recovery mechanism. It should be noted that the climb of <a> dislocations can also accommodate <c> axis strains, as their motion is perpendicular from the basal plane (Figure 2). This is of great interest to the current body of work, as the ability of climb to accommodate significant strain in HCP materials is currently unknown and methods to interrogate its role in high temperature deformation have recently been developed ([23], [24]).

*The shortcomings of a <c+a> controlled model and the merits of a climb incorporating model*

In the literature, <c+a> slip has been proposed to be the operative mechanism during high temperature deformation, as it is typically inactive at room temperature and its activation can allow Mg to satisfy the Von Mises criterion. In addition, crystal plasticity modeling work by Agnew & Duygulu demonstrated that the activation of <c+a> slip can reduce the strain anisotropy in agreement with uniaxial tension experiments [20]. However, a dominant <c+a> slip model for high temperature deformation is a deficient explanation in several ways. First, it cannot simultaneously model the texture evolution and the strain anisotropy, as the addition of <c+a> slip causes an extraneous texture component in the basal pole figure [20]. This is due to the intrinsic shear imposed on the grain as the <c+a> dislocation glides, which attempts to rotate the <c> axes away from the sheet normal direction (assuming that the sheet initially has an as-rolled and annealed texture, which aligns the <c> axes with the sheet normal direction). The activation of <c+a> slip is also unlikely to explain an increase in rate sensitivity and a plateau in activation energy with the emergence of the power law regime [19]. It is not obvious how the addition of another glide mode with similar rate sensitivity to basal and prismatic glide would dramatically change the observed macroscopic rate sensitivity. Changes in macroscopic rate sensitivity in viscoplastic self-consistent (VPSC) simulations are typically incorporated by *ad hoc* adjustments to the glide mode rate sensitivities [25]. Similar arguments can be made for the

plateauing activation energy. While it is clear that <c+a> slip should have a higher activation energy than other glide modes due to the higher temperature dependence on its CRSS, it is unlikely to result in a plateau in activation energy. The activation energy of glide modes is typically believed to be stress dependent [26]

$$\Delta G = \Delta F \left[1 - \left(\frac{\sigma_s}{\hat{\tau}}\right)^p\right]^q \qquad Equation\ 5$$

where $\Delta F$ is the free energy necessary to activate slip without assistance from stress, $\sigma_s$ is the applied shear stress, $\hat{\tau}$ is the stress required to active glide without thermal energy. $p$ and $q$ determine the arrangement of obstacles interfering with glide. It is well known that the flow stress (and therefore the applied shear stress) decreases with increasing temperature, which suggests that the activation of energy of <c+a> slip (and other glide modes) should monotonously increase with temperature.

The issues raised in a <c+a> glide based model can be explained if climb is able to accommodate significant strain. As previously stated, climb can behave as the 5$^{th}$ independent slip mode and act as a convenient mechanism to accommodate <c> axis strains. The kinematics of climb also explain the experimental observations of texture evolution, strain anisotropy, rate sensitivity and activation energy. Climbing dislocations do not impart shear strains during their motion (assuming they are pure edge dislocations [23]) and therefore do not contribute to texture evolution; significant strain accommodation via climb could explain experimental observations of slowed texture evolution [20]. The rate sensitivity and activation energy of climb are much higher (~1/7-1/5 - ~1/5-1/3 and 92 - 135 kJ/mol, respectively) than glide modes and could explain the rapid increase in rate sensitivity and activation energy seen experimentally [19]. The temperature dependence on the activation energy is also much less pronounced in climb and therefore more likely to result in a plateau. Interestingly, allowing climb to accommodate significant amounts of strain would suggest that climb can operate independently of glide, in contrast to the climb and glide model (Figure 3).

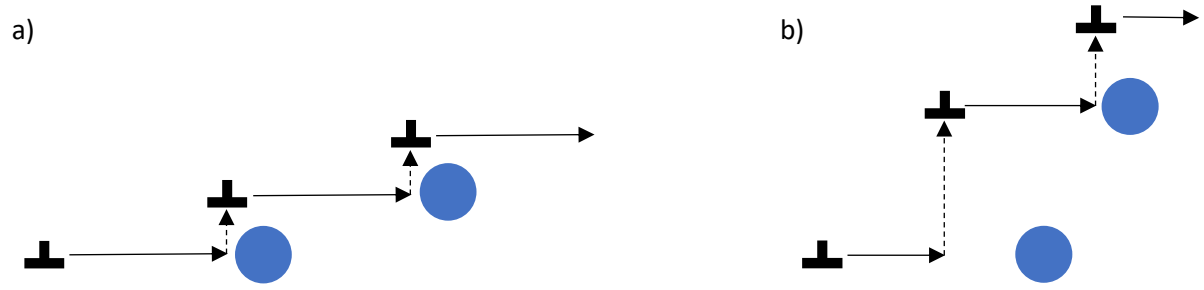


Figure 3: A schematic of a) a dislocation undergoing climb and glide creep (note that the distance traversed by glide (and therefore the accommodated strain) is much larger than climb) and b) a dislocation moving assuming that glide and climb are independent. Here, climb can activate in the absence of obstacles and is not limited to the minimum distance needed to avoid the obstacle's stress field. Note that the strain contributions from climb and glide are closer to equal in this case.

*Role of pipe diffusion in high temperature deformation*

Deformation in materials can be described by the glide and climb of dislocations in most temperatures and rates of interest [27] [1]. Near ambient temperature deformation is dominated by glide, as vacancy diffusion (and therefore climb) is sluggish. At elevated temperatures, climb becomes active due to the increased vacancy diffusion. Vacancies have 2 major pathways to facilitate climb: through the lattice and dislocation cores[2]. At intermediate temperatures, core (or pipe) diffusion dominates as the activation energy is lower (92 kJ/mol in Mg [27]); pathways for vacancy diffusion and the diffusivity are dependent on the dislocation density (and indirectly, the applied stress). At even higher temperatures (>~ 200 °C), there is sufficient thermal energy for lattice diffusion to dominate, even though the activation barrier is higher (~135 kJ/mol in Mg [27]). An effective diffusivity [27] is used to define contributions from lattice ($D_l$) and pipe ($D_p$) diffusion. $a_c$ defines the cross sectional area of the dislocation core, $b$ is the burgers vector and $\mu$ is the shear modulus.

$$D_{eff} = D_l\left(1 + \frac{10a_c}{b^2}\left(\frac{\sigma}{\mu}\right)^2 \frac{D_p}{D_l}\right) \qquad Equation\ 6$$

Expressions such as Equation 6 typically assume that the dislocations are homogeneously distributed throughout the sample when determining which mechanism controls vacancy diffusion. In reality, materials form cell structures which have sparse densities in their interiors and high densities (>$10^{16}$ 1/m$^2$) in their walls([28], [29])(Figure 4). As a result, pipe diffusion can theoretically occur in the cell walls at temperatures where lattice diffusion is expected to be dominant. Therefore, the limiting conditions for significant pipe diffusion are currently uncertain. These conditions are important, as the diffusivity controls the strain that can be accommodated by climb and may extend the viability of climb strain accommodation outside of the power law regime.

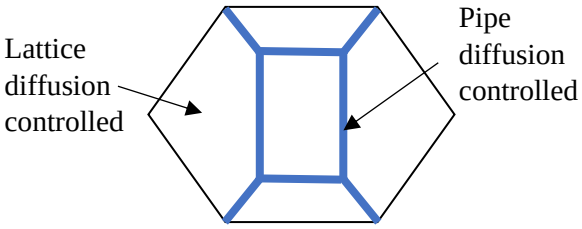


Figure 4: Idealized model of a heterogeneously distributed dislocation microstructure. Light black lines represent grain boundaries and thick blue lines represent regions of high dislocation densities

[1] At very high temperatures and low strain rates that are generally outside the scope of this body of work, grain boundary sliding and diffusional flow creep may become the dominant mechanism.

[2] Grain boundaries can also serve as a diffusion mechanism for vacancies; however, it is unlikely to be the primary diffusion path as most dislocations are likely in the grain interior.

## 2- Additional repercussions of climb and controlling factors in its activation

*Reprecussions of a climb incorporating model: forming limit diagram predictions*

As mentioned previously, industrial use typically requires materials to be formed into specific shapes. Adoption of a material requires understanding the mechanisms by which the material deforms, but also an understanding of its ductility under different loading conditions. Thus far, the focus has been on the physics of deformation; the practicality of sheet forming is yet to be addressed. The formability of an alloy is typically represented by a forming limit diagram (FLD) [30], which describes the conditions under in-plane biaxial straining where the material fails (Figure 5). The FLD typically encompasses three important strain paths: uniaxial stretching (minor strain is half the major strain and negative), plane strain (zero minor strain), equibiaxial stretching (minor strain equals major strain). Each condition is experimentally obtained by punch testing sheet samples machined into different geometries to enforce the various strain paths [31]. As noted in Figure 6, three outcomes are possible: safety – the punched sample shows no localized yielding, necking and failure. The forming limit curve (FLC) is drawn between the safe forming conditions and predicts where the material will begin to localize deformation.

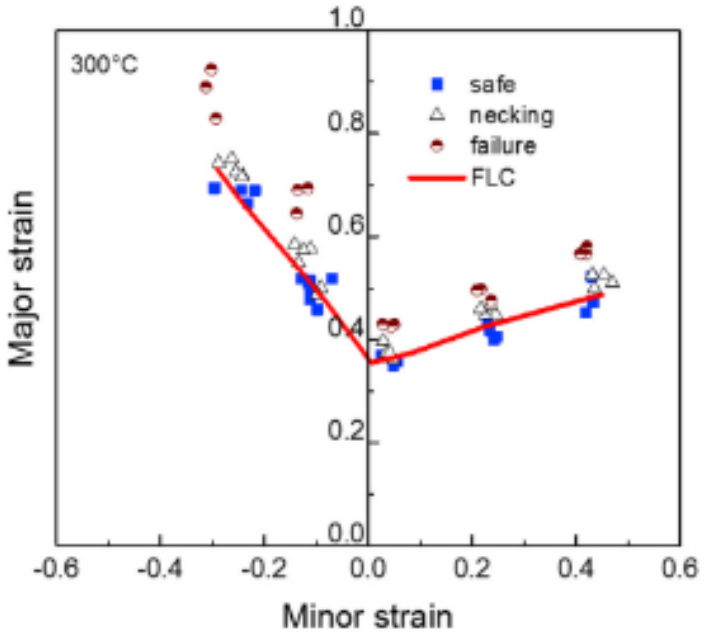


Figure 5: Forming limit diagram of AZ31B at 300 °C taken from Li et al. [1]. Above the forming limit curve (FLC), the material is likely to neck or fracture.

The experimental determination of FLDs is a time consuming and expensive process, as it requires the machining numerous samples in different geometries to determine the FLC at a specific temperature and strain rate for a single alloy. Thus, many means of predicting formability have been developed. The most common method of predicting FLCs uses the Marciniak-Kuczyński (M-K) method [32]. It is assumed that the sheet material being deformed through in-plane biaxial straining contains a defective region of lower strength or thickness,

which will fail during deformation by plastic instability, defined as the defect region thinning much faster (usually 20 times) as the matrix. Compatibility and equilibrium between the matrix and the defect are enforced and a description of yield behavior is required. Several analytical models for yield behavior exist [33]–[35]; however, using a viscoplastic self-consistent (VPSC) model can also incorporate plastic anisotropy and texture evolution into the formability predictions [25], which is important in non-cubic materials. Previous formability predictions of AZ31B [25] could not account for the role of climb and instead accommodated significant strain through <c+a> slip at elevated temperatures. The reported texture evolution of uniaxial strained and plane strained AZ31B at 200 °C displayed obvious splitting of the basal pole figure, which is at odds with the measured textures of Bohlen et al. [36] at 200 °C. This parallels the work of Agnew & Duygulu [20] that attempted to model the uniaxial tension of AZ31B using <c+a> glide and further suggests that <c+a> slip cannot accommodate large amounts of strain at high temperature and behooves the inclusion of climb into the prediction of high temperature deformation of other strain paths.

*The role of texture on slip mode selection*

As alluded to previously in Figure 2 and Equation 4, Schmid factors influence which glide modes activate due to the relative orientation of the slip plane and direction to the applied stress. It has been discussed that a change in the applied loading direction can result in the activation of different slip modes, but the same effect can be obtained by rotating the lattice (i.e., changing the texture). This is corroborated by previous studied which have noted that stronger textures lead to reduced formability ([36], [37]), which may limit the number of slip modes activated. The formation of texture is dependent on the deformation imposed on the untextured cast material. The typical texture for rolled Mg alloy AZ31B has the basal planes aligned with the sheet normal direction (ND) and an almost random distribution of prism planes around the <c> axes (ND) (Figure 6a). A similar dilute alloy, ZK10 (Mg-1 wt% Zn -0.3 Zr), will also be studied, as it has been reported to have a different texture (a split peak in the basal plane (Figure 7) [38]), yet the diffusivities of Al, Zn and Mg in Mg [39] are very similar, suggesting that solute effects on gliding dislocations may be insignificant between each alloy.

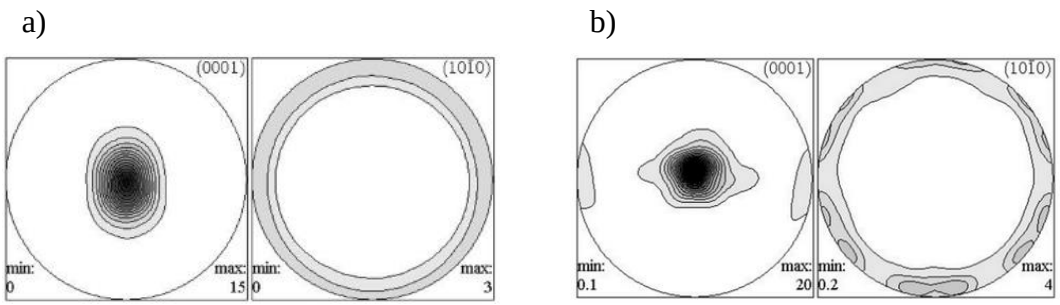


Figure 6: Initial as-deformed texture of a) rolled and annealed and b) extruded and annealed AZ31B [36]. The rolling and extruded directions are vertical and the transverse directions are horizontal in the figure.

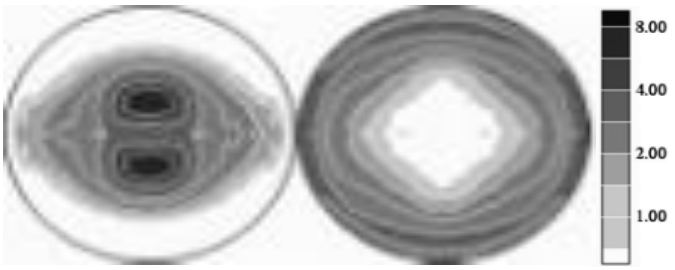


Figure 7: As rolled and annealed texture of ZK10 [38]. The rolling direction is vertical and the transverse direction is horizontal in the figure.

While alloy chemistry may not affect the glide of dislocation, it may play a role in the dislocation populations present in ZK10. It has been reported that ZK60 (an alloy with a very similar solute content in the matrix to ZK10) has a significant population of <c> dislocations present [40] in contrast to AZ31B [29]. These dislocations are believed to be generated from the sweeping of the matrix by twins generated during rolling and present during the anneal. These twin boundaries become the grain boundaries as exhibited by ZK60 [41], which has many adjacent grains with twinning misorientations. <a> dislocations swept by the twin boundaries become ½ <c+a> in the twinned region [29], which form perfect <c+a> dislocations. <c+a> dislocations are inherently high energy due to their large burgers vectors and are likely to dissociate. Molecular dynamics simulations have shown that <c+a> dislocations can dissociate into partial or perfect <c> and <a> dislocations under applied load [42]. The dissociation reaction into perfect <c> and <a> dislocations has been shown to be energetically favorable if the <c+a> dislocation is pinned on both sides to the twin boundary [29]. The presence of significant densities of <c> and <c+a> dislocations may require additional considerations of their climb and would serve to further understand the ability of climb to accommodate strain.

**3- Outline of thesis contents**

Substantial work has been previously done to understand the high temperature deformation of Mg and its alloys. Most of it has been centered around the idea that the activation

of <c+a> slip is critical to enhance ductility due to the fulfillment of the Von Mises criterion, which Mg cannot satisfy at room temperature using softer basal and prism slip. However, much of the literature ignores the strain carrying capacity of climb and instead invokes a "climb and glide" model which assumes that climb is the rate limiting step in creep and exists only as a recovery mechanism to overcome obstacles to glide. This body of work intends to address the potential role of climb strain accommodation during high temperature deformation and perhaps explain discrepancies between experimental measurements and crystal plasticity modeling predictions.

Chapter 1 will entail measurements of flow stress, texture evolution and strain anisotropy (r-value) at discrete temperature and strain rates for a common wrought alloy, AZ31B. Crystal plasticity modeling using a viscoplastic self-consistent framework that can account for the activity of climb (VPSC-CLIMB) will be performed to determine the CRSSs and climb stress required to predict the strain anisotropy and texture evolution of each selected condition. Optimization of the CRSSs and climb stress to the experimental r-values and texture evolution will be implemented through a genetic algorithm. Predicted climbing dislocations densities will be presented to determine if the amount of climb accommodated deformation is reasonable.

Chapter 2 will extend the discrete values of CRSSs and climb stresses to interpolate the behavior of AZ31B between room temperature and the power law creep regime. Additional simulations using the methodology proposed in Chapter 1 for intermediate temperatures investigate the role of climb outside the power law regime. Chapter 2 will also include comparisons of the rate sensitivity and activation energy from experimental measurements and predictions derived from an independent summation of the strain contributions of glide and climb.

Chapter 3 will endeavor to repeat the study performed in Chapter 1 using another dilute alloy, ZK10. The purpose of this chapter is to understand the extent to which initial texture influences the ability of climb to accommodate strain and to extend the idea of significant climb strain accommodation to other dislocation types.

Chapter 4 will present the results of x-ray line profile analysis (XLPA), which will estimate the dislocation densities (and the fractions of each type) present after deformation. This will allow an experimental comparison with the predicted densities in Chapters 1 and 3 and allow a discussion of the effects of pipe diffusion in the deformation of Mg alloys and the prevalence of static recovery on ex-situ dislocation density measurements in Mg alloys.

Chapter 5 will explore additional strain paths aside from uniaxial tension to establish the limits of strain accommodation via climb. Forming limit curves (FLCs) will also be predicted using the M-K method and a yield description generated by VPSC-CLIMB. These new predictions will be compared against glide only predictions and experimentally observed FLCs. Chapter 5 may also elucidate the mechanisms resulting in the onset of plastic instability.

A list of conclusions and future work follows.

# Chapter 1: Accounting for the effect of dislocation climb-mediated flow on the anisotropy and texture evolution of Mg alloy, AZ31B

*This chapter has been accepted for publication in Materials Science and Engineering A with co-authors Ricardo Lebensohn, Laurent Capolungo and Sean Agnew. The conceptualization and investigation of the study and drafting of this chapter was done at the University of Virginia. Collaborators at Los Alamos National Laboratory provided the VPSC-CLIMB code and edits to the manuscript.*

*The results presented in this chapter have been updated from the 2022 MSEA paper. Here, the CRSS and climb stress optimizations in the genetic algorithm allowed for larger ratios of nonbasal to basal CRSS and climb stress to basal CRSS. This resulted in increased basal slip in the sample deformed in uniaxial tension along the rolling direction, which better represents the large strain anisotropy difference between uniaxial tension along the rolling and transverse directions at room temperature and at high temperatures and strain rates.*

## 1- Introduction

Many attempts have been made to explain the improved ductility of magnesium alloys at moderately high temperatures (> 100 $^{\circ}$C). They tend to focus *either* on the phenomenological aspects (i.e., increased strain rate sensitivity, lowered flow stress) *or* the possibility of increased activation of non-basal slip mechanisms. There is no doubt that increases in strain rate sensitivity forestall catastrophic plastic instability and thereby increase post uniform elongation [1] and a lowered flow stress will lower the driving force for fracture. There is also no doubt that nonbasal slip mechanisms play a critical role in the deformation of Mg and its alloys, even at low temperatures. The seminal work of Couret & Caillard [2] demonstrated the importance of the cross glide of <a> dislocations into prism and pyramidal planes during tensile deformation. This has implications for the macroscopic deformation as it leads to high r-values and a characteristic texture evolution which aligns the prism planes [3].

Other non-basal slip modes are also thought to play a large role in deformation in order to satisfy the Von Mises criterion, which states that 5 independent slip systems are needed in order to accommodate arbitrary deformation [4]. At room temperature, basal and prism glide alone only account for 4 (2 from basal and 2 from prism) independent slip systems and cannot accommodate straining along the <c> axis. These concerns can be addresssed through the activation of <c+a> slip, which has been linked to the enhanced room temperature ductility of Mg-Li [5,6] and Mg-Y [6,7] alloys. However, <c+a> slip is known to have a higher critical resolved shear stress (CRSS) than basal and prism slip <a> [8], which accounts for its relatively low activity during uniaxial tension in common Mg alloys (e.g., AZ31). The role of <c+a> slip in these alloys has been emphasized under other straining conditions, most notably uniaxial

compression [9]. The ease of <c+a> motion was successfully used as a predictor for enhanced ambient temperature ductility of various Mg alloy systems [10]. In that model, failure is seen as a competition between two processess: the dissociation of <c+a> dislocations onto basal planes where they are sessile (the pyramidal to basal transition) and their cross slip between pyramidal planes. It is suggested that ductility of Mg alloys may be increased through alloying by lowering the energetic barrier to <c+a> cross glide.

In addition to its effects on room temperature deformation, the activation of <c+a> glide is viewed as the critical mechanism for high temperature deformation of Mg alloys in the literature for several reasons. First, the density of <c+a> dislocations is observed to increase with increasing deformation temperature [11], which suggests increased slip activity consistent with the knowledge that the CRSS of <c+a> slip is strongly temperature sensitive [8]. From the work of Wu et al. [10], it seems reasonable that increasing the temperature would also enhance the ease of <c+a> slip, since the proposed critical barrier, cross slip, is a thermally activated process. Agnew & Duygulu [3] explored this line of thinking earlier by using <c+a> slip to match the reduced strain anisotropy observed at high temperatures and claimed it could explain the texture evolution. However, their texture data showed that employing sufficient <c+a> glide to explain the low r-value led to a clear splitting of the peaks in basal pole figure intensity toward the tensile axis, which is a direct result of the motion of <c+a> dislocations, since it causes the crystals with c-axes initially close to the normal direction to rotate toward the tensile direction. In addition, other characteristics of high temperature deformation cannot be explained through <c+a> slip; namely, the strongly increased strain rate sensitivity and the stress-independent activation energy of deformation within the power law regime. The strain rate sensitivity of Mg alloys at ambient temperature (m~0.01-0.02) where the glide of dislocations clearly dominates the deformation [12]. Some alloys are known to exhibit increased strain rate sensitivity despite being glide-controlled creep (i.e., viscous glide), but this is attributed to the solute drag [13], rather than the activation of additional glide modes. Wu et al.[10] estimate the activation free energy energy of <c+a> cross slip between pyramidal planes in the Mg alloy AZ31B to be ~ 0.55 eV/atom (~53 kJ/mol) [10], which is much lower than the stress-independent activation energies typically found in literature for the power law creep regime (110 kJ/mol [14], 140 kJ/mol [15]). In light of these inconsistencies, it is clear that another mechanism must be at work.

When compared to glide modes, less attention has been given to the role of dislocation climb mechanisms within recent crystal plasticity studies of Mg alloys, even though classical studies of creep deformation noted the importance of dislocation climb in certain temperature and strain rate regimes [16–18]. Incorporation of dislocation climb also has the potential to address the shortcomings of prior studies to adequately account for the texture evolution [19], as will be explained in greater detail later. The activation of significant climb can also address the activation energy and increased rate sensitivity as climb is controlled through the diffusion of vacancies (Q = 92 – 135 kJ/mol, depending on whether the rate-controlling step is along high diffusivity paths such as dislocation cores/grain boundaries or the lattice, respectively) and has

been theorized to result in increased strain rate sensitivity [20]. This study tests the hypothesis that the reduced strain accommodation through dislocation glide and increased activation of climb is the cause of the observed slowed texture evolution during high temperature deformation and associated changes in the constitutive response.

There are at least three other mechanisms which may affect the plasticity and texture evolution at high temperatures: grain growth, grain boundary sliding (GBS), and dynamic recrystallization (DRX) [21]. Stress-assisted grain growth has been previously observed in nanocrystalline Cu [22] and Al [23] as a mechanism to reduce the interfacial energy stored in the grain boundaries. Previous studies in AZ31 have shown that grain growth has two major effects on texture: the strengthening of the basal texture [24] and the strengthening of a $< 11\bar{2}0 >$ component due to anomalous grain growth [25]. The existing basal texture from the rolling process tends to be disrupted during GBS [26,27], which was only observed in the texture collected in the GBS regime. Staroselsky and Anand (2003) found it was necessary to use a non-crystallographic term representing GBS during their crystal plasticity finite element modeling (CPFEM) to simulate room temperature deformation of HCP Mg [28]. DRX is also a possibility; however, this tends to randomize the texture since the newly recrystallized grains have essentially random orientations [21,29]. Furthermore, a recent study of grain boundary serration (an important mechanism of DRX) has emphasized the role of grain boundary dislocations and grain boundary sliding [30] demonstrating the interconnected nature of all these mechanisms.

Finally, it is noted that climb is not exclusive to dislocations. Disconnections – line defects found on interfaces (including grain boundaries) with a Burgers vector and step height – are believed to glide and climb during processes such as GBS [31]. Some amount of GBS is required to suppress void formation during deformation, whether the bulk deformation is diffusional (Lifshitz GBS) [32] or dislocation-based (Rachinger GBS) [33]. Following the model proposed by Ball and Hutchinson [34], GBS (possibly induced by the motion of grain boundary dislocations and/or disconnections impeded by triple junctions and other obstacles) can itself use a "glide and climb" approach to overcome the obstacles and continue sliding. The process is generally believed to be rate-controlled by climb and plays a key role in superplasticity. The role of intragranular dislocation motion in temperature and strain rate regimes where GBS is operative is still a matter of debate. Some authors have suggested that a primary role of intragranular dislocation motion is to generate grain boundary dislocations in order to accommodate GBS [35], whereas early work by Ashby & Verrall [36] suggested that GBS and dislocation creep could both contribute to the deformation over a relatively wide range of strain rate. Prior work by the one of the present authors [15] revealed that moderate grain size differences (6 vs 8 μm) between sheets with nearly identical chemistry and texture resulted in higher rate sensitivities (0.27 vs 0.23) for the finer grained material. The difference was abscribed to the activation of GBS in the sample with the smaller grain size in accordance with the findings of Barnett et al [37], placing it on the boundary between high temperature creep and GBS.

The present study employs a combination of mechanical testing, texture measurements by x-ray diffraction, and crystal plasticity modelling using a new version of the viscoplastic selfconsistent (VPSC-CLIMB) code that explicitly incorporates the kinematics of dislocation climb to model the response of Mg alloy AZ31B. The goal of the study is to test the hypothesis that the climb of <a> type edge dislocations can explain the transitions in texture evolution and strain anisotropy which are observed to occur in Mg alloy samples deformed at moderately elevated temperatures.

## 2- Deformation Mechanisms Considered in the Present Study

Gliding dislocations induce simple shear on the glide plane and in the glide direction (parallel to its Burgers vector). Depending upon the boundary conditions to which a crystal is subjected, it will undergo rigid-body rotation, lattice rotation or both. This is the main reason why deformed polycrystals develop preferred orientations (crystallographic texture). Each glide mode has a characteristic impact on the texture and plastic anisotropy, a point which will play a critical role in the present study of the extent to which climb mechanism accommodate strain during high temperature deformation. Out of the several major glide modes known to operate in magnesium in this temperature and strain rate regime, the simulations in this study will rely on three of the most prominent: basal $\{0001\}\langle 11\bar{2}0\rangle$ (the easy slip mode in Mg), prism $\{1\bar{1}00\}\langle 11\bar{2}0\rangle$, and 2nd order pyramidal $\{11\bar{2}\bar{2}\}\langle 11\bar{2}3\rangle$(<c+a> slip) which has been experimentally observed [8], and used in prior simulations (e.g., [3,38,39]). Pyramidal <a> $\{1\bar{1}01\}\langle 11\bar{2}0\rangle$ slip is also a possibility, however, it cannot be readily discriminated from the concurrent operation of basal and prismatic <a> slip [6].

Deformation twinning on $\{10\bar{1}2\}$ type planes is also an important mechanism in Mg, which is taken into account, though its role is minimized in the present study by the initial sheet texture and in-plane tensile strain paths under consideration. The influence of twinning on the constitutive behavior and texture evolution of Mg is a topic which has been deeply investigated (e.g.,[40–42]).

The most obvious candidate dislocations to consider the role of climb are the prominent basal <a>, $\{0001\}\langle 11\bar{2}0\rangle$, type dislocations due to their ubiquity in Mg alloys. Another possibility is the climb of prism <c>, $\{10\bar{1}0\}\langle 0001\rangle$, dislocations. Typically, <c> dislocations are not observed to glide and multiply in single crystals because crystals well oriented for this glide mode will deform instead via the softer basal glide mechanism. Previous experimental observations of <c> dislocation climb were made by Stohr & Poirier [43] in their landmark study of <c+a> slip after compressive deformation of c-axis aligned crystals at the highest temperatures. Edelin & Poirier [44] also observed the importance of <c> dislocation climb in <c> compression, at the highest temperatures (T ~ 500 °C). However, the effects of <c>

climb are excluded in this study due to their significantly lower densities compared to <a> dislocations. Similar to glide, dislocation climb has unique texture and strain anisotropy characteristics that can be used to discriminate its activity using polycrystal plasticity simulations. The kinematics of crystal plasticity associated with dislocation climb remains an open research question, which is taken up in the present study.

**3- Temperature, stress, and strain rate regime of interest**

Flow stress – strain rate data from recent studies of [14](solid lines) and [45](dashed lines) are presented to illustrate the regimes in which particular deformation mechanisms dominate (Figure 1). The strain rate sensitivities of the flow stress can aid in the determination of the dominant deformation mechanism: ~0.125 – 0.143 ("low temperature" pipe diffusion-controlled dislocation climb and glide), ~0.2-0.25 ("high temperature" lattice diffusion-controlled dislocation climb and glide), ~0.33 – 0.5 (grain boundary sliding (GBS)), and ~1 (diffusional flow by Coble (grain boundary diffusion) creep). Nabarro-Herring creep is not relevant to the present study, due to the small grain size (< 10 μm) of the examined samples, which favors Coble creep. Employing established constitutive relationships, e.g., from the seminal work of Frost & Ashby [46], activation energies for pipe and lattice diffusion from Antoniswamy et al. [14], the remaining material constants needed to describe high and low temperature creep and GBS of $1.1 \times 10^6$ and 1.71, respectively, were obtained by performing least-squares regression of all the available data. Thick solid lines in the figure represent the borders of a deformation mechanism map [46] for the material with a grain size of ~5.3 μm [14] and thick dashed lines represent the borders for a material with a grain size of 4.5 μm [45]. Note that the material used by Antoniswamy et al. [14] was tested in the H24 temper, which made initial grain size measurements difficult. The quoted grain size was measured after recrystallization at 250 °C.

In this study, we *focus* our modeling efforts on higher stress conditions where GBS is expected to be absent as the most appropriate cases to study the effect of dislocation climb on the texture evolution and strain anisotropy. Strictly speaking, the VPSC-CLIMB modeling strategy we employ strictly enforces equilibrium and compatibility between each individual grain and the surrounding homogeneous effective medium, and therefore, cannot be used to investigate GBS directly. Like <c+a> slip, the activation of GBS has been held responsible for the aforementioned reduction in r-value in AZ31B and alteration of texture[14,37]. Therefore, it is of interest to investigate the impact of including the kinematics of dislocation climb on the results of crystal plasticity modeling of deformation under similar conditions.

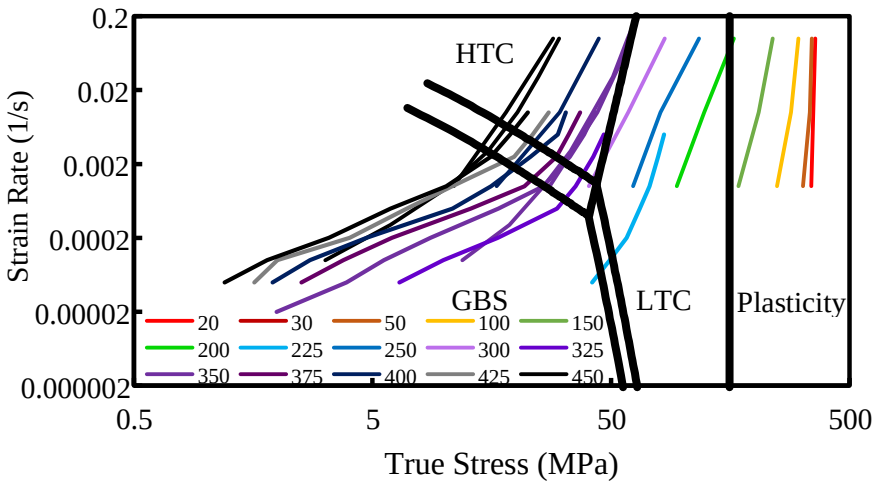


Figure 1: Comparison of constitutive data from Antoniswamy et al.[14] (solid lines), Abu-Farha & Khraisheh [45](dashed lines). The thick black lines denote the boundaries of each deformation mechanism (high temperature creep (HTC), low temperature creep (LTC), grain boundary sliding (GBS), and plasticity) for different grain sizes - Antoniswamy et al.[14] (solid) and Abu-Farha & Khraisheh [45](dashed).

## 4- Experimental and Modeling Methods

*Material*

Sheets of rolled magnesium alloy AZ31B (designated "X" in [15]) were received from Magnesium Elektron North America in the O temper with a nominal thickness of 1 mm. The composition of the AZ31B sheet was characterized by energy dispersive spectroscopy (EDS) to be 2.9 wt% Al, 0.95 wt% Zn, 0.53 wt% Mn, balance Mg. The Mn content is slightly higher than typically observed (but still within reasonable bounds). Linear intercept measurements done with optical microscopy yielded an average grain size of 8.3 μm and x-ray diffraction performed on the samples identified an α-Mg phase with small amounts of Mn-rich precipitates.

*Mechanical Testing*

ASTM E-8 subsized samples of rolled Mg alloy AZ31B sheet obtained in the O-temper condition had a gage length of approximately 25 mm, a width of 6 mm and thickness of 1 mm with gage parallel (RD) or perpendicular (TD) to the rolling direction. 5 roughly equally sized regions were marked along the gage length to ensure accurate post-deformation strain measurements. Uniaxial tensile tests were performed on the samples using an MTS Sintech 10\GL load frame and an ATS 3610 split furnace operating at various temperatures (20 – 350 °C) and strain rates (0.00001 – 0.1 1/s). Error bars were generated by taking into account the load cell sensitivity (± 5 MPa) into the measured values of stress. Testing conditions were selected to

rather evenly span a range of the temperature compensated strain rate known as the ZenerHollomon parameter

$$Z = \dot{\varepsilon} \exp\left(\frac{Q}{RT}\right) \qquad Equation\ 1$$

where $\dot{\varepsilon}$ is the strain rate, Q is the activation energy, R is the universal gas constant, and T is the temperature on an absolute scale. After deformation to ~ 10%, the final dimensions for each of the aforementioned 5 regions were measured and the true plastic strain was determined, along with an average strain level and standard deviation of the strains within the gage. The r-values were used to quantify the anisotropy during deformation,

$$r = \frac{\varepsilon_w}{\varepsilon_t} \qquad Equation\ 2$$

where $\varepsilon_w$ is the true plastic strain in the width direction and $\varepsilon_t$ is the true plastic strain in the thickness direction. Some tensile tests were run to ~30% strain, in order to gain more information about the texture and r-value evolution at the higher temperatures.

*Texture Collection and Analysis*

Tensile samples were prepared for texture analysis through a series of polishing steps with SiC polishing pads, culminating with a chemical polish of 2% Nital (2% by volume nitric acid in methanol) and a methanol rinse. Texture measurements were collected from samples deformed to ~10% strain at selected Z conditions (and subsequently polished to mid-thickness) using a Panalytical X'Pert Pro diffractometer with a Cu $K_\alpha$ X-ray tube operating at 45 kV and 40 mA in point focus mode on a 5° × 5° measurement grid of tilt and azimuth angles. Texture measurements were also collected on select samples deformed to ~30% true plastic strain in order to study texture evolution to higher strain levels. Regardless of sample orientation, RD was always aligned with the goniometer to ensure that sample coordinates line up with pole figure and simulation coordinates. MTEX, a Matlab toolbox, was used to plot experimental (0002), $(10\bar{1}0)$ and$(10\bar{1}1)$ pole figures and compute Orientation Distribution Functions (ODFs) [47]. Defocusing, background corrections, and pole figure normalization were also performed using MTEX. The resulting ODFs were discretized to obtain 2,000 equally weighted orientations ("grains") with a kernel size of 10° arranged in orientation space to best represent the initial texture, which were in turn used as input for the VPSC-CLIMB simulations described below.

Figure 2 shows the initial texture of the rolled AZ31B sheet measured in this study as the $\varphi_2 = 0°$ slice of the ODF (Bunge Euler angle convention ($\varphi_1$, $\Phi$, $\varphi_2$)). There are many appropriate representations of texture, including: 3 complete, recalculated pole figures, a single 2-D ($\varphi_2 = 0°$) section of the ODF (Bunge Euler angle convention ($\varphi_1$, $\Phi$, $\varphi_2$)), and the complete ODF presented

in the fundamental zone of Rodrigues (axis/angle) space with hexagonal crystal and orthotropic sample symmetry enforced. Pole figures are the most common texture representation used in the Mg alloy literature due to the way in which bulk textures are frequently measured using x-ray or neutron diffraction. Note that the current pole figures of the initial texture (not shown in the interest of space) are identical to those reported previously for the same sheet material [15].

A major drawback of pole figures is that the intensity at a location within a pole figure is not due to a single orientation; it is the integration of the intensity within the ODF along a path of *many* different orientations within orientation space, which all share a particular spatial and crystallographic rotation axis [48]. This is rectified by generating an ODF from experimentally collected pole figures to describe the orientations of each grain. Figure 2 shows several sections of the ODF at constant $\varphi_2$ (per Bunge's convention). This presentation highlights the fact that even the initial texture has some preferred alignment of the $< 10\bar{1}0 >$ directions of the crystals with the RD. This is not immediately obvious from the pole figures. The $\varphi_2 = 0°$ slice was deemed representative of the texture in rolled AZ31B since no additional texture components are revealed in the other slices. The apparent shift in the peak intensity positions is a result of symmetry and the curved boundaries of the fundamental zone in the employed Euler space. (The nodes are in symmetrically equivalent positions [49].) In fact, even the two nodes present in the $\varphi_2 = 0°$ slice are symmetrically equivalent.

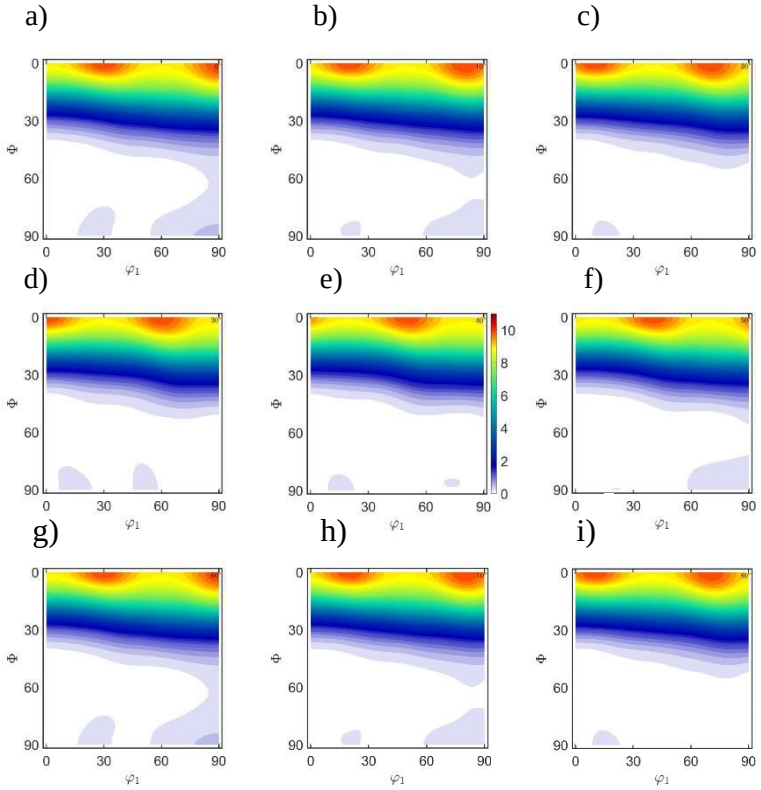


Figure 2: The ODF of as-rolled AZ31B is presented as slices of Euler space (Bunge convention) in 10° increments of $\varphi_2$ (a) = 0°, b) = 10°, c) = 20°, d) = 30°, e) = 40°, f) = 50°, g) = 60°, h) = 70°, i) = 80°). Note that the texture intensity is relatively constant along $\varphi_2$ and the same texture component is present in all slices, only the location of the node changes. (One of the nodes shown in the ODF slices is symmetrically equivalent to the other due to the curved nature of the fundamental zone in Euler space [49]). Thus, all textures will be presented as ODF slices when $\phi_2 = 0°$. The same intensity scale and axes are used on all texture plots presented in this paper.

*Crystal Plasticity Modeling*

Figure 3 defines a dislocation-level, local coordinate system used in the following schematic illustrations of the distortions produced by a) glide, b) climb of an edge dislocation, c) crossglide of an initially screw dislocation, and d) climb of a mixed dislocation. In general, a crystal will experience a simple-shear distortion as a result of dislocation glide, which involves rigid body rotation (Figure 4a). The Taylor axis about which this rotation takes place is given by the cross product $(\widehat{\boldsymbol{b}} \times \widehat{\boldsymbol{n}})$of the Burgers vector direction $\widehat{\boldsymbol{b}}$ and the slip plane normal vector $\widehat{\boldsymbol{n}}$. The situation is different for the non-conservative, diffusion-controlled climb of edge dislocations of the same slip mode. Such climb induces pure shear, i.e. stretch with no accompanying rigid body rotation (Figure 4b). The climb of mixed dislocations, however, will

induce a rigid body rotation consistent with the cross slip of a dislocation (Figure 4c) whose Burgers vector is equivalent to its screw component (Figure 4d). Depending upon the boundary conditions of the crystal, the aforementioned rigid body rotations (plastic spin) will often cause the lattice to rotate around a distinct Taylor axis ($\widehat{\boldsymbol{b}}_{\boldsymbol{s}} \times \widehat{\boldsymbol{\chi}}$), where $\widehat{\boldsymbol{b}}_{\boldsymbol{s}}$ corresponds to the screw portion of the dislocation and $\widehat{\boldsymbol{\chi}}$ corresponds to the normal to the plane of dislocation climb/cross-glide, i.e., the extra half-plane. For example, when mixed dislocations with <a> type Burgers vectors climb, they will induce lattice rotations similar to that of prismatic glide, except these rotations will be proportionally less, for a given amount of dislocation motion, due to the fact that the rotations correspond solely to the screw component of the climbing dislocations. This is in contrast to the case of glide, where both edge and screw portions give rise to the same rotations. In summary, and as originally shown in Lebensohn et al. [19], the rate of texture evolution caused by climb motion is slower than that of the same amount of glide motion.

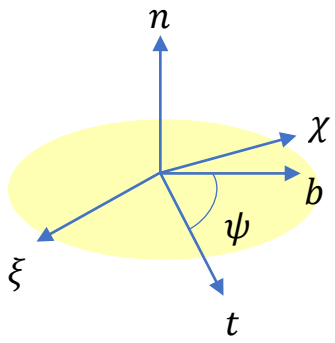


Figure 3: Coordinate system for considering the forces on dislocations within VPSC-CLIMB. $\hat{n}$ is the glide plane normal, $\hat{b}$ is the burgers vector, $\hat{t}$ is the line direction, $\hat{\chi}$ is the climb plane normal and $\hat{\xi} = \hat{b} \times \hat{n}$. $\psi$ is the angle that defines the character of the dislocation.

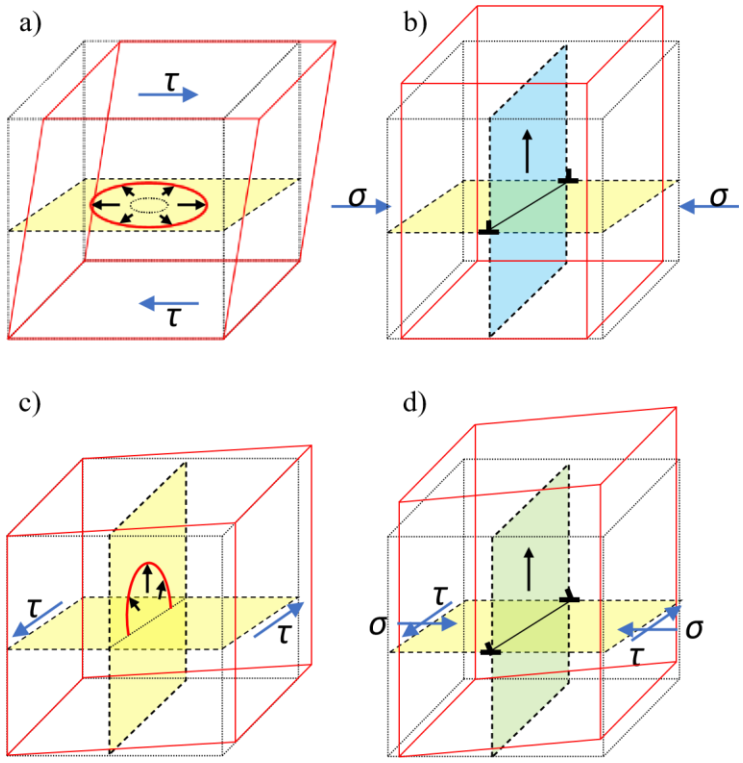


Figure 4: Schematic illustration of the distortions imparted by: a) glide of a basal dislocation, b) climb of a basal edge dislocation, c) prismatic cross-slip of a basal dislocation, and d) climb of a mixed basal dislocation. In each case, the Burgers vector of a basal dislocation is of <a> type. The black arrows within the plane of motion indicates the direction of dislocation motion. Glide (yellow) and climb (blue) planes are shown in each figure for orientations purposes. The climb plane for mixed dislocations is denoted as green to show that the motion is a combination of prism glide and basal climb.

The crystal-level constitutive model parses the viscoplastic (*vp*) strain rate into two parts, that due to glide (*g*) and that due to climb (*c*).

$$\dot{\varepsilon}_{ij}^{vp} = \dot{\varepsilon}_{ij}^{g} + \dot{\varepsilon}_{ij}^{c} \qquad Equation\ 3$$

As discussed previously, a complete deformation may involve a combination of stretch and rigidbody rotation. Equation 4 provides the well-known relationship between the deformation rate tensor, $\dot{\boldsymbol{\varepsilon}}^{g}$(boldface denotes a tensor), the shear rate on the $s^{\text{th}}$ slip system, $\dot{\gamma}^{g,s}$, and the Schmid tensor, $\boldsymbol{m}^{s}$which is the symmetric portion of the dyadic cross product of the slip direction and slip plane normal unit vectors, $sym(\hat{\boldsymbol{b}}^{s} \otimes \hat{\boldsymbol{n}}^{s})$ .

$$\dot{\varepsilon}_{ij}^{g} = \sum_{s} \dot{\gamma}^{g,s} m_{ij}^{s} \qquad Equation\ 4$$

Similarly, Equation 5 gives the associated plastic spin (or rate of rotation) in terms of the slip system shear rates and the antisymmetric portion of the same dyadic product, denoted $q_{ij}^{s}$.

$$\dot{\omega}_{ij}^{g} = \sum_{s} \dot{\gamma}^{g,s} q_{ij}^{s} \qquad Equation\ 5$$

The shear deformation rate due to dislocation climb can be expressed similarly to Equation 4

$$\dot{\varepsilon}_{ij}^{c} = \sum_{s} \dot{\beta}^{s} k_{ij}^{d,s} \qquad Equation\ 6$$

where $\boldsymbol{k}^{d,s}$ is the deviatoric portion of the symmetric part of the Hartley climb tensor, $\dot{\beta}^{s}$ is the resolved strain rate due to climb, $\boldsymbol{k}^{d,s} = sym(\widehat{\boldsymbol{b}}^{s} \otimes \widehat{\boldsymbol{\chi}}^{s})$, and $\widehat{\boldsymbol{\chi}}^{s}$ denotes the positive glide direction (or climb plane normal direction) [50]. There is a distinction between climb, which in principle can give rise to both deviatoric strain and dilatation, and glide which can only produce deviatoric strain. We will return to the issue of dilatational strains in the discussion section. For now, it suffices to say that the dilatation concerns local fluctuations in vacancy concentration. These fluctuations do not have an appreciable impact upon the net strain of the crystal, and, hence, are not addressed in Equation 6. Similar to Equation 5, Equation 7 gives the plastic spin that occurs due to dislocation climb.

$$\dot{\omega}_{ij}^{c} = \sum_{s} \dot{\beta}^{s} r_{ij}^{s} = \frac{1}{2} \sum_{s} \dot{\beta} \cos(\psi^{s}) \left( b_{j}^{s} \xi_{i}^{s} - b_{i}^{s} \xi_{j}^{s} \right) \qquad Equation\ 7$$

where $\psi^{s}$ is the angle between the Burgers vector and the line direction (Figure 3), which defines the character of the average dislocation climbing from the slip system, *s*, and $\boldsymbol{r}^{s}$ is the skew symmetric portion of the Hartley climb tensor [50]. In principle, $\psi^{s}$ could evolve with deformation, but we presently assign it to be a constant value in all of the simulations of the present study. Specifically, we examine three cases. The first, $\psi^{s} = \frac{\pi}{2}$, indicates that all of the climbing dislocations are of pure edge character. This is a limiting case, since all such climb will accommodate strain without causing any lattice rotation. Considering another limiting case, $\psi^{s} = 0$, involving dislocations of solely screw character, it is shown that Equations 6 and 7 can be used to describe the kinematics of prismatic cross-glide of <a> dislocations as well as climb. This is an interesting case for Mg alloys in which screw dislocations with an <a> Burgers vector

are the same ones which are responsible for prismatic slip. The results obtained for this case were indistinguishable from those in which prism slip with the same critical stress is employed.

Up to this point, only the kinematics has been discussed for simplicity. The strain rate caused by dislocation glide is understood to have an exponential dependence upon stress [51], which can be approximated as a power law, over a limited range of strain rates.

$$\dot{\varepsilon}_{ij}^{g} = \dot{\gamma}_0 \sum_{s=1}^{N_s} m_{ij}^{s} \left( \frac{|\boldsymbol{m^s}:\boldsymbol{\sigma'}|}{\tau^{g,s}} \right)^{\frac{1}{m_g}} sgn(\boldsymbol{m^s}:\boldsymbol{\sigma'}) \qquad Equation\ 8$$

where $\dot{\gamma}_0$ is the reference shear strain rate (which was set equal to the applied strain rate of the test), $m_g$ the rate sensitivity governing glide is assumed equal to 1/20 in the present study (high enough to distinguish it from climb, yet low enough to ensure ready convergence[3]), and $\tau^{g,s}$ is the critical resolved shear stress of the $s^{\text{th}}$ slip system. Dislocation glide only depends on the deviatoric portion of the stresses applied to the crystal, $\boldsymbol{\sigma'}$. At the dislocation level, one can consider the generalized Schmid law $\boldsymbol{m^s}:\boldsymbol{\sigma'}$ as related to that portion of the Peach-Koehler force which lies within the glide plane, i.e., $f_g = \boldsymbol{f} \cdot \hat{\boldsymbol{\chi}}^s = (\boldsymbol{m^s}:\boldsymbol{\sigma'})b$.

The constitutive relationship used to describe climb is similar to the one employed for glide [19]

$$\dot{\varepsilon}_{ij}^{c} = \dot{\gamma}_0 \sum_{s=1}^{N_s} k_{ij}^{d,s} \left( \frac{\left|\boldsymbol{k^{d,s}}:\boldsymbol{\sigma'}\right|}{\sigma^{c,s}} \right)^{\frac{1}{m_c}} sgn\left(\boldsymbol{k^{d,s}}:\boldsymbol{\sigma'}\right) \qquad Equation\ 9$$

where $k_{ij}^{d,s}$ functions analogously to $m_{ij}^{s}$, $\sigma^{c,s}$ is a critical stress for climb analogous to $\tau^{g,s}$ for glide, and $m_c$ is the rate sensitivity governing climb. Again, this expression can be rationalized in terms of the component of the Peach-Koehler force on a dislocation which is normal to the glide plane, i.e., $f_c = \boldsymbol{f} \cdot \hat{\boldsymbol{n}}^s = (\boldsymbol{k^s}:\boldsymbol{\sigma'})b$. As written, Equation 9 ignores the effect of hydrostatic pressure on dislocation climb. The possible effect of pressure is taken up in the discussion and will be revealed negligible for the current study. In theory, $m_c$ and $\sigma^{c,s}$ are temperature dependent, but $m_c = 1/3$ is taken as a constant in the power law regime. Again, the implications of these choices will be addressed in the discussion section. The optimal CRSSs (including $\sigma^{c,s}$) relative to basal glide are determined from minimizing a total residual error objective function, as described below.

[3] Recent advancements in the numerical techniques employed in crystal plasticity modeling allow for more realistic (even lower) values [76,77] were not employed in this first exploration of climb effects.

The glide critical resolved shear stress evolves per the empirical Voce strain hardening relationship [52].

$$\tau^{g,s} = \tau_0^s + \tau_1^s \left(1 - \exp\left(-\Gamma \left|\frac{\theta_0^s}{\tau_1^s}\right|\right)\right) \qquad Equation\ 10$$

where $\Gamma = \sum_s \Delta\gamma^s$ is the accumulated shear in the grain; $\tau_0^s$ is the initial CRSS, $\theta_0^s$ is the initial hardening rate, and $(\tau_0^s + \tau_1^s)$ is the back-extrapolated CRSS. As a first-order approximation, the critical stress for climb ($\sigma^{c,s}$) is assumed to remain constant at a given temperature and strain rate. It is acknowledged that more rigorous treatments of the hardening evolution have been developed, based upon evolution of the dislocation density [53]. However, this simpler approach has been adopted in the present inaugural attempt to incorporate the effects of dislocation climb kinematics into the polycrystal plasticity modeling of Mg alloy deformation.

The VPSC model [12], adapted to account for the kinematics of dislocation climb (VPSC-CLIMB) as summarized above, was used to simulate the experimentally measured textures and r-values. For a complete discussion of the model, readers are directed to the original articles [19,54]. VPSC employs an explicit strain integration scheme, and hence, straining increments were maintained as 0.002 in order to avoid error accumulation. By comparing the simulated results with experimentally measured values, mechanistic understanding regarding the transition from low to high temperature deformation behavior of an archetypal Mg alloy AZ31B is obtained.

*Parametric study*

The root mean squared difference between the experimental and simulated textures is chosen as a means of quantifying the level of agreement per

$$TexErr = \sqrt{\int \left(\left(f_{exp}(g) - f_{sim}(g)\right)\right) dg} \qquad Equation\ 11$$

where $f_{exp}(g)$ refers to the orientations that comprise the experimental ODF and $f_{sim}(g)$ refers to the orientations belonging to the simulated ODF. This is akin to calculating the norm of the difference between the experimental and simulated ODFs or the standard deviation of a dataset using statistics. This is, in fact, a *relative* error because the ODFs are normalized to unity, $\int f(g)dg = 1$. The typical average texture "error/change" between deformed samples and the initial rolled texture was found to be 0.3, providing a sense of the magnitude of this texture measure. A metric for the total residual error between the experiment and simulation, including texture and strain anisotropy (r-values) provides an objective function

$$f_0 = w_{Tex}(TexErr_{TD} + TexErr_{RD}) + w_r\left(\frac{|r_{sim} - r_{exp}|_{TD}}{r_{TD\_exp}} + \frac{|r_{sim} - r_{exp}|_{RD}}{r_{RD\_exp}}\right) \quad Equation\ 12$$

for both RD and TD sample orientations. The errors in texture are weighted more strongly than the r-values ($w_{Tex}$ = 0.75 $vs.$ $w_r$ = 0.25) because the texture showed more specificity than the r-values. Each slip mode has a unique texture evolution (through the distortion created by dislocation motion) for the initial rolled texture (Figure 4), but some have similar effects on r-value.

Final best-fits of the VPSC-CLIMB model to the cases of greatest interest were obtained by varying the model parameters (the critical resolved shear and normal stresses of the various modes under consideration) using a genetic algorithm (GA) [55,56] to minimize the objective function (Equation 12). This novel approach adjusts CRSS values to match simulations to the experimental evidence of dislocation kinematics (texture evolution and strain anisotropy) rather than past attempts which have attempted to match macroscopic stress-strain tests [57]. On average, ~ 800 (32 simulations per generation × 10-15 generations) simulations were run per experimental test condition; therefore, simulations were run in parallel to increase computational efficiency. The best fit set of CRSSs and climb stresses were scaled for the predicted flow stresses to match the macroscopic yield point. Slip mode hardening was ignored in this study, though this only strongly affects the room temperature simulations.

## 5- Results

*Constitutive behavior*

Figure 5a shows the effect of temperature and sample orientation (RD vs. TD) on the stress-strain behavior of AZ31B tested in the current study. The flow stresses and strain hardening rates were observed to decrease with increasing temperature, as observed with prior studies [3,14,15]. The flow stress at a strain of 0.1, along with the testing conditions, permit the results to be overlaid with the previously introduced Ashby-type deformation mechanism map (Figure 5b). From this presentation, we can highlight the 5 cases that will be examined most closely with an orange ring.

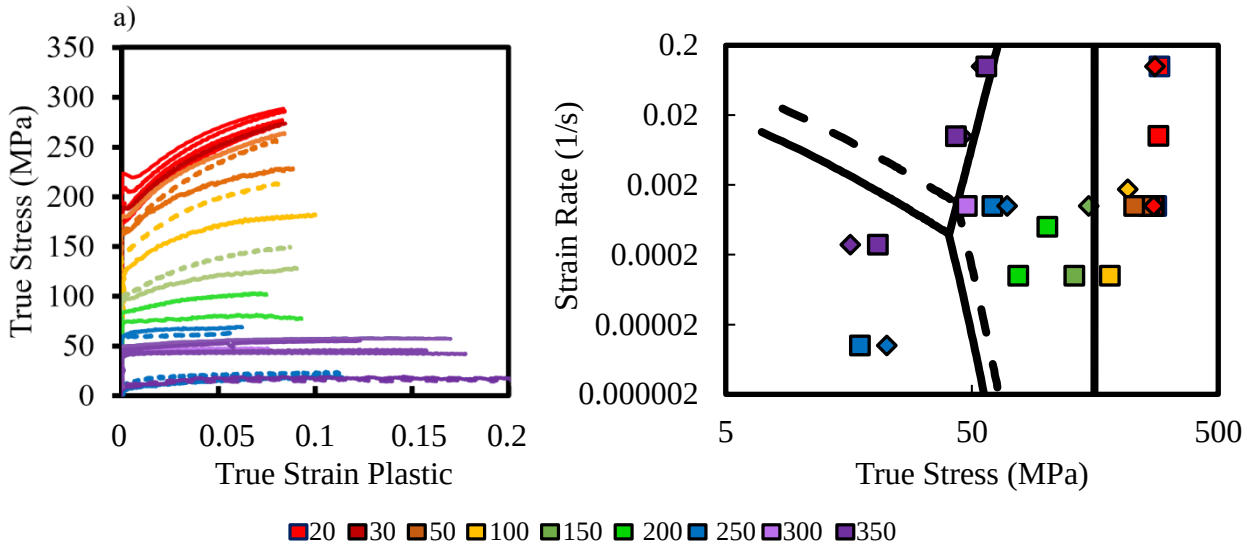


Figure 5: a) Tensile test results (TD = solid lines, RD = dashes), b) Ashby map with current data overlaid.

Although the primary aim of the study is assessing the role of dislocation climb, which may be illuminated through careful examination of kinematics of plasticity (texture evolution and plastic anisotropy), it is also noteworthy to show that if one is more concerned with constitutive flow alone, the empirical [58] model well describes the constitutive response over the entire range explored,

$$Z = \dot{\varepsilon} \exp\left(\frac{Q}{RT}\right) = A[\sinh(\alpha\sigma)]^{\frac{1}{m}} \qquad Equation\ 13$$

where $A$, $\alpha$, and $m$ are temperature-independent material constants, $\sigma$ is the flow stress at a strain of 0.1, and $Z$ is the Zener-Holloman parameter introduced in Equation 1. This empirical relationship was proposed to bridge between the low temperature, high strain rate regime which is well described by an exponential and the high temperature, low stress regime characterized by a power law. The "hinge-point" between the two regimes is the condition where $\alpha\sigma = 1$. Although it was originally used to describe the hot deformation behaviors of FCC metals such as Al, Ni and Cu, it has frequently been shown to yield a good fit with data collected from tensile tests using HCP metals over a wide range of temperatures and strain rates [15,59].

A best fit of the Sellars–Tegart model through nonlinear least squares regression yielded the following parameters: $m$ = 0.326, $A$ = 4.16 x $10^8$, $\alpha$ = 0.031 and $Q$ = 135 kJ/mol. It should first be noted that the observed constitutive response is generally in agreement with those found previously [14,15,45], albeit over a narrower temperature and strain rate range (Figure 6a). Differences in the near ambient flow stresses are attributed to differences in grain size and

temper condition. Differences in the strain rate sensitivity of prior studies by one of the present authors are attributed to previously using an assumed activation energy of 140 kJ/mol [15], rather than fitting it as was done here. For conditions where ln(Z) > 20, the dependence of the strain rate on stress is well approximated as exponential, and in the range ln(Z) < 20 the data may be described by a power law expression with a slope of 3 (indicative of climb-and-glide creep behavior). If one takes the log of both sides of the above empirical expression (Equation 13) and takes the derivative with respect to ln(σ) at a fixed temperature, one can determine the instantaneous strain rate sensitivity, *m*. At high temperatures (i.e., within the power law regime (> 200 °C (~0.5$T_M$))), *m* = 0.326, and at ambient conditions of 293 K and a nominal strain rate of 0.001 1/s, the strain rate sensitivity decreases to *m* ~ 1/79 = 0.0127.

In addition to the observed decrease in the flow stress and increase in strain rate sensitivity, the strain anisotropy (as indicated by the r-value given in Equation 2) undergoes a characteristic decrease with decreasing Z (Figure 6b). Both RD and TD tensile conditions exhibit a low temperature plateau followed by a gradual decline until the samples exhibit isotropic strain behavior (i.e., r = 1) with the only difference being that the low temperature plateau is at a higher level for TD than it is for the RD case. This is due to details of the typical rolling texture in AZ31B-O temper sheet/plate material in which the main basal texture component is tipped slightly more toward the RD than it is the TD. This promotes a higher activity of prismatic slip in the TD case [3]. Interestingly, there is a gradual decline in strain anisotropy with decreasing Z, reaching isotropy in the power law creep regime (ln(Z) < 20). Historically, power law creep has been understood to be controlled by dislocation climb and glide [13]. This observation, along observations related to texture evolution discussed below, caused the present authors to begin questioning the earlier conclusion that increased activation of <c+a> slip is the reason why the rvalues of Mg alloys tend to decrease at higher temperatures [3].

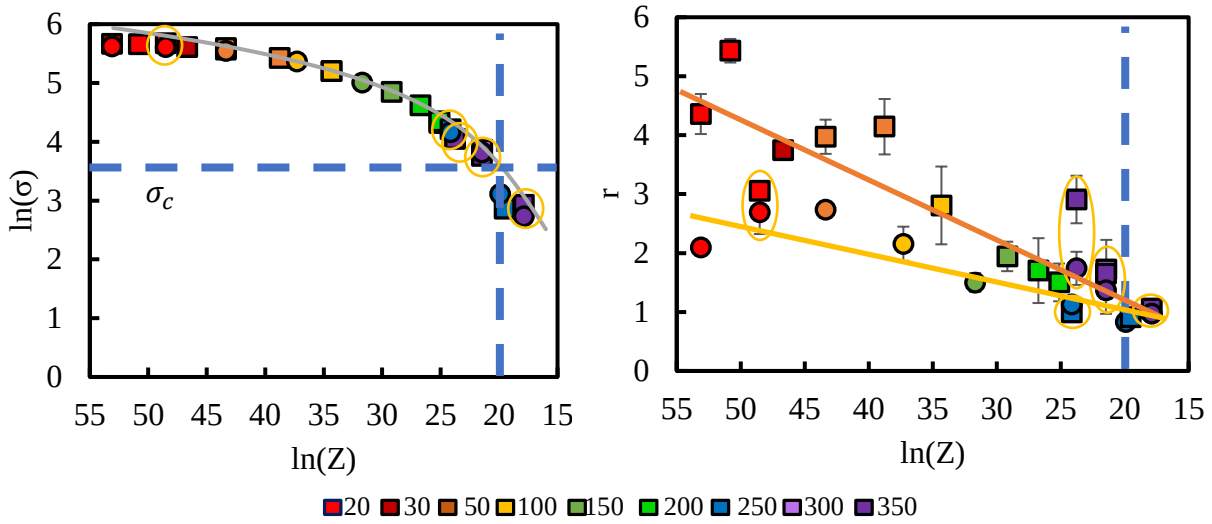


Figure 6: a) flow stress (at ε ~ 0.1) and b) r-value as a function of testing conditions (strain rate, temperature and sample orientation (RD = circle, TD = square). The dashed line in 6a shows the critical stress between the exponential and power law regimes. Vertical dashed lines denote the approximate transition into power law creep as defined by the critical stress. The blue and orange lines in b) serve as guides to the eye for the reduction in r-value for TD and RD sample, respectively.

*Texture Evolution and Anisotropy at Ambient Temperatures – Experiment and Simulation*

The main texture component of the low temperature TD tension texture after 10% strain (Figure 7a) is rotated about the z-axis of Euler space (from $\phi_1$ = 30° to 0°) and strengthened relative to the initial rolled and annealed texture presented in Figure 2, whereas the main texture component of the as-received material is simply strengthened after uniaxial tension deformation along the RD (Figure 7c). This rotation about the sample z-axes (in both cases) is because the initial "basal" texture has a preferred orientation which places the crystals' c-axes nearly parallel to the sheet normal direction. The slip mode which is responsible for this characteristic rotation about the crystals' c-axes is prismatic slip. The relatively high r-values observed at low temperature are another characteristic of prismatic slip in these basal-textured sheets.

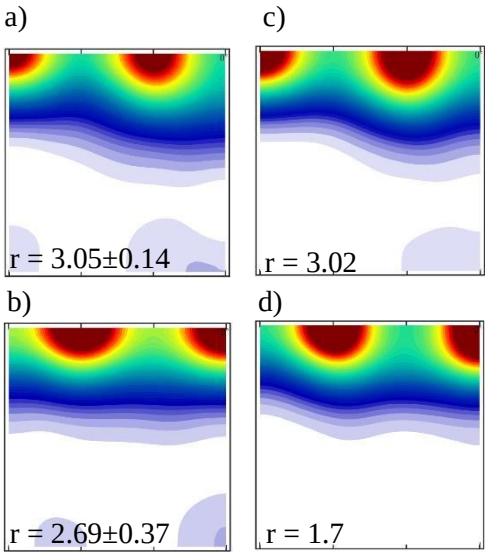


Figure 7: The importance of the prismatic slip of <a> dislocations during room temperature tensile testing (20 °C, 0.001 1/s) is indicated by the appearance of a node-like component in the texture and higher r-values of both the experiments and simulations of tension along (a) & (b) TD and (c) & (d) RD directions, respectively.

As described earlier, minimization of the objective function (Equation 12) was performed using a genetic algorithm to obtain a best-fit simulations of the observed r-values (Figure 6b) and textures of TD and RD samples (Figures 7a & 7c, respectively). Once the ratios of the relative strengths were obtained by the aforementioned optimization process, the Voce strain hardening parameters (Equation 9) required to model the low temperature response (i.e., at temperatures where climb activity is insignificant) were fit and are reported in Table 1. Notably, values for prism and <c+a> slip determined for RT deformation are similar to those used in previous studies [9]. In all conditions of interest, the global minimum in the objective function corresponded to a high CRSS value for twinning, which corresponds to the fact that most of the grains are unfavorably oriented for twinning during in-plane tension, making that parameter rather unconstrained. These optimized parameters for low temperature simulations yield *a* *TexErr* = 0.21 for RD and *TexErr* = 0.34 for TD orientations (resulting in an overall error of $f_0$= 0.50). The simulations confirm that the dominant slip mechanism during low temperature tensile deformation of basal textured sheets is prismatic slip, with smaller contributions from basal and <c+a> slip and tensile twinning.

Table 1: Voce hardening parameters for low and high temperature simulations

| | LT (20 °C, 0.001 1/s) | | LTC (250 °C, 0.001 1/s) | | LTC/HTC Boundary (350 °C, 0.1 1/s) | HTC (350 °C, 0.01 1/s) | GBS (350 °C, 0.00028 1/s) |
|---|---|---|---|---|---|---|---|
| | $\tau_0$ | $\theta_0$ | $\tau_0$ | $\theta_0$ | $\tau_0$ | $\tau_0$ | $\tau_0$ |
| Basal Glide | 16.4 | 300 | 17.0 | 300 | 7.5 | 13.4 | 4.9 |
| Prism Glide | 84.0 | 300 | 27.7 | 300 | 24.8 | 21.4 | 56.4 |
| <c+a> Glide | 94.5 | 300 | 94.7 | 300 | 29.4 | 23.5 | 56.4 |
| <a> Climb | n/a | n/a | 29.3 | n/a | 39.8 | 23.2 | 7.7 |
| Tensile Twinning | 165.1 | 100 | 117.0 | 100 | 74.7 | 106.5 | 61.3 |

*Texture Evolution and Anisotropy at Elevated Temperatures – Experiment and Simulation*

As the Zener-Holloman parameter is decreased from 40 down to around 10, the dominant mechanism changes from low temperature plasticity to power law creep to GBS (Figures 5 & 6). Figure 8 shows an example of how the corresponding texture strength decreases. Compare the experimental textures in Figures 8a and 8c with those presented in Figures 7a and 7c. These results suggest that the activity of the non-basal, prismatic slip mode responsible for the texture evolution and high r-values which are characteristic at low temperatures is decreased. Measurements repeated at a higher strain level (~30%) reveal only a modest evolution of the texture and r-values between 10 and 30% strain (Figure 8). The features which do evolve are similar to those observed at lower strains at ambient temperature, which is consistent with the continued but lower relative activity of prismatic slip of <a> type dislocations. One thing to note from these results and the original results of Agnew & Duygulu [3] is that the experimental textures obtained after high temperature deformation do not exhibit a signature feature of extensive <c+a> slip, a splitting of the basal texture toward the tensile direction, a point which will discussed further below.

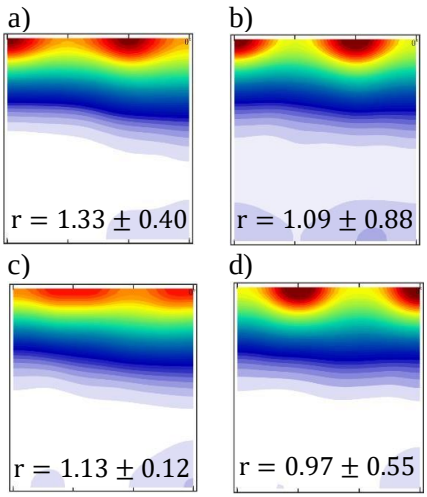


Figure 8: Experimental deformation textures observed after straining at a rate of 0.001 1/s at 250 °C to various strain levels: a) & c) 0.1 and b) & d) 0.3 for each orientation (TD – a) & b) and RD – c) & d)). Note that the textures continue to evolve with strain toward the node like texture shown in Figure 7, due to the continued activation of dislocation glide (i.e., prism slip).

The following results poignantly illustrate the advantage of genetic algorithm (GA) parameter determination and of introducing the kinematics of dislocation climb by comparing the results of three approaches to determine crystal plasticity model parameters to best-fit the case of deformation at 250 °C and a strain rate of 0.001 1/s up to a tensile strain of 0.3:

- parameters taken from the literature [3], which were "hand fit," (Figures 9c & 9d)
- GA without climb (Figures 9e & 9f), and
- GA with climb of <a>-type dislocations (Figures 9g & 9h).

The experimental textures and r-values presented in Figures 8b & 8d and are reproduced in Figures 9a & 9b for ease of comparison with the simulated results. It is clear that the use of a genetic algorithm resulted in a much better fit than the parameters taken from Agnew & Duygulu ($f_0$ = 1.90 vs 4.64, respectively). The GA method converged to a ratio between the CRSS of <c+a> to prism of 1, the lower bound of the aforementioned CRSS constraint, which resulted in decreased r values and weaker node texture component. However, including climb resulted in another large quantitative improvement (note decrease in error to $f_0$ = 0.67) as well as qualitative improvement in the general appearance of the textures. The extension of the texture components off the upper edge of the ODF sections of Euler space shown in Figures 9c through 9f are characteristic of the significant activity of <c+a> slip in the simulations, but these features are not observed experimentally. This new, physically-motivated approach provides a definitive improvement over modeling prior strategies and suggests that dislocation climb plays a

significant role in strain accommodation over a range of temperature and strain rate regimes (Figures 9 and 10), as detailed further below.

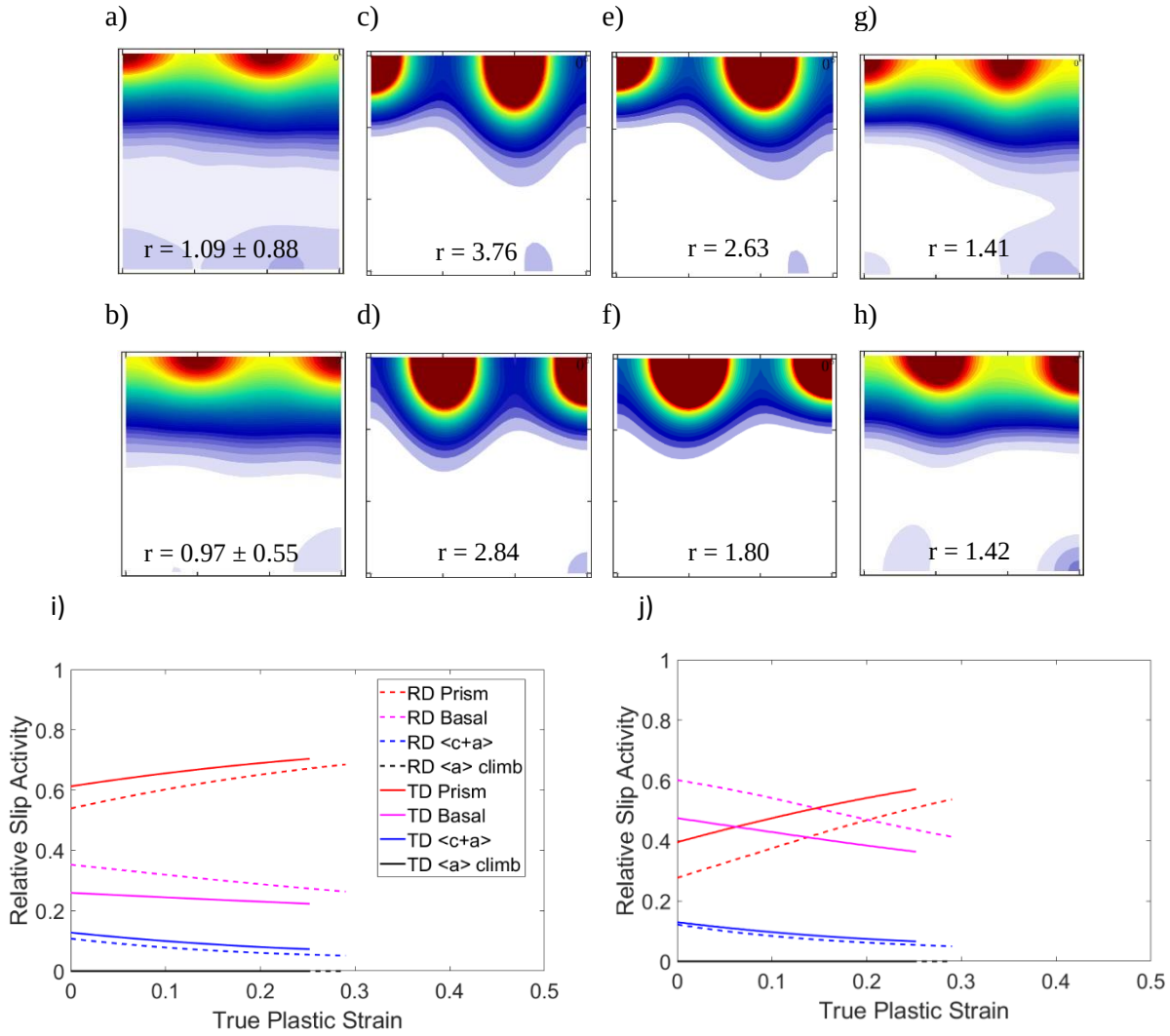


Figure 9: The importance of the climb of <a> dislocations during tensile deformation within the low temperature creep regime (e.g., 250 °C, 0.001 1/s) is indicated by the slower texture evolution and lower r-values of both the experiments and simulations of tension along TD (a,) c), e) and g)) and RD (b), d), f) and h)) directions, respectively. The efficacy of the incorporation of climb and machine learning are demonstrated through comparisons between: a) & b) experimental, c) & d) Agnew & Duygulu ($f_0$ = 3.08) [3], fits from a genetic algorithm without climb (e) & f)) ($f_0$ = 2.71) and with climb (g) & h))( $f_0$ = 0.94). Figures i) and j) show the fraction of strain accommodated by the glide modes activated in Agnew & Duygulu and GA without climb simulations, respectively. The relative slip activity plot for simulations involving climb can be found in Figure 11d).

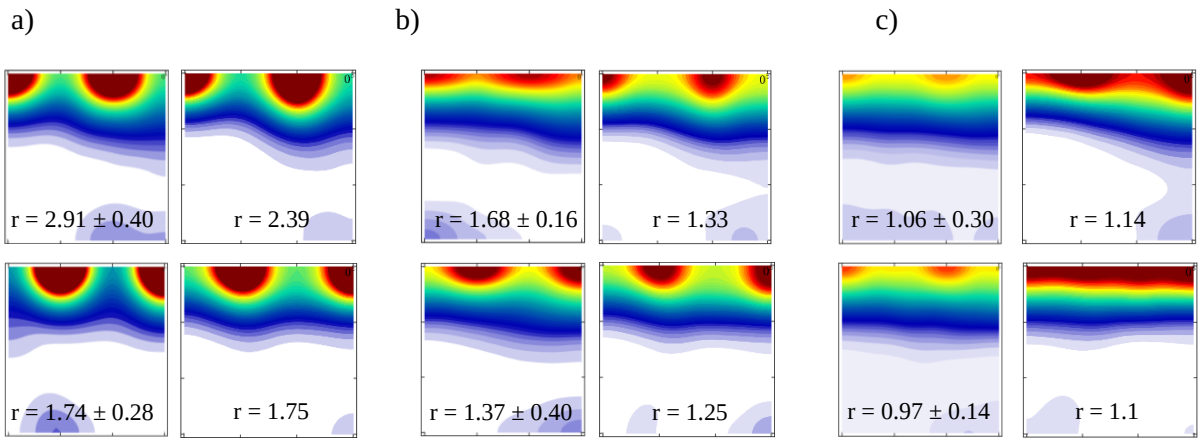


Figure 10: The influence of strain rate on isothermal tensile testing at 350 °C: a) 0.1 1/s, b) 0.01 1/s and c) 0.00028 1/s. Each row (top – TD, bottom-RD) of the block shows the experimental (left) and simulation (right) texture evolutions and associated r-values. Note that the texture evolution diminishes significantly as the strain rate decreases, denoting increased climb activation.

The amount of strain predicted to be accommodated by dislocation climb and glide during elevated temperature tensile tests by the VPSC-CLIMB model shows some expected and surprising trends (Figures 11d and 12d-f). While the samples strained at room temperature (~ $0.3T_m$) do not require strain accommodation by climb, the samples tested at higher temperatures (250 °C, 0.001 1/s and 350 °C, 0.1 1/s) do. This is not surprising. On the other hand, those two high temperature cases are predicted to exhibit distinct levels of climb, despite the fact that the two tests were conducted at a similar value of the Zener-Holloman parameter (Equation 1) and have correspondingly similar flow stresses (Figure 6a). This result emphasizes the inadequacy of the traditional constitutive modeling approach, which can capture the variations of flow stress, but does not acount for distinctions in the anisotropy (Figure 6b) and texture evolutions of the two test conditions. For the sample tested at 250 °C and 0.001 1/s, more than 50% of the strain is predicted to be accommodated by basal <a> dislocation climb, and the rest of the strain is almost equally distributed amongst the glide modes. This is a surprising result, since classical considerations of climb and glide creep typically hold glide responsible for the bulk of the strain accommodation, even in cases where the climb mode is rate controlling (e.g., [60]).

However, the replacement of prism slip, in particular, is essential in order to induce the reduced r-values (r ~ 1.1-1.5) of high temperature deformation. At 350 °C, and a strain rate of 0.1 1/s, most of the strain is predicted by VPSC-CLIMB to be accommodated by prismatic and basal slip with only a small amount of basal climb activity (Figure 12d), similar to the low temperature results (Figure 11c). This helps to explain why the relatively high r-values and

similar texture to that observed at low temperature persist to such a high temperature (Figure 10a). When varying just the strain rate at a fixed temperature of 350 ℃, the trend is straightforward. Note the increasing incidence of dislocation climb predicted by VPSC-CLIMB as the strain rate decreases from 0.1 to 0.01 to 0.00028 1/s (Figure 12d, 12e, & 12f). At 350 °C, 0.00028 1/s, which resides within the GBS regime (Figure 5b), the best fit simulation requires ~ 80% of the strain to be accommodated by climb. This is probably not physically accurate; however, it is interesting to note that one can describe many aspects of the response using the present VPSC-CLIMB model.

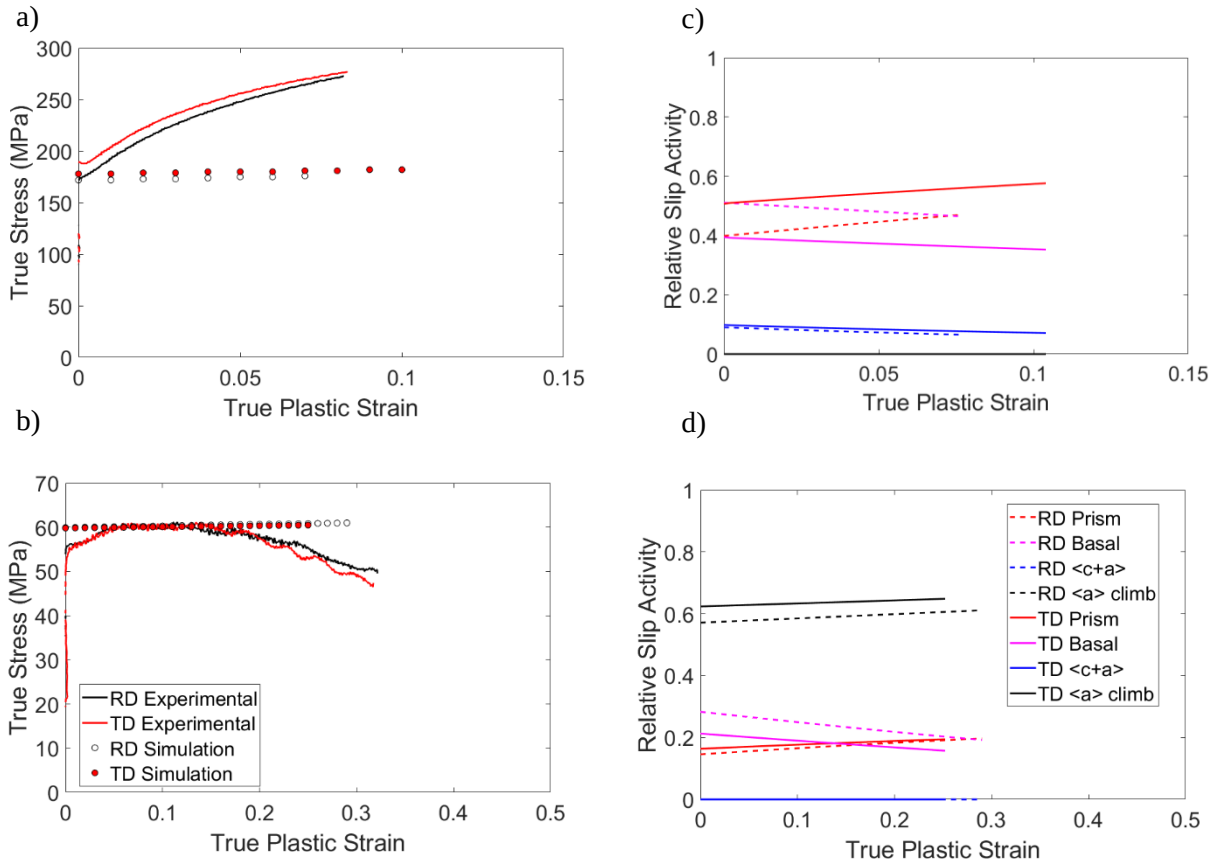


Figure 11: Experimental and simulated stress strain curves: a) Conventional Plasticity (20 °C, 0.001 1/s) and b) Low Temperature Creep (250 °C, 0.001 1/s) and their respective relative slip (& climb) activity plots: c) Conventional Plasticity (20 °C, 0.001 1/s) and d) Low Temperature Creep (250 °C, 0.001 1/s)

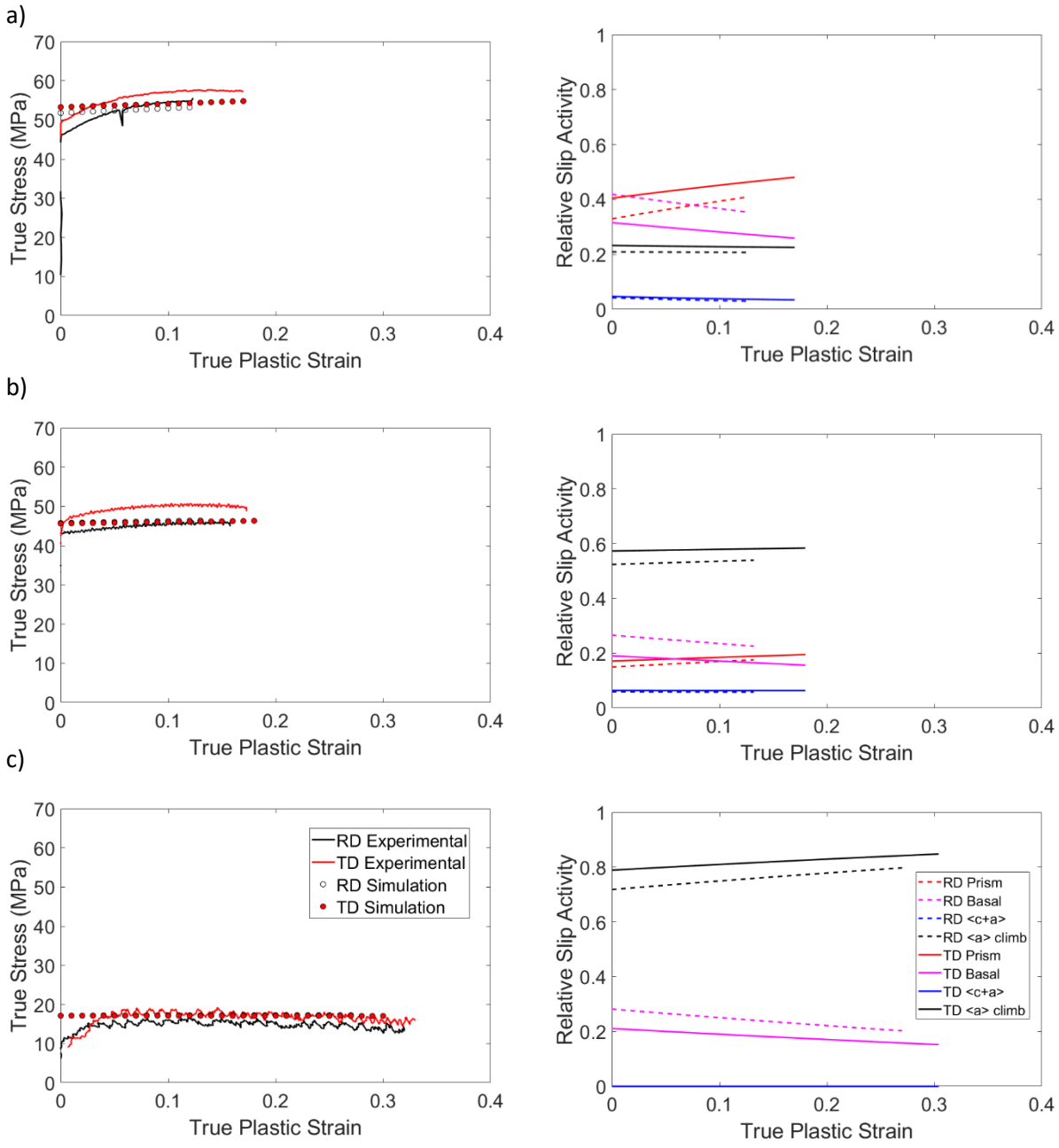


Figure 12: Experimental and simulated stress strain curves (a)-c)) and relative activity plots (d)-f)): Low Temperature Creep/High Temperature Creep Boundary (350 °C, 0.1 1/s), High Temperature Creep (350 °C, 0.01 1/s) and Grain Boundary Sliding (350 °C, 0.00028 1/s)

Once the best-fit critical stress values (relative to that of basal glide) for the investigated climb and glide modes were obtained by fitting the simulation results to the experimentally measured texture and r-value by minimizing the objective function (Equation 12), the Voce hardening parameters presented in Table 1 were fit to best represent the experimental stress strain curves, as shown in (Figures 11a-b and 12a-c). It is interesting to note that the CRSS values for the nonbasal slip and the climb mode obtained by the employed genetic algorithm are only slightly larger than that of basal slip, suggesting that there must be rather balanced activity of all the modes in order to best describe the observed texture and strain anisotropy.

Finally, simulations were performed to examine the effect of the character of the climbing dislocations and their results are summarized here. As suggested previously, "climb" of basal <a> screw dislocations results in identical contributions to the texture and r-value as prism <a> glide (i.e., a texture component that rotates the texture towards $\varphi_1 = 0°$ (TD) or $\varphi_1 = 30°$ (RD) in Euler space and an increase in the r-value). This was shown to be true for both TD and RD simulations in which the "climbing" dislocations were assumed to be 100% <a> type screw dislocations. Relative to the results presented in Figures 9g and 9h, such cross glide simulations (Figure 13) involving the same Voce parameters presented in Table 1 resulted in higher r-values (14.0 vs 1.24 for TD and 10.5 vs 1.19 for RD) and a texture evolution reminiscent of the effect of prismatic glide (node-like texture signatures), when compared to simulations with <a> edge climb. Thus, dislocation character will not be discussed further, since "climb" of screw dislocation behavior can be described by an existing mechanism (i.e., the glide of <a> dislocations on prism planes). This makes the initial assumption of edge-only dislocation climb plausible, though this is a topic which is certainly worthy of further investigation by lower length-scale modeling techniques such as discrete dislocation dynamics (DDD) simulation or experiments such as in-situ transmission electron microscopy.

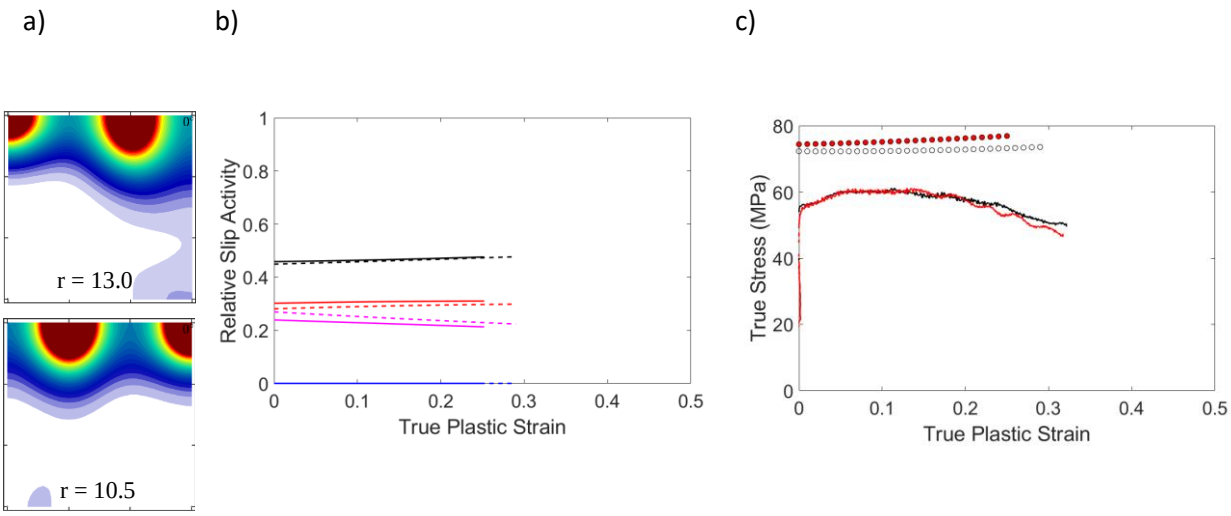


Figure 13: The importance of the character of the climbing dislocations on high temperature simulations (250 °C, 0.001 1/s): a) TD (top) and RD (bottom) textures with b) associated relative slip activity plots (TD – red, RD – white) using only basal screw dislocation "climb," and c) experimental (TD – red and RD – white) and simulated stress strain curves (circles).

Not surprisingly, modeling of the high temperature response of Mg required the addition of a climb slip mode of deformation. The hypothesis that prism slip is supplanted by <a> climb at high temperatures is supported by a coincident drop in r-value, a dramatic change in the dominant texture component, and a transition to a power-law constitutive regime. What is surprising is the large degree to which climb participates in strain accommodation itself. A sanity check on the requisite climb velocities of these edge dislocations predicted by VPSC-CLIMB is performed in the discussion section by comparing them with theoretical, diffusion-limited velocities.

## 5- Discussion

*Plausibility of dislocation climb strain accommodation*

The Orowan expression links the shear rate of deformation associated with a given mode of climb, $\dot{\beta}^s$, to the mobile density of climbing dislocations, $\rho_c^s$ , their Burgers vector, $b^s$, and their average velocity, $\bar{v}_c^s$.

$$\dot{\beta}^s = \rho_c^s b^s \bar{v}_c^s \qquad Equation\ 14$$

The fraction of strain accommodated by climb depends on the testing regime (rate and temperature). To check if these VPSC-CLIMB predictions are realistic, the required density of

mobile dislocations is computed, based upon a physical model of the steady-state climb velocity. An average value of the shear rate due to climb, $\dot{\beta}^s$, was calculated for each of the four high temperature cases we considered in detail, one at 250 °C, 0.001 1/s and three at 350 °C with distinct strain rates, by the summing the shear strain rates of each applicable climb system in each grain of the VPSC-CLIMB simulation. The flow stresses at the relevant conditions were obtained from best-fit Sellars-Tegart model (Equation 13) shown to well-describe the response of the material (Figure 6a).

Since the flow stress is essentially saturated during the test conditions of interest (Figure 5a) one may reasonably assume steady-state motion of the climbing dislocations, i.e., the climb component of the Peach-Koehler force, $f_c^s$, is balanced by the chemical (drag) force, $f_c^s + f_{chem}^s = 0$. The chemical force was proposed by Bardeen & Herring [61] and Weertman [62] as

$$f_{chem}^s = b\left[\frac{k_B T}{\Omega}\ln\left(\frac{c_v}{c_v^{th}}\right)\right]\boldsymbol{I}:\boldsymbol{k^s} \qquad Equation\ 15$$

$$c_v^{th} = c_v \exp\left(-\frac{p\Omega}{k_B T}\right) \qquad Equation\ 16$$

where $b$ is the magnitude of the Burgers vector, $k_B$ is Boltzmann's constant, $\Omega$ is the volume change due to the formation of a vacancy, $c_v$ is the vacancy concentration at the dislocation core, $c_v^{th}$ is the thermal equilibrium vacancy concentration at a given temperature (T) and *pressure* ($p$), **I** is the identity matrix and $\boldsymbol{k}^s$ is the aforementioned Hartley tensor. It is noted that the dislocation climb velocity can be affected by the hydrostatic stress due to its effect on the background concentration of vacancies, which will in turn affect the chemical (or osmotic) force on a climbing dislocation and can either slow or accelerate dislocation climb. [4]

Given the direct connection between the rate of vacancy creation or annihilation at the dislocation core and climb velocity, diffusion theory thus provides a direct linkage between the applied deviatoric stress and climb velocity, given the temperature dependent vacancy lattice diffusivity ($D_l$)

$$v_c^s = \frac{\Omega}{b}\left\{z_v D_l c_v^{th}\left[\exp\left(\frac{\Omega\left(\boldsymbol{k^{d,s}}:\boldsymbol{\sigma'}\right)}{k_B T}\right) - 1\right]\right\} \qquad Equation\ 17$$

where $z_v = 2\pi/\ln(R_{\text{cutoff}}/b)$, with $R_{\text{cutoff}}$ being the dislocation core cutoff radius, is the vacancy capture efficiency for a dislocation and has been found to be approximately equal to unity in

[4] As a historical note, Lebensohn et al. [19] rationalized an absence of a chemical force (i.e., the vacancy concentration is everywhere at equilibrium with the surrounding pressure), by assuming that vacancy sources and sinks are so close together that the fluctuations in vacancy concentration induced by dislocation climb are removed as quickly as they are created. Later, the chemical force was treated as a sort of backstress on the climbing dislocation, such that the incompressibility condition ($\dot{\varepsilon}_{kk}=0$) could be explicitly enforced, with 5 constitutive equations relating to the components of the deviatoric stress and strain rate (Equations 8 and 9) and a 6th equation relating to the hydrostatic pressure

several studies [63–66]. Notably, this equation directly accounts for the aforementioned effect of pressure because it influences the equilibrium vacancy concentrations in the vicinity (at a distance $R$) of climbing dislocations. At the typically small values of $\exp(\Omega(\boldsymbol{k}^{\boldsymbol{d},\boldsymbol{s}}:\boldsymbol{\sigma}')/k_BT) - 1 \approx \Omega(\boldsymbol{k}^{\boldsymbol{d},\boldsymbol{s}}:\boldsymbol{\sigma}')/k_BT$. Hence, Equation 17 implies an essentially linear dependence of the climb velocity on the applied stress. This equation was used to calculate the steady state climb velocities using an effective, scalar value of the Hartley tensor $k \sim 0.55$ selected to account for the stress state, texture, and possible dislocation characters of interest. Note that unlike its glide analogy, the Schmid factor (which has a maximum value of 0.5), the Hartley factor has a maximum value of 1. The diffusivity prefactor was taken from [67] and the vacancy migration and formation energies were taken from [68].

Inserting the obtained velocities into the Orowan expression (Equation 14) yields *mobile* dislocation densities of $3.5 \times 10^{12} - 2.6 \times 10^{14}$ 1/m$^2$ for tests performed at elevated temperatures in this study (Table 2). Given that only the dislocations with an edge component are really subject to climb, this implies a total dislocation density of at least a factor of 2 more, assuming approximately half of the basal dislocations are of edge character. Note further that these estimates were made assuming that the steady state climb rate is controlled by the lattice diffusion (Equation 17) and neglects the likely role of pipe diffusion, especially in cases close to power law breakdown. Regardless, total dislocation densities 10 times larger than these mobile dislocation density estimates seem plausible.

Table 2: Densities of mobile, climbing <a> dislocations for each elevated temperature condition tested

| Temperature (°C) | Rate (1/s) | Mobile, Dislocation Density (1/m$^2$) | Flow stress (MPa) | Global Mechanism |
|---|---|---|---|---|
| 250 | 0.001 | $2.6 \times 10^{14}$ | 58.22 | LT power law creep |
| 350 | 0.1 | $2.3 \times 10^{14}$ | 57.20 | LT/HT creep |
| 350 | 0.01 | $4.0 \times 10^{13}$ | 42.97 | HT power law creep |
| 350 | 0.00028 | $3.5 \times 10^{12}$ | 18.71 | GBS |

In the present work, which is focused on the kinematics (strain anisotropy and texture evolution), the effect of applied pressure is shown to be of little consequence. By definition, the pressure has an effect on the overall vacancy concentration (Equation 16), but at the given stress and temperature conditions of interest, this leads to an increase in vacancy concentration of less than 10%. Furthermore, this change in vacancy concentration leads to an infinitesimal increase in sample volume which would be recovered upon unloading of the sample. The local fluctuations in vacancy concentration at the dislocation cores are present and what is responsible for the dilatational portion of the Hartley climb tensor. They are accounted for, in the present analysis,

by the chemical force (Equation 15). Their effect on the total volume of the sample is again deemed inconsequential for crystal-scale calculations.

*Possibility of Grain Boundary Sliding and Other High Temperature Mechanisms*

A preliminary method for evaluating the effects of other high temperature mechanisms (grain growth, dynamic recrystallization and GBS) in the current simulation results would be to examine their effects on texture evolution and r-value. Grain growth has two effects on texture evolution in AZ31B: a strengthening of the basal texture [24] and the development of a $< 11\bar{2}0 >$ texture component [25]. It is difficult to identify the source of the basal component strengthening in the experimental textures since it will also occur with the activation of basal slip which is shown to remain active during high temperature deformation. The latter is not experimentally observed in Figures 9 and 10, making its contributions small; additionally, grain growth does not typically accommodate strain and therefore cannot describe the reduction in rvalue at high temperatures. Dynamic recrystallization has been shown to cause texture randomization [21,29] and could explain the softening observed in some of the tensile tests performed at high temperatures (Figure 11b). However, it appears that the texture evolution is slowed rather than randomizing during high temperature deformation (Figure 9), suggesting that another mechanism is dominant. The same figure also points out that glide motion is not suppressed as VPSC-CLIMB simulations show that prism <a> slip is responsible for the texture evolution between 10 and 30% strain. Texture randomization is also characteristic of grain boundary sliding, which suggests that it is unlikely to be solely responsible for the transition into the power law regime. Unlike dynamic recrystallization, grain boundary sliding has also been shown to lead to reduced r-values in AZ31B [37] and could be active during high temperature creep, particular at high temperatures and low strain rates (Figure 1).

We have shown that strain accommodation through dislocation climb is plausible from a density standpoint, but it does not rule out the possibility that GBS works in concert with the aforementioned dislocation climb mechanism, but rather emphasizes the importance of dislocation climb during high temperature deformation and suggests that strain accommodations by dynamic recrystallization and GBS processes may be empirically described by accounting for the kinematics of dislocation climb. The nonlinear regression of the Sellars–Tegart expression (Equation 12) yielded an activation energy (Q = 121 kJ/mol) that do not correspond to either self- or solute-diffusion through the lattice, both of which have activation energies closer to 135 kJ/mol [13]. GBS tends to have an activation energy related to grain boundary diffusion (~90 kJ/mol in Mg) with a sufficiently small grain size [69]. Low temperature power law creep is often associated with pipe diffusion, having a similar activation energy as boundary diffusion. While no single mechanism seems to match the experimentally observed phenomena, it must be noted that some of the tests examined in the present study are near boundaries on the deformation mechanism map (Figure 5b).

A second, more nuanced approach would be to examine if the "non-dislocation" mechanisms of DRX and GBS can be explained by the motion of dislocations and *disconnections* – line defects which are restricted to interfaces such as grain boundaries and have both a Burgers vector and interfacial step height. In general, grain boundaries in metals tend to be curved, which provides an obstacle to simple glide of disconnections. Analogous to dislocations avoiding an impediment (e.g., a precipitate) during deformation, disconnections use a combination of in plane glide and out of plane climb to the move within boundaries during grain growth. MD simulations have shown that grain boundary migration, as in the case of grain growth, is intrinsically linked to the motion of disconnections [70]. In addition, the study suggested that grain boundary sliding can be described as a scenario of grain boundary migration under zero shear stress and non-zero energy density difference between the adjacent grains. A similar mechanism could be used to describe the coupled motion of grain boundaries in Zn bicrystals, as modeled by Cahn et al. [71]. The disconnection climb rate is also important to the possibility of continuous DRX at higher strain rates [72]. As discussed above, the dislocation climb velocity is intrinsically linked to the rate of vacancy diffusion. In short, many of the effects of "non-dislocation" based deformation mechanisms on deformation texture evolution might be attributable to dislocation climb. VPSCCLIMB simulations were performed on a sample tested within the GBS regime (Figure 5b) as a preliminary test of this theory (Figure 10c). Extremely high climb accommodation (>85% of strain) appears to predict the r-value and slowed texture evolution which occur in this regime, however, there appears to be a mismatch between experimental and simulated textures. Both of the experimental textures have nodes at $\varphi_1 = 0°$ regardless of testing condition, while the simulated textures have nodes at $\varphi_1 = 30°$ (the same orientation as in the initial as-rolled texture) due to suppressed texture evolution from dominant strain accommodation by climb. Here, it is unclear whether this difference is significant due to the near uniformity of the texture, but it warrants further study to elucidate the distinction between climb and grain boundary sliding on texture evolution.

We conclude with a final reflection on previous work [14], in which the most rapid decrease in strain anisotropy was found to occur below the recrystallization temperature (~200 °C) and was attributed to the activation of non-basal slip, following Agnew & Duygulu [3]. The VPSC simulations performed in this study show that the reduction in r-value is not the result of increased non-basal slip, but rather the activation of dislocation climb and accompanied *decrease* in non-basal slip activity. It is emphasized that the activation of dislocation climb explains the reduction in r-value and the increase in rate sensitivity [73] as well as the slowed texture evolution. GBS was offered as a plausible explanation for observations of isotropic flow at lower strain rates [14]. Indeed, that is likely, yet many of the effects of such "non-dislocation" based deformation mechanisms on deformation texture evolution are shown to be describable in terms of the kinematics of dislocation climb. So far, the present modeling strategy of incorporating dislocation climb within the matrix appears to best capture the trends in anisotropy and texture evolution during high temperature deformation of a Mg alloy. Further research is required to integrate and reconcile these findings with concurrent findings related to grain growth, dynamic

recrystallization, and in particular, grain boundary sliding [27,74,75] especially at the highest temperatures and lowest strain rates explored.

## 6- Conclusions

This study was performed to examine the extent to which dislocation climb accommodates strain during the high temperature, in-plane tensile deformation of a model Mg alloy, AZ31B, sheet material. In agreement with previous studies, decreases in anisotropy and slowed texture evolution were experimentally observed to occur simultaneously as the test temperature was raised. The following major conclusions can be drawn:

- VPSC-CLIMB simulations run with parameters best-fit by a genetic algorithm show that the climb of abundant <a> dislocations sustains a significant amount of strain during in-plane tensile deformation of basal textured AZ31B sheet in the power law creep regime.

- VPSC-CLIMB simulations suggest that decreasing the strain rate leads to increased strain accommodation by dislocation climb.

- Densities of climbing dislocations required of each simulated condition were estimated using an Orowan expression based upon the steady-state, lattice diffusion-controlled climb velocity, and they were found to be plausible for every condition ($< 10^{15}$ $m^{-2}$).

- While a strong increase in <c+a> slip activity can explain the decreased r-values of Mg alloys at moderately elevated temperatures, it cannot simultaneously explain the observed changes in texture evolution, rate sensitivity, and activation energy that attend this transition.

- The enhanced climb of edge dislocations at elevated temperatures can explain the observed changes in constitutive response, in addition to the kinematic elements (texture and strain anisotropy) on which the present work focused.

**Acknowledgements:** The researchers at UVA would like to express their gratitude to the United States National Science Foundation, Division of Materials Research, Metals and Metallic Nanostructures (NSF-DMR-MMN) program, Grant No. 1810197, overseen by Dr. Judith Yang. LANL researchers would like to acknowledge BES project E8C5 and XMAT.
**Data availability:** The raw/processed data required to reproduce these findings cannot be shared at this time due to technical or time limitations.

# Chapter 2: Investigating the transition between ambient temperature and power law regime deformation using VPSC-CLIMB simulations optimized by genetic algorithm


## Abstract

Previous studies into the role of climb in AZ31B suggest that climb can accommodate larger amounts of strain than expected (>50%) under a classical glide and climb model. However, these conclusions were obtained through simulating 5 discrete conditions in the power law regime. Additional simulations in intermediate temperatures demonstrate that VPSC-CLIMB simulations optimized via genetic algorithm could describe the evolution of texture and strain anisotropy using climb strain accommodation. The temperature and rate dependency of optimized resolved shear and climb stresses at the experimental flow stress appears to follow the mechanical threshold stress model and a steady state climb model (using an Orowan expression) and suggests that the implementation of these mechanisms in VPSC-CLIMB simulations could lead to a holistic description of the constitutive behavior of AZ31B at a range of temperatures and strain rates. Additionally, the veracity of independent climb and glide activation suggested in the preceeding chapter was supported through estimations of the rate sensitivity and activation energy of climb incorporating and glide only VPSC-CLIMB simulations against experimental measurements. It was determined that climb strain accommodation resulted in higher rate sensitivities than glide only predictions and a plateau in the activation energy at high temperatures (> 200 °C) in keeping with experimental observations.


## 1- Introduction

Crystal plasticity modeling is a powerful tool for linking nano- or microscale information to macroscopic experiments. However, the goal of the present crystal plasticity study is to extract mechanistic information such that the results can be generalized to a wide range of conditions. In the previous chapter, the determination of critical resolved shear strengths (CRSSs) and climb threshold stresses was undertaken using a combination of machine learning via a genetic algorithm and VPSC-CLIMB to model the texture evolution and strain anisotropy for 5 specific temperature and strain rate conditions:

- 20°C at 0.001 1/s (room temperature deformation),
- 250°C at 0.001 1/s (low temperature deformation),
- 350°C at 0.1 1/s (boundary between low and high temperature deformation),
- 350°C at 0.01 1/s (high temperature deformation) and
- 350°C at 0.00028 1/s (grain boundary sliding)

Each of these conditions was selected for its value in determining specific aspects of the deformation behavior of the archetypal wrought Mg alloy, AZ31B. Overall, they permitted an assessment of the impact of climb activation in the power law regime, which offers additional degrees of freedom in how deformation is accommodated. The previous chapter showed that incorporation of dislocation climb permitted more accurate descriptions of the texture evolution and strain anisotropy of AZ31B at the above conditions than was previously achievable using solely dislocation glide- and twinning-based strain accommodation. The goal of the present chapter is to accurately predict these CRSSs and the climb threshold stress at any temperature and strain rate within the previously explored range through the incorporation of classic, thermally activated plasticity models. Note that it is not the intention to directly implement these models within the VPSC-CLIMB code. Rather, it is to explore the potential of such an implementation by predicting appropriate CRSS values to employ within the present power law model within VPSC to describe the behavior at specific rates and temperatures and to identify any major outstanding challenges of the overall approach.

The second objective of this chapter is to investigate the interaction of climb and glide during high temperature deformation. Classically, high temperature deformation has been assumed to follow a glide and climb model [43], where it is assumed that climb and glide operate in series and most of the strain is accommodated by glide. In this model, climb serves as a recovery mechanism to overcome obstacles to glide and is assumed to be the rate limiting step. When climb and glide operate in series, the rate sensitivity and characteristic activation energy are that of the rate limiting step (climb) and appear to coincide well with experimental observations in the lower and high temperature regimes. As mentioned previously, climb has rate sensitivities of 1/5 -1/3 and activation barriers equal to the self-diffusion energy in agreement with Weertman's natural creep law [22] assuming lattice diffusion-controlled climb where an SRS of 1/3 and self-diffusion activation barrier is recovered. In addition, the reduced rate sensitivity (1/7 - 1/5) and decreased activation energy (about ~90 kJ/mol [27]) observed experimentally in low temperature creep can be explained by accounting for pipe diffusion which can reduce the SRS due to dependence on the dislocation density and the relevant activation energy becoming that of pipe diffusion (~1/2-2/3 of the lattice activation energy (135 kJ/mol in Mg)). The additional role of dislocation density during pipe diffusion increases the stress exponent by 2 if a Taylor relation (Equation 1) between dislocation density and stress is assumed (the rate sensitivity is now $\frac{1}{n+2}$).

$$\tau = \alpha\mu b\sqrt{\rho} \rightarrow \rho = \left(\frac{\bar{k}\sigma}{\alpha\mu b}\right)^2 \qquad Equation\ 1$$

While the predicted activation energy and SRS of the climb and glide model appear to agree with experimental observations, the assumptions of the climb and glide model is at with odds with the

previous VPSC-CLIMB simulations for two reasons: 1) climb was demonstrated to accommodate significant amounts of strain within the power law regime and 2) VPSC assumes that the strain accommodations occur independently (Equation 2).

$$\dot{\varepsilon} = \dot{\varepsilon}_g + \dot{\varepsilon}_c \qquad Equation\ 2$$

In addition, the climb and glide model cannot predict the continuous evolution of SRS and activation energy experimentally determined as the temperature decreases since climb remains the dominant mechanism within the power law regime and would remain as the rate limiting step while sufficient vacancy diffusion exists. In contrast, when climb and glide operate independently, the strain accommodated by $\dot{\varepsilon}_g$ and $\dot{\varepsilon}_c$ can influence the activation energy and rate senstivity. The decrease in temperature would reduce the amount of strain accommodated by climb, leading to a reduction in rate sensitivity and activation energy. These strains are resolved onto slip modes with the highest maximum Schmid ($\overline{m}_i$) and Hartley ($\bar{k}$) orientation factor, respectively (Equation 3) averaged over every orientation in the sample. The Schmid factors of each slip system in every grain was calculated under in-plane tension using the microtexture measurement of the initial texture performed by electron backscattered diffraction (EBSD).

$$\dot{\varepsilon} = \sum_{i=1}^{N} \overline{m}_i \dot{\bar{\gamma}}_i + \bar{k}\dot{\bar{\beta}} \qquad Equation\ 3$$

SRS and activation energy predictions can be obtained from Equation 3 using the correct derivations (Equations 4 and 5) using appropriate choices for modeling $\dot{\bar{\gamma}}_i$ and $\dot{\bar{\beta}}$.

$$n = \frac{\partial ln\dot{\varepsilon}}{\partial ln\sigma} \rightarrow m = \frac{1}{\frac{\partial ln\dot{\varepsilon}}{\partial ln\sigma}} \qquad Equation\ 4$$

$$Q = -R\frac{\partial ln\dot{\varepsilon}}{\partial \frac{1}{T}} \qquad Equation\ 5$$

The various glide modes of HCP materials (basal, prismatic and <c+a> slip) are agglomerated into $\dot{\varepsilon}_g$. Only the climb of <a> dislocations was necessary to predict the texture and strain anisotropy evolution of rolled AZ31B deformed via uniaxial tension; therefore, other dislocation types are excluded in the current analysis. Equation 2 could be extended to incorporate the climb of different dislocations in other alloys.

This chapter will begin with a description of the Mechanical Threshold Stress (MTS) model used to predict the CRSSs of glide modes (basal <a>, prism <a> and pyramidal II <c+a>) and the Orowan type model for predicting the climb threshold stress before detailing the fitting procedure for constants pertaining to these models. Slip mode hardening will be implemented

using expressions derived from dislocation density based models [44]. The derivation of temperature and strain rate sensitive equations to predict the SRS and activation energy will be presented next, followed by the results of the MTS model/Orowan expression fitting and recreations of the texture evolution, strain anisotropy and constitutive behavior. The results section will end with predictions of the SRS and activation energy as a function of temperature at a fixed rate compared with experimentally determined values. The discussion section will focus on potential disparities between experimental and predicted constitutive behavior and avenues for improvement in the methodology for predicting SRS and activation energy followed by a list of conclusions.

## 2- Theory

The model chosen in the current study for predicting thermally activated plasticity is the mechanical threshhold stress (MTS) model. This model is based on the idea of the thermally activated glide shear rate ($\dot{\gamma}$) is represented by an Arrhenius expression with a stress dependent activation energy, $\Delta G(\tau)$, relative to a reference strain rate ($\dot{\gamma}_0$) (Equation 6) [27].

$$\dot{\gamma} = \dot{\gamma}_0 \exp\left(-\frac{\Delta G(\tau)}{k_B T}\right) \qquad Equation\ 6$$

This empirical expression can be fit to a wide range of obstacles with varying arrangements and strengths. The nature of the stress dependence on the activation energy varies by obstacle, but has the general form of Equation 7 [45], where $\Delta F$ is the intrinsic strength of the obstacles ($\sim\mu b^3$), $\hat{\tau}$ is the critical stress needed to activate a slip mode at absolute zero and $p$ and $q$ represent the arrangement of the dominant obstacles.

$$\Delta G(\tau) = \Delta F\left[1 - \left(\frac{\tau}{\hat{\tau}}\right)^p\right]^q \qquad Equation\ 7$$

Rearranging Equation 7 in terms of strain rate and accounting for athermal obstacles (e.g., grain size effects), $\tau_a$, results in the final MTS model (Equation 8).

$$\tau = \tau_a + \hat{\tau}\left(1 - \left[\frac{k_B T}{\Delta F}\, ln\left(\frac{\dot{\gamma}_0}{\dot{\gamma}}\right)\right]^{\frac{1}{q}}\right)^{\frac{1}{p}} \qquad Equation\ 8$$

Past studies of other materials (Ti [46] and Al [47] alloys) have used the MTS model to describe thermally activated glide of dislocations interacting with obstacles within VPSC simulations; however, to the author's knowledge, the MTS model has not been implemented into the descriptions of individual slip modes for Mg alloys, though it has been used in describing the macroscopic deformation behavior for Mg [45]. This may be due to the large number of

parameters necessary to fully describe the temperature and strain rate dependence for a glide modes as noted in the aforementioned papers. In addition, Mg alloys has the added complexity of having 3 major glide modes that have been observed to accommodate strain, further complicating the implementation of the MTS model (basal <a>, prism <a> and pyramidal <c+a>). Nevertheless, the strength of the MTS model lies in its ability to accurately describe the slip behavior of all major slip modes, as the arrangement and strength of the obstacles encountered is an adjustable parameter. It is thought that the MTS model will be able to describe the constitutive properties (texture evolution, strain anisotropy and flow stress) by enabling interpolation between the aforementioned CRSSs determined by the previous, time-consuming optimizations via genetic algorithm.

*The Orowan Model*

Classically, the shear strain rate ($\dot{\gamma}$) generated through dislocations moving at an average velocity ($\bar{v}$) is described using an Orowan expression (Equation 9), where $\rho_m$ is the mobile dislocation density and b is the Burgers vector [48]. An analogous expression can be developed for climb, which relates strain rate due to climb ($\dot{\beta}$) to the climbing dislocation density ($\rho_m^c$) and their average velocity ($\bar{v}^c$).

$$\dot{\beta} = \rho_m^c b \bar{v}^c \qquad Equation\ 9$$

The velocity of the climbing dislocations in the power law regime, where climb has been shown to be a significant strain carrier, was assumed to be controlled by the lattice diffusion of vacancies in accordance with Equation 10 [49]

$$\bar{v}^c = \frac{z_v D_{sd}}{b}\left(\exp\left(\frac{\Omega \bar{k} \sigma'}{k_B T}\right) - 1\right) \qquad Equation\ 10$$

where Ω is the atomic volume, $z_v$ is the vacancy capture efficiency (~1), $D_{sd}$ is the lattice self-diffusivity, $k$ is the Hartley tensor (0.55 for a strong basal texture)and $\sigma'$ is the deviatoric component of the applied stress. Substituting Equation 10 into Equation 9 and solving for stress yields an expression that describes the effect of temperature and strain rate on the climb stress (Equation 11).

$$\sigma_c = \frac{k_B T}{\Omega} \ln\left(\frac{\dot{\beta}}{\rho_m^c D_{sd}} + 1\right) \qquad Equation\ 11$$

The self diffusivity ($D_{sd}$) within the power law regime can be adequately described using lattice diffusion. However, at lower temperatures, lattice diffusivity becomes increasingly difficult and the contributions of diffusion through the dislocation cores becomes non-negliglible. The

effective self-diffusivity (Equations 12) contains contributions of pipe diffusion ($D_p$) and lattice diffusion ($D_l$) and replaces $D_{sd}$ in Equation 11

$$D_{eff} = D_l\left(1 + \frac{10a_c}{b^2}\left(\frac{\sigma}{\mu}\right)^2 \frac{D_p}{D_l}\right) \qquad Equation\ 12$$

where lattice and pipe diffusivities are governed by Arrhenius expression using preexponential factors from Frost and Ashby [27] and activation energies of 124 [39] and 92 kJ/mol [27], respectively, and a core area ($a_c$) of ~$10b^2$. In the following expressions, the shear rates ($\dot{\gamma}$) and climb rates ($\dot{\beta}$) due to glide and climb are approximated to be equal to the macroscopically applied strain rate. Under most cases investigated, this assumption is valid and precise knowledge of these values is not crucial as they are contained within logarithmic expressions.

where $\bar{k}$ is the Hartley factor associated with climb for a strongly textured (taken to be 0.55), rolled AZ31B sample under uniaxial tension and $\alpha$ is a geometric constant that describes the interactions between mobile dislocations and immobile, forest dislocations (chosen to be ~0.25 in accordance with materials that have slip along multiple planes [50]). Equation 1 is modified to reflect that only a fraction of the <a> dislocations present will climb using a variable defined as $\tilde{\rho}(T, \dot{\varepsilon})$ (Equation 13).

$$\rho_m^c = \tilde{\rho}(T, \dot{\varepsilon})\left(\frac{\bar{k}\sigma}{\alpha\mu b}\right)^2 = (A - BT + C\dot{\varepsilon})\left(\frac{\bar{k}\sigma}{\alpha\mu b}\right)^2 \qquad Equation\ 13$$

In this case, it is assumed that the fraction of dislocations that climb has linear dependencies on temperature and rate to develop a simple model for the mobile dislocation density. Values for $A, B,$ and $C$ will be obtained by multiple linear regression on values of $\tilde{\rho}$ calculated by dividing the predicted mobile dislocation densities from VPSC by the results of Equation 1.

*Critical resolved shear stress adjustment for <c+a> slip to account for future strain paths*

The CRSS values optimized by a genetic algorithm in Chapter 1 were used in all subsequent fitting procedure with the exception of <c+a> slip. The original study performed in Chapter 1 only examined in-plane uniaxial tension of a strongly texture Mg alloy, and does not adequately constrain <c+a> slip as it is not required to accommodate significant strain in these loading conditions. Using these CRSSs for <c+a> slip under other loading conditions (e.g., equibiaxial stretching) results in a strong, anomalous <c+a> texture component. This is not consistent with the results of Bohlen et al. [36], who performed formability tests under uniaxial and biaxial conditions and found little evidence of texture evolution consistent with <c+a> slip in either strain path at 250 °C. This suggests that additional loading conditions should be considered when making CRSS determinations in the future. To account for these limitations, the CRSSs for <c+a> slip were fit by hand to remove the errant texture component. This was done

by simulating through thickness compression (which promotes <c+a> slip and provides an adequate means of bounding its activity) at the tested rates and temperatures while adjusting the <c+a> CRSS. This is in keeping with the work of Bohlen et al. [36] whose equibiaxial stretching tests at lower temperatures and higher strain rates than those tested here (and therefore should require increased strain accommodation via <c+a> slip) resulted in experimental textures without this characteristic texture component.

*Strain rate sensitivity and activation energy in high temperature plasticity*

In keeping with the theme of understanding the mechanistic underpinnings of high temperature deformation, another aim of this chapter is to understand the implications of the employed methodology for assessing the role of climb in high temperature deformation since diffusion-controlled dislocation climb can strongly impact strain rate sensitivity (SRS) and activation energy. Exploring the SRS and activation energy will test the assumption that glide and climb may operate independently, as the strains accommodated by these mechanisms are summed additively in viscoplastic self-consistent (VPSC) modeling.

Measurements of the SRS and activation energy are commonly estimated from creep experiments and elevated temperature mechanical tests in a variety of materials in the literature (e.g., Mg ([19], [51]), steel [52] and Al [53]). Current literature has measured the ambient SRS of most materials as being low (~1/100 for Mg [19], ~1/100 - ~1/50 for Cu [54]) in most testing conditions (i.e., strain rate does not have a large effect on the flow stress), as virtually all strain is accommodated by glide, which is known to be nearly rate insensitive at ambient temperatures. SRS is defined as Equation 14

$$m = \left(\sigma \frac{\partial ln\dot{\varepsilon}}{\partial \sigma}\right)^{-1} = \left(\frac{1}{\sigma}\frac{\partial \sigma}{\partial ln\dot{\varepsilon}}\right) \qquad Equation\ 14$$

where $\sigma$ is the applied stress and $\dot{\varepsilon}$ is the applied strain rate. Evaluating the derivative of Equations 14, leads to Equation 15 where an inverted form of Equation 8 is substituted for the strain rate.

$$m_g = \left(\frac{\tau\dot{\gamma}}{k_B T} \times \mu b^3 \times q\left(\left(1-\frac{\tau}{\hat{\tau}}\right)^p\right)^{q-1} \times p\left(1-\frac{\tau}{\hat{\tau}}\right)^{p-1} \times \frac{1}{\hat{\tau}}\right)^{-1} \qquad Equation\ 15$$

At ambient temperatures, the applied stress is very high, which results in decreased rate sensitivity. Rate sensitivity increases dramatically with increasing temperature, especially during power law breakdown. Previous efforts of incorporating rate sensitivity into forming limit diagram predictions of AZ31B [25] assumed that the rates sensitivity of glide modes was highly temperature sensitive to match the macroscopically observed rate sensitivity. However, the results of Chapter 1 demonstrate the importance of climb, a highly rate sensitive mechanism (the simplest model of climb via Weertman [22] estimates $m_c = 1/3$, which is very high in comparison

to ambient predictions of the SRS at m ≤ 0.02). If climb can operate independent of glide as suggested by Equation 2, then the predicted SRS should agree with experimental measurements due to differences in slip mode rate sensitivity. While other mechanisms may be important at even higher temperatures (e.g., GBS), their effects will be neglected in the current study as they were not used in the texture evolution and strain anisotropy predictions in Chapter 1.

*Selection of MTS parameters*

The selection of parameters for the MTS model was performed following Follansbee [45]. The temperature dependence on the shear modulus was incorporated by fitting experimental resonant ultrasound spectroscopy (RUS) data [55] to the Varshni equation (Equation 16).

$$\mu = \mu_o - \frac{D_o}{\exp\left(\frac{T_o}{T}\right) - 1} \qquad Equation\ 16$$

where $\mu_o$, $D_o$ and $T_o$ are fitted parameters. These parameters will be fit using the linear regression method discussed later. In an effort to reduce the amount of fitted parameters, the arrangement of dominant obstacle for each slip mode was assumed from prior literature. The most common obstacles encountered by dislocations are listed in Table 1 [26]. Basal slip has been known to be strengthened by the presence of solutes ([56], [57]), which are modeled as random discrete obstacles (p = 2/3, q = 3/2). Prismatic slip is known to be controlled by double kink nucleation and migration ([58], [59]). As noted previously, <c+a> slip has important interactions with both glide and cross slip, so a specific obstacle was not assumed *a priori*. Instead, the methodology of Follansbee [45] was followed and the obstacle which led to the most linear relationship between $\left(\frac{\tau_i - \tau_{a,i}}{\mu}\right)^{p_i}$ and $\left[\frac{k_B T}{\mu b_i^3} \ln\left(\frac{\dot{\gamma}_o}{\dot{\gamma}_i}\right)\right]^{\frac{1}{q_i}}$ was chosen.

Table 1: Common obstacle types and associated arrangements

| Obstacle | p | q |
|---|---|---|
| Linear array, Peierls-Nabarro | 1 | 3/2 |
| Double kink nucleation | 1/2 | 1 |
| Bowing | 1 | 2 |
| Random discrete | 2/3 | 3/2 |

Values for the athermal stresses were selected using experimental single crystal data of pure Mg and listed in Table 2. Other values relating to the hardening of each slip mode with decreasing temperature were determined by linear regression.

Table 2: Experimental values of the athermal stress for each slip mode

| Slip Mode | Athermal Stress (MPa) | Source |
|---|---|---|
| Basal | 0.5 | Akhtar and Teghtsoonian [60] |
| Prism | 2 | Flynn et al. [61] |
| <c+a> | 6 | Obara et al. [16] |

In the case of <c+a> slip , the values of $q_i$ and $p_i$ are determined by plotting $\left(\frac{\tau_i-\tau_{a,i}}{\mu}\right)^{p_i}$ against $\left[\frac{k_BT}{\mu b_i^3}\ln\left(\frac{\dot{\gamma}_o}{\dot{\gamma}_t}\right)\right]^{\frac{1}{q_i}}$ as in Figure 2 and Equation 17. The adjusted CRSS values for <c+a> slip used for this linear regression can be found in Table 3.

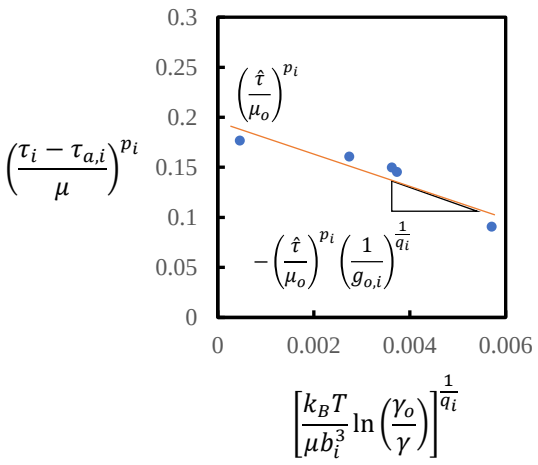


Figure 1: The determination of slip mode hardening parameters. Here, the slip mode hardening parameters ($p_i$, $q_i$, $\left(\frac{\hat{\tau}}{\mu_o}\right)$ and $g_{o,i}$) of <c+a> slip are fit calculated using linear regression. For simplicity, the applied strain rate is used in place of the slip mode level shear rates. This will have a negligible effect on the predicted CRSS as $\dot{\gamma} \approx \dot{\varepsilon}$ and it is within a logarithmic term.

$$\left(\frac{\tau_i-\tau_{a,i}}{\mu}\right)^{p_i} = \left(\frac{\hat{\tau}}{\mu_o}\right)^{p_i} - \left(\frac{\hat{\tau}}{\mu_o}\right)^{p_i}\left(\frac{1}{g_o,i}\right)^{\frac{1}{q_i}}\left[\frac{k_BT}{\mu b_i^3}\ln\left(\frac{\gamma_o}{\gamma}\right)\right]^{\frac{1}{q_i}} \qquad \textit{Equation 17}$$

Values for $\frac{\hat{\tau}}{\mu_o}$ and $g_{o,i}$ can be derived from the intercept and slope, respectively, once the shape of the obstacle is known. In the example shown, the data for the <c+a> slip is well represented when random discrete obstacles are assumed to be rate controlling (p = 1 and q = 3/2), yielding a goodness of fit $R^2 = 0.8511$. Other choices of p and q yield worse linearity.

Table 3: Corrected <c+a> slip CRSS

| Temperature (°C) | Strain rate (1/s) | CRSS (MPa) |
|---|---|---|
| 20 | 0.001 | 100.0 |
| 250 | 0.001 | 60.0 |
| 350 | 0.00028 | 12.2 |
| 350 | 0.01 | 43.0 |
| 350 | 0.1 | 55.0 |

Thus far, only the stress required to activate each slip mode (i.e., the CRSS) has been described by the MTS model, yet work hardening is undoubtably important in the description of the flow stress evolution during straining (Chapter 1) outside of the power law regime (< 250 °C). Strain hardening in VPSC-CLIMB simulations are controlled by a Voce equation (Equation 18)

$$\tau^s = \tau_0^s + \tau_1^s\left(1 - \exp\left(-\Gamma\left|\frac{\theta_0^s}{\tau^s{}_1}\right|\right)\right) \qquad Equation\ 18$$

where $\tau^s$ is the shear stress required to activate glide on a slip system, $\tau_0^s$ is the initial CRSS, $\tau_0^s + \tau_1^s$ is the back-extrapolated CRSS, $\Gamma$ is the accumulated shear in a grain and $\theta_0^s$ is the initial hardening rate. Past studies have yielded expressions for $\tau_1^s$ and $\theta_0^s$ in terms of steady state, dislocation density based parameters [62] (Equations 19 and 20)

$$\tau_1^s = \frac{C_1 \mu b k_1^s}{k_2^s} \qquad Equation\ 19$$

$$\theta_0 = \frac{C_1 \mu b k_1^s}{2} \qquad Equation\ 20$$

where $C_1$ is an interaction parameter (taken as unity), $k_1^s$ is a material constant relating to the storage of dislocations for each slip mode and $k_2^s$ is a constant controlling the dynamic recovery behavior of each slip mode. The temperature and strain rate dependence of $k_2^s$ was determined by fitting Equation 21 to tensile tests from room temperature to 200 °C [44]

$$k_2^s = \frac{C_1 b \mu}{\tau_{sat}^s} k_1^s = \frac{C_1 b k_1^s\left(D^s b^3 - k_B T ln\left(\frac{\dot{\varepsilon}_0}{\dot{\varepsilon}}\right)\right)}{D^s b^3 g_{ss}} \qquad Equation\ 21$$

where $D^s$ is the drag stress, $\dot{\varepsilon}_0$ is the reference strain rate ($10^7$ 1/s) and $g_{ss}$ is the normalized, stress-independent activation energy. Predicted flow stress strain curves at temperatures of 20, 100, 150 and 250 °C and a strain rate of 0.001 1/s were compared against experimental flow curves measured in Chapter 1. For temperatures where a strain rate of 0.001 1/s was not employed (100 and 150 °C), conditions with nearly identical Zener Hollomon parameters were chosen (50 °C at a strain rate of 0.00001 1/s and 100 °C at a strain rate of 0.0001 1/s, respectively). These are valid approximations of the necessary flow curves as the Zener Hollomon parameter was previously shown in Chapter 1 to accurately model the steady flow stress over the temperatures and strain rates of interest.

The results of the fitting procedure of the MTS and Orowan expressions detailed above were relegated to Appendix B. While it was successful in predicting the flow stresses, it is based on a model that attempted to predict the constitutive behavior of AZ31B assuming the hardening response could be implemented separately from the optimization of CRSSs and climb stresses. This assumption is untrue in conditions where work hardening is significant and it can be expressed in the MTS model using Equations 22 and 23. For more accurate predictions of the strain anisotropy, these effects must be accounted for during GA optimization.

$$\frac{\tau_i}{\mu} = \frac{\tau_a}{\mu} + s_p\left(\frac{\hat{\tau}_p}{\mu_o}\right) + s_i\left(\frac{\hat{\tau}_i}{\mu_o}\right) + s_\varepsilon\left(\frac{\hat{\tau}_\varepsilon}{\mu_o}\right) \qquad Equation\ 22$$

where $\frac{\tau_a}{\mu}$ denotes the athermal component to the stress, $s_p\left(\frac{\hat{\tau}_p}{\mu_o}\right)$ the intrinsic resistance to glide due to the lattice, $s_i\left(\frac{\hat{\tau}_i}{\mu_o}\right)$ the resistance due to impurity particles and $s_\varepsilon\left(\frac{\hat{\tau}_\varepsilon}{\mu_o}\right)$ the resistance due to the stored dislocation density. $s_p$, $s_i$ and $s_\varepsilon$ have the form of

$$\left\{1 - \left[\frac{k_B T}{g_0 \mu b_i^3}\ln\left(\frac{\dot{\gamma}_o}{\dot{\gamma}}\right)\right]^{\frac{1}{q_i}}\right\}^{\frac{1}{p_i}}$$

$\frac{\hat{\tau}_\varepsilon}{\mu_o}$ is stress dependent and evolves following a modified Voce expression

$$\frac{d\hat{\tau}_\varepsilon}{d\varepsilon} = \theta_{II}\left(1 - \frac{\hat{\tau}_\varepsilon}{\hat{\tau}_{\varepsilon s}}\right)^{\kappa} \qquad Equation\ 23$$

where $\hat{\tau}_{\varepsilon s}$ is the saturation stress, $\theta_{II}$ is the work hardening rate and $\kappa$ is a constant.

Additional conditions in the intermediate temperature regime were simulated using the methodology developed in Chapter 1 to investigate the transitional regime between ambient temperature deformation and the power law regime. Genetic algorithm-based optimization of

resolved shear stresses and climb stresses was employed using texture evolution and strain anisotropy measurements of a single loading condition (i.e., tension along the rolling or transverse direction). As these loading conditions cannot excite the activation of <c+a> slip, the RSS of <c+a> slip was manually reduced to the point where the texture evolution began to show clear signs of <c+a> slip.

*SRS and activation energy prediction*

As mentioned above, VPSC assumes that climb and glide operate independently (Equation 1). Each contribution can be resolved on the slip system using the correct orientation factors (Equation 3). The overbars represent that these values are averages of the slip system with the highest Schmid factor in each grain. It is assumed that the shear rate components for glide and the strain rate component for climb can be represented by the MTS model (Equation 11), assuming one obstacle, and Orowan model, respectively (Equation 16). Like the orientation factors, these shear rates are assumed to be the average of the most active slip modes in every grain. This is presumed to be satisfactory for the climb component which is typically active only within the power law regime and classically described by Weertman using the natural law of creep ($\dot{\bar{\beta}} \propto \sigma^3$) and acceptable in the glide portion to yield a qualitative measure for how the stress exponent varies as a function of temperature and strain rate.

The stress exponent (the reciprocal of the strain rate sensitivity) is thus related to the strain rate by Equation 24. For compactness, the MTS and Orowan expressions are not displayed as in the above equation, but are still enforced.

$$n = \frac{\partial ln\dot{\varepsilon}}{\partial ln\sigma} = \sigma \frac{\partial}{\partial \sigma}\left( ln\left( \sum_{i=1}^{N} \bar{m}_i \dot{\bar{\gamma}}_i + \bar{k}\dot{\bar{\beta}} \right) \right) \qquad Equation\ 24$$

The details of the strain rate sensitivity derivation are left to Appendix C. The final result is shown in Equation 25.

$$m = \frac{1}{\sum_{i=1}^{N} f_i n_{g,i} + f_c n_c} \qquad Equation\ 25$$

where

$$n_{g,i} = \left(\frac{\mathrm{g_{0,i}}\mu b^3}{k_B T}\right) q \left[1 - \left(\left(\frac{\tau - \tau_a}{\mu}\right)\left(\frac{\mu_0}{\hat{\tau}}\right)\right)^p\right]^{q-1} p\left(\left(\frac{\tau - \tau_a}{\mu}\right)\left(\frac{\mu_0}{\hat{\tau}}\right)\right)^{p-1} \left(\frac{\mu_0}{\hat{\tau}}\right)\left(\frac{\tau}{\mu}\right)$$

$$n_c = 2 + 200\frac{D_p}{D_{sd}}\left(\frac{\sigma}{\mu}\right)^2 + \frac{\Omega\bar{k}\sigma}{k_B T}\left(1 + \frac{1}{\left(exp\left(\frac{\Omega\sigma_{0,c}}{k_B T}\right) - 1\right)}\right)$$

All parameters maintain their values and definitions as listed above. The fraction of strain accommodated by each slip and climb mode, $f_i$, can is defined as Equation 26.

$$f_i = \frac{\bar{m}_i\dot{\bar{\gamma}}_i}{\sum_{i=1}^{N}\bar{m}_i\dot{\bar{\gamma}}_i + \bar{k}\dot{\bar{\beta}}} \qquad Equation\ 26$$

VPSC-CLIMB simulations yield values of the shear strain rates for each glide mode and the resolved strain rate for climb after each straining step. A representative average strain rate for each glide and climb mode was obtained by averaging over strain level and each loading condition (RD and TD tension). These fractions will be interpolated from the 5 datapoints calculated from the previous VPSC simulations (Appendix D) to obtain a first approximation of the SRS and activation energy evolution of temperature.

The activation energy can be derived in a similar manner starting with Equation 4. Here, the derivative of this expression is taken with respect to 1/T (Equation 27).

$$Q = -R\frac{\partial ln\dot{\varepsilon}}{\partial\frac{1}{T}} = -R\frac{\partial}{\partial\frac{1}{T}}\left(ln\left(\sum_{i=1}^{N}\bar{m}_i\dot{\bar{\gamma}}_i + \bar{k}\dot{\bar{\beta}}\right)\right) \qquad Equation\ 27$$

Similar to the rate sensitivity calculation, the activation energy has contributions due to glide and climb as well, which are left to Appendix C.

The activation energy can thus be written as Equation 28.

$$Q = -R\left(\frac{\left(\sum_{i=1}^{N}\bar{m}_i\left(\frac{\partial\dot{\bar{\gamma}}}{\partial\frac{1}{T}}\right) + \bar{k}\frac{\partial\dot{\bar{\beta}}}{\partial\frac{1}{T}}\right)}{\sum_{i=1}^{N}\bar{m}_i\dot{\bar{\gamma}}_i + \bar{k}\dot{\bar{\beta}}}\right) = -R\left(\sum_{i=1}^{N} f_i\,Q_g + f_c Q_c\right) \qquad Equation\ 28$$

where the functional forms of $Q_g$ and $Q_c$ are found in Appendix C.

Using Equation 28, the activation energy can be predicted from room temperature, glide controlled plasticity through the power law regime. Although this is outside the scope of the current thesis, it is possible to expand these analyses to include other thermally activated creep

mechanisms such as grain boundary sliding and diffusional flow as these mechansims operate in concert with the intragranular climb and glide mechanisms already incorporated.

The SRS values calculated by this method were also compared to values calculated using flow stress-strain rate data from Antoniswamy et al. [19]. Each flow stress-strain rate (at a constant temperature) curve was fitted to exponential or power law functions to obtain two datapoints closely bracketing the strain rate of interest (0.001 1/s) which will yield a close estimate of the SRS when used in Equation 24. These fits yielded an $R^2$ value greater than 0.99 on average; a finite difference method was used to evaluate the derivative in Equation 25. The experimental activation energy used in comparisons with the predictions from the MTS model were obtained from the data of Antoniswamy et al.. The lower temperature activation energies (<200 °C) was calculated using flow stress – temperature data via Equation 25, while the barriers in the power law regime were taken directly from their data.

The effect of climb in these predictions of rate sensitivity and activation energy will be elucidated through comparisons with calculations which are strictly glide only. Here, the genetic algorithm was employed to optimize VPSC simulations without dislocation climb using the experimental textures and r-values measured in Chapter 1. The obtained CRSSs from the optimized simulations were then scaled to the experimental flow stress at ~5% strain to avoid the elastoplastic transition and fit to the flow stress using Equation 18 and then fitted to the MTS model.

## 3- Results

Tables 4 and 5 lists the results of the GA-based optimization of RSSs and climb stresses. It is clear that when climb is absent, additional strain is accommodated by basal slip, as its RSS is lower than prism and <c+a> slip. There are a few outliers in the climb incorporating simulations due to nonbasal slip modes being unbounded during in plane tension. This is particularly true for prismatic stress at 350 °C and a very low strain rates, as the apparent RSS increases. Table 5 reports the results of adjusting <c+a> slip.

Table 4: Optimized RSS values for climb incorporating after GA optimization and rescaled to experimental flow stresses in intermediate temperatures

| | 50 °C, 0.001 1/s | 100 °C, 0.0001 1/s | 100 °C, 0.00173 1/s | 150 °C, 0.001 1/s |
|---|---|---|---|---|
| **Climb Incorporating Simulations** | | | | |
| Basal | 48.5 | 37.6 | 46.3 | 30.9 |
| Prism | 109.0 | 67.9 | 81.3 | 67.0 |
| <c+a> | 260.5 | 120.8 | 217.3 | 99.0 |
| <a> climb | 215.0 | 124.0 | 135.0 | 90.4 |

Table 5: Glide mode CRSSs and climb threshold stresses for climb incorporating simulations after bounding nonbasal slip

| | 50 °C, 0.001 1/s | 100 °C, 0.0001 1/s | 100 °C, 0.00173 1/s | 150 °C, 0.001 1/s |
|---|---|---|---|---|
| **Climb Incorporating Simulations** | | | | |
| Basal | 48.5 | 37.6 | 46.3 | 30.9 |
| Prism | 109.0 | 67.9 | 81.3 | 67.0 |
| <c+a> | 150 | 85.0 | 100.0 | 80.0 |
| <a> climb | 215.0 | 124.0 | 135.0 | 90.4 |

Figure 2 presents the texture evolution VPSC-CLIMB simulations compared to experiment. All conditions have similar experimental texture evolutions, suggesting that prism slip remains an important strain carrier to 150 °C. As noted previously, increases in temperature and decreases in rate lead to a reduction in prism slip activity as denoted by reduced strain anisotropy during in-plane, uniaxial tension. In the power law regime, this reduction in prism slip activity was accompanied by an increase in climb strain accommodation. Noticeably, the experimental texture begins to measured at 150 °C begins to demonstrate a slowed texture evolution reminiscent of climb. Simulations of these conditions in the intermediate temperature regime well describe both the texture evolution and strain anisotropy, suggesting that use of the VPSC-CLIMB model with parameters optimized by genetical algorithm is still applicable outside the power law regime. These observations are replicated in relative slip activity plots of the simulated deformation conditions (Figure 3). The strain accommodation via prism slip is shown to decrease with increasing temperature and decreasing rate. These decreases in strain accommodation by prism slip are mirrored by increases in climb activity in agreement with the

results of Chapter 1. Attempts to investigate the <c+a> strain accommodation in these conditions show a nonmonotonic trend.

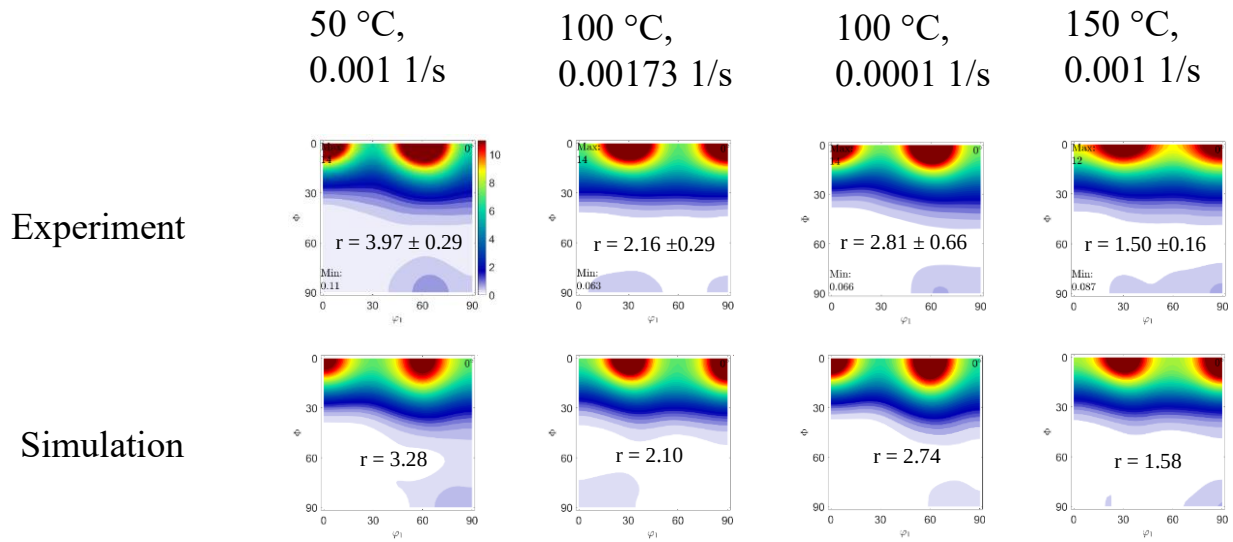


Figure 2: Comparison of the experimental texture evolution and r-values with predictions in intermediate temperatures

50 °C, 0.001 1/s | 100 °C, 0.0001 1/s | 100 °C, 0.00173 1/s | 150 °C, 0.001 1/s

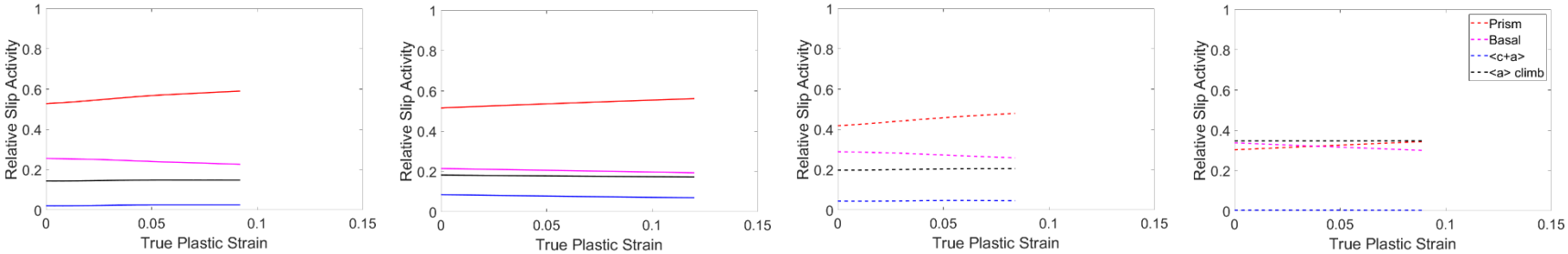


Figure 3: Relative strain accommodation for a range of temperature and strain rates in the intermediate temperature regime. Solid lines display TD tension simulations and dashed lines represent RD tension.

The RSSs and climb stresses obtained in the intermediate temperature conditions were incorporated into existing data optimized at ambient temperature and the power law regime (these data points were rescaled to their respective experimental flow stresses to recover the RSSs and climb stresses at flow conditions of interest). As expected, the RSSs and climb stresses required for the material to flow decrease with increasing temperature and decreasing strain rate (lnZ decreases) (Equation 29)

$$Z = \dot{\varepsilon} \exp\left(\frac{Q}{RT}\right) \qquad Equation\ 29$$

where $\dot{\varepsilon}$ is the applied strain rate, $Q$ is the activation energy, $R$ is the ideal gas constant and $T$ is the temperature. It is clear that the RSSs adopt a linear relationship in a semilog plot of stress and Z; this is a similar strain rate dependence to the MTS model (Equation 8), which suggests that a proper treatment of the MTS model could be fit to the current data. The optimized climb stresses are also linear in a semi log plot, which suggests that they can be described by an Orowan expression (Equation 8) provided that acceptable estimates of the mobile dislocation density and diffusivity are incorporated. Clearly, based on slope, climb has the highest temperature and rate dependence of all slip modes investigated due to its reliance on vacancy diffusion, which leads to a high activation energy and rate sensitivity. <c+a> and prism glide appear to have similar dependence on temperature and rate; though <c+a> is more difficult to activate as noted in the literature [15]. Basal slip has the lowest temperature and strain rate dependence in agreement with conventional understanding that it is nearly athermal [15].

The simulated flow stresses and strain anisotropies were plotted against experimental values in Figure 5. It is clear that the experimental flow stresses are well represented by the current GA simulations over a range of temperatures and strain rates. In addition, the simulated r-values are in agreement with experimental measurements for most conditions observed.

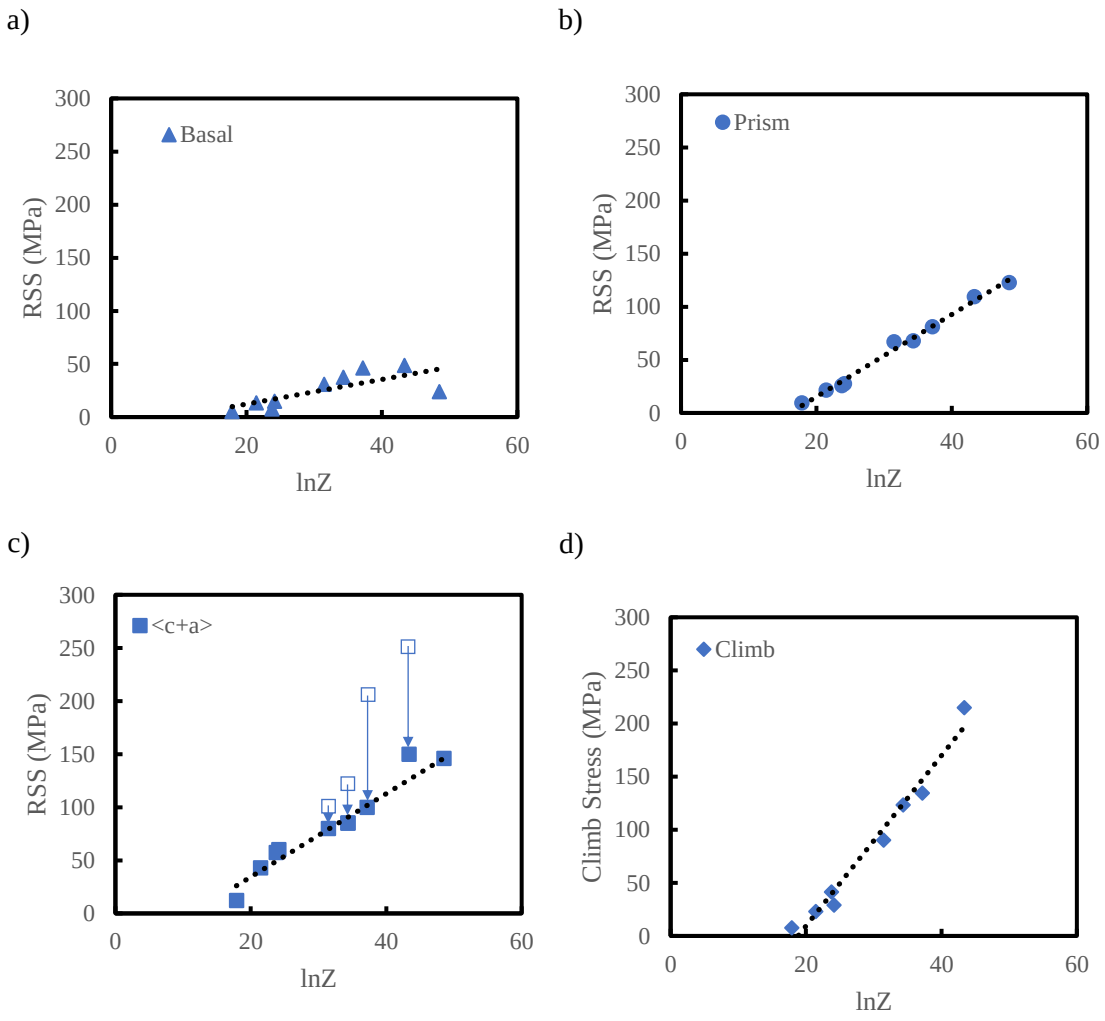


Figure 4: Temperature and rate dependencies of a) basal slip, b) prism slip, c) <c+a> slip RSSs and d) climb stress against the Zener Hollomon parameter. Open symbols on the <c+a> RSS denote the GA optimized values that were subsquently handfit. Dashed lines represent a linear relationship between the RSS and climb stress and Zener Hollomon parameter (a temperature compensated strain rate)

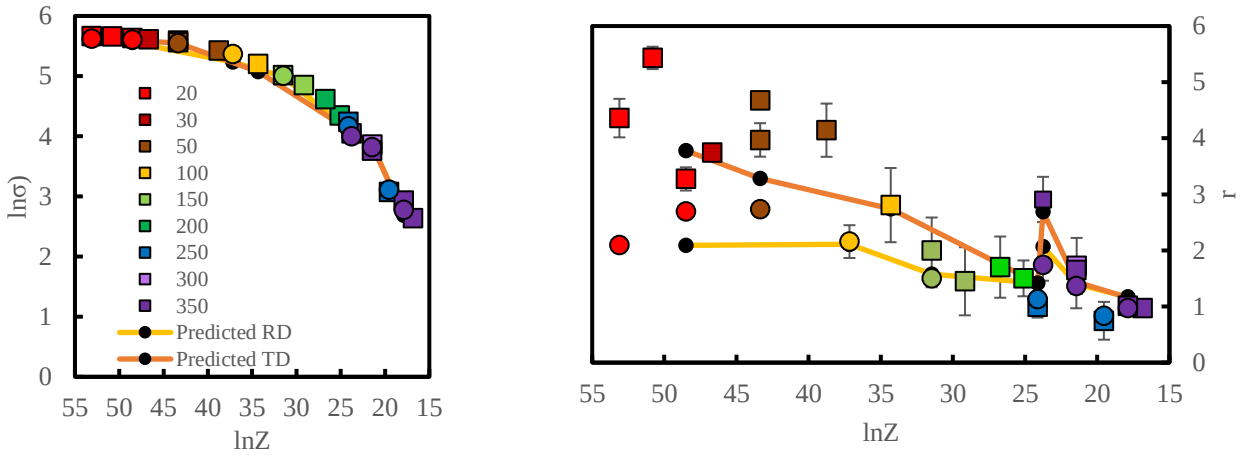


Figure 5: a) Predicted flow stress and b) strain anisotropy measurements against experimental values obtained in Chapter 1. Lines with black dots denotes the simulated data calculated using the values of RSS and climb stress found in Figure 4.

*Strain rate sensitivity and activation energy predictions*

Figure 6 shows the results of Equation 25 plotted in comparison with the experimental rate sensitivity observed by Antoniswamy et al.[19] using the MTS and Orowan equation fits found in Appendix B. Good agreement between prediction and experimental model when climb accommodation was incorporated for most conditions analyzed. The climb incorporating model shows clear improvement over glide-only predictions using the same methodology. This is simply due to the higher rate sensitivity of climb (1/5-1/3, depending on the dominant diffusional mechanism) relative to glide (1/50 - 1/7, from room temperature to 350 °C). The two predictions are very similar at ambient conditions, as climb is inactive in both scenarios. Above 50 °C, there is a large increase in the rate sensitivity when climb begins to accommodate significant strain. Under conditions where climb is inactive, an increase in the rate sensitivity still occurs as defined in Equation 26, but it is more gradual and less potent as the SRS only reaches 0.15 at 350 °C. While this initial investigation did not yield a quantitative means of predicting the strain rate sensitivity, it did bolster the proposed idea that the activation of climb is essential to increasing the SRS. Note that the calculated values of SRS bracketing a strain rate of 0.001 1/s are very similar to the SRS data reported by Antoniswamy et al. except at the highest temperatures investigated. This difference is a consequence of applying the tangent rule to a large difference in strain rate to approximate the slope (i.e., the SRS). Climb accommodates less strain at the higher rates used to estimate the SRS in Antoniswamy et al. (0.01 and 0.1 1/s), necessarily reducing the overall rate sensitivity.

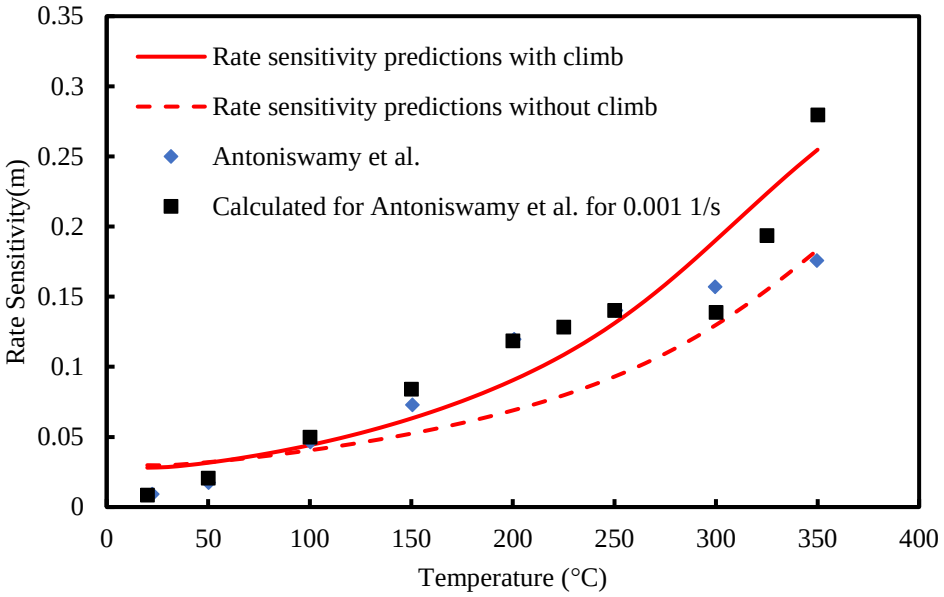


Figure 6: Strain rate sensitivity predictions using Equation 25 with and without climb. Data directly from Antoniswamy et al. and isolating a strain rate of 0.001 1/s is shown as a comparison.

The role of climb in the activation energy prediction is shown in Figure 7 for in-plane tensile deformation of a basal-textured sheet material at a given strain rate of 0.001 1/s. Like in the rate sensitivity case, climb-incorporating and climb-excluding predictions were compared to experimental data points. Neither prediction well described the activation energy for deformation at room temperature, though the climb incorporating model does accurately predict the qualitative reduction in activation energy relative to the power law regime. Within the power law regime, it is clear that climb accommodation is important to predict the activation energy. When climb is included, the activation energy reaches a maximum at ~125 kJ/mol, which is in good agreement with data obtained from Antoniswamy et al. for the power law regime, and significant strain accommodation through climb greatly slows the increase in activation energy. It is noted that the decrease in the predicted activation energy at temperatures greater than 300 °C is not experimentally observed due to the $-\frac{bT^2}{\tilde{\rho}}$ term, which dominates at high temperatures. Future work in investigating alternative expression for the mobile dislocation density or other mechanisms that operate at high temperatures (e.g. grain boundary sliding (GBS)) is merited and may improve the disparity between the current predictions and experimental measurements. Regardless, the predictions which include climb are in much better agreement with the experiments than the activation energy of glide only predictions which increase approximately linearly with temperature. From the comparisons of experimental SRS and activation energy and predictions including and excluding climb, it is clear that significant strain accommodation through climb, already known to be important to the deformation kinematics associated with texture evolution and strain anisotropy, is also essential for describing the SRS and activation

energies within the power law regime (designated as a homologous temperature above 0.5 at moderate strain rates of 0.001 1/s).

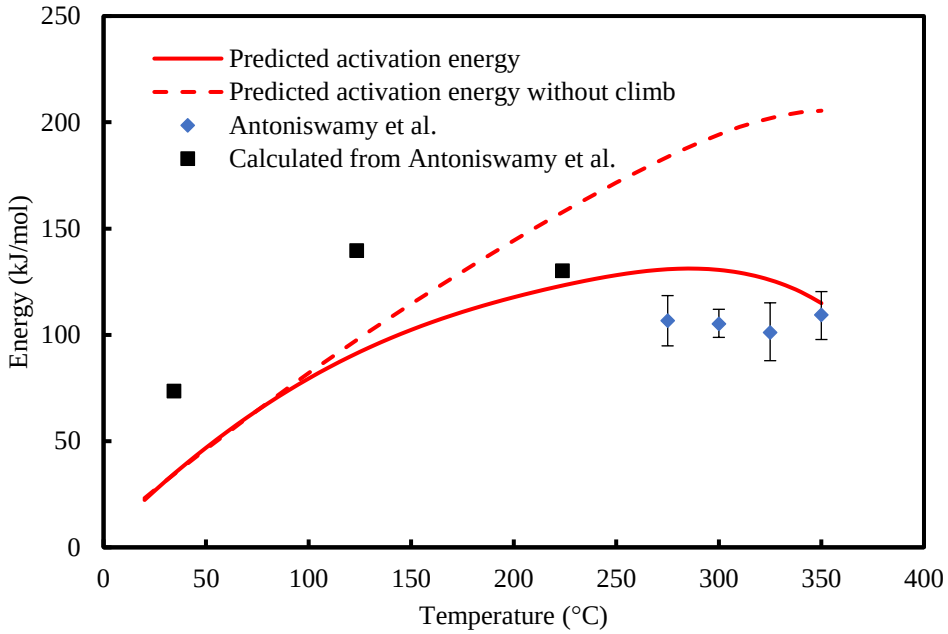


Figure 7: Predicted activation energies using the MTS model with and without climb incorporation assuming a strain rate of 0.001 1/s compared against the experimental observations of Antoniswamy et al. [19]

Two general conclusions can be made from these predictions in the strain rate sensitivity and activation energy. First, it appears that modeling deformation as the independent activation of glide and climb appears to describe the evolution of SRS and activation energy from ambient temperature into the power law regime. These derivatives assume (as does the VPSC-CLIMB climb model), that the contributions of glide and climb to the total strain rate are cumulative (i.e., these mechanisms must operate in parallel) (Equation 2). While this may appear surprising, it is likely due to lower symmetry materials (e.g., Mg) requiring climb to accommodate significant amounts of strain along specific loading directions to satisfy the Von Mises criterion [8]. The second conclusion is that there is merit in implementing a combined MTS – steady state climb model (Equation 11) into the VPSC-CLIMB methodology, as predictions generated by these models appear to describe experimental rate sensitivities and activation energies.

## 4- Discussion

*The potential role of <c+a> slip in elevated temperature deformation in Mg*

In the above simulations, the evolution in texture and strain anisotropy measurements from room temperature to intermediate temperatures are attributed to the activation of climb, in agreement with previous simulations (Chapter 1). Again, <c+a> slip does not appear to accommodate much strain, though the loading conditions employed in the current study were

inadequate in activating <c+a> slip. This is due to the lack of <c> axis strain imposed by in-plane tension on a basal-textured Mg alloy; softer basal and prism slip are unable to accommodate these strains. Past studies have shown that the activation of <c+a> slip can greatly reduce the strain anisotropy [17] and that its CRSS is highly temperature sensitive and begins to decrease above 100 °C based on the seminal work of Obara et al. [18]. It is unlikely to play a significant role at higher temperatures within the power law regime, as the texture measurements of uniaxially strained and equibiaxially stretched AZ31B sheet at 200 °C performed by Bohlen et al. ([36], [37]) show slowed texture evolution indicative of climb strain accommodation (Figure 8). This is somewhat surprising, as equibiaxial stretching conditions (similar to through thickness compression) should promote <c+a> slip. Indeed, other experimental results [63] suggest that <c+a> slip must be present to maintain a split in the basal pole figure present initially (Figure 9) in the as-rolled texture, as the shearing imposed by basal glide rotates the <c> axes towards ND. In addition to experimental evidence suggesting that <c+a> slip should accommodate strain in these intermediate temperature conditions where climb is not the dominant strain carrying mechanism, the required mobile dislocation densities necessary (Table 6) for climb to activate also suggest that some, if not the majority, of strain attributed to climb in the VPSC-CLIMB could instead be due to <c+a> slip. The required mobile dislocation densities were calculated from an Orowan expression (Equation 8) assuming that the resolved strain rate ($\dot{\beta}$) is similar to the applied strain rate ($\dot{\varepsilon}$) and the Taylor density is calculated from Equation 12.

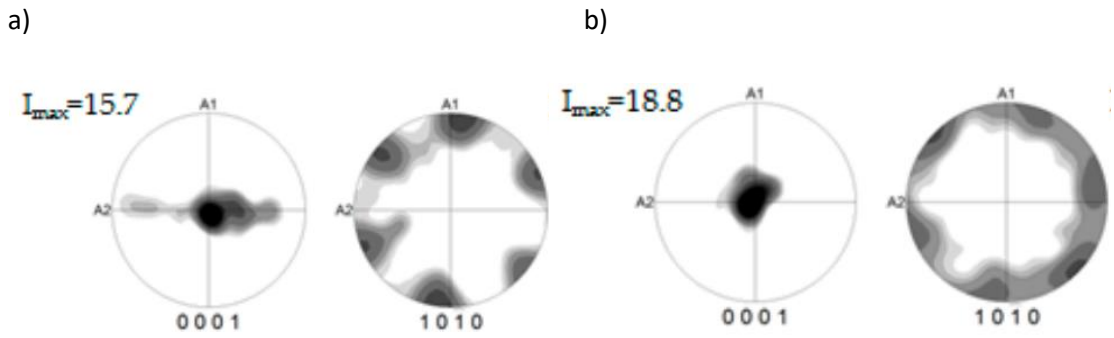


Figure 8: Texture evolution of as-extruded AZ31B samples under a) uniaxial straining and b) equibiaxial stretching. Figures reproduced from Bohlen et al. [36].

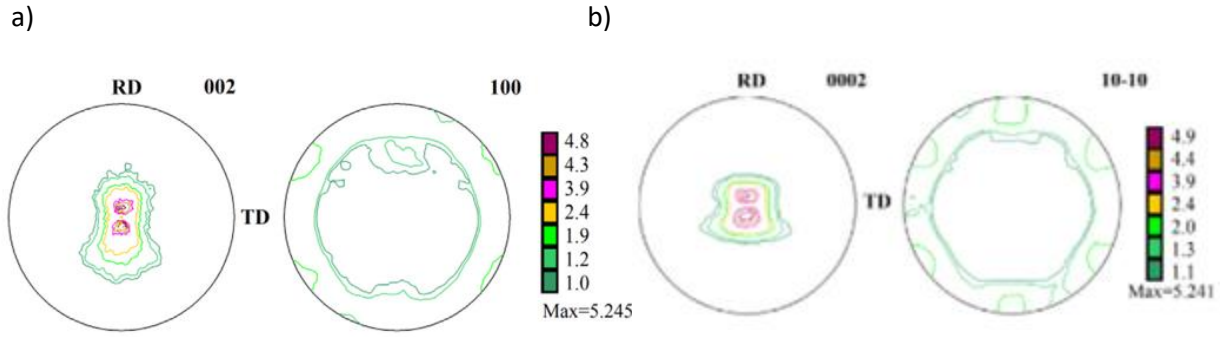


Figure 9: Texture evolution of as-rolled sheet AZ31B deformed in RD tension at 200 °C. a) Initial texture, b) Deformed texture. Figures reproduced from Zhou et al. [63]

Table 6: Predictions of the mobile dislocation densities required to accommodate the strain attributed to climb and Taylor densities

| Temperature | Strain rate | Mobile dislocation density ($1/m^2$) | Taylor density ($1/m^2$) | Fraction of Taylor density that must climb |
|---|---|---|---|---|
| 323 | 0.001 | $6.01 \times 10^{20}$ | $1.24 \times 10^{16}$ | 48372.9 |
| 373 | 0.0001 | $3.38 \times 10^{17}$ | $6.22 \times 10^{15}$ | 606.0 |
| 373 | 0.00173 | $5.21 \times 10^{18}$ | $8.60 \times 10^{15}$ | 54.4 |
| 423 | 0.001 | $5.10 \times 10^{16}$ | $4.41 \times 10^{15}$ | 11.6 |

While available experimental evidence suggests that <c+a> slip is not a significant strain carrier within the power law regime, <c+a> slip is likely active at lower temperatures and could explain the reduced experimental strain anisotropy measurements relative to predictions made in the current study. Therefore, future studies should endeavor to rigorously understand the role of <c+a> slip at these intermediate temperatures and incorporate other strain paths in addition to in-plane uniaxial tension (e.g., through thickness compression) to better capture the evolution of the <c+a> CRSS over temperature and avoid the *ad hoc* hand fitting performed here.

*Mechanistic understanding of the rate sensitivity and activation energy*

The rate sensitivity and activation energy predictions incorporating climb better captured the evolution of the experimental SRS and activation energy than glide only predictions (Figures 7 and 8), providing additional support to the notion that climb accommodation of strain is vital in

describing the high temperature deformation of Mg alloys. These qualitative improvements in the SRS and activation energy also suggest that the climb and glide model may be inaccurate in Mg alloys. The climb and glide model of creep originated from the seminal work of Weertman [64] to describe the experimentally observed creep phenomena of the steady state creep rate ($\dot{\varepsilon}_c$) described by Equation 30 as determined by Dorn [65]

$$\dot{\varepsilon}_c = C_2 \sigma^{\alpha_1} \exp\left(-\frac{Q}{k_B T}\right) \qquad Equation\ 30$$

where $C_2$ and $\alpha_1$ are constants. Weertman's theoretical derivation of Equation 27 assumed that multiple possible slip modes must be active and therefore excluded single crystal HCP metals (but not polycrystalline materials), whose dislocations were only observed to glide on basal planes (for Mg). This theory requires an obstacle that can impede the motion of gliding dislocations. In the original iteration, the formation of Lomer locks (the formation of sessile dislocations via the reaction of two glissile dislocations from different slip systems) was required to act as obstacles to glide. However, Lomer locks are expected to be rare in Mg as most dislocations are of <a> type ([66], [67]) and will be on the closed packed basal plane. The reaction between two <a> dislocations either results in annihilation (e.g., $<a_1>$ reacts with $-<a_1>$) or a glissile dislocation (e.g., $<a_1>$ reacts with $<a_2>$ to form $-<a_3>$). Other possible obstacles, precipitates and solute atoms, are not expected to dominate. Al-Mn particles that precipitate are typically too large (~2 μm) and too widely spaced to act as obstacles [68], leaving grain boundaries and solute atoms as the remaining mechanisms by which dislocations are impeded.

Rather than assume that climb only activates in situations where glide is impeded, it is worthwhile to explore the situations in which climb may be required to accommodate strain. There is a significant difference in how cubic and non-cubic materials satisfy the Von Mises criterion [8], which requires that 5 independent active slip modes to accommodate an arbitrary deformation. In cubic metals, particularly those that are face centered cubic (FCC), there is an overabundance of possible slip modes (12 choices (of which 8 are independent) for the possible 5 independent slip modes needed) (Figure 10) and therefore, climb is not required to accommodate large amounts of strain. The same cannot be said for Mg (an HCP material) as it has 4 independent slip modes at room temperature (2 from basal slip and 2 from prismatic slip as the $a_3$ direction is a linear combination of $a_1$ and $a_2$). It is also important to note the straining directions that each slip mode can accommodate. In FCC materials, the possible slip modes are inclined to the 3 Cartesian directions (assumed to be the $[100]$ directions in cubic crystallography). When the other unique (111) planes are considered, all possible straining directions can be accommodated by a combination of slip systems highlighted in Figure 12. This restatement of the Von Mises criterion demonstrates the need for 5 independent slip modes as there are 5 independent components to the strain tensor (symmetry requires $\varepsilon_{ij} = \varepsilon_{ji}$ and plastic deformation assumes incompressibility, $\varepsilon_{11} + \varepsilon_{22} + \varepsilon_{33} = 0$). This is not the case for Mg, which can only accommodate strain within the basal plane using basal and prism slip. Past studies ([14], [20]) have suggested that <c+a> slip could serve in the capacity of accommodating <c> axis strains; however, the present work also suggests that <a> climb, which appears to accommodate a large amount of strain in the power law regime, offers a similar capacity. This

does not necessarily mean that <c+a> slip is inactive. Rather, the stress levels required to activate <c+a> slip may be too high except in cases where compatibility must be enforced, such as near the boundaries between two grains undergoing different types of slip as described by Koike et al. [17].

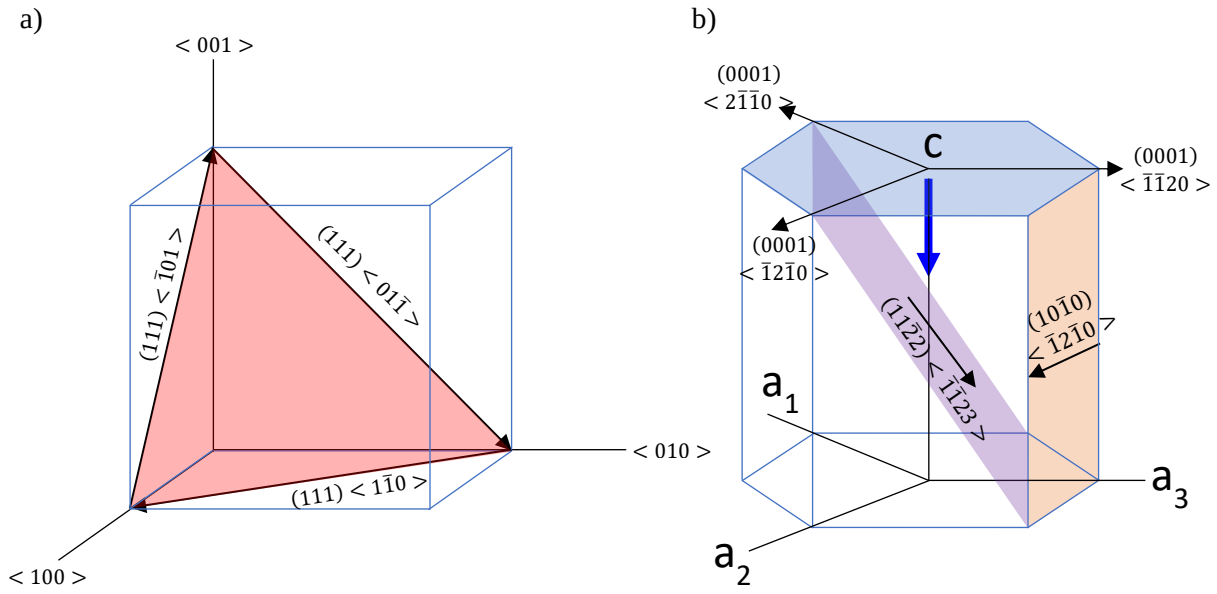


Figure 10: Schematic of the slip modes available in a) FCC and b) HCP metals. Large font denotes a cardinal direction in each crystal structure and small font represents a slip system. Arrows denote the slip direction of the dislocation (the straining direction). Black and blue arrows represent glide and climb, respectively. The major slip planes are highlighted in each crystal structure: FCC (111) – red, HCP basal plane – blue, HCP prism plane – orange, HCP pyramidal II plane – purple.

The results of the current work and that of Chapter 1 support the notion of required strain accommodation via climb. As mentioned previously, climb is necessary to simultaneously predict the texture and strain anisotropy evolution (Chapter 1). In this chapter, the addition of climb also allows for better predictions of rate sensitivity and activation energy. The increase in SRS is of particular importance as it may explain the increase in ductility observed at elevated temperatures [19]. It has been well documented that increased rate sensitivity leads to stable neck formation and delays strain localization [69]. The fact that climb is potentially required to accommodate significant amounts of strain to satisfy the Von Mises criterion suggests that the basic assumption that climb only exists as a recovery mechanism is incorrect when describing HCP metals. This is supported by the presented model for the SRS (Figure 6) and activation energy (Figure 7) having good agreement with experimental measurements in the power law regime, suggesting that deformation in AZ31B can be represented as the independent activation of climb and glide.

*Disparities between the experimental measurements and predictions*

The predictions presented qualitatively describe the trends in SRS and activation energy and are a vast improvement over glide only predictions, yet significant discrepancies exist when compared to the experimental measurements. These disparities can partly be attributed to errors in the methodology employed to calculate the experimental SRSs and activation energies as well as the predicted values. As implied by Equations 24 and 27, the SRS and activation energies are calculated under the assumption that variables such as final strain level, the microstructure [70], the temperature (for the SRS) and the stress (for the activation energy) remain constant. These first two parameters are related, as the strain level will influence the texture evolution and dislocation density of the sample. Experimental measures of SRS and activation energy were obtained through uniaxial tensile tests [19] of multiple samples, each with potentially different thermomechanical histories and microstructures, which may impact the SRSs and activation energies. Confidence in these values can be improved by employing tests which change the strain rate (strain rate jump and stress relaxation tests) and temperature (dead load mechanical tests with variable temperature) during the test while keeping over parameters constant.

While both strain rate jump tests and stress relaxation tests are more advantageous in rate sensitivity measurements as they can interrogate multiple strain rates while keeping the microstructure constant, strain rate jump tests (where the applied rate is increased after steady state flow has been established in the material) have been shown to be more accurate than stress relaxation tests in materials which deform by multiple slip modes [56]. In this instance, the accumulation of strain and texture evolution between rate jumps will be very small, as steady state flow is quickly reestablished at constant temperature, leading to a good approximation of the instantaneous rate sensitivity at the applied rate. Another important factor is that predictions of rate sensitivity must be done at strain rates very close to the applied rate, as Equation 24 is evaluated using a tangent rule. This was the impetus for fitting Antoniswamy et al.'s data and recalculating the SRS around a strain rate of 0.001 1/s. In a similar manner to rate jump tests, measuring activation energies with dead load mechanical tests offers the advantage of keeping the microstructure and load (and therefore, the stress) constant by adjusting the temperature during the test. However, the return to steady state flow after temperature adjustment will be slower than an equivalent change in strain rate, suggesting that the error in activation energy will be larger than rate sensitivity under ideal circumstances. In the data of Antoniswamy et al., temperature differences of 50 °C between tests were used to calculate the activation energy. Such a large change in temperature could contribute large amounts of error to the experimental activation barriers (particularly at lower temperatures outside the power law regime). As a result, the activation energies calculated from Antoniswamy et al.'s data at near ambient temperatures may be overestimated and may begin to explain the discrepancy between the experimental and predicted values.

Another source of error could be from the methodology used to predict the SRS and activation energy. An important assumption derived in Equations 24 and 27 is that the polycrystalline material (and the VPSC simulations which yielded glide mode CRSSs and climb stresses to fit to the MTS model and Orowan expression) can be represented as a single crystal with the applied strain rate being parsed into the various active slip modes as determined by

Figure D1. The fractions listed in the figure are calculated using the averaged shear rates over the course of deformation and loading conditions (tension along the rolling and transverse directions). This is most likely a good first order approximation of the SRS and activation energy predicted by VPSC simulations. One potential source of error is in the calculation of the weighting fractions (Equation 26). These fractions included the orientation factors for glide and climb ($\overline{m}_i$ and $\bar{k}$, respectively) which are calculated from knowledge of the orientations in the initial texture. The orientation factors are assumed to be constant in Equation 24, which is only true under circumstances where the texture evolution is minimal (i.e., when climb accommodates a significant fraction of strain within the power law regime). Closer to room temperature, the activation of glide modes will initiate texture evolution. A reduction in the Schmid factor occurs as the lattice orientation rotates relative to the loading direction, reducing the fraction of strain accommodated by the mode. This would be most evident in the prismatic slip mode due to its large strain accommodation at ambient temperatures. Furthermore, these fractions were calculated using VPSC-CLIMB simulations which assumed that $n_g = 20$ and $n_c = 3$ for all temperatures, which is does not reflect the very low rate sensitivity of glide at ambient temperatures (this has been investigated elsewhere in the literature [71]) and the possibility of significant pipe diffusion at moderately elevated temperatures which would lower the SRS of climb [27]. Finally, the current predictions do not account for the role of slip mode hardening, as described in Equations 25 and 28. From Figure 11, it is clear that overestimating the amount of prismatic slip occurring will lead to an apparent reduction in activation energy at room temperature, as it has an intermediate energetic contribution. This does not explain the relatively small discrepancy in the room temperature rate sensitivity, as reducing the fraction of strain accommodated by prism slip will further increase the rate sensitivity (Figure 11). Rather, this is a function of the MTS model, which is used to describe the rate sensitivities of each glide mode. Future work might also include using the same derivations as presented here, but with different thermally activated plasticity models (e.g., Leyson & Curtin [57], Yasi et al.[72]) for glide which may yield better results.

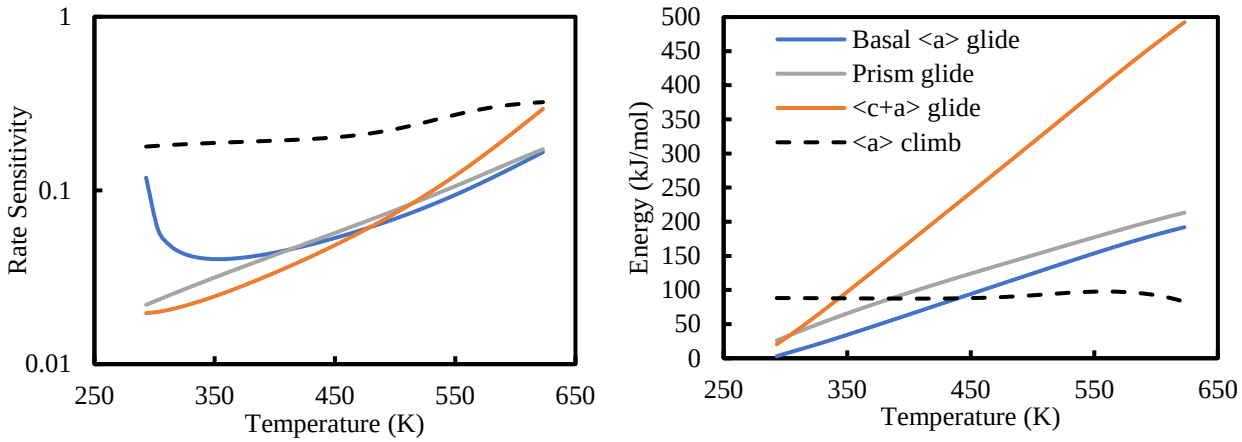


Figure 11: Evolution of a) rate sensitivity and b) activation energy for each investigated slip mode in AZ31B at an applied strain rate of 0.001 1/s

*Possible extension of the SRS and activation energy prediction method*

In the scope of the current work, the prediction of constitutive behavior, SRS and activation energy has been performed using the independent activation of glide and climb due to the temperatures and strain rates of interest. Additional mechanisms could be included in these predictions, such as grain boundary sliding (GBS) and diffusional flow creep, to investigate higher temperatures and lower strain rates. VPSC modeling has been extended to include GBS ([73], [74]); therefore, the implementation of GBS into these predictions is straightforward using the machine learning approach described in Chapter 1. Prediction of rate sensitivity and activation energy incorporating additional strain accommodating mechanisms is also straightforward, as each strain contribution is additive to the total strain rate (Equation 1) and the equation which governs GBS is given by Equation 31 [75]

$$\dot{\varepsilon} = \frac{A_{GBS} D \mu b}{k_B T} \left(\frac{b}{d}\right)^g \left(\frac{\sigma}{\mu}\right)^n \qquad Equation\ 31$$

where $A_{GBS}$ is a material constant, $D$ is the diffusivity, $g$ determines the grain since dependence, $d$ is the grain size and $n$ is the stress exponent. Diffusional flow creep, which accommodates strain at higher temperatures and lower strain rates than GBS, can also be included in predictions of the SRS and activation energy (Equation 32)

$$\dot{\varepsilon} = \frac{A_{dc} \sigma \Omega}{k_B T d^2} D \qquad Equation\ 32$$

## 5- Conclusions

- Preliminary exploration of the implications of a model which treats the mechanisms of climb and glide independently rather than in series suggests that the *status quo*, which assumes the latter, must be reexamined. It is hypothesized that the current reigning hypothesis has been consistent with existing data because most of that data was collected on materials with cubic crystal structures. More plastically anisotropic materials with lower symmetry crystal structures (hcp, tetragonal, orthorhombic, monoclinic, etc.) may exhibit cases where climb accommodates a large fraction of the imposed strain.
- Derivations of the strain rate sensitivity and activation energies based upon a shear strain accommodated weighting of glide mechanisms described by the mechanical threshold stress (MTS) model and a diffusion-controlled steady-state climb model suggest that it would be worthwhile to invest in a comprehensive implementation of those models within the VPSC-CLIMB framework. Quantitative aspects of the current results must be viewed as preliminary because the shear rates used in this weighted average approach were derived from VPSC simulations that employed a power law description of both climb $n_c = 3$) and glide ($n_g = 20$).
- The results of this chapter further emphasize that VPSC-CLIMB simulations optimized through genetic algorithm (GA) could describe the texture evolution and strain anisotropy after in-plane tension at intermediate temperatures (RT < T < 250 °C) and strain rates ($0.0001 < \dot{\varepsilon} < 0.001$ 1/s).
- This study highlights the fact that in-plane tension experiments are inadequate to constrain the determination of parameters which govern <c+a> slip. In fact, <c+a> slip was not observed in any of the elevated temperature results of this modeling effort. Future attempts must constrain <c+a> slip using out of plane deformation (i.e., through thickness compression or even in-plane compression which first aligns the c-axes of individual crystals with the compression axis after deformation twinning).
- It is proposed that the additional requirement of flow curve fitting into GA optimization would facilitate accurate determination of the critical stress evolution for all modes.
- The same sort of dislocation density estimates which were made for higher temperature deformation in Chapter 1 revealed that climb is overactive in the current simulations. This is consistent with the conclusion that future work could involve enforcing additional restrictions of the amount of climb that can be accommodated by taking into account the limitations enforced by diffusion and the required mobile dislocation density.
- Again, the implementation of a combined VPSC-CLIMB, MTS and dislocation density based (even Voce) hardening model optimized by GA would be fruitful and could potentially lead to a holistic understanding of the constitutive behavior of magnesium alloys as a function of temperature and strain rate.

## Appendix A: Alternative Models to Predict the CRSS of Glide Modes as a Function of Temperature and Strain Rate

Several models have been developed for describing the stress needed to initiate thermally activated slip over different glide modes. Some authors advocate for a model which describes the motion of dislocations through solute field, known as the multiscale bowout model, first proposed by Leyson and Curtin [57], which well describes systems that only harden through solute strengthening (i.e., dilute alloys which do not contain precipitates). In a randomly arranged solute field, a dislocation will attempt to adopt the configuration resulting in the lowest energy. This requires that the dislocation forgo its naturally straight line configuration and adopt a wavy configuration. At low temperatures, deformation is governed by the bowing of dislocations at a single wavelength (i.e., the dislocation curvature) defined by the stress required to bypass the solute pinned regions. The energetic barrier under these low temperature conditions is given by Equation A1

$$\Delta G(\tau) = \Delta E_b \left[1 - \left(\frac{\tau}{\tau_{y0}}\right)\right]^{\frac{3}{2}} \qquad Equation\ A1$$

where $\Delta E_b$ is the characteristic energy barrier, $\tau$ is the resolved shear stress and $\tau_{y0}$ is the yield stress at absolute zero. At higher temperatures, additional thermally activated events can occur which generate larger scale bowouts, which influence the characteristic energetic barrier, $\Delta E_b$. Leyson and Curtin found that several simple analytical expressions over a range of normalized shear stress can well describe these behaviors (Equations A2- A4)

$$\tau = \begin{cases} \tau_{y0}\left(1 - \left(\frac{k_B T}{\Delta E_b}\ln\left(\frac{\dot{\varepsilon}_0}{\dot{\varepsilon}}\right)\right)^{\frac{2}{3}}\right) for \frac{\tau}{\tau_{y0}} > 0.5\ \#Equation\ A2 \\ \tau_{y0}\exp\left(-\frac{k_B T}{\mathrm{C_l}\Delta E_b}\ln\left(\frac{\dot{\varepsilon}_0}{\dot{\varepsilon}}\right)\right)\ for\ 0.2 < \frac{\tau}{\tau_{y0}} < 0.5\ \#Equation\ A3 \\ \tau_{y0}\left(\frac{k_B T}{\mathrm{C_p}\Delta E_b}\ln\left(\frac{\dot{\varepsilon}_0}{\dot{\varepsilon}}\right)\right)^{-\frac{1}{\phi}} for \frac{\tau}{\tau_{y0}} < 0.03\ \#Equation\ A4 \end{cases}$$

where $\dot{\varepsilon}_0$ is the reference strain rate ($10^4$ -$10^6$ 1/s) and $\mathrm{C_l}$, $\mathrm{C_p}$ and $\phi$ are fitted constants. These expressions only account of the static interactions between the dislocations and the obstacles. At higher temperatures, additional strengthening due to the formation of solute atmospheres around mobile dislocation cores is also likely.

The multiscale bowout method has been used to describe slip in materials where the controlling step is the interaction between gliding dislocations and solute atoms, such as Cu and Mn alloys [57]. In the present case, the multiscale bowout model accurately described basal slip in HCP materials; however, this model cannot model prismatic slip, which is an important strain accommodation mechanism at ambient temperatures in strongly textured Mg sheet (particularly in alloys). Prismatic slip is the cross slip of screw <a> dislocations from the basal plane (where

they are most stable) to the prism plane. In this instance, the rate limiting step is not the glide of the dislocation, but rather the constriction of <a> partial dislocations at low temperatures (the Friedel – Escaig mechanism [76]) or the thermally activated nucleation of double kink pairs [77] at ambient temperatures and above necessary for cross slip. In the temperature regime of interest (20 – 350 °C), it is inappropriate to assume that constriction limits the activation of prism slip. Other cross slip limited models have been proposed for cases where double kink nucleation controls the strength of the slip mode. A model proposed by Yasi et al. [58] assumes that cross slip occurs by the nucleation and migration of double kink pairs, as observed in prismatic slip of pure Mg by Couret & Caillard [77] at elevated temperatures. At low solute concentrations, cross slip is controlled by the stress needed for nucleation of the double kink pair, as the stress needed to migrate the kinks is very low. This stress is given by Equations A5.

$$\tau(c_s) = \tau^o + \frac{d\tau}{dc_s} c_s \qquad Equation\ A5$$

where $\tau^o$ is the cross slip stress (Equation A6) in pure Mg and $\frac{d\tau}{dc_s}$ (Equation A7) is the change in cross slip stress with solute content ($c_s$).

$$\tau^o = \tau^\bigstar \left(1 - \frac{k_b T}{H^o_{dk}}\right)^2 \qquad Equation\ A6$$

where $\tau^\bigstar$ is the Peierls stress for the prismatic plane, $k_b$ is Boltzmann's constant, $T$ is the absolute temperature and $H^o_{dk}$ is the enthalpy of double kink formation.

$$\frac{d\tau}{dc_s} = -\tau^\bigstar (1 - \alpha^o_{dk}) \alpha^o_{dk} P_{dk} \qquad Equation\ A7$$

where $\alpha^o_{dk} = \frac{k_b T}{H^o_{dk}}$ and $P_{dk}$ is the softening parameter, is given by Equation A8.

$$P_{dk} = \frac{H^o_{dk}}{2E_f}(4S)\left[\exp\left(-\frac{\overline{\Delta E}}{H^o_{dk}} + \frac{1}{2}\left(\frac{\delta E}{H^o_{dk}}\right)^2\right) - 1\right] \qquad Equation\ A8$$

where $S$ is the number of sites that solute can occupy in the kink (120 in [58]), $\overline{\Delta E}$ is the mean energy of the 8 sites within the screw dislocation core and $\delta E$ is the standard deviation of these sites. Values of the softening parameter for various solutes were tabulated by Yasi et al.. The addition of solutes typically lowers the energetic barrier to nucleating the double kink pair, thereby resulting in a softening of the material; however, the athermal stress ($\tau^a$) needed for kink migration is increased by the presence of solute (Equation A9).

$$\tau^a(c_s) \approx \frac{2}{\sqrt{e\pi}} \frac{2S_c}{4b^3} (\delta E^2 + \overline{\Delta E}^2)^{\frac{1}{2}} c_s \qquad Equation\ A9$$

where $e$ is the total energy change for solutes entering and leaving the core and $S_c$ is the number of unique core energies (8). The final result is that an optimal concentration of each

solute exists for which the stress needed to nucleate and migrate a double kink pair is minimized. At lower concentrations relative to this optimal concentration, the prismatic slip is controlled by the nucleation of the double kink pair, while it is controlled by the migration of the kinks at higher concentrations. This model has shown promise in predicting the effects of multiple solutes on the prismatic CRSS and could be used in conjunction with their earlier work to predict the deformation of Mg alloys due to basal and prism slip. However, the major drawback to these models are that they rely heavily on *a priori* knowledge of the interactions between the core structure of each dislocation type and the solutes.

It is unclear to what extent the cross slip model proposed in Yasi et al. describes the motion of <c+a> dislocations, which are thought to be an important strain carrier in Mg ([17], [20], [78]). Like prism slip, the capacity of <c+a> dislocations to accommodate strain has been linked to their ability to cross slip [14]. It has been proposed that the continual activation of <c+a> slip is a competition between between pyramidal I and II planes and a pyramidal to basal transition (PBT). In this case, cross slip increases the dislocation density while the PBT creates sessile dislocations on the basal plane which will deactivate <c+a> slip. While <c+a> slip has not been found to be an important strain carrier during in-plane tension of strongly textured AZ31B, future chapters will investigate other strain paths that demand more <c+a> slip, this model could not be used in the present study. However, future studies may involve investigating a cross slip governed model for <c+a> slip.

**Appendix B: Previous simulation work fitting resolved shear stresses and climb stresses using the mechanical threshold stress model and Orowan expression**

The mechanical threshold stress (MTS) model and Orowan expression were employed to the critical resolved shear stresses and climb stresses fit to the yield stress. This approach used CRSS and climb stress values modeled at ambient and power law conditions to predict the intermediate temperature constitutive behavior of AZ31B. Tables B1 -B4 lists the results of this fitting procedure. It is clear that when climb is absent, additional strain is accommodated by basal slip, as its CRSS is reduced relative to prism and <c+a> slip. There are a few outliers in the climb incorporating simulations due to nonbasal slip modes being unbounded during in plane tension. This is particularly true for prismatic stress at 350 °C and a very low strain rates, as the apparent CRSS increases. Table B2 reports the results of bounding <c+a> slip (and prism slip for the lowest rate at 350 °C). It was also found that the CRSSs for basal slip, when fit to the MTS model, led to values of $g_0$ and $\frac{\hat{\tau}}{\mu_0}$ which made evaluating $\frac{\partial \dot{\gamma}}{\partial \sigma}$ and $\frac{\partial \dot{\gamma}}{\partial \frac{1}{T}}$ impossible for the predictions of SRS and activation energy at room temperature. The basal CRSSs were adjusted to result in values that allowed for the calculation of SRS and activation energy and predicted in Table B2. This does not result in a large deviation from the original GA simulations, as basal slip remain several times softer than the non basal slip modes, particularly at room temperature, where the majority of the adjustment was performed.

Table B1: Optimized CRSS values for climb incorporating and glide only simulations after GA optimization and rescale to experimental yield stress

| | 20 °C, 0.001 1/s | 250 °C, 0.001 1/s | 350 °C, 0.1 1/s | 350 °C, 0.01 1/s | 350 °C, 0.00028 1/s |
|---|---|---|---|---|---|
| **Climb Incorporating Simulations** | | | | | |
| Basal | 16.4 | 17. | 7.5 | 13.4 | 4.9 |
| Prism | 84 | 27.7 | 24.8 | 21.4 | 56.4 |
| <c+a> | 94.5 | 94.7 | 29.4 | 23.5 | 7.9 |
| <a> climb | N/A | 29.3 | 39.8 | 23.2 | 7.7 |
| **Glide Only Simulations** | | | | | |
| Basal | 16.4 | 3.8 | 5.7 | 3. | 1.1 |
| Prism | 84 | 28.8 | 24.1 | 23.2 | 7.8 |
| <c+a> | 94.5 | 29.7 | 26.3 | 23.2 | 7.9 |

Table B2: Glide mode CRSSs and climb threshold stresses for climb incorporating and glide only simulations after bounding nonbasal slip and adjusting basal slip

| | 20 °C, 0.001 1/s | 250 °C, 0.001 1/s | 350 °C, 0.1 1/s | 350 °C, 0.01 1/s | 350 °C, 0.00028 1/s |
|---|---|---|---|---|---|
| **Climb Incorporating Simulations** | | | | | |
| Basal | 21.9 | 11.9 | 7.8 | 3.4 | 1.5 |
| Prism | 84.0 | 27.7 | 24.8 | 21.4 | 9.5 |
| <c+a> | 100.0 | 60.0 | 55.0 | 43.0 | 12.2 |
| <a> climb | N/A | 29.3 | 39.8 | 23.2 | 6.4 |
| **Glide Only Simulations** | | | | | |
| Basal | 21.9 | 4.0 | 5.5 | 2.9 | 1.0 |
| Prism | 84.0 | 28.8 | 24.1 | 23.2 | 7.8 |
| <c+a> | 100 | 29.7 | 26.3 | 23.2 | 7.9 |

After fitting the experimental CRSSs to the MTS model, it is clear that basal slip is the softest slip mode, as it has the lowest hardening rate ($\frac{\hat{\tau}}{\mu_0}$) with decreasing temperature and increasing rate in addition to the lowest athermal stress in agreement with classical understanding of easy slip modes in Mg. Prism slip is the next softest and <c+a> slip is the hardest for similar reasons. <c+a> slip appears to have the lowest temperature dependence; however, the difference between the temperature dependence between basal and <c+a> slip is removed when the disparity in burgers vector length between <a> and <c+a> dislocations is taken into acccount as the true activation energy is $g_0 \mu b^3$. It appears from the result of this fitting that prism slip has the highest temperature dependence of the glide modes. Comparing the climb incorporating and glide only simulations shows that only the temperature dependences basal and <c+a> slip are significantly altered. It appears that basal slip becomes less temperature dependent while the opposite is true for <c+a> slip. Hardening parameters were not changed between climb incorporating and glide only simulations, as the GA optimization fit to the stress denoting the elastoplastic transition. Therefore, the necessary hardening parameters will not change between the two sets of simulations.

Table B3: Fit parameters for glide CRSSs and hardening in climb incorporating and glide only simulations

| Slip Mode | $\tau_a$ (MPa) | $p$ | $q$ | $\hat{\tau}/\mu_0$ (x $10^{-3}$) | $g_0$ | $g_0 b^3$ (x $10^{-29}$) | $k_1$ | $D$ (MPa) | $g_{ss}$ |
|---|---|---|---|---|---|---|---|---|---|
| | Climb Incorporating Simulations | | | | | | | | |
| **Basal <a>** | 0.5 | 2/3 | 3/2 | 3.53 | 0.643 | 2.13 | 2 x $10^7$ | 20 | 0.005 |
| **Prism <a>** | 2 | 1/2 | 1 | 9.29 | 0.699 | 2.31 | 2 x $10^8$ | 200 | 0.06 |
| **<c+a>** | 6 | 1 | 3/2 | 11.1 | 0.093 | 2.12 | 2 x $10^8$ | 200 | 0.01 |
| | Glide Only Simulations | | | | | | | | |
| **Basal <a>** | 0.5 | 2/3 | 3/2 | 3.5 | 0.549 | 1.82 | 2 x $10^7$ | 20 | 0.005 |
| **Prism <a>** | 2 | 1/2 | 1 | 9.74 | 0.682 | 2.26 | 2 x $10^8$ | 200 | 0.06 |
| **<c+a>** | 6 | 1 | 3/2 | 11.4 | 0.740 | 16.9 | 2 x $10^8$ | 200 | 0.01 |

Table B4: Fit parameters for predicting the mobile dislocation density for climb

| Slip Mode | A | B ($1/m^2$ T) | C ($1/m^2$ s) |
|---|---|---|---|
| <a> Climb | 0.42070 | 0.00059 | 1.20682 |

The predicted stress strain curves employing the hardening parameters defined in Table B4 resulted in good agreement with the experimental flow curves (Figure B1). For the simplicity of the preceding equations, the evolution in the steady state flow stress predicted by VPSC-CLIMB simulations is relatively close (Figure B2a)). There is good agreement between strain anisotropy predictions and experimental measurements at the conditions that were optimized with a genetic algorithm; however, the predictions overestimate the r-values in the intermediate temperatures. This is due to the overstimulation of prismatic slip under these conditions, which is known to result in elevated r-values. At these temperatures, diffusion is too slow to allow dislocation climb to accommodate significant strain with the density of mobile dislocations predicted by Equation 13. The seemingly erratic dips in the strain anisotropy between 100 and 200 °C are due to the activation of climb at the lowest strain rates simulated at the cost of prism slip.

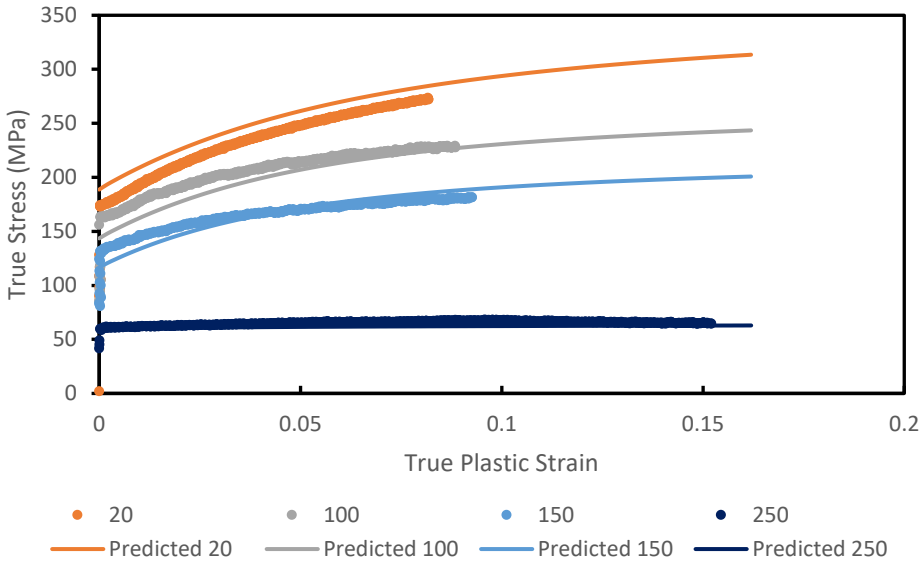


Figure B1: Fitted hardening parameters to experimental flow curves. The experimental flow curves representing 100 and 150 °C at a rate of 0.001 1/s loading conditions are substituted by conditions with lower temperatures and rates (50 °C, 0.00001 1/s and 100 °C, 0.0001 1/s, respectively).

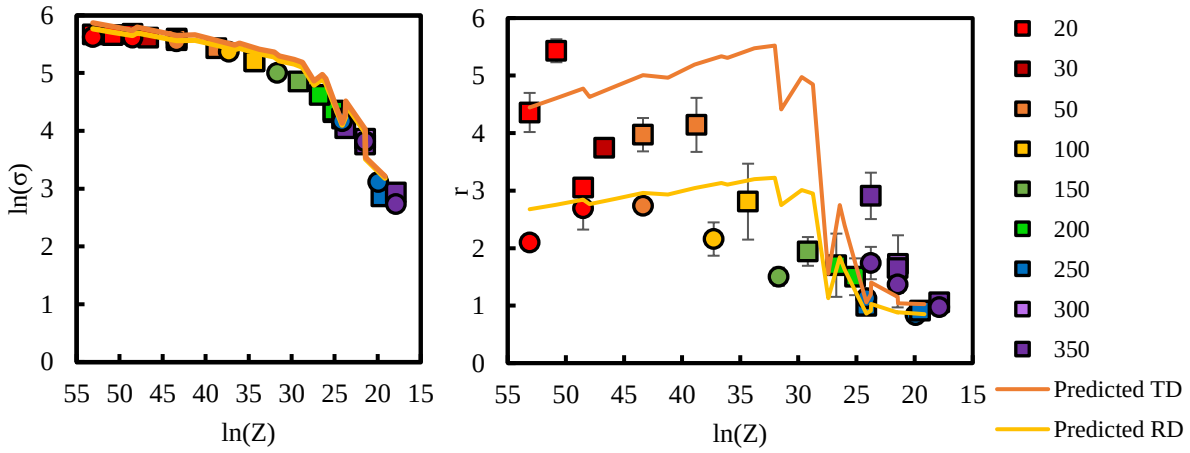


Figure B2: a) Predictedd flow stress and b) strain anisotropy measurements against experimental values obtained in Chapter 1.

The varying degree to which fitting the hardening parameters and CRSSs to the flow stresses and strain anisotropy provides additional evidence to the viability of the "bottom up" method of crystal plasticity modeling. This method, as advocated in this thesis, uses macroscopic measurements of the constitutive behavior (texture evolution and strain anisotropy) which relate to the motion of specific dislocation types (i.e., the kinematics of deformation) in contrast to the "top down" method which traditionally models the flow curves to obtain the glide mode CRSSs ([1], [79]). The benefits are twofold, as presented here; first, r-value and texture evolution measurements are much more sensitive to errors in CRSS than macroscopic flow curves and second, the motion of each dislocation type has unique effects on the strain anisotropy and, more importantly, the texture evolution, making it accessible to machine learning.

*Extension of texture and strain anisotropy prediction*

Figure B3 presents the texture evolution from VPSC-CLIMB simulations using Equations 8 and 11. It is clear that the texture evolution is strongly dependent on the temperature and applied strain rate. An increase in temperature at constant strain rate causes a slowing of the texture evolution with a concomitant decrease in strain anisotropy (r-value) (as seen in Figure B2b)). At high temperatures in the power law regime (>200 °C and strain rates less than or equal to 0.001 1/s), decreasing the strain rate has a similar effect. These results are in qualitative agreement with the findings of Chapter 1 (which tied these macroscopic changes with an increasing strain accommodation by climb) and suggests that this method is appropriate for interpolating CRSS values for any strain rate and temperature within the ranges previously explored.

The fractions of strain accommodated by each slip mode (known as relative slip activity) show a transition from strain accommodation via glide to a regime where climb is an integral component to the deformation (Figure B4). The predicted CRSSs and threshold stresses result in the same transition from prism slip dominated deformation at ambient temperatures to climb controlled deformation in the power law regime, confirming that the use of the Orowan based expression is a suitable method for estimating the amount of climb necessary to enforce the texture and r-value evolution seen experimentally.

At the lowest temperature presented, climb is essentially inactive under all strain rates, as the lattice diffusion of vacancies is not fast enough for climb to accommodate any significant strain. As the temperature is increased and the deformation conditions approach the power law regime, climb begins to accommodate significant amounts of strain. At 250 °C, this amount is highly dependent on the strain rate, owing to the higher rate sensivity of climb relative to glide. At lower rates ($\leq$ 0.001 1/s), climb can accommodate the majority of the strain, which is reflected in the reduced texture evolution in Figure B3. As the strain rate increases, climb becomes less active and the texture evolution proceeds to a prism slip dominated state, similar to ambient temperature. However, even when climb does not accommodate enough strain to noticeably affect the texture, it can still have a potent effect on the strain anisotropy. This is best seen under conditions of 250 °C and strain rates of 0.01 and 0.1 1/s. Here, the CRSSs of each glide mode are roughly constant, as the strain rate has only a small effect on the CRSS due to its

inclusion into a logarithmic term in Equation 8, yet the r-value (inset of Figure B3) increases by 75% as the rate is increased. From the presented relative strain activity plots (Figure B4), it is clear that this is the direct result of the replacement of climb with prism slip at the higher rate, as the basal slip accommodation is essentially constant and the small increase in <c+a> slip present in the higher rate simulation would reduce its r-value. At the highest temperature presented (350 °C), lattice diffusion is so prevalent that climb accommodates a large fraction of strain in all cases reported. At intermediate temperatures (250 °C), it is clear that the strain rate has a large influence on the texture evolution and r-value due to the strain accommodation via climb.

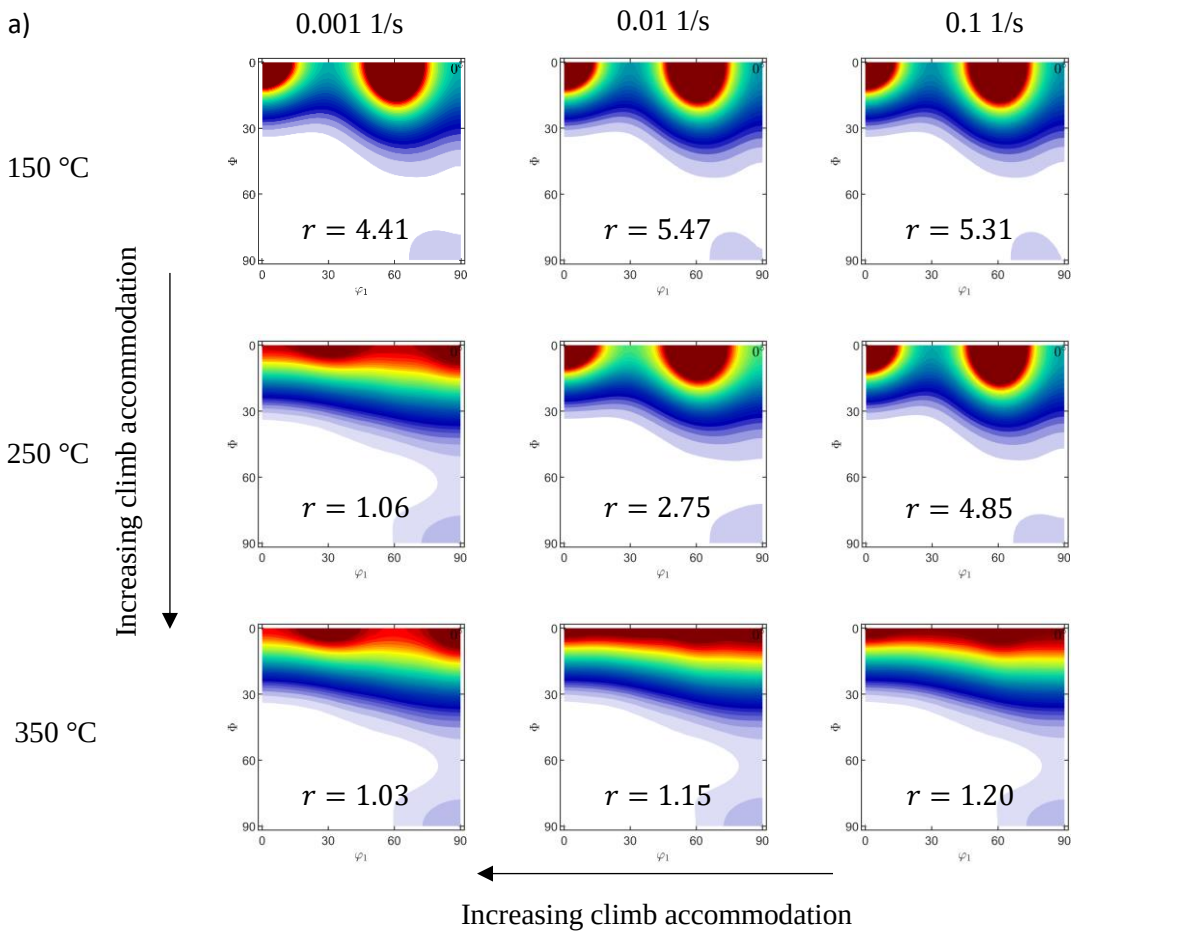


Figure B3: a) Predicted texture and strain anisotropy evolution for a range of temperatures and strain rates for the TD condition. Texture evolution and strain anisotropy predictions are very similar to those at 150 °C. b) Experimental textures at the listed testing conditions for transverse uniaxial (TD) tension.

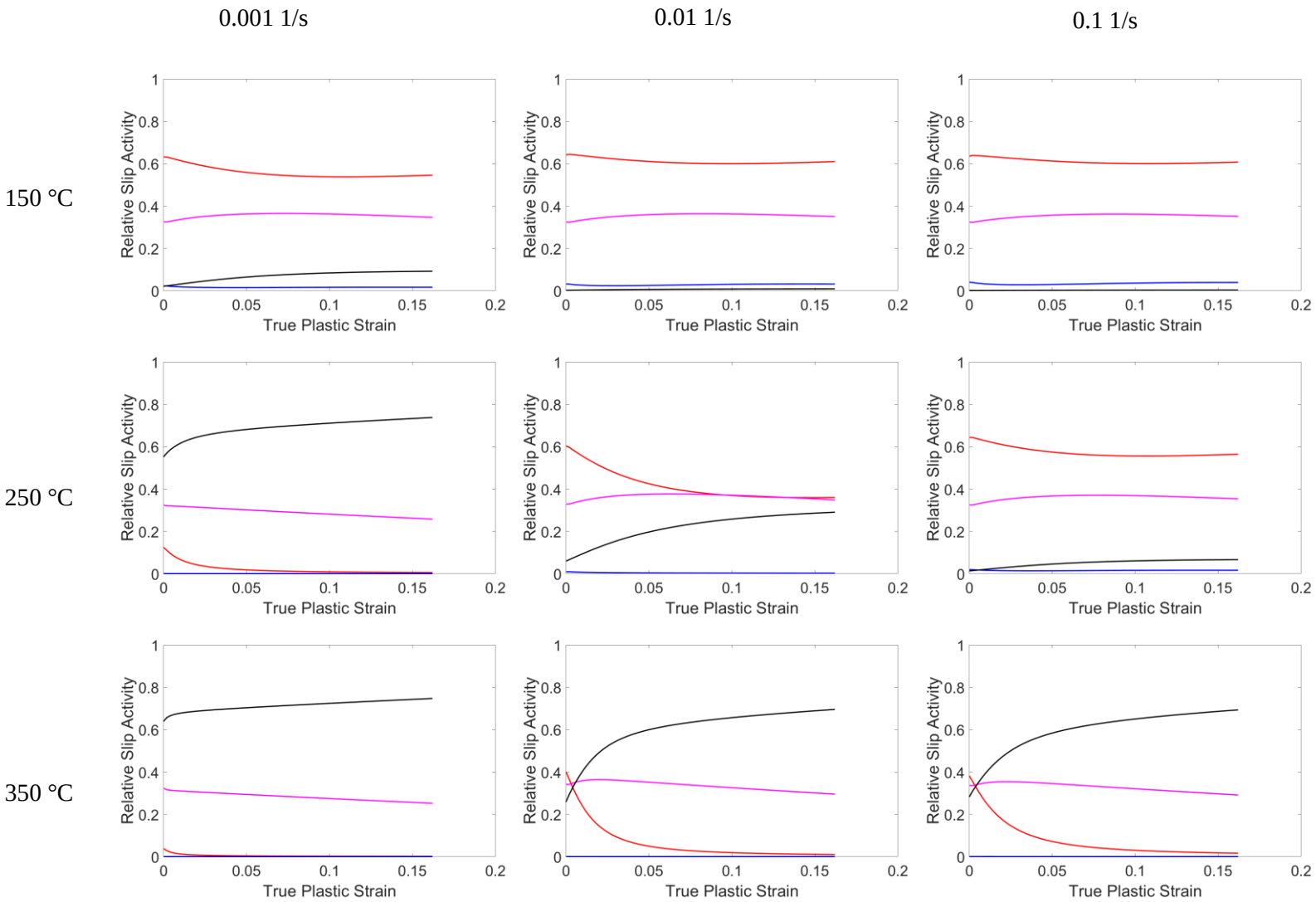


Figure B4: Relative s train accommodation for a range of temperature and strain rates

At present, two flaws remain in this methodology. First, the r-values are overpredicted at intermediate temperatures. More investigation into the transition from ambient deformation to power law breakdown (50 < T < 150 °C) is merited and investigating the role of <c+a> slip at intermediate temperatures may improve the fit between experimental observations and predictions. The other flaw is that slip mode hardening dominates the resistance to slip in the highest temperature investigated, resulting in very weak texture evolution irrespective of strain rate. In the current model, climb does not harden leading to an overestimation in its slip activity deep in the power law regime where slip mode hardening dominates the glide mode CRSS. When slip mode hardening is removed, the qualitative trends in the texture evolution and r-values are restored and are in better agreement with experiments (Figure B5), suggesting that further improvements are necessary to describe the climb strain hardening behavior. The strain accommodation due to prism slip is increased relative to the simulations that incorporated slip mode hardening, as nodes form at $\varphi_1 = 30°$ and $\varphi_1 = 90°$, which are absent in the initial as-rolled and annealed texture (Chapter 1). This is characteristic of prism slip during TD tension as the grains attempt to rotate around their <c> axes (along $\varphi_1$). This is also apparent in the increased strain anisotropy; however, it is clear that prism slip is overly active in these simulations as the r-values at higher strain rates become unrealistic. These results are corroborated by the RSA in each simulation (Figure B6).

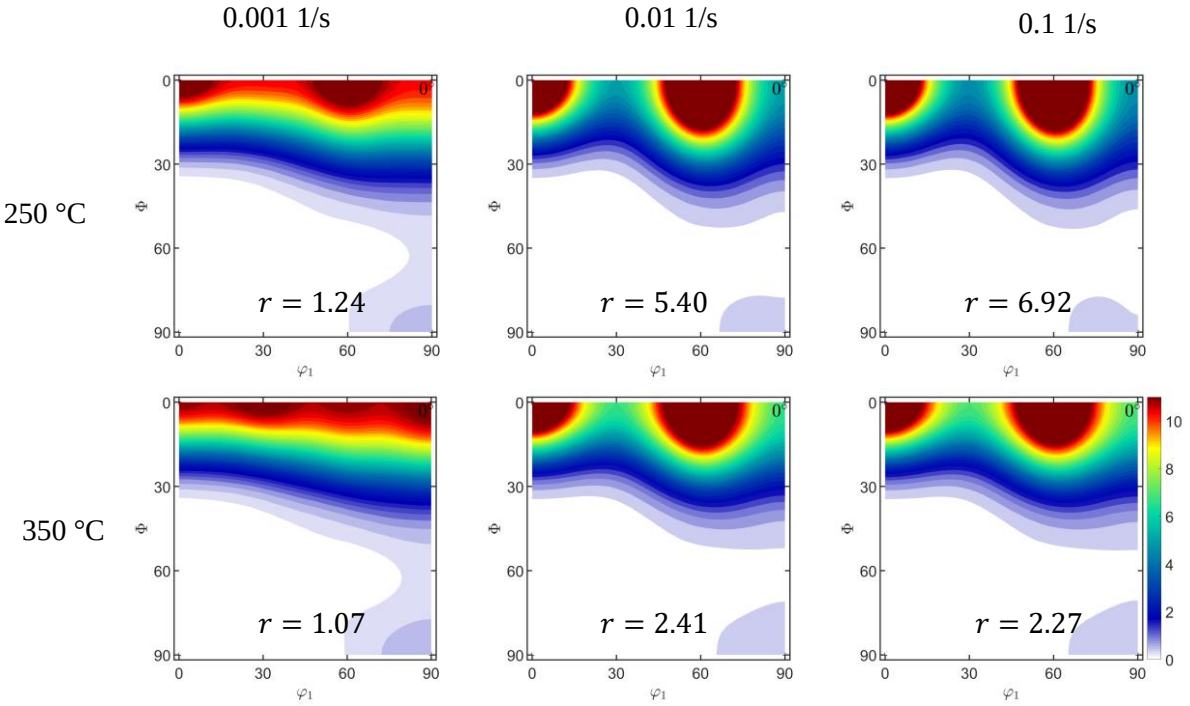


Figure B5: Texture evolution and strain anisotropy predictions without strain hardening responses. It is clear that prism slip texture component is more apparent in the conditions simulated, as nodes are forming at $\varphi_1 = 30°$ and $\varphi_1 = 90°$, which are not present in the initial as-rolled and annealed texture, but are present in the deformed samples.

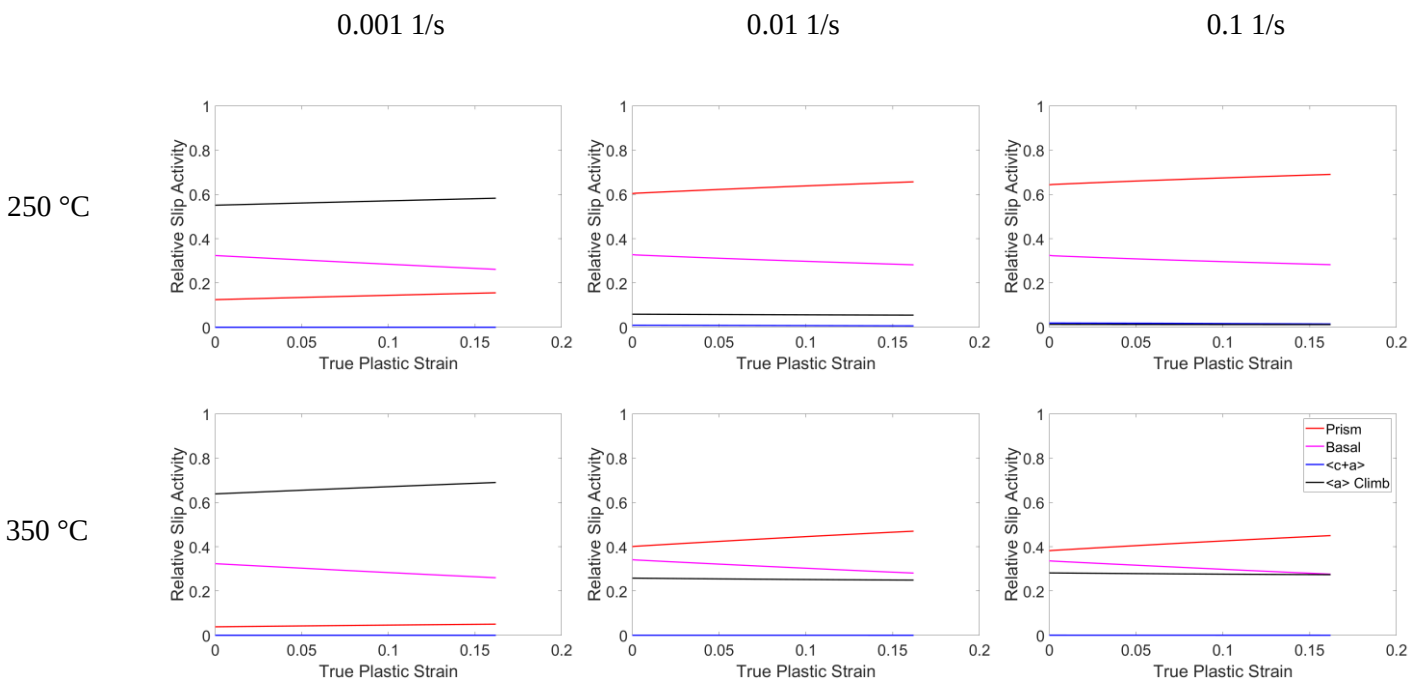


Figure B6: Relative slip activity plots of 250 and 350 °C simulations without hardening

## Appendix C: Expressions for strain rate sensitivity and activation energy assuming an MTS model relationship for glide and an Orowan type relationship for climb with fitted dislocation densities

*SRS derivation*

The alternative explanation for the increased stress exponent and lower activation energy can be explained as an increased dependence on glide at higher stress levels. We start by writing the total strain rate as an additive composite of glide and climb (Equation C1). The various glide modes of HCP materials (basal, prismatic and <c+a> slip) are agglomerated into $\dot{\varepsilon}_g$.

$$\dot{\varepsilon} = \dot{\varepsilon}_g + \dot{\varepsilon}_c \qquad Equation\ C1$$

Accounting for Schmid effects for glide and climb ($m_i$ and $k$) allows us to resolve the strain rates onto the appropriate glide or climb planes (Equation C2). The overbars represent that these values are averages over all possible slip systems within a slip mode.

$$\dot{\varepsilon} = \sum_{i=1}^{N} \bar{m}_i \dot{\bar{\gamma}}_i + \bar{k}\dot{\bar{\beta}} \qquad Equation\ C2$$

It is assumed that the shear rate components for glide and the strain rate component for climb can be represented by the MTS model (Equation 17), assuming one obstacle, and Orowan model (Equation 11), respectively. This is presumed to be satisfactory for the climb component which is typically active only within the power law regime and classically described by Weertman using the natural law of creep ($\dot{\beta} \propto \sigma^3$) and acceptable in the glide portion to yield a qualitative measure for how the stress exponent varies as a function of temperature and strain rate.

$$\dot{\varepsilon} = \sum_{i=1}^{N} \bar{m}_i \dot{\gamma}_0 \exp\left(-\frac{\mathrm{g}_{0,\mathrm{i}}\mu b^3}{k_B T}\left[1-\left(\left(\frac{\tau-\tau_a}{\mu}\right)\left(\frac{\mu_0}{\hat{\tau}}\right)\right)^p\right]^q\right) + \bar{k}\rho_m^c b\left(\frac{z_v D_{sd}}{b}\left(\exp\left(\frac{\Omega\sigma_{0,c}}{k_B T}\right)-1\right)\right) \qquad Equation\ C3$$

where $\dot{\gamma}_0$ is the reference shear rate, $\tau$ is the resolved applied stress and $\sigma_{0,c}$ is the stress needed for a dislocation to climb.

The stress exponent (the reciprocal of the strain rate sensitivity) is thus related to the strain rate by Equation C4. For compactness, the MTS and Orowan expressions are not displayed as in the above equation, but are still enforced.

$$n = \frac{\partial ln\dot{\varepsilon}}{\partial ln\sigma} = \sigma\frac{\partial}{\partial\sigma} ln\left(\sum_{i=1}^{N} \bar{m}_i \dot{\gamma}_\iota + \bar{k}\dot{\beta}\right) \qquad Equation\ C4$$

This derivative can be simplified using the chain rule to yield Equation C5 with Equations C6 and C7 defining $\frac{\partial\dot{\gamma}}{\partial\sigma}$ and $\frac{\partial\dot{\beta}}{\partial\sigma}$, respectively.

$$n = \sigma\left(\frac{1}{\sum_{i=1}^{N}\bar{m}_i\dot{\gamma} + \bar{k}\dot{\beta}}\left(\sum_{i=1}^{N}\bar{m}_i\frac{\partial\dot{\gamma}_i}{\partial\sigma} + \bar{k}\frac{\partial\dot{\beta}}{\partial\sigma}\right)\right) \qquad Equation\ C5$$

$$\frac{\partial\dot{\gamma}}{\partial\sigma} = \dot{\gamma}\left(-\frac{g_{0,i}\mu b^3}{k_B T}\right) q\left[1-\left(\left(\frac{\tau-\tau_a}{\mu}\right)\left(\frac{\mu_0}{\hat{\tau}}\right)\right)^p\right]^{q-1}\left(-p\left(\left(\frac{\tau-\tau_a}{\mu}\right)\left(\frac{\mu_0}{\hat{\tau}}\right)\right)^{p-1}\right)\left(\frac{\mu_0}{\hat{\tau}}\right)\left(\frac{\bar{m}_i}{\mu}\right) Equation\ C6$$

$$\frac{\partial\dot{\beta}}{\partial\sigma} = \rho_m^c z_v D_{sd}\left(\exp\left(\frac{\Omega\bar{k}\sigma'}{k_B T}\right)-1\right) = z_v D_{sd}\frac{\partial}{\partial\sigma}\left(\rho_m^c\left(\exp\left(\frac{\Omega\bar{k}\sigma'}{k_B T}\right)-1\right)\right) \qquad Equation\ C7$$

For vacancies, $z_v \approx 1$. Equation C7 can be further simplified by resolving the product rule in the derivative (Equation C8)

$$\frac{\partial\dot{\beta}}{\partial\sigma} = \left(\frac{\partial(\rho_m^c D_{sd})}{\partial\sigma}\left(\exp\left(\frac{\Omega\sigma_{0,c}}{k_B T}\right)-1\right) + \rho_m^c D_{sd}\frac{2}{3}\frac{\Omega\bar{k}}{k_B T}\exp\left(\frac{\Omega\bar{k}\sigma'}{k_B T}\right)\right) \qquad Equation\ C8$$

since $\sigma'$ is the deviatoric component of the applied stress (in the case of uniaxial tension, $\sigma' = 2/3\ \sigma$). The specific functional forms of $\frac{\partial\rho_m^c}{\partial\sigma}$ and $\rho_m^c$ will be described later, but it is clear that Equation C8 can be written in terms of the climb strain rate, $\dot{\beta}$, via rearrangement (Equation C9 and C10)

$$\frac{\partial\dot{\beta}}{\partial\sigma} = \begin{pmatrix}\left[\frac{\partial\rho_m^c}{\partial\sigma}\left(\frac{\rho_m^c}{\rho_m^c}\right)D_{sd} + \rho_m^c\frac{\partial D_{sd}}{\partial\sigma}\frac{D_{sd}}{D_{sd}}\right]\left(\exp\left(\frac{\Omega\sigma_{0,c}}{k_B T}\right)-1\right) \\ +\rho_m^c D_{sd}\frac{2}{3}\frac{\Omega\bar{k}}{k_B T}\left(\exp\left(\frac{\Omega\bar{k}\sigma'}{k_B T}\right)-1+1\right)\end{pmatrix} \qquad Equation\ C9$$

$$\frac{\partial\dot{\beta}}{\partial\sigma} = \dot{\beta}\left(\frac{\partial\rho_m^c}{\partial\sigma}\left(\frac{1}{\rho_m^c}\right) + \frac{\partial D_{sd}}{\partial\sigma}\frac{1}{D_{sd}} + \frac{2}{3}\frac{\Omega\bar{k}}{k_B T}\left(1+\frac{1}{\exp\left(\frac{\Omega\bar{k}\sigma'}{k_B T}\right)-1}\right)\right) \qquad Equation\ C10$$

$$\frac{\partial D_{sd}}{\partial\sigma} = \frac{20 a_c}{b^2}D_p\left(\frac{\sigma}{\mu^2}\right)$$

where $\dot{\beta} = D_{sd}\rho_m^c\left(\exp\left(\frac{\Omega\sigma_{0,c}}{k_B T}\right)-1\right)$

Currently, the mobile density of climbing dislocations, $\rho_m^c$, is fit to values obtained from the Orowan expression (Equation 11) using the climb stresses and strain rates derived from VPSC simulations and can be described with a Taylor hardening rule with the fraction of dislocations that are required to climb ($\tilde{\rho}$) (Equation C11)

$$\rho_m^c = \tilde{\rho}\left(\frac{\bar{k}\sigma}{\alpha\mu b}\right)^2 \qquad Equation\ C11$$

where $k$ is the Hartley factor and $\alpha$ is a constant that relates to the type of dislocation-dislocation interaction [50], taken to be 0.25. As a first approximation, $\tilde{\rho}$ is defined as being linear in both temperature and strain rate (Equation C12).

$$\tilde{\rho} = A - BT + C\dot{\varepsilon} \qquad Equation\ C12$$

The contribution of climb to the stress exponent is obtained by computing the derivative of the dislocation density (Equation C13) and some rearranging.

$$\frac{\partial \rho_m^c}{\partial \sigma} = \frac{2\tilde{\rho}\bar{k}^2}{(\alpha\mu b)^2}\sigma \qquad Equation\ C13$$

$$\frac{\partial \dot{\beta}}{\partial \sigma} = \dot{\beta}\left(\frac{2\tilde{\rho}\bar{k}^2}{(\alpha\mu b)^2}\sigma\left(\frac{1}{\tilde{\rho}\left(\frac{\bar{k}\sigma}{\alpha\mu b}\right)^2}\right) + \frac{\frac{20a_c}{b^2}D_p\left(\frac{\sigma}{\mu^2}\right)}{D_{sd}} + \frac{2}{3}\frac{\Omega\bar{k}}{k_BT}\left(1 + \frac{1}{\exp\left(\frac{\Omega\bar{k}\sigma'}{k_BT}\right) - 1}\right)\right) \qquad Equation\ C14$$

The final expression for the climb component to the SRS is given in Equation C15.

$$\frac{\partial \dot{\beta}}{\partial \sigma} = \dot{\beta}\left(\frac{2}{\sigma} + 200\frac{D_p}{D_{sd}}\left(\frac{\sigma}{\mu}\right)^2 + \frac{2}{3}\frac{\Omega\bar{k}}{k_BT}\left(1 + \frac{1}{\left(exp\left(\frac{\Omega\bar{k}\sigma'}{k_BT}\right) - 1\right)}\right)\right) \qquad Equation\ C15$$

Substituting Equations C6 and C15 back into Equation C5 yields the stress exponent (Equation C16).

$$n = \sigma\frac{\partial}{\partial \sigma}\ln\left(\sum_{i=1}^{N}\bar{m}_i\dot{\gamma}_i + \bar{k}\dot{\beta}\right) = \left(\sum_{i=1}^{N} f_i\, n_g + f_c n_c\right) \qquad Equation\ C16$$

where

$$n_g = \sigma\left(-\frac{\mathrm{g}_{0,\mathrm{i}}\mu b^3}{k_BT}\right)q\left[1 - \left(\left(\frac{\tau - \tau_a}{\mu}\right)\left(\frac{\mu_0}{\hat{\tau}}\right)\right)^p\right]^{q-1}\left(-p\left(\left(\frac{\tau - \tau_a}{\mu}\right)\left(\frac{\mu_0}{\hat{\tau}}\right)\right)^{p-1}\right)\left(\frac{\mu_0}{\hat{\tau}}\right)\left(\frac{\bar{m}_i}{\mu}\right)$$

And

$$n_c = 2 + 200\frac{D_p}{D_{sd}}\left(\frac{\sigma}{\mu}\right)^2 + \frac{2}{3}\frac{\Omega\bar{k}\sigma}{k_BT}\left(1 + \frac{1}{\left(exp\left(\frac{\Omega\bar{k}\sigma'}{k_BT}\right) - 1\right)}\right)$$

*Activation energy derivation*

The activation energy can be derived in a similar manner starting with Equation C2. Here, the derivative of this expression is taken with respect to 1/T (Equation C17).

$$Q = -R\frac{\partial ln\dot{\varepsilon}}{\partial \frac{1}{T}} = -R\frac{\partial}{\partial \frac{1}{T}}\left(ln\left(\sum_{i=1}^{N}\bar{m}_i\dot{\bar{\gamma}}_i + \bar{k}\dot{\bar{\beta}}\right)\right) \qquad Equation\ C17$$

The temperature dependence on the shear modulus was incorporated by fitting experimental resonant ultrasound spectroscopy (RUS) data by [55] to the Varshni equation (Equation 16).

Evaluating the derivative in Equation C17 with the chain rule yields Equation C18.

$$Q = -R\left(\frac{1}{\sum_{i=1}^{N}\bar{m}_i\dot{\gamma}_i + \bar{k}\dot{\beta}}\left(\sum_{i=1}^{N}\bar{m}_i\frac{\partial\dot{\bar{\gamma}}_i}{\partial\frac{1}{T}} + \bar{k}\frac{\partial\dot{\bar{\beta}}}{\partial\frac{1}{T}}\right)\right) \qquad Equation\ C18$$

Similar to the rate sensitivity calculation, the activation energy has contributions due to glide (Equation C19) and climb (Equation C20) as well.

$$\frac{\partial\dot{\bar{\gamma}}_i}{\partial\frac{1}{T}} = \dot{\gamma}\left(-\frac{g_{0,i}b^3}{k_B}\right)\frac{\partial}{\partial\frac{1}{T}}\left(\left(\frac{\mu}{T}\right)\left[1-\left(\left(\frac{\tau-\tau_a}{\mu}\right)\left(\frac{\mu_0}{\hat{\tau}}\right)\right)^p\right]^q\right) \qquad Equation\ C19$$

$$\frac{\partial\dot{\bar{\beta}}}{\partial\frac{1}{T}} = \frac{\partial}{\partial\frac{1}{T}}\left(\rho_m^c D_{sd}\left(\exp\left(\frac{\Omega\sigma_{0,c}}{k_B T}\right)-1\right)\right) \qquad Equation\ C20$$

The derivative in Equation C19 was evaluated in Equation C21.

$$\frac{\partial}{\partial\frac{1}{T}}\left(\left(\frac{\mu}{T}\right)\left[1-\left(\left(\frac{\tau-\tau_a}{\mu}\right)\left(\frac{\mu_0}{\hat{\tau}}\right)\right)^p\right]^q\right) = \left(\left(\frac{1}{T}\frac{\partial\mu}{\partial\frac{1}{T}}+\mu\right)\left[1-\left(\left(\frac{\tau-\tau_a}{\mu}\right)\left(\frac{\mu_0}{\hat{\tau}}\right)\right)^p\right]^q\right)$$
$$+\frac{\mu}{T}\left(q\left[1-\left(\left(\frac{\tau-\tau_a}{\mu}\right)\left(\frac{\mu_0}{\hat{\tau}}\right)\right)^p\right]^{q-1}\left(p\left(\frac{\tau-\tau_a}{\mu}\right)\frac{\mu_0}{\hat{\tau}}\right)^{p-1}(\tau-\tau_a)\left(\frac{\mu_0}{\hat{\tau}}\right)\left(\frac{1}{\mu^2}\right)\frac{\partial\mu}{\partial\frac{1}{T}}\right) \quad Equation\ C21$$

The derivative of the shear modulus with respect to temperature is evaluated in Equation C22.

$$\frac{\partial\mu}{\partial\frac{1}{T}} = \frac{D_0 T_0\exp\left(\frac{T_0}{T}\right)}{\left(\exp\left(\frac{T_0}{T}\right)-1\right)^2} \qquad Equation\ C22$$

Evaluating the derivative in Equation C20 for the climb component yields Equation C23.

$$\frac{\partial}{\partial \frac{1}{T}}\left(\rho_m^c D_{sd}\left(\exp\left(\frac{\Omega \bar{k}\sigma}{k_B T}\right)-1\right)\right)=\frac{\partial}{\partial \frac{1}{T}}\left(\rho_m^c D_{sd}\right)\left(\exp\left(\frac{\Omega \bar{k}\sigma}{k_B T}\right)-1\right)$$
$$+\rho_m^c D_{sd}\frac{\partial}{\partial \frac{1}{T}}\left(\exp\left(\frac{\Omega \bar{k}\sigma}{k_B T}\right)-1\right) \qquad Equation\ C23$$

with

$$\frac{\partial}{\partial \frac{1}{T}}\left(\rho_m^c D_{sd}\right)=\frac{\partial \rho_m^c}{\partial \frac{1}{T}}D_{sd}+\rho_m^c\left(D_{sd}\left(-\frac{Q_{sd}}{R}\right)\right)$$

$$\frac{\partial}{\partial \frac{1}{T}}\left(\exp\left(\frac{\Omega \bar{k}\sigma'}{k_B T}\right)-1\right)=\frac{\Omega \bar{k}\sigma'}{k_B}\exp\left(\frac{\Omega \bar{k}\sigma'}{k_B T}\right)$$

Substituting in the derivatives listed above into Equation C23 yields Equation C24.

$$\frac{\partial}{\partial \frac{1}{T}}\left(\rho_m^c D_{sd}\left(\exp\left(\frac{\Omega \bar{k}\sigma'}{k_B T}\right)-1\right)\right)=$$
$$\left(\frac{\partial \rho_m^c}{\partial \frac{1}{T}}D_{sd}+\rho_m^c\frac{\partial D_{sd}}{\partial \frac{1}{T}}\right)\left(\exp\left(\frac{\Omega \bar{k}\sigma'}{k_B T}\right)-1\right)+\rho_m^c D_{sd}\frac{\Omega \bar{k}\sigma'}{k_B}\exp\left(\frac{\Omega \bar{k}\sigma'}{k_B T}\right) \qquad Equation\ C24$$

Substituting Equation C24 into C20 yields Equation C25

$$\frac{\partial \dot{\bar{\beta}}}{\partial \frac{1}{T}}=\left(\left(\frac{\partial \rho_m^c}{\partial \frac{1}{T}}D_{sd}+\rho_m^c\frac{\partial D_{sd}}{\partial \frac{1}{T}}\right)\left(\exp\left(\frac{\Omega \bar{k}\sigma'}{k_B T}\right)-1\right)+\rho_m^c D_{sd}\frac{\Omega \bar{k}\sigma'}{k_B}\exp\left(\frac{\Omega \bar{k}\sigma'}{k_B T}\right)\right) Equation\ C25$$

As in the derivation of the rate sensitivity, Equation C25 can be rewritten in terms of $\dot{\beta}$ (Equation C26).

$$\frac{\partial \dot{\bar{\beta}}}{\partial \frac{1}{T}}=\dot{\bar{\beta}}\left(\left(\frac{\partial \rho_m^c}{\partial \frac{1}{T}}\left(\frac{1}{\rho_m^c}\right)+\frac{\partial D_{sd}}{\partial \frac{1}{T}}\left(\frac{1}{D_{sd}}\right)\right)+\frac{\Omega \bar{k}\sigma'}{k_B}\left(1+\frac{1}{\left(exp\left(\frac{\Omega \sigma_{0,c}}{k_B T}\right)-1\right)}\right)\right) \quad Equation\ C26$$

If the dislocation density is again assumed to follow Equation C11, then Equation C26 reduces to Equation C27.

$$\frac{\partial \dot{\tilde{\beta}}}{\partial \frac{1}{T}} = \dot{\tilde{\beta}} \left( \begin{array}{c} \frac{BT^2}{\tilde{\rho}} - \frac{2}{\mu} \frac{D_0 T_0 \exp\left(\frac{T_0}{T}\right)}{\left(\exp\left(\frac{T_0}{T}\right) - 1\right)^2} \\ - \frac{\left( D_l \frac{Q_l}{R} + 100 D_p \left(\frac{\sigma}{\mu}\right)^2 \left( \frac{Q_p}{R} + \frac{2}{\mu} \frac{D_0 T_0 \exp\left(\frac{T_0}{T}\right)}{\left(\exp\left(\frac{T_0}{T}\right) - 1\right)^2} \right) \right)}{D_{sd}} \\ + \frac{\Omega \bar{k} \sigma'}{k_B} \left( 1 + \frac{1}{\left(\exp\left(\frac{\Omega \bar{k} \sigma'}{k_B T}\right) - 1\right)} \right) \end{array} \right) \qquad Equation\ C27$$

The activation energy can thus be written as Equation C28.

$$Q = -R \left( \frac{\left( \sum_{i=1}^{N} \bar{m}_i \left( \frac{\partial \dot{\bar{\gamma}}}{\partial \frac{1}{\bar{T}}} \right) + \bar{k} \frac{\partial \dot{\bar{\beta}}}{\partial \frac{1}{\bar{T}}} \right)}{\sum_{i=1}^{N} \bar{m}_i \dot{\bar{\gamma}} + \bar{k} \dot{\bar{\beta}}} \right) = \left( \sum_{i=1}^{N} f_i \, Q_g + f_c Q_c \right) \qquad Equation\ C28$$

where

$$Q_g = -R \left( -\frac{g_{0,i} b^3}{k_B} \right) \left( \left( \frac{1}{T} \frac{\partial \mu}{\partial \frac{1}{T}} + \mu \right) \left[ 1 - \left( \left( \frac{\tau - \tau_a}{\mu} \right) \left( \frac{\mu_0}{\hat{\tau}} \right) \right)^p \right]^q + \frac{\mu}{T} \left( q \left[ 1 - \left( \left( \frac{\tau - \tau_a}{\mu} \right) \left( \frac{\mu_0}{\hat{\tau}} \right) \right)^p \right]^{q-1} \left( p \left( \frac{\tau - tau_a}{\mu} \right) \frac{\mu_0}{\hat{\tau}} \right)^{p-1} (\tau - \tau_a) \left( \frac{\mu_0}{\hat{\tau}} \right) \left( \frac{1}{\mu^2} \right) \frac{\partial \mu}{\partial \frac{1}{T}} \right) \right)$$

and

$$Q_c = -R\left(\frac{B}{\tilde{\rho}} - \frac{2}{\mu}\frac{D_0 T_0 \exp\left(\frac{T_0}{T}\right)}{\left(\exp\left(\frac{T_0}{T}\right)-1\right)^2} - \frac{\left(D_l \frac{Q_l}{R} + 100 D_p \left(\frac{\sigma}{\mu}\right)^2 \left(\frac{Q_p}{R} + \frac{2}{\mu}\frac{D_0 T_0 \exp\left(\frac{T_0}{T}\right)}{\left(\exp\left(\frac{T_0}{T}\right)-1\right)^2}\right)\right)}{D_l\left(1 + 100\left(\frac{\sigma}{\mu}\right)^2 \frac{D_p}{D_l}\right)} + \frac{\Omega \bar{k} \sigma'}{k_B}\left(1 + \frac{1}{\left(\exp\left(\frac{\Omega \bar{k} \sigma'}{k_B T}\right)-1\right)}\right)\right)$$

**Appendix D: Approximating the fractions of macroscopic strain accommodated by each slip mode**

As noted in Appendix C, the strain rate sensitivity and activation energy predictions are a function of the amount of strain accommodated by each slip mode as described in Equation D1.

$$f_i = \frac{\bar{m}_i \dot{\bar{\gamma}}_i}{\sum_{i=1}^{N} \bar{m}_i \dot{\bar{\gamma}}_i + \bar{k}\dot{\bar{\beta}}} \qquad Equation\ D1$$

These fractions are defined as the amount of macroscopic strain each slip system accommodates ($\bar{m}_i \dot{\bar{\gamma}}_i$) relative to the total strain rate. These values were calculated for the 5 conditions for which the relevant shear rates and orientation factors ($\bar{m}_i$ and $\bar{k}_i$) were known from previous VPSC simulations and calculations using knowledge of the orientations from electron backscatter diffraction (EBSD) assuming an in-plane stress direction of the initial texture (Table C1), respectively.

Table D1: Orientation factors for each slip mode using an initial rolled and annealed texture for AZ31B

| Slip Mode | Orientation Factor |
|---|---|
| Basal Glide | 0.18 |
| Prism Glide | 0.44 |
| <c+a> Glide | 0.44 |
| Basal <a> Climb | 0.55 |

The results of Equation D1 assume that the orientation factors do not change significantly which is only rigorously true in cases where texture evolution is minimal (i.e., under conditions of power law creep where climb is the dominant deformation mechanism). Prism slip will be the most affected at intermediate and ambient temperatures where this assumption does not hold, as past studies have shown that prismatic slip dominates at temperatures where climb is inactive under uniaxial tension. This may explain why the model strongly underpredicts at room temperature; the prism slip component is overrepresented, which has a relatively lower activation barrier (Figure D1) compared to basal and <c+a> slip. This cannot explain any discrepancy between the model and experimental SRS data. Equation D1 was interpolated to different strain rates and temperatures using the empirical Zener Hollomon parameter (Figure D1). 3 things are clear from these calculations: 1) climb becomes more active as the temperature is increased and/or the strain rate is reduced (lnZ decreases), 2) prism slip strain accommodation is the most severely impacted mode out of all glide modes and 3) basal glide is unaffected by temperature or strain rate, as expected, since it is the easy slip mode in Mg and typically described as being athermal.

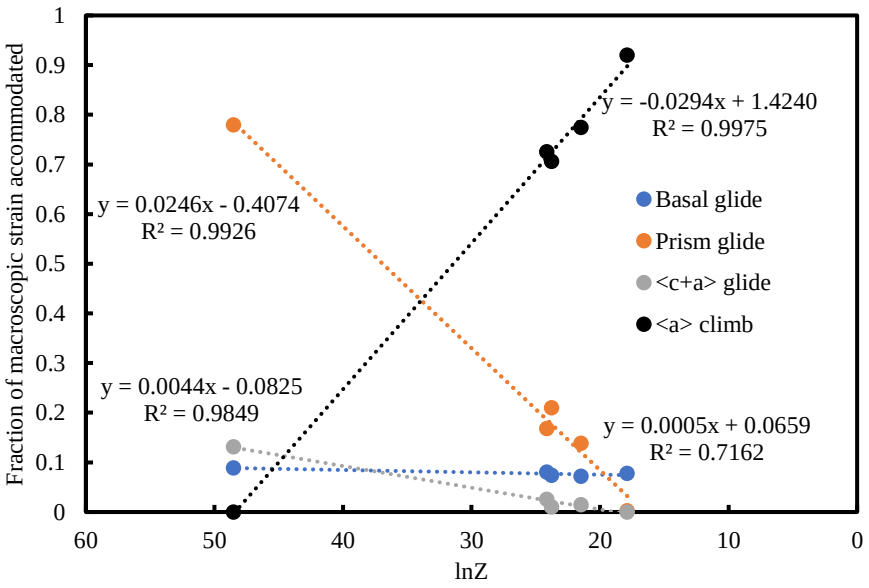


Figure D1: Interpolation of fractions accommodated by each glide mode.

# Chapter 3: Exploration of texture and alloy chemistry on the generality of significant dislocation climb using Mg alloy ZK10


## Abstract

In-plane tensile tests were performed on as-rolled and annealed Mg alloy, ZK10, to compare with the constitutive behavior of AZ31B. The experimental flow stresses and strain anisotropy (r-value) were observed to be lower than in AZ31B and the texture evolution was more subtle in ZK10. Simulations using a climb-incorporating viscoplastic self-consistent (VPSC-CLIMB) crystal plasticity model simulations using parameters optimized by machine learning via genetic algorithm. The reduced r-values at ambient temperature in ZK10 is attributed to increased basal slip. The climb of <a> dislocations was again necessary to predict the r-values at elevated temperatures. Lower r-values (<1) within the power law regime were attributed to the presence of climbing <c> dislocations in ZK10. Samples deformed at either ambient or elevated temperatures were found to have similar texture evolution (due to the increased strain accommodation via basal slip), which stymied direct assessment of the active slip modes from the texture measurements. Regardless, comparison with optimized glide-only simulations and simulations using previously determined parameters for AZ31B demonstrate the need for the climb of both <a> and <c> dislocations in order to better describe the strain anisotropy evolution with temperature and strain rate.


## 1- Introduction

Classical understanding of climb and glide power law creep assumes that the strain accommodation via climb is minimal due to its vacancy diffusion dependence; its role is that of a recovery mechanism to assist glide overcome obstacles. This has been demonstrated to be an oversimplication in strongly textured Mg alloys (i.e. AZ31B [80]) under uniaxial tension where the easy glide modes (basal and prism <a> glide) cannot accommodate <c> axis strains to satisfy the von Mises criterion [8]. Currently, significant strain accommodation via climb has only been suggested in a single alloy and further study is necessary to generalize its role in the constitutive behavior in Mg alloys in the power law regime since the critical resolved shear stresses (CRSSs) of glide modes are known to be dependent on solute content (Mg-Zn ([15], [16]), Mg-Y [13], Mg-Li [81], AZ31B [82]). The last study is of particular importance, as it suggests that AZ31B is unique amongst the Mg alloys as it deforms through tensile twinning during <a> direction tension (another form of in plane tension in single crystal materials) rather than the motion of <c+a> dislocations on pyramidal II planes at room temperature, suggesting that the inactivity of <c+a> slip in prior AZ31B simulations (Chapter 1) may have also been a result of solute content.

Previous investigations into the role of climb in the high temperature deformation of Mg alloys assumed that climb strain accommodation was limited to <a> dislocations; however, <c> and <c+a> dislocations are also capable of climbing. In AZ31B, this was a reasonable

assumption since the majority of dislocations present were of <a> type [29]. In contrast, previous studies of ZK60 (Mg – 6 wt% Zn – ~0.5% Zr) have observed large populations of <c> dislocations within the grain interior [40]. This is surprising for two reasons. First, <c> dislocations are higher energy defects than <a> dislocations due to their larger Burgers vectors ($\frac{b_c}{b_a} \approx 1.6$) and thus there should be a higher driving force for annihilation. Second, the multiplication of <c> dislocations through glide is unlikely, as basal <a> glide is similarly oriented with a lower CRSS. While the increase of <c> dislocation density via glide is unlikely, twinning transmutation of matrix dislocations has been shown to generate a significant population of non <a> type dislocations within the twinned region [29]. As the matrix is swept by the twin boundary, <a> dislocations are converted into ½ <c+a> dislocations; <c> dislocations are the product of the transmutation of $[10\bar{1}0]$ dislocations (from the reaction of different <a> dislocations) or the decomposition of a <c+a> dislocation into <c> and <a> components. The former case is energetically favored via Frank's rule ($2b^2_{<a>}$ for the two <a> dislocations and ¾ $b^2_{<a>}$ for the $[10\bar{1}0]$ dislocation; previous studies have shown that the transmutation reaction is favorable [29]). The latter case is also been shown to be energetically favorable [29].

Studies into extruded ZK60 have suggested that extension twins are present in recrystallized grains after annealing and become grain boundaries [41]. It is believed that these twin boundaries are formed during the extrusion and grow during the subsequent anneal designed to remove the twinned microstructure (i.e. full recrystallization)[38]. As the boundaries sweep across the matrix, the dislocations present (most likely <a> type) are transmuted into ½ <c+a> which could react to from <c> dislocations. As rolled ZK10 samples have also been observed to have significant extension twin content [38] and may also generate <c> dislocations in a similar manner to extruded ZK60. Regardless, the potential for <c> dislocations suggests the possibility of significant non <a> type dislocation climb. Further study to understand its importance relative to <a> climb in the high temperature constitutive behavior of Mg alloys.

This chapter is begins with a summary of the material and the methods employed in the current study of ZK10. The constitutive behavior of ZK10 (i.e., flow stress, strain anisotropy and texture measurements) and modeling results (VPSC-CLIMB simulations and fitting via thermally activated plasticity models and a discussion of the feasibility of significant <a> and <c> climb follows. A list of conclusions and references follows.

## 2- Methods

*Material*

Sheets of rolled magnesium alloy ZK10 were received from Magnesium Elektron North America in the F temper (as-rolled) with a nominal thickness of 1 mm and annealed at 300 °C for 1 hour to fully recrystallize the twinned microstructure [38]. The composition of the sheet was characterized by energy dispersive spectroscopy (EDS) to be 1 wt% Zn, 0. 3 wt% Zr (balance Mg). Linear intercept measurements done with optical microscopy yielded an average grain size

of 9 μm and SEM/EDS performed on the samples identified an α-Mg phase with small amounts of Zr-rich precipitates [38].

Many methods employed in Chapter 1 with AZ31B were reused for the testing of ZK10 and will be only summarized here.

*Mechanical Testing*

ASTM E-8 subsized samples were employed in uniaxial tensile tests performed on the samples at a range of temperatures (20 – 300 °C) and at strain rates of 0.0001 and 0.001 1/s. Testing conditions were selected to evenly span a range of the Zener-Hollomon parameter and the true plastic strain of each tensile sample was measured by dividing the gauge into 5 equal sections whose dimensions were measured pre- and post-test. An average strain level and standard deviation of the strains within the gage and strain anisotropy measurements (r-values) were obtained by measuring the displacement of scribe marks on the sample.

*Texture Collection and Analysis*

Tensile samples were prepared for texture analysis through a series of polishing steps with SiC polishing pads and finished with a chemical polish of 2% Nital (2% by volume nitric acid in ethanol) and a methanol rinse. Texture measurements were collected from samples deformed to ~10% strain and polished to mid-thickness using a Panalytical X'Pert Pro diffractometer with the same operating conditions as listed in Chapter 1. Regardless of sample loading orientation, RD was always aligned with the goniometer to ensure that sample coordinates line up with pole figure and simulation coordinates. MTEX, a Matlab toolbox, was used to plot experimental pole figures and compute Orientation Distribution Functions (ODFs) [83]. The resulting ODFs were discretized to obtain 2,000 orientations ("grains") weighted to best represent the experimental textures. The representative ODF for the as-rolled material was used as an input for the VPSC-CLIMB simulations described below. It is immediately apparent that the initial texture of ZK10 is much weaker than that of AZ31B due to a splitting in the basal pole along the rolling direction, as seen previously [38] (Figure 1).

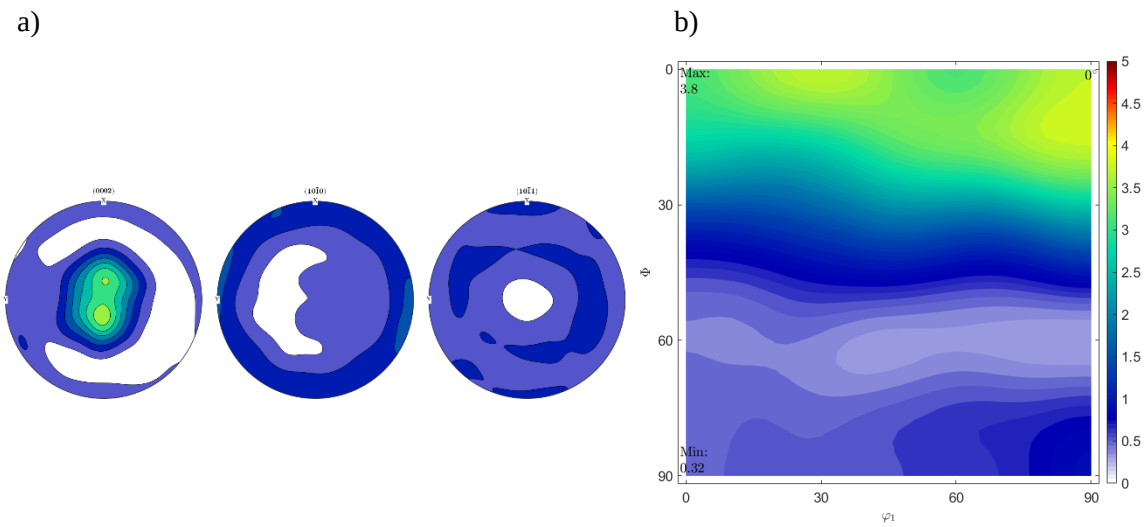


Figure 1: The initial texture of the rolled ZK10 sheet measured in this study using a) 3 pole figures and b) a 2-D ($\varphi_2 = 0°$) section of the ODF (Bunge Euler angle convention ($\varphi_1$, $\Phi$, $\varphi_2$)).

A Matlab script written to calculate the Hartley tensor in each grain for <a> and <c> dislocations by rotating an in-plane tension stress into the crystallographic orientation of each grain as denoted by the initial as-rolled texture in Euler angles. In each case, the most well oriented slip mode is assumed to be the only climb mode to activate in the grain. Then, the most probable Hartley factors were averaged over every grain for <a> and <c> climb in the as-rolled texture in ZK10.

Details about the crystal plasticity model and parametric study were unchanged from Chapter 1 and, hence, only summarized here. The genetic algorithm was used to optimize the ratios between the basal and non-basal critical resolved shear stresses (CRSSs) and threshold stresses for climb to the texture evolution and r-value for the TD and RD conditions. Absolute values of the glide mode CRSSs and threshold stresses were obtained by scaling the predicted stress strain response to the experimentally measured flow curves. Climb was assumed to be inactive at room temperature due to the slow vacancy diffusion rates. At elevated temperatures, the possibility of <c> climb out of the prism planes was explored in a similar manner to basal <a> climb due to prior studies noting the relative abundance of <c> dislocations in ZK60 [40]. The only additional stipulation enforced in the genetic algorithm was that <c> climb could not be softer than <a> climb. This was rationalized as the <c> dislocation has a larger Burgers vector than the <a> dislocation ($\frac{b_{<c>}}{b_{<a>}} = 1.6$) and the formation of a jog to initiate climb adds to the total self-energy of the dislocation, $\frac{1}{2}\mu b^2 l$ by increasing the total dislocation length. Since the increase in the energy of a <c> dislocation is higher, it is reasonable to assume that the resolved stress must also be higher for the <c> dislocation to climb. This is a simple first order approximation; a more thorough treatment can be found in Chapter 4.

*Microstructure analysis via electron backscatter diffraction (EBSD)*

Electron backscatter diffraction (EBSD) as performed to compare the grain boundary misorientations between the two alloys, as a previous study found that ZK series alloys can have twin boundaries, nucleated during extrusion and grown during annealing, masquerading as grain boundaries with a misorientation angle of ~86° between neighboring grains [41]. Samples were prepared first by mechanical polishing using a series of decreasing particles sizes and then using glycol based diamond slurries and 0.05 μm silica. Polishing damage caused by silica polishing was removed using an ion beam for 15 minutes at a 5 degree angle at 6kV. EBSD scans were performed at 30 keV at a step size of 1.5 μm on samples of as-rolled and annealed AZ31B and ZK10. This sample preparation was deemed acceptable as 88% and 75% of the sample surface could be indexed for AZ31B and ZK10, respectively. The raw data was processed in mTEX using a half quadratic filter to fill in regions that could not be indexed. The mean orientation of every grain was plotted alongside the recalculated boundaries from mTEX. Energy dispersive spectrometry (EDS) was performed simultaneously to identify secondary phases that did not index during EBSD.

*VPSC-CLIMB simulations of constitutive behavior in ZK10*

The constitutive behavior (i.e., texture evolution, strain anisotropy) measured at discrete temperature and strain rates were modeled using a climb-incorporating viscoplastic self consistent (VPSC-CLIMB) crystal plasticity model. The appropriate CRSSs and climb stresses were determined by machine learning using a genetic algorithm to minimize the total error in the texture and strain anisotropy after deformation along the rolling or sheet transverse directions (RD and TD, respectively). The optimized CRSSs were fit to the mechanical threshold stress (MTS) model (Equation 1)[45] to interpolate between the analyzed conditions.

$$\tau_i = \tau_{a,i} + \mu \sum_{i=1}^{N} \left(\frac{\hat{\tau}_i}{\mu_o}\right) \left(1 - \left[\frac{k_B T}{g_{o,i} \mu b_i^3} \ln\left(\frac{\dot{\gamma}_o}{\dot{\gamma}}\right)\right]^{\frac{1}{q_i}}\right)^{\frac{1}{p_i}} \qquad Equation\ 1$$

where $\tau_{a,i}$ is the athermal stress, $\mu$ is the shear modulus, $\frac{\hat{\tau}_i}{\mu_o}$ is the slip mode strengthening factor, $k_B$ is the Boltzmann constant, $T$ is the temperature, $g_{o,i}$ is the stress normalized activation energy, $b_i$ is the length of the burgers vector, $\dot{\gamma}_o$ is the reference strain rate (~$10^8$ 1/s), $\dot{\gamma}$ is the shear rate (taken to be the applied strain rate) and $q_i$ and $p_i$ are constants which describe the arrangement of the dominant obstacles.

Unlike in AZ31B, multilinear regression on the fraction of dislocations required to climb could not be performed due to the low number of conditions investigated in the power law. Instead, climb stresses for <a> and <c> dislocations were fit to an exponential relationship with lnZ (Equation 2)

$$\sigma_c = a \exp(blnZ) \qquad Equation\ 2$$

where $a$ and $b$ are fitted constants.

Slip mode hardening was implemented for gliding dislocations via Equations 3 and 4 [62]

$$\tau_1^s = \frac{C_1 \mu b k_1^s}{k_2^s} \qquad Equation\ 3$$

$$\theta_0 = \frac{C_1 \mu b k_1^s}{2} \qquad Equation\ 4$$

where $\tau_0^s + \tau_1^s$ is the back extrapolated CRSS, $C_1$ is an interaction parameter, $k_1^s$ is a material constant related to dislocation storage and $k_2^s$ is a temperature and strain rate dependent parameter controlling the dynamic recovery of dislocations.

**3- Results**

The constitutive behavior of rolled ZK10 followed similar trends to that which was found in AZ31B (Figure 2). The yield strength (in addition to the flow stress and the amount of strain hardening) decreases with increasing temperature.

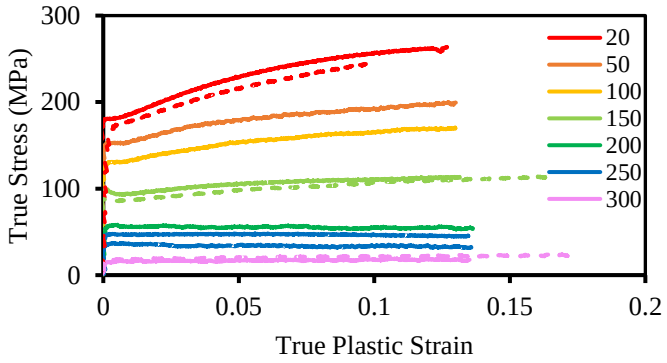


Figure 2: Constitutive behavior of ZK10. The flow stress and amount of strain hardening decrease with increasing temperature. The disparity in strength between TD (solid line) and RD (dashed line) decreases with increasing temperature. All of these findings are in keeping with the initial study of AZ31B.

Using the same Garafalo-Sellars-Tegart approach as AZ31B, some parameters associated with dominant creep can be obtained (Figure 3a): A= $7.28 \times 10^9$, α = 0.023, n = 4.81 (assuming lattice diffusion control, Q = 135 kJ/mol). As before, the stress exponent is found to be within 3 - 5, so it appears that the power law regime in ZK10 is also controlled by dislocation glide and climb. This is in keeping with a study of a similar alloy ZK60, which calculated the stress exponent at 250 °C at similar strain rates to be 3.5 [84]. The quoted grain size in this cited study was much finer than the examined material (1.7 μm in the as-rolled state compared to ~8 μm in the studied material), which would increase the likelihood of straining by grain boundary sliding (n = 2 - 3) and explain the discrepancy between the cited stress exponent and the one measured here. Three conditions of interest were chosen and marked with an orange circle as being

representative of ambient, power law breakdown and power law regime conditions through knowledge of the critical stress ($\sigma_c = \frac{1}{\alpha}$) which separates the ambient (exponential dependence on stress) and the power law responses (power dependence on stress).

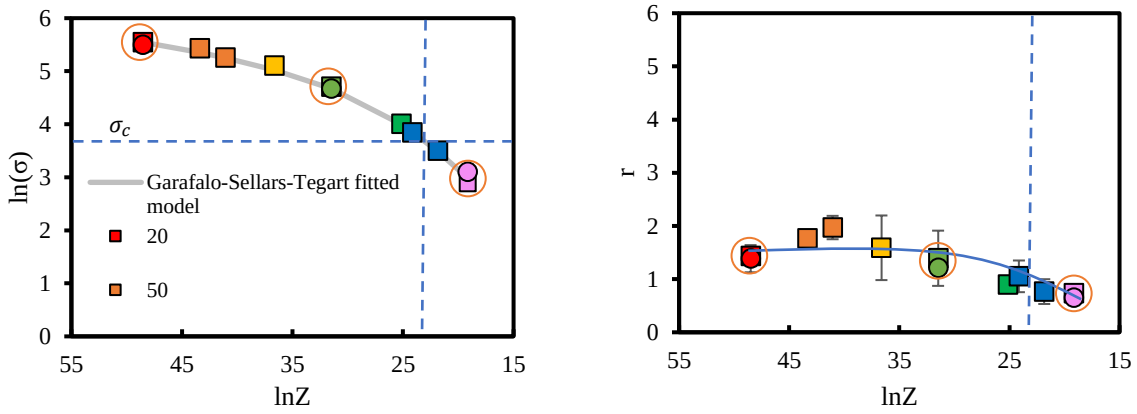


Figure 3: Evolution of the a) flow stress at 10% true plastic strain with a Garafalo-Sellars-Tegart fit and b) strain anisotropy as a function of lnZ (The curve is meant as a guide to the eye, not as a model of best fit).

The evolution in strain anisotropy was also examined (Figure 3b). At near ambient temperatures, the strain anisotropy is found to be much lower than in AZ31B (1.4 vs 4), suggesting that prism slip may not be as active in the more weakly textured material. Agnew & Duygulu found that when the $\frac{\tau_{<c+a>}}{\tau_{prism}} > 1$ (i.e., prism slip is more active than <c+a> slip), the strain anisotropy increases dramatically [20]. Additionally, strain direction anisotropy (TD vs RD loading) was noticeable absent in the r-value measurements. This is also likely a result of the weaker initial texture in ZK10 which minimizes Schmid effects. Therefore, basal slip (the easy slip mode in Mg) could activate primarily under both loading conditions. If the active slip modes are similar between loading directions, there should be no difference in strain anisotropy measurements. At lower Z values, particularly those in the power law regime as denoted by the blue dashed line, the strain anistropy reaches isotropic flow (r = 1), similar to AZ31B. However, unlike AZ31B, the r-values in the power law regime decrease beyond isotropic flow, suggesting that an additional mechanism is activated in ZK10, as <a> climb does not reduce the strain anisotropy below 1 as demonstrated by prior simulations of AZ31B where ~80 % of strain was accommodated by <a> climb and isotropic flow was observed (Chapter 1).

Texture evolution for the ambient, power law breakdown and power law regime conditions tested are found in Figure 4. At ambient temperatures, shallow node formation is observed relative to the initial as-rolled and annealed texture (Figure 1b), indicating that prism slip is active in addition to basal slip [80]. Under conditions of power law breakdown, the texture evolution and strain anisotropy are almost unchanged from ambient conditions, indicating that climb may not be a significant strain carrier outside the power law regime, as expected from the Garafalo-Sellars-Tegart model predictions. In the power law regime, the texture shows very

modest evolution from the as-rolled state, which suggests that climb is active in the power law regime. There is no evidence of significant <c+a> slip from the texture evolution, as that would rotate the <c> axes toward the tensile axis, causing significant splitting in the basal pole figure (or the motion of the nodes off $\Phi = 0°$ and smearing along the $\phi_1$ axis). Climb accommodation via strain would also explain the change in the r-value, which is best seen in the RD samples. <a> climb has previously been linked to isotropic flow (r = 1) in Chapter 1, yet this does not appear to fully explain the r-value evolution. Predicting the r-value evolution required the climb of <c> dislocations which can reduce the strain anisotropy below 1. Like <a> climb, the out of plane motion of <c> dislocations cannot contribute to texture evolution due to the absence of shear stresses; however, the climb direction (i.e., the straining direction) is perpendicular to <a> climb (along the basal plane in contrast to out of the basal plane for <a> climb).

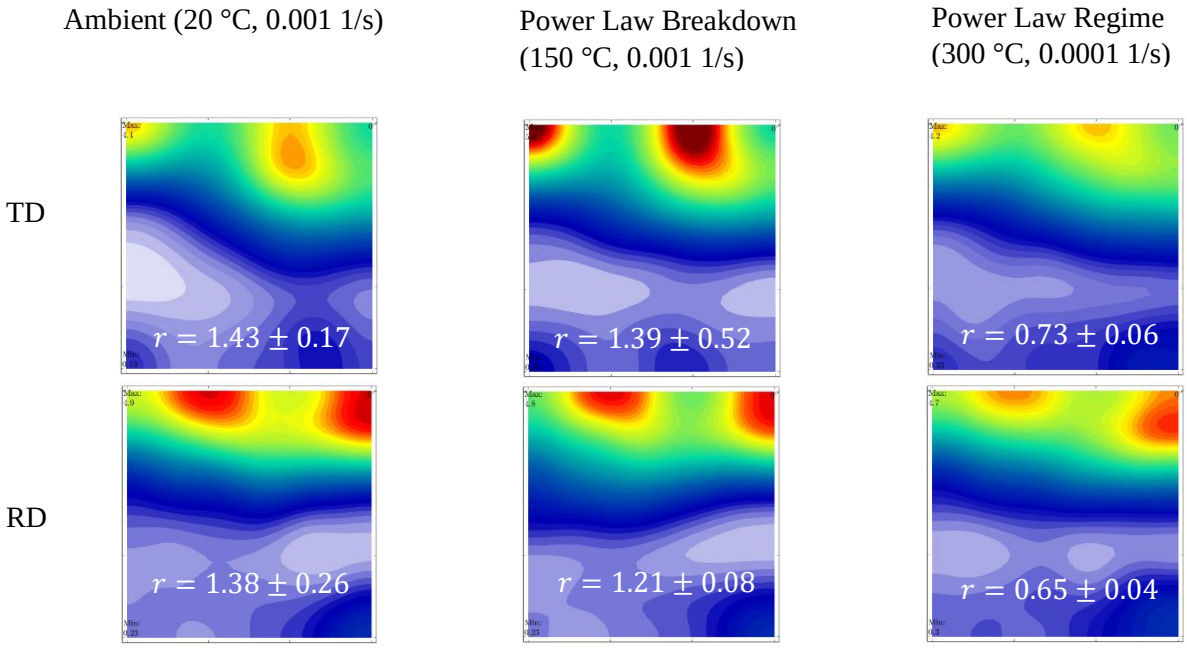


Figure 4: Texture evolution after deformation under various loading conditions (temperature, strain rate and direction). All ODFs share the same scale as listed in Figure 1b.

Best fit CRSSs and climb stresses are presented in Table 1. Room temperature deformation of ZK10 should be dominated by basal slip as it is much softer than the nonbasal slip modes and texture effects are less predominant than in more strongly textured materials such as AZ31B. The same is most likely true in the intermediate regime wich the possible addition of strain accommodation via <a> climb. At the highest temperature explored, it is more difficult to predicted from the CRSSs and threshold stresses, but it is likely that basal slip and climb will be active, as in AZ31B. Generally, the CRSSs and threshold stresses decrease with increasing temperature and decreasing strain rate and as expected. The only exception to this trend is that basal slip hardens in the intermediate temperatures. This likely an artifact of the GA attempting to optimize a poorly constrained CRSS due to the weak initial texture which makes basal slip always highly active.

Table 1: Optimized Voce hardening parameters for low and high temperature simulations for ZK10

| | Ambient (20 °C, 0.001 1/s) | | | Power Law Breakdown (150 °C, 0.001 1/s) | | | Power Law Regime (300 °C, 0.0001 1/s) | |
|---|---|---|---|---|---|---|---|---|
| | $\tau_0$ | $\tau_1$ | $\theta_0$ | $\tau_0$ | $\tau_1$ | $\theta_0$ | $\tau_0$ | $\tau_1$ |
| **Basal Glide** | 20 | 0.0 | 300 | 23.8 | 0.0 | 300 | 4.6 | 0.0 |
| **Prism Glide** | 91.2 | 0.0 | 300 | 40.7 | 0.0 | 300 | 22.7 | 0.0 |
| **<c+a> Glide** | 98.9 | 0.0 | 300 | 92.5 | 0.0 | 300 | 42.0 | 0.0 |
| **<a> Climb** | n/a | n/a | n/a | 48.2 | 0.0 | 0 | 10.3 | 0.0 |
| **<c> Climb** | n/a | n/a | n/a | 228.1 | 0.0 | 100 | 11.3 | 0.0 |

Fitting the GA results to the MTS and Orowan expressions yielded the parameters listed in Tables 2 and 3. Identical athermal stresses, dominant obstacles and hardening parameters were used as in AZ31B; however, the fitting resulted in different stress independent activation energies ($g_0$) and thermal hardening parameters ($\hat{\tau}/\mu_0$). The slip modes in ZK10 follow the same trends as determined in AZ31B. Like in AZ31B, basal slip is the easy slip mode as it hardens much more slowly than the other slip modes and has the lowest temperature dependence due to its low activation energy and <c+a> slip is the hardest due to its higher hardening rate and activation energy.

Table 2: Glide mode CRSS and hardening parameters for ZK10

| Slip Mode | $\tau_a$ (MPa) | $p$ | $q$ | $\hat{\tau}/\mu_0$ (x $10^{-3}$) | $g_0$ | $g_0 b^3$ (x $10^{-29}$) | $k_1$ | $D$ (MPa) | $g_{ss}$ |
|---|---|---|---|---|---|---|---|---|---|
| **Basal <a>** | 0.5 | 2/3 | 3/2 | 3.37 | 0.741 | 2.45 | 2 x $10^7$ | 20 | 0.005 |
| **Prism <a>** | 2 | 1/2 | 1 | 9.29 | 0.781 | 2.58 | 2 x $10^8$ | 200 | 0.06 |
| **<c+a>** | 6 | 1 | 3/2 | 11.1 | 0.115 | 17.8 | 2 x $10^8$ | 200 | 0.06 |

Table 3: Climb stress parameters for ZK10

| Slip Mode | a | b |
|---|---|---|
| **<a> Climb** | 0.9439 | 0.1249 |
| **<c> Climb** | 0.1077 | 0.2433 |

The simulated flow stresses (Figure 5) were compared to the experimental measurements in Figure 2. At room temperature, the predictions are in good agreement with the experimental flow curves and any discrepancies can be explained by slight differences in slip mode hardening between the two alloys. The simulations of the intermediate and high temperatures data have excellent agreement with the TD experimental data, where slip mode hardening is less important.

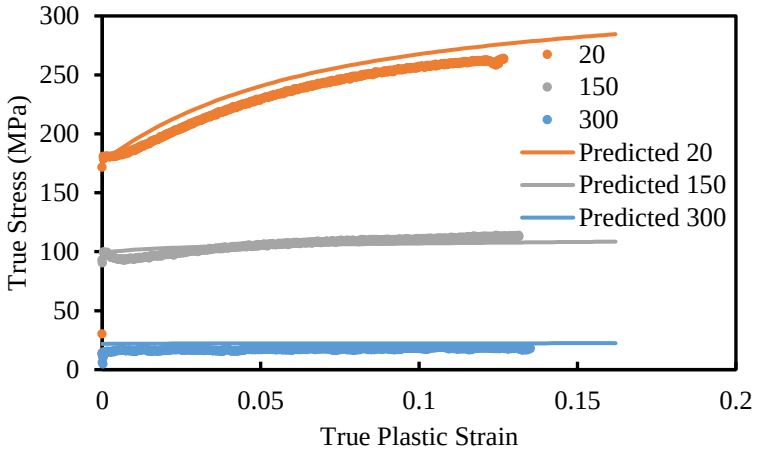


Figure 5: Experimental flow stresses when pulled along the transverse direction are compared against VPSC predictions.

Simulated texture (the error between experimental and simulated texture is denoted by $t$) and r-values (Figure 6) are in good agreement with the experimental measurements, particularly in the RD case. In the TD case, the absolute intensity of the ODF is much lower than the simulated texture, but the key components are still present, suggesting that strain is carried by predominantly basal and prism glide. The texture evolution is slowed at elevated temperatures and r-values are roughly identical between room temperature and 150 °C since a combination of prism and <c+a> slip are replaced by climb, which have similar effects on r-value. At higher temperatures within the power law regime, the minimal texture evolution and low r-values are resultant from climbing <a> and <c> dislocations. It is possible that the simulation results presented here underestimate the contributions of <c> climb, as a disparity between the predicted and experimental r-values still exists.

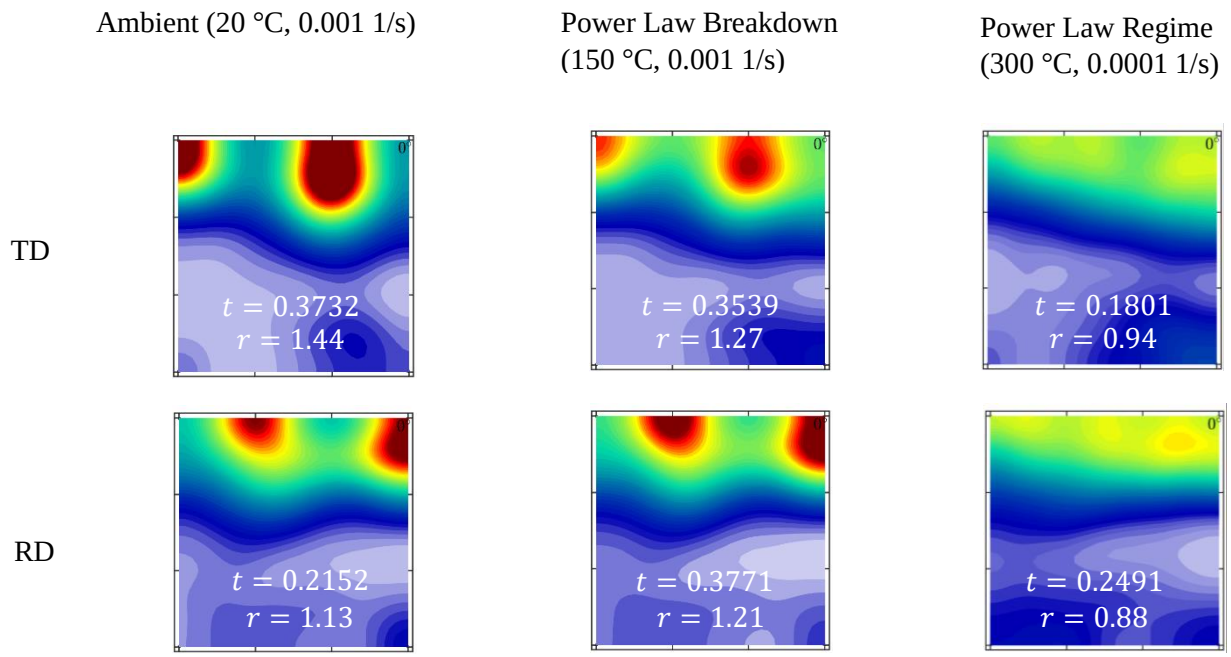


Figure 6: Optimized simulations for ZK10 using VPSC-CLIMB at elevated temperatures. The t values represent the difference between the experimentally measured texture and predicted texture, as in Equation 11 of Chapter 1.

The relative slip activity plots in Figure 7 corroborate the dominant slip modes determined from the CRSS and threshold stress values listed in Table 1 and the texture evolution in Figure 6. Ambient temperature deformation was indeed dominated by basal slip with significant strain accommodation from prism and <c+a> slip. At higher temperatures (150 °C), <a> climb begins to accommodate significant strain in place of basal, prism and <c+a> glide. <c> dislocations also begin to climb, but their strain carrying capacity is insignificant (<0.5% of all strain) under these conditions due to the higher energetic barrier associated with the initiation of <c> climb. At the highest temperature investigated, most of the strain previously accommodated by prism glide is carried by <c> climb; the strain accommodation of <a> climb increases slightly and that of basal slip is unchanged.

Predictions using the MTS expression were compared to the experimental data presented in Figure 3. The flow stresses were well represented by the currently employed parameters; however, the strain anisotropy was underpredicted (Figure 8). The apparent plateau in r-value beginning at lnZ = 40 suggests that climb may accommodate too much strain at intermediate temperatures, though the predicted r-values remain within the margins of error for most conditions. This possibility is corroborated by the calculated fraction of dislocations needed to climb being greater than unity at 150 °C. The influence of climb is also noted in the predicted texture evolution (Figure 9), which shows a distinctive slowing of the texture evolution before 200 °C concomitant with isotropic flow (r = 1).

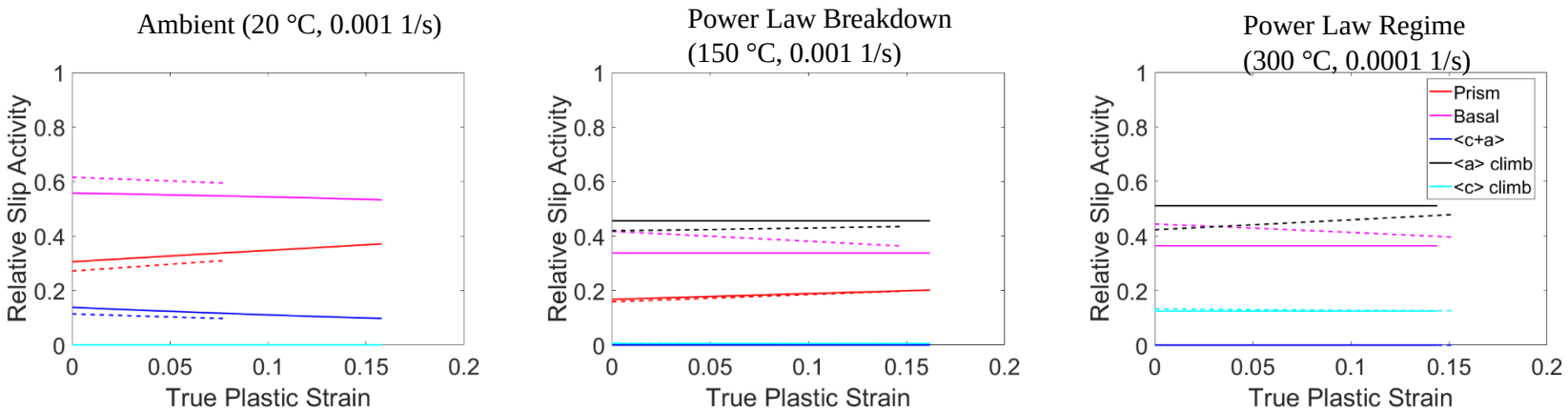


Figure 7: Relative slip activity plots for VPSC simulations modeling the presently studied conditions. TD simulations are represented by solid lines and RD simulations by dashed line.

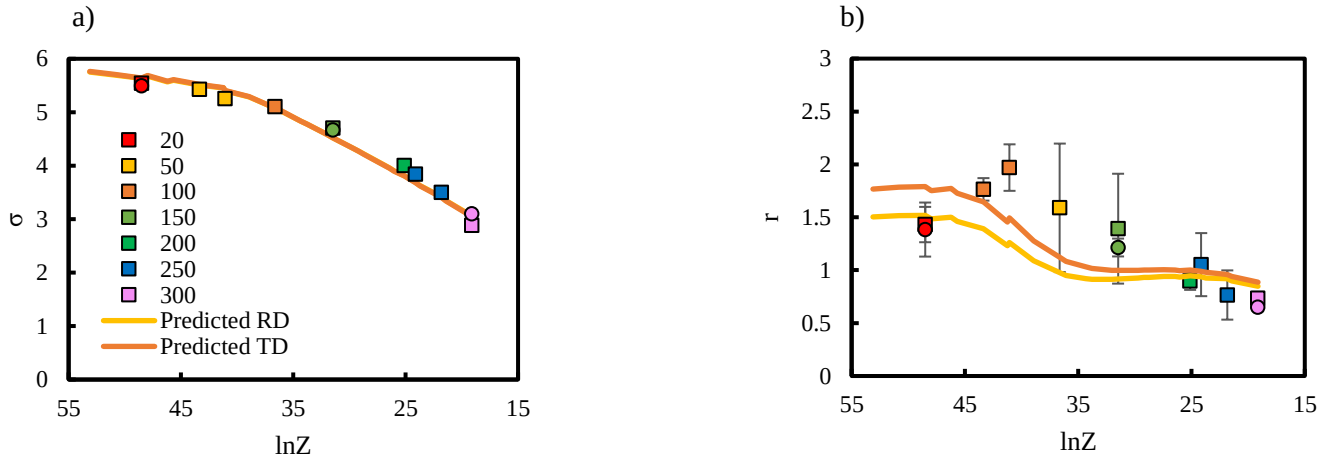


Figure 8: Comparison of the experimental and predicted a) flow stress and b) strain anisotropy of ZK10

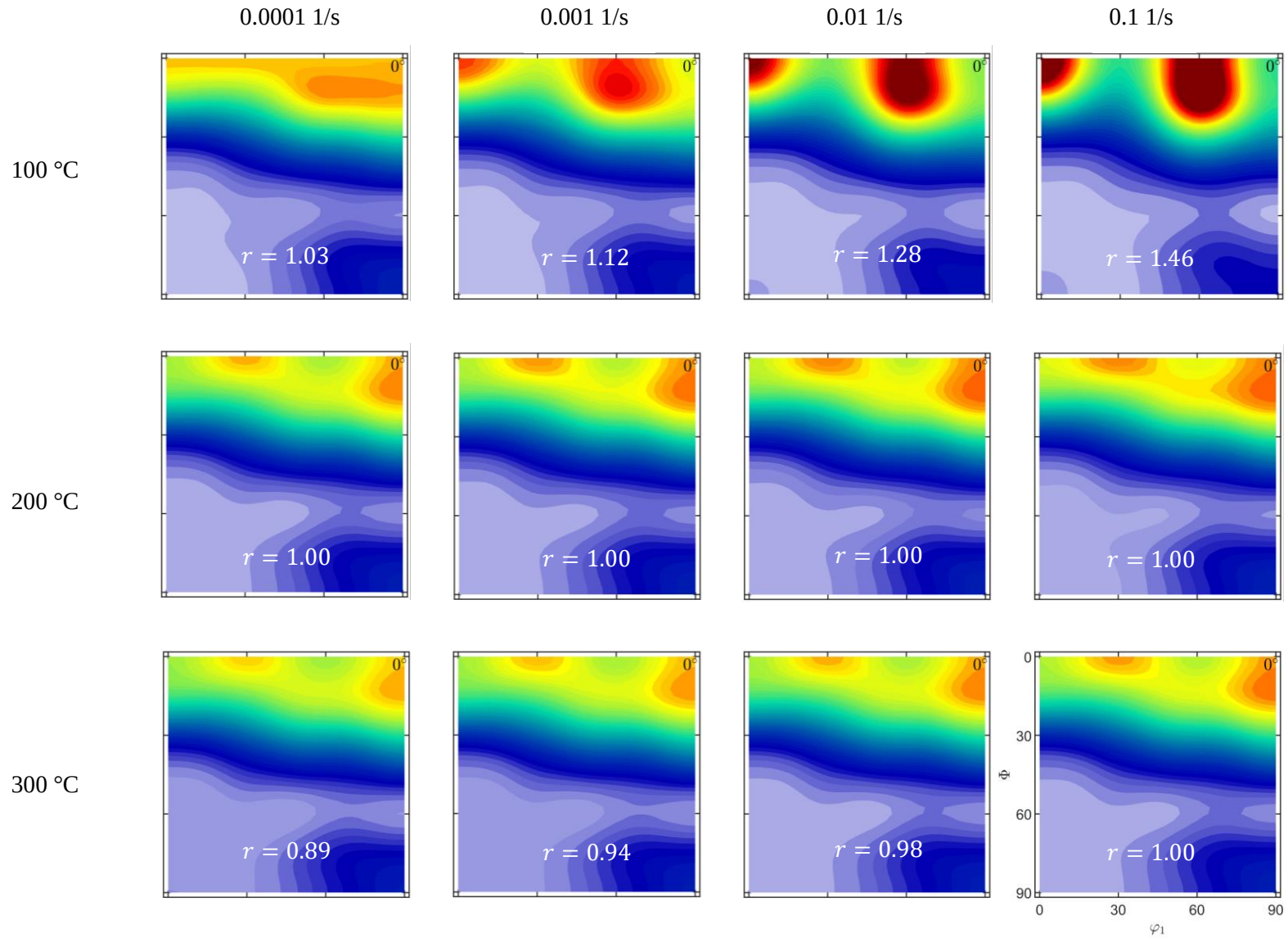


Figure 9: Texture evolution and r-values using the MTS and climb stress parameters listed in Tables 2 and 3.

The genetic algorithm based approach was used to optimize simulations that excluded climb (Table 4) to determining the its efficacy in predicting the texture evolution and r-values (Figure 10) in elevated temperature simulations. This was important as the role of climb is less clear in a more weakly textured material (Figure 3), where basal slip accommodates a larger fraction of strain at room temperature. As the texture signature for basal slip is similar to the initial as-rolled and annealed texture, the texture evolution in room temperature and power law conditions is more similar than in a more strongly texture material, AZ31B (Chapter 1). Parameters for the fit MTS expressions for basal, prism and <c+a> glide are found in Table 5. The dominant obstacles, athermal stresses and hardening parameters are identical to the climb-incorporating simulations and can be found in Table 2. The room temperature simulations reported in Table 2 are, by definition, glide only and therefore are not duplicated in Table 4.

Table 4: Voce parameters for best fit, climb-excluding VPSC simulations

| Slip Mode | LTC (150 °C, 0.001 1/s) | GBS (300 °C, 0.0001 1/s) |
|---|---|---|
| | $\tau_0$ | $\tau_0$ |
| **Basal Glide** | 7.7 | 2.1 |
| **Prism Glide** | 47.0 | 7.6 |
| **<c+a> Glide** | 49.1 | 8.3 |

Table 5: MTS parameters of glide only simulations in ZK10

| Slip Mode | $\hat{\tau}/\mu_0$ (x $10^{-3}$) | $g_0$ | $g_0 b^3$ (x $10^{-29}$) |
|---|---|---|---|
| **Basal <a>** | 2.97 | 0.547 | 1.81 |
| **Prism <a>** | 11.9 | 0.579 | 1.91 |
| **<c+a>** | 11.7 | 0.069 | 0.968 |

Like in the climb-incorporating simulations, basal slip is the easy slip mode as it hardens much more slowly than the other slip modes and a low temperature dependence due to its low activation energy. However, when climb is excluded, <c+a> slip is required to activate at lower temperatures to maintain a low strain anisotropy and consequentially has a low activation energy. The surprisingly low activation energy to activate <c+a> is a consequence of needing to balance the softening of prismatic slip at elevated temperatures relative to basal slip, which would increase the strain anisotropy.

Simulations performed in the intermediate temperature are also in good agreement with the experimental texture evolutions and r-values (Figure 10), which corroborates with the proposal that climb strain accommodation is overestimated at 150 °C. However, this is decidedly

not the case in the power law regime where glide only simulations result in much stronger texture evolution than experimentally observed. In addition, the r-values are unchanged from room temperature, which is indictative of the strain accommodation between intermediate temperatures and power law conditions being constant (Figure 10). These trends in r-value are also represented in the MTS fits when compared against the experimental trends (Figure 11). Outside the power law regime, the r-value predictions well describe the experimental measurements (approximately 1.3 - 1.5 in the TD condition). Closer to the power law regime (lnZ < 31), the experimental strain anistropy approaches isotropic flow. While the predicted r-values also decrease, they do not decrease below unity due to relative inactivity of <c+a> slip (known to dramatically reduce the strain anisotropy [20]) when compared to prism and basal slip (Figure 12). The flow stresses within the power law regime are also greatly overestimated in glide only simulations due to the significant slip mode hardening present and removal of climb strain accommodation, which does not harden in the current model. In short, it is apparent that strain accommodation via climb is an important mechanism in ZK10, though the weaker initial texture and its influence on predicting the texture evolution is an additional complicating factor that can result in anomalous answer by solely relying on CRSS and climb stress optimization via the gentic algorithm.

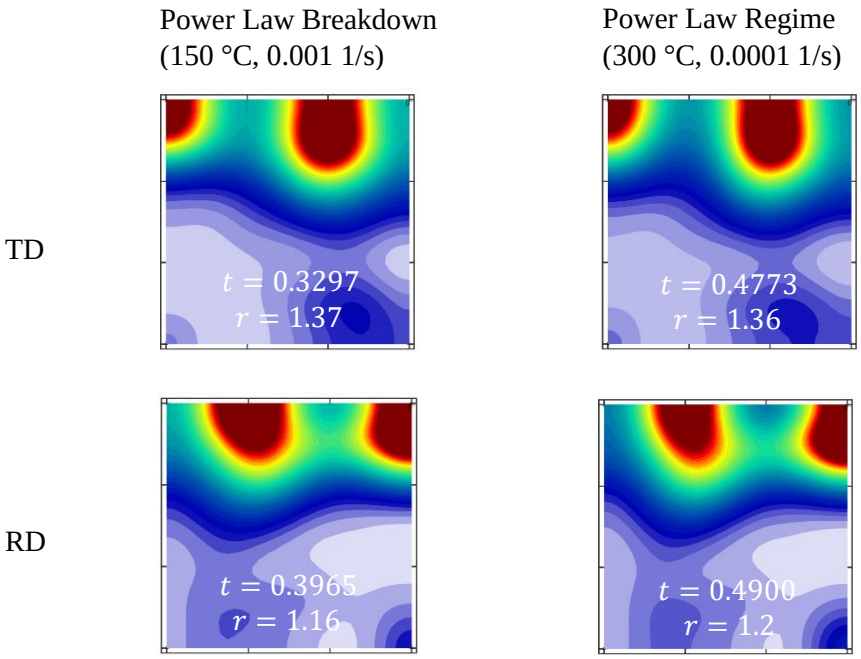


Figure 10: Optimized simulations for ZK10 when climb is excluded

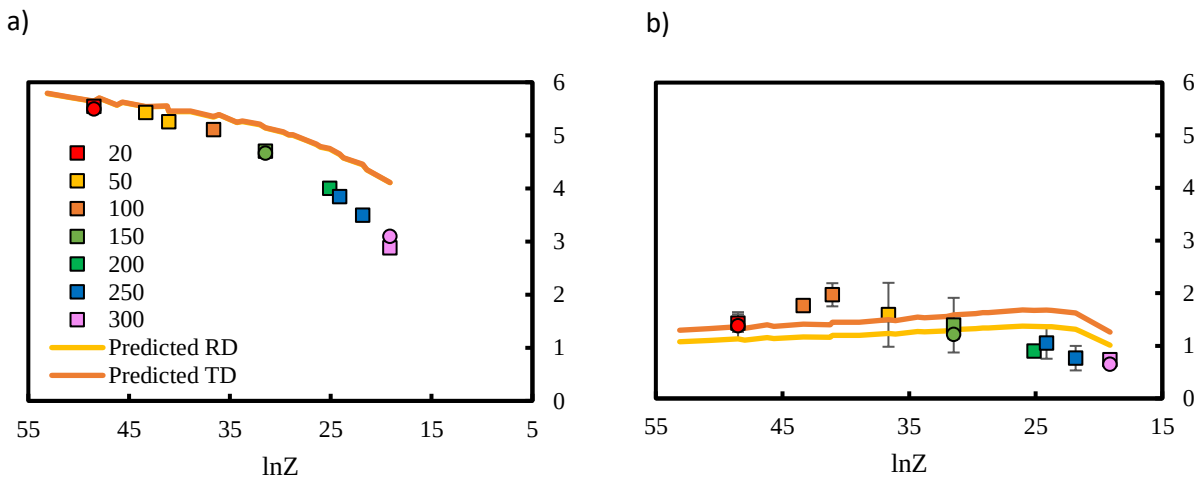


Figure 11: Comparison of experimental a) flow stress and b) strain anisotropy with glide only predictions

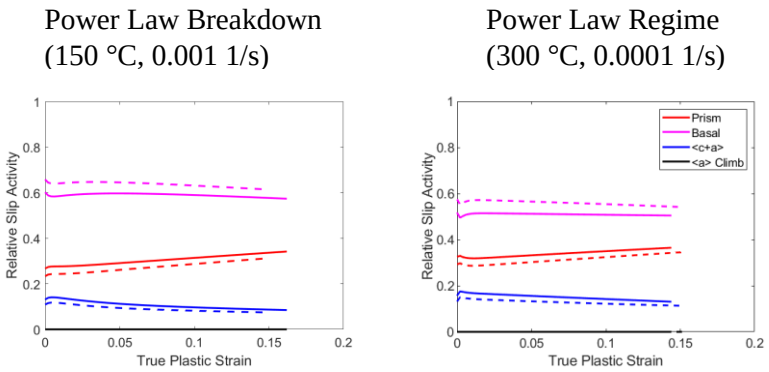


Figure 12: Relative slip activity plots for climb excluded VPSC simulations

## 4- Discussion

The purpose of this study was to test the applicability of significant strain accommodation via climb that was first studied in AZ31B. The results presented suggest that dislocation climb is also a necessary strain accommodation mechanism in ZK10, but several questions remain. Namely,

1) Are the results of the genetic algorithm unique to ZK10? That is to say, could similar results be obtained using parameters derived from the work on AZ31B in Chapter 1?

2) Are the dislocation densities required for the stated strain accommodation by climb reasonable, as in AZ31B?

3) Is there a mechanism for <c> dislocation generation to facilitate significant <c> climb?

Each of these questions will probe the potential of other climb modes accommodating significant strain in Mg alloys. The uniqueness of the current GA results was tested by simulating the deformation using MTS and Orowan parameters derived from the optimized VPSC simulations on AZ31B to calculate the CRSSs and climb stresses at the appropriate temperatures and strain rates. <c> dislocation climb was ignored, as it was not studied in Chapter 1, nor did its exclusion harm the prediction of the texture evolution and strain evolution of AZ31B.

The results from the VPSC simulations using the CRSS and climb stress values calculated by Equations 1 and 2 for AZ31B (Chapter 2) are found in Figure 13. From the room temperature simulations, two conclusions can be drawn. First, the weaker initial texture in rolled and annealed ZK10 results in lower measurements of strain anisotropy; the simulated strain anisotropy in AZ31B under these conditions was 4.70 and 2.83 under TD and RD tension, respectively. This is not terribly surprising, as the weaker texture promotes basal slip at the expense of prism slip in ZK10 as the grains are less oriented for prism slip (Figure 14). The second is that the CRSS of prism slip appears to be lower relative to basal slip in AZ31B than in ZK10, as prism slip is more active when the parameters for AZ31B are used when compared to the optimized simulations of ZK10 (Figure 7). This is observed by the much more intense nodes in the simulated textures in Figure 13, as well as the increased r-value in the TD condition and larger loading direction anisotropy (r = 1.44 and 1.13 for TD and RD tension, respectively) compared to Figure 6. These findings are repeated in the intermediate temperature regime. At the highest temperature investigated in the power law regime, there is a noticeable decrease in strain anisotropy and stalling of the texture evolution due to the emergence of <a> climb; however, the addition of <c> climb in the optimized simulations (Figure 9) lead to a further reduction in the texture evolution and r-values closer to the experimentally measured values (<1). These results are corroborated in the relative slip activity plots (Figure 14), which show that the differences in texture evolution and strain anisotropy are related to activation of climb, as in AZ31B. It should also be noted that the addition of <a> climb in the AZ31B parameters better predicts the texture evolution and strain anisotropy over glide only predictions (Figure 10). Therefore, it appears that while the activation of any climb mode better approximates the constitutive behavior of Mg, the type of dislocations which are climbing is also important. In conclusion, the optimized parameters yielded by the genetic algorithm appear to be unique to ZK10 due to the increased activation of basal slip and importance of <c> climb.

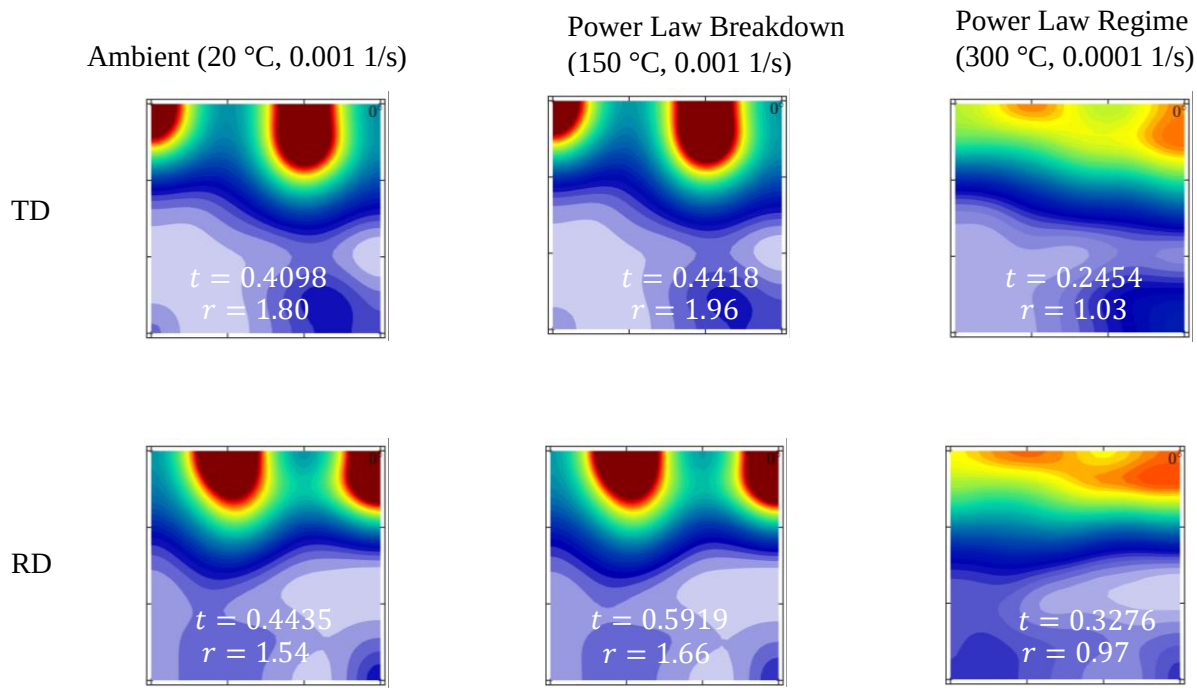


Figure 13: VPSC simulations of ZK10 using AZ31B parameters.

Ambient (20 °C, 0.001 1/s)

Power Law Breakdown
(150 °C, 0.001 1/s)

Power Law Regime
(300 °C, 0.0001 1/s)

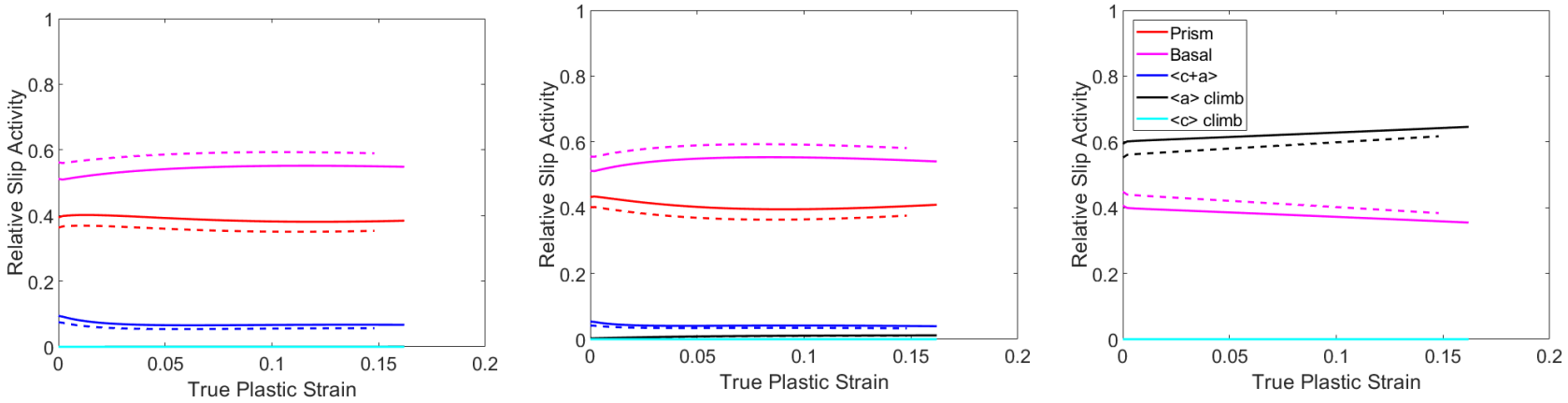


Figure 14: RSA of VPSC simulations using AZ31B parameters

*The plausibility of significant <a> and <c> climb in ZK10*

As in AZ31B, the mobile dislocation density ($\rho_{m,i}^{c}$) can be estimated using an Orowan expression to link the strain rate associated with climb ($\dot{\beta}_i$) and their average velocity ($\bar{v}_i^c$) (Equation 5)

$$\dot{\beta}_i = \rho_{m,i}^{c} b_i \, \bar{v}_i^c \qquad Equation\ 5$$

where $b_i$ is the Burgers vector length and the steady state climb velocity is given by Equation 6

$$\bar{v}_i^c = \frac{D_{sd}}{b}\left(\exp\left(\frac{\Omega\left(\bar{k}:\sigma'\right)}{k_B T}\right) - 1\right) \qquad Equation\ 6$$

where $\bar{k}$ is the Hartley tensor to resolve the applied deviatoric stress, $\sigma'$, onto the climb plane. The final equation is given as Equation 7 after rearrangement.

$$\rho_m^c = \frac{\dot{\beta}}{D_{sd}\left(\exp\left(\frac{\Omega\bar{k}:\sigma'}{k_B T}\right) - 1\right)} \qquad Equation\ 7$$

The mobile dislocation density ($\rho_m^c$) is assumed to be a fraction of the Taylor density ($\tilde{\rho}$) and Equation 8 was used to determine if the required mobile density was plausible ($\tilde{\rho} < 1$).

$$\tilde{\rho} = \frac{\rho_m^c}{\rho_T} = \frac{\rho_m^c}{\left(\frac{\bar{k}\sigma}{\alpha\mu b}\right)^2} \qquad Equation\ 8$$

where $\bar{k}$ is the maximum Hartley factor averaged over each orientation with the ZK10 texture (0.3335 for <a> climb and 0.4232 for <c> climb), $\alpha$ defines the interaction between mobile and forest dislocations ($\alpha$ = 0.25) and $\rho_T$ is the Taylor density. The results of Equation 8 are the maximum Taylor densities, as they predict the density if only each type of dislocation is present. $\dot{\beta}$ is obtained from the VPSC simulations, $D_{sd}$ is calculated from an Arrhenius expression using $D_0 = 0.0001\frac{m^2}{s}$ [27] and a lattice activation energy of 124 kJ/mol following atomistic studies of solute diffusion in Mg [39]. The resulting mobile dislocation densities were listed in Table 6. For <a> dislocations, the absolute densities are reasonable at both temperatures ( of order $10^{15}$ 1/m$^2$); however, the maximum Taylor density of <a> dislocations is predicted to be 9 x $10^{14}$ 1/m$^2$ at 150 °C, suggesting that the strain accommodation of climbing <a> dislocations is overstated by the VPSC-CLIMB simulations. This explains the unusual plateau in r-value predicted in Figure 8 by simulations fit using the MTS and Orowan expressions. This is likely due to the weaker initial texture hampering a discrimination between the effects of basal glide (the mode present during the rolling and room temperature deformation processes) and <a> climb (the mode present at higher temperatures, which does not impose texture evolution) on the texture evolution. The required <c> density is also implausibly high at 150 °C, though the climb of <c> dislocations does not accommodate significant strain under these conditions (Figure 7) and therefore is unbounded (i.e., the climb stress associated with <c> climb could be increased without significant changes to the texture evolution and r-value). Within the power law regime,

both <a> and <c> dislocations have mobile dislocation densities lower than their respective Taylor densities, suggesting that the amount of strain attributed to climb is plausible. While it may be surprising to consider significant <c> climb as their density is thought to be much lower than that of <a> dislocations, studies have observed high densities of prismatic <c> dislocations arranged into low angle boundaries [40], which may serve as sources of <c> dislocations. Pipe diffusion offers an alternative mechanism for vacancy diffusion at 150 °C due to the increased dislocation density. The self diffusivity can be modified following Frost & Ashby [27]

$$D_{sd} = \left[D_l\left(1 + \frac{10a_c}{b^2}\left(\frac{\sigma}{\mu}\right)^2 \frac{D_p}{Dl}\right)\right]c_v \qquad Equation\ 9$$

where $D_l$ is the lattice diffusivity, $a_c$ is the cross-sectional area of the dislocation core (~10 $b^2$), $\sigma$ is the appleid stress, $\mu$ is the shear modulus, $D_p$ is the pipe diffusivity estimated using constants from Frost & Ashby, and $c_v$ is the vacancy concentration at thermal equilibrium.

Table 6: Taylor and mobile dislocation densities and the required fraction for dislocations to climb for ZK10

| | <a> Climb | | <c> Climb | |
|---|---|---|---|---|
| | 150 °C, 0.001 1/s | 300 °C, 0.0001 1/s | 150 °C, 0.001 1/s | 300 °C, 0.0001 1/s |
| **Taylor** | 9.38 x $10^{14}$ | 3.63 x $10^{13}$ | 5.73 x $10^{14}$ | 2.22 x $10^{13}$ |
| **Mobile** | 6.45 x $10^{15}$ | 6.57 x $10^{12}$ | 2.21 x $10^{15}$ | 6.17 x $10^{12}$ |
| **Fraction** | 6.88 | 0.18 | 3.85 | 0.28 |

In short, it appears that the required dislocation densities for significant <a> and <c> strain accommodation are reasonable within the power law regime. At more modest temperatures, it is likely that the current simulations overpredict the accommodation via climb as <c> climb is unbounded and strain accommodation via <a> climb leads to underpredictions in the strain anisotropy.

*Potential sources of <c> dislocations*

Thus far, it has been demonstrated that 1) <c> climb is an important mechanism in ZK10 which has a unique effect on modeling the constitutive behavior (i.e., r-value) which cannot be replicated by the climb of <a> dislocations and 2) that the dislocation density required for such a mechanism to activate is plausible within the power law regime, where its strain accommodation is significant. The goal of this section is to investigate the most likely source of <c> dislocations; transmutation of <a> dislocations via twin boundary migration.

Electron backscatter diffraction has been used to measure the misorientation between neighboring grains to identify potential twin boundaries [41], as a misorientation angle of ~86° with a mirror plane of $\{10\bar{1}2\}$ (Figure 15). Note that the matrix $(\bar{1}010)$ plane is nearly parallel to the twinned $(0001)$ plane due the rotation around the $a_2$ direction.

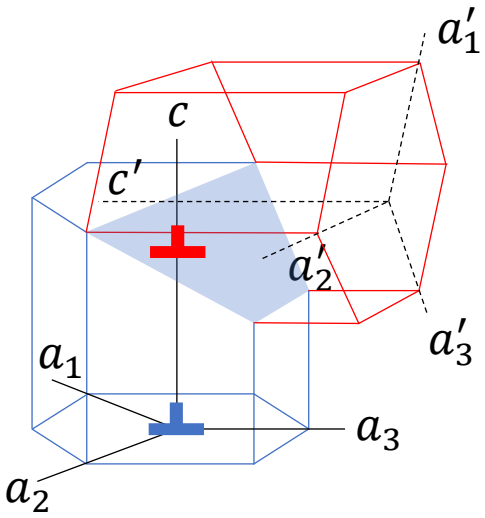


Figure 15: Orientation relationship of a matrix (blue) and twinned grain (red) after extension twinning. The blue plane is the shared $\{10\bar{1}2\}$ plane and primed directions relate to the twinned grain (unprimed directions relate to the matrix grain). The blue dislocation is an <a> dislocation in the matrix on the basal plane while the red dislocation has been incorporated into the twin boundary (blue plane) as a ½ <c+a> dislocation.

The EBSD inverse pole figure maps and EDS results of AZ31B and ZK10 are found in Appendix A, but a map of the misorientations between the neighboring grains (Figure 16) demonstrate that ZK10 has significantly more grain boundaries with the correct misorientation angle than in AZ31B (7% vs 2%, respectively). However, when the additional criterion of having a rotational axis of $[\bar{1}\bar{1}20]$ is added, it appears that there are an insignificant number of grain boundaries with a twinning orientation in either alloy (Figures 17 and 18). Therefore, the source of the <c> dislocations is still unknown. However, it should be noted that only independent $\{10\bar{1}2\} < \bar{1}011 >$ extension twinning was investigated, as the twinning transmutation reaction in [29] has only been observed in this twin system. Prior studies have noted the existence of other twinning mechanisms; namely the $\{11\bar{2}1\} < \bar{1}\bar{1}26 >$ extension twinning [85] and $\{11\bar{2}2\} < \bar{1}\bar{1}23 >$ and $\{10\bar{1}1\} < \bar{1}012 >$ compression twinning modes [86]. While these mechanisms are less common than $\{10\bar{1}2\} < \bar{1}011 >$ extension twinning, transmutation reactions may also exist and could be a potential source for <c> dislocations, though more study is required to establish these mechanisms. In addition, extension twinning can occur after compression twinning in a "double twinning" mechanism [86] which could offer additional transmutations paths for obtaining <c> dislocations.

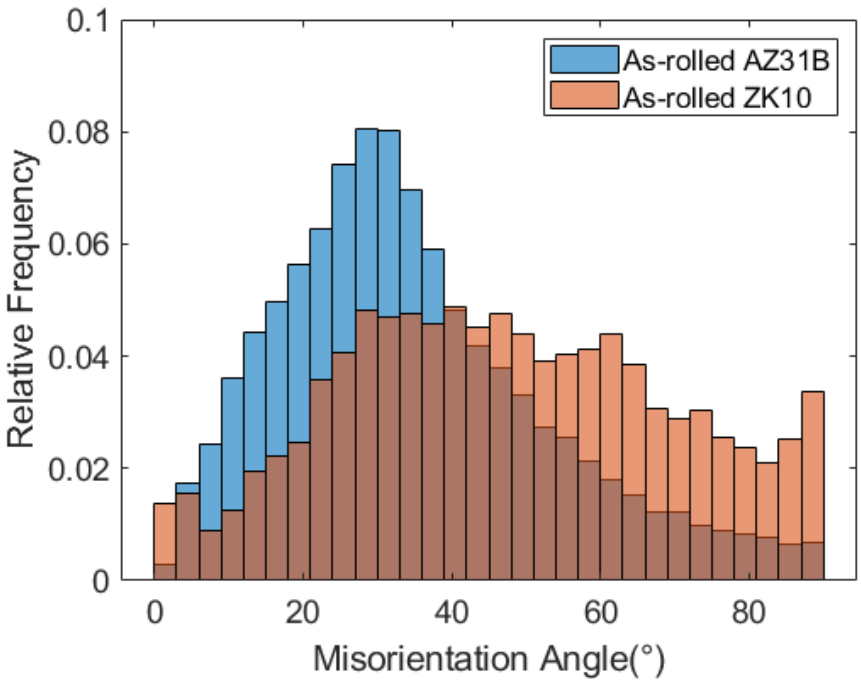


Figure 16: Fractional abundance of grain boundary misorientations of AZ31B and ZK10.

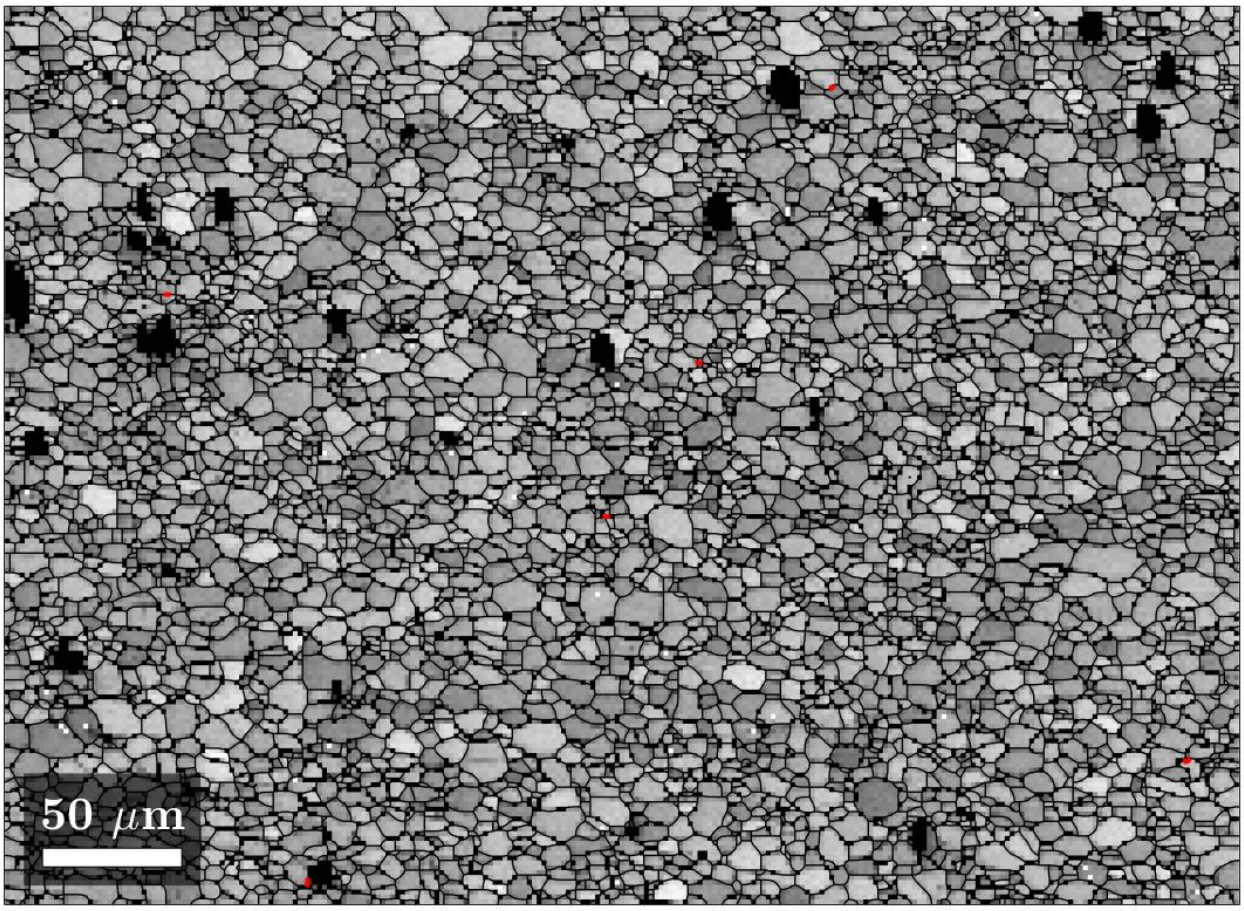


Figure 17: Band contrast image of as-rolled and annealed AZ31B. There is a complete absence of extension twin boundaries (red).

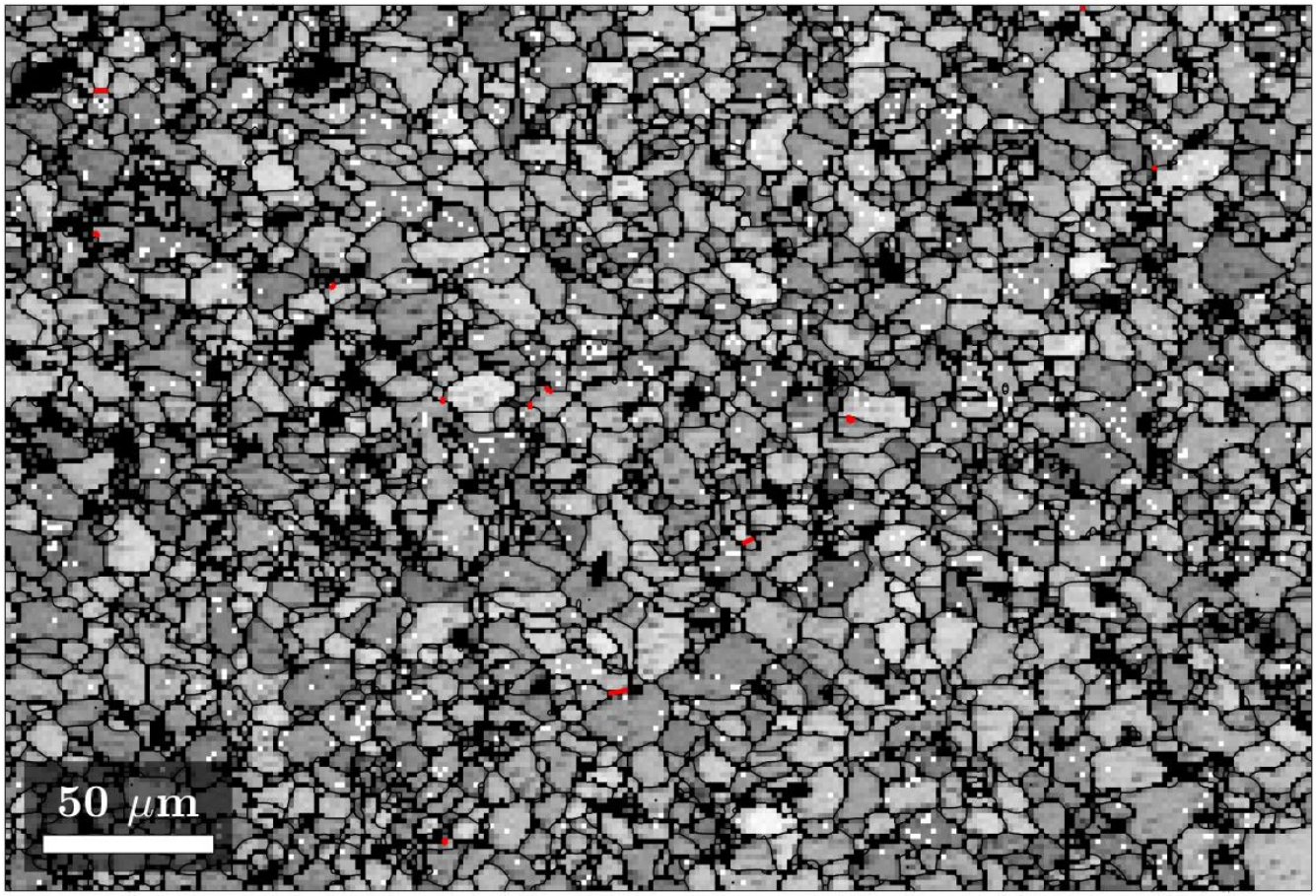


Figure 18: Band contrast image of as-rolled and annealed ZK10. Extension twin boundaries (red) are very rare.

In summary, the climb of <c> dislocations has been found to be necessary at the highest temperature and lowest strain rate observed through optimization of the dislocation kinematics (i.e., texture evolution and strain anisotropy measurements) via genetic algorithm and that the density of dislocations necessary to accommodate this strain are reasonable. However, the source of <c> dislocations in as-rolled and annealed ZK10 is currently unknown; the twinning misorientation between neighboring grains that would suggest that <a> dislocations were swept by a twin boundary and transmuted into ½ <c+a> dislocations were not observed in EBSD measurements. The outstanding question of plausible <c> densities in ZK10 will be investigated in the next chapter using x-ray line profile analysis (XLPA), which will form a comparison study between samples of as-rolled AZ31B and ZK10 (along with samples deformed at ambient and elevated temperatures).

The next chapter will attempt to answer two questions proposed by this work. First, are the necessary mobile densities predicted in AZ31B and ZK10 observable? This is particularly important for <c> dislocations in ZK10, as the Taylor densities reported here likely overestimate the real dislocation densities present in the material. Second, why is there a difference in the

propensity of different dislocation types to climb in these alloys? From the current simulations of ZK10, it appears that the climb of <c> dislocations is important, whereas the constitutive behavior of AZ31B could be modeled without invoking this mechanism. One possible reason is that differences in Burgers vector length making the jog formation of <c> climb harder, but other factors such as initial texture and chemistry differences may also play a role.

## 5- Conclusions

- The constitutive response in ZK10 was found to be controlled by climb (as in AZ31B) with a Garafalo-Sellars-Tegart model fit with the following parameters: A= $7.28x10^9$, $\alpha = 0.023$, Q = 135 kJ/mol, n = 4.81.
- The texture and strain anisotropy evolution are much more subtle in ZK10 than AZ31B due to the initial weaker texture.
- The room temperature texture evolution is controlled more strongly by basal slip than in AZ31B
    - The weaker and, hence, reduced activity of prismatic slip in ZK10 explains the lower strain anisotropy at ambient temperatures.
- Dislocation climb was found to be integral to the high temperature constitutive response of ZK10, as in AZ31B.
    - Comparisons to glide only simulations found that the strain accommodation via climb was necessary to slow the texture evolution and reduce the strain anisotropy.
        - The climb of <a> dislocations was found to activate at lower temperatures than <c> dislocations.
            - Comparisons with simulations that only included the climb of <a> dislocations demonstrated that the climb of <c> dislocations was necessary to predict the strain anisotropy in the power law regime, which was below 1.
    - Estimations of the necessary densities of <a> and <c> dislocations to accommodate the strain attributed to climb in the power law regime were plausible, as they did not exceed the Taylor dislocation density assuming that each type of dislocation was the dominant dislocation type present.
    - At lower temperatures, the densities were too large, but found to be within an order of magnitude of the Taylor density.
        - It was proposed that the unreasonable densities were a consequence of attributing too much strain to climb at the intermediate temperatures.
            - The weaker initial texture made optimizing the CRSSs and climb stresses via genetic algorithm (GA) more difficult.
- Nevertheless, less distinct changes in the texture evolution between the as-rolled and annealed material and those deformed under ambient temperature and power law conditions made GA optimization invaluable.
- Fitting of the optimized CRSSs using the mechanical threshold stress (MTS) model with a best fit exponential relation for the climb stresses and Voce hardening parameters resulted in an acceptable prediction of the flow stresses, strain anisotropy and texture over a range of temperatures and strain rates.

- The underpredicted r-values in intermediate temperatures suggests that the optimized simulation attribute too much strain to climb at lower temperatures, further demonstrating the difficulty in optimizing CRSSs and climb stresses in a weakly textured material.

**Appendix A: EBSD and EDS data of as rolled and annealed AZ31B and ZK10**

The EBSD results of as-rolled AZ31B and ZK10 are displayed in Figures A1. In AZ31B, the majority of grains have their <c> axes ((0001) planes) parallel (or nearly parallel) to the sheet normal direction. In contrast, ZK10 has few grains with their <c> axes parallel to the sheet normal direction. The <c> axes of most grains in ZK10 are inclined ~30° to the sample surface. For clarity and ease of comparison with the previous x ray diffraction work, the orientation data displayed in Figure A1 was converted into pole figures for AZ31B and ZK10 (Figure A2). Due to uncertainty between placement of the sample in the SEM and EBSD coordinate system, the textures reported had to be rotated 90° around the sheet normal direction. This rotation is also in keeping with the understanding that the spreading in the basal pole figure must be along the direction of shear during rolling (i.e., the rolling direction). These observations are replicated in the macroscopic texture collected using x-ray diffraction, suggesting that enough grains were examined to be treated as a representative sample of the bulk material. From the EDS results (Figure A3), it is clear that the large regions that failed to index were intermetallic Al-Mn particles in AZ31B. EDS results of ZK10 suggest that the zero solutions were caused by carbon-based particles. A potential source could be embedded SiC particles from the polishing pads. In both alloys, the Zn content was evenly distributed in the matrix.

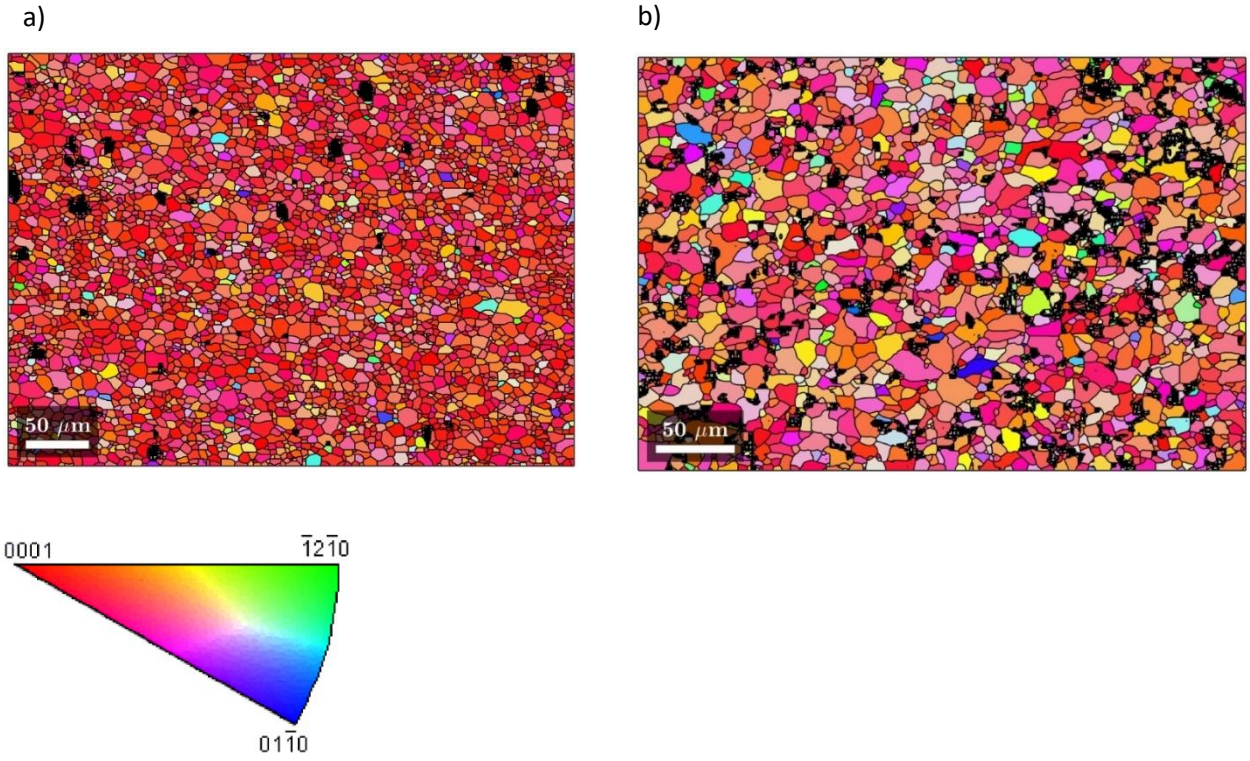


Figure A1: Inverse pole figure maps of as-rolled and annealed a) AZ31B and b) ZK10. The surface shown is the sheet normal direction (ND).

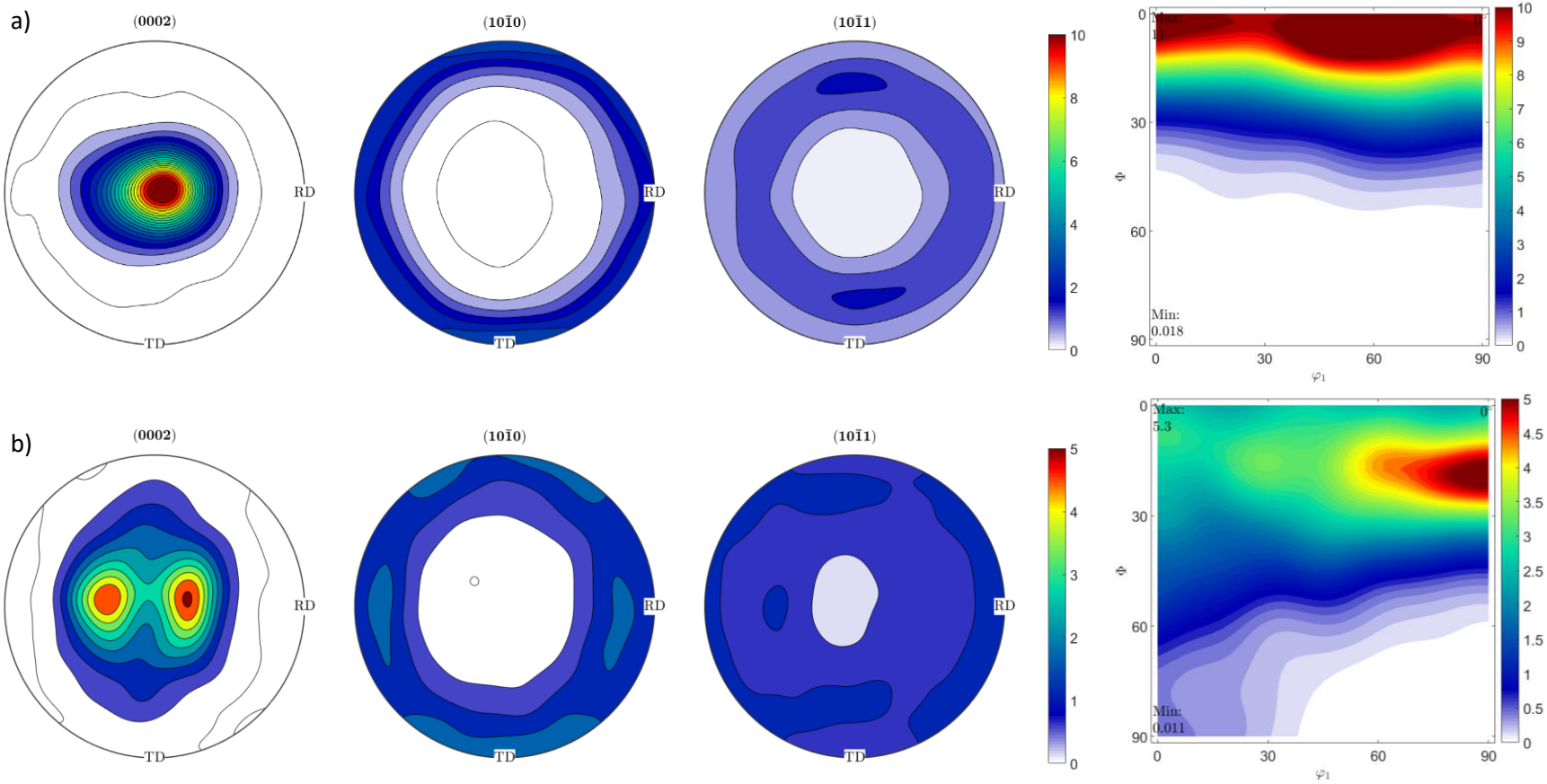


Figure A2: a) pole figure of as-rolled and annealed AZ31B and b) ZK10 rotated 90 degrees around ND in order to compare with bulk measurements of the texture via x-ray diffraction.

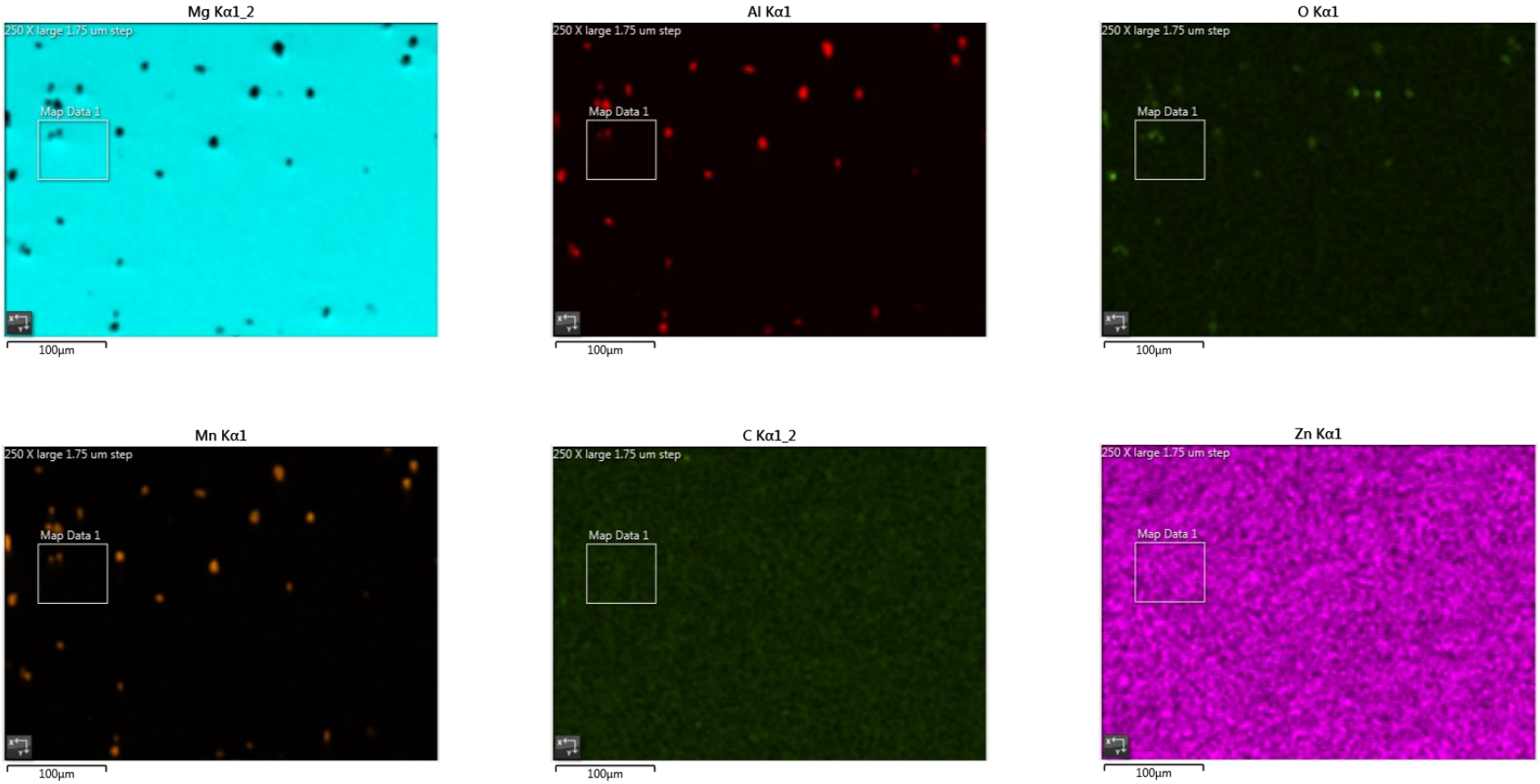


Figure A3: EDS results of as-rolled and annealed AZ31B. Note that the Zn content is nearly equally distributed between the Mg matrix and the secondary particles, which are mainly Al-Mn intermetallics. The unindexed regions in the EBSD maps are comprised mainly of these particles, with Zn oxide particles also being present.

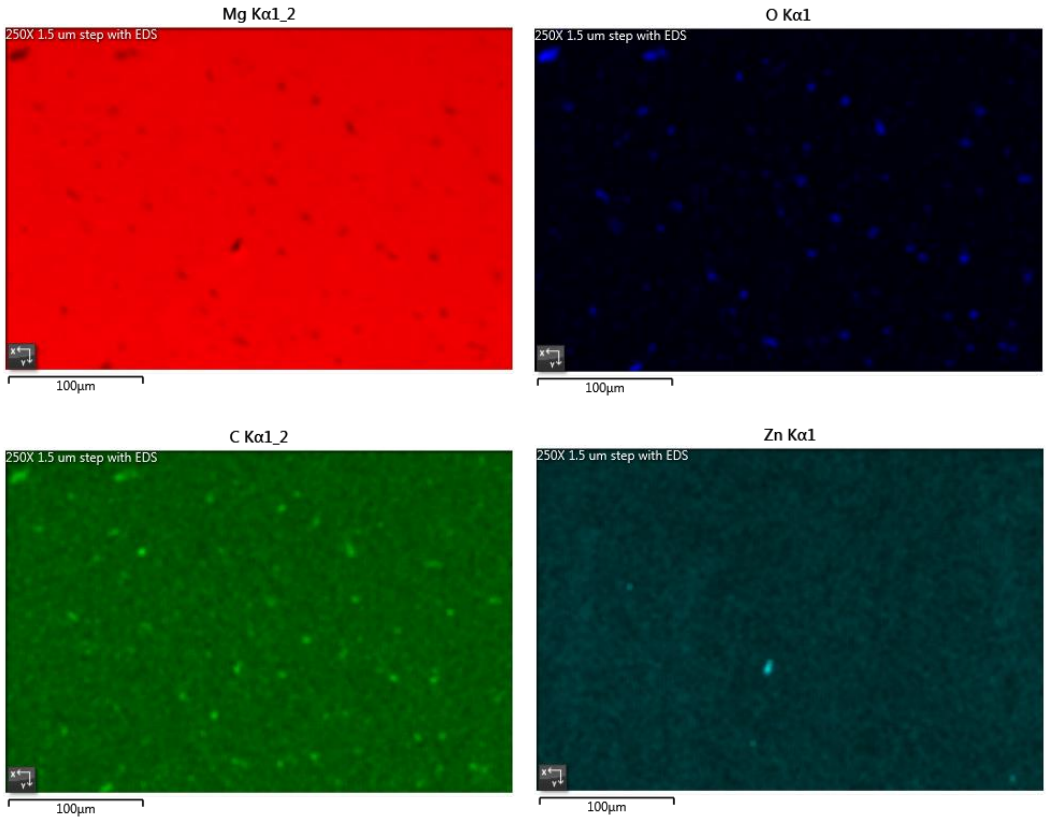


Figure A4: EDS results of as-rolled and annealed ZK10. Note that the Zn content is nearly equally distributed between the Mg matrix and the secondary particles, which are carbon and oxygen rich. The unindexed regions in the EBSD maps are likely embedded SiC particles from 800 and 1200 grit polishing steps, as they are similar sizes to the particles observed.

# Chapter 4: Analyzing the plausibility of significant climb activity through dislocation density measurements

*The work in this chapter has been performed in cooperation with co-authors Péter Nagy, Kristián Máthis, Gergely Farkas, Jenő Gubicza and Sean Agnew. Rolled AZ31B samples were uniaxially deformed and polished at the University of Virginia and analyzed by ex-situ X-ray diffraction and line profile analysis by collaborators in the Czech Republic. The contextualization of the results was done by the co-authors at the University of Virginia.*


**Abstract**

The implementation of modern, dislocation density-based models requires accurate, statistically significant knowledge of the evoltion of dislocation densitu within materials. Here, ex-situ X-ray line profile analysis (XLPA) was employed to determine the <a>, <c> and <c+a> densities of AZ31B and ZK10 samples tested in uniaxial tension from at ambient temperature and high temperatures, including those at wwhich the material undergoes power law creep. It was found that the relative density of <a> dislocations dropped with increasing ttemperature more rapidly than <c> and <c+a> in AZ31B, whereas the relative densities remained constant in ZK10. After comparison with literature data, it is suggested that both solute content and initial texture play important roles in determining the degree to which climb participates in the strain accommodation. The impacts of static recovery and pipe diffusion on the observable dislocation densities were considered. It was concluded that disparities between experimentally measured densities via XLPA and previous predictions of mobile dislocation densities likely resulted from static recovery post-test and pipe diffusion was ruled out as an imporant contributor at the temperatures and strain rates investigated (>250 °C).


## 1- Introduction

Climb is often relegated to the role of recovery assisting the rearrangement and annihilation of dislocations as the rate limiting step during “climb and glide” creep at high temperatures. However, inclusion of climb-mediated flow improves the description of texture and strain anisotropy (r-value) evolution of Mg alloy AZ31B deformed at temperatures greater than half the melting temperature [80]. This demonstration was made possible by VPSC-CLIMB, a version of the viscoplastic self-consistent crystal plasticity modeling code in which the kinematics of climb are rigorously taken into account [23]. This addition of climb into VPSC is supported by the notion that power law creep is controlled by climb (both low temperature and high temperature power law creep [27], with activation energies of pipe and lattice diffusion, respectively).The previous study which demonstrated the efficacy of climb in describing high temperature deformation suggested that climb may accommodate a significant amount of strain during power law creep and ended with a discussion of the required mobile dislocation densities, which were determined to be plausible (~$10^{14}$ $1/m^2$). This study tests this contention by experimentally measuring these densities. Few techniques exist to provide quantitative

dislocation density measurements, including transmission electron microscopy (TEM), electron backscatter diffraction (EBSD) and x-ray line profile analysis (XLPA). Each of these methods have their strengths and weaknesses. TEM, the most ubiquitous method of quantifying dislocation density, is ideal for discriminating dislocations according to their Burgers vector via the invisibility criterion [87] given images collected using multiple diffraction conditions. However, TEM typically cannot offer statistically significant results, as only a few grains are interrogated within a polycrystalline sample. In contrast, the sample preparation for EBSD is somewhat more straightforward and the amount of usable sample area is much larger, as it is not necessary for the sample to be electron transparent (i.e., there is no thickness requirement when operating in reflection). However, only the geometrically necessary dislocations (GNDs), those that accommodate the net lattice curvature, are measured via EBSD [88]. In addition, the GND density is dependent on the step size and binning parameters [89]. The final technique of interest, XLPA, has been previously used to determine the total dislocation density in pure Mg [66] by attributing the peak broadening due to strain contributions from each type of dislocation (<a>, <c> and <c+a>). Sample preparation for x-ray diffraction is very straightforward and a large volume of sample can be irradiated at a given time, thereby giving a statistically significant density of dislocations either in-situ or ex-situ. XLPA requires a highly monochromatic beam to minimize instrumental broadening and also requires assumptions be made regarding the active slip systems, as there are generally more slip modes available than experimentally measurable constraints. Nevertheless, we employ ex-situ XLPA in this study to obtain quantitative measures of dislocation density of the samples previously tested in [80] to make direct comparisons to the predicted mobile densities controlled by lattice diffusion and experimentally determined values. A related question is also addressed, namely what role does pipe diffusion play in determining the mobile dislocation densities?

## 2- Methods

*Materials and sample preparation*

Samples of rolled magnesium alloy sheet, AZ31B (Mg-3 wt% Al-1 wt% Zn-0.5 wt% Mn) 1and ZK10 (Mg-1 wt%Zn-0.2 wt% Zr), were sourced from Magnesium Elektron North America in the O and F temper, respectively. The samples of ZK10 were then annealed at 300 °C for 1 hour following Bohlen et al. [38] to recrystallize the heavily twinned microstructure and recover the O temper. Linear intercept methods conducted for AZ31B [90] and for ZK10 in the current study suggest that the average grain sizes of each material are similar (8.3 μm and 10 μm, respectively). The microstructures of each alloy are composed of equiaxed α-Mg grains with small secondary particles (Mn-rich in AZ31B [90] and Zn/Zr rich in ZK10 [38]).

*X-ray diffraction-based texture measurements*

Sample preparation for texture analysis was performed by mechanical with increasingly fine SiC paper to the sample midplane, followed by a 2 minute chemical polish in 2 vol% nital (2% nitric acid in methanol). X ray diffraction was performed with Cu $K_\alpha$ radiation in a

Panalytical X'Pert diffractometer operating at 45 kV and 40 mA in point focus using an open Eulerian cradle. The rolling direction was always oriented parallel the goniometer axis to maintain a consistent coordinate system during analysis with the mTEX toolbox of MATLAB. More details regarding texture analysis can be found in Ritzo et al. [80].

*Deformation experiments*

Uniaxial tension samples of rolled and annealed AZ31B and ZK10 were machined into the subsized ASTM E8 geometry (25 mm long, 6 mm wide and 1 mm thick gage) with the gage section parallel (rolling direction loading) or perpendicular (transverse loading) to the rolling direction. Tests were performed with an MTS Sintech 10\GL load frame to investigate various strain rates ($10^{-5}$ – $10^{-1}$ 1/s) and an ATS 3610 split furnace to vary the temperature between 20-350 °C. In the context of the current study, these tests provided the samples needed to examine the dislocation densities present in each condition tested.

*X-ray Line Profile Analysis*

Total dislocation densities of AZ31B and ZK10 sheets polished to midplane were collected through *ex-situ* X-ray line profile analysis (XLPA) using a high-resolution Rigaku RA-MultiMax9 rotating anode diffractometer with Cu $K\alpha_1$ radiation ($\lambda$ = 0.15406 nm, parallel beam dimensions: 1.5 x 0.2 mm) and at the DESY P07 beamline at the PETRA III synchrotron source in Hamburg, Germany, respectively. Peaks of the standard $\theta/2\theta$ scan were fit using a convolutional multiple whole profile (CMWP) procedure, which accounts for background intensity and broadening effects due to crystallite size and strain (i.e., dislocations) effects [91]. HCP Mg reflections from $2\theta$ = 30 – 150° were used in the calculation of area-weighted mean crystallite size and dislocation densities. The dislocation densities recovered from XLPA in the current study will be compared against literature results of ZK10 [67] and pure Mg [66] to investigate the role of static recovery and alloy chemistry and texture on the final dislocation populations.

*CMWP fitting procedure*

The full description of the CMWP profile can be found in the literature [91], but a brief summary is provided here. The shape of a Bragg peak can be represented as a convolution of size and strain effects ($I^S$ and $I^D$, respectively) (Equation 1). The broadening due to crystallite size assumes that all crystallites are spherical and follow a lognormal size distribution (see Eqs. 12 - 15 in [92] for more details).

$$I^P = I^S I^D \qquad Equation\ 1$$

Equation 1 is typically transformed into Fourier space (Equation 2) as the Warren-Averbach equation.

$$A_L = A_L^S A_L^D = A_L^S \exp\left(-2\pi^2 L^2 g^2 < \varepsilon_{g,L}^2 >\right) \qquad Equation\ 2$$

where $A_L$ are the Fourier coefficients of the diffraction profile, $A_L^S$ are the size Fourier coefficients and $A_L^D$ are the Fourier coefficients related to the lattice distortion caused by dislocations. The Fourier coefficients due to strain is written in terms of the Fourier length, $L$, the

diffraction vector, $g$, and the mean square strain $< \varepsilon_{g,L}^2 >$ [92]. At small values of $L$, the mean square strain is related to the density, the Burger vector and outer cut-off radius of dislocations ($\rho$, $b$, $R_e$, respectively, in Equation 3). [67]

Contrast factors ($C$) are included to account for the orientation of Burgers vector and line direction with respect to the diffraction vector. In polycrystalline samples, the contributions of each dislocation type to the mean square strain are averaged over all subslip systems within a given deformation mode. In XLPA, slip systems are defined in terms of the associated reflection; in Mg, there are three: basal, prismatic and pyramidal. Each slip system contains distinct populations of dislocations that can glide on each defined slip plane. For example, the prismatic$\{01\bar{1}0\}$ plane contains the <$\bar{2}$1 1 0> (<a> type), <0001> (<c> type) and <$\bar{2}$1 1 3> (<c+a> type) burgers vectors. Screw dislocations are handled separately since they do not have a defined slip plane. Table 1 has been reproduced from Dragomir and Ungár [93] to list the common slip systems. Materials with more than one slip mode and dislocation type must have their contrast factors averaged; the discussion of which can be found in [66].

Table 1: Slip systems involved in XLPA of Mg alloys (reproduced from Dragomir and Ungár [93])

| Major slip systems | Sub slip systems | Burgers vector | Slip plane | Burgers vector type |
|---|---|---|---|---|
| Edge Dislocations | | | | |
| Basal | BE | <2 $\bar{1}$ $\bar{1}$ 0> | $\{0001\}$ | <a> |
| Prismatic | PrE | <2 $\bar{1}$ $\bar{1}$ 0> | $\{01\bar{1}0\}$ | <a> |
| | PrE2 | <0 0 0 1> | $\{01\bar{1}0\}$ | <c> |
| | PrE3 | <$\bar{2}$ 1 1 3> | $\{01\bar{1}0\}$ | <c + a> |
| Pyramidal | PyE | <$\bar{1}$ 2 $\bar{1}$ 0> | $\{10\bar{1}1\}$ | <a> |
| | Py2E | <$\bar{2}$ 1 1 3> | $\{2\bar{1}\bar{1}2\}$ | <c + a> |
| | PyE3 | <$\bar{2}$ 1 1 3> | $\{11\bar{2}1\}$ | <c + a> |
| | PyE4 | <$\bar{2}$ 1 1 3> | $\{10\bar{1}1\}$ | <c + a> |
| Screw Dislocations | | | | |
| | S1 | <2 $\bar{1}$ $\bar{1}$ 0> | | <a> |
| | S2 | <$\bar{2}$ 1 1 3> | | <c + a> |
| | S3 | <0 0 0 1> | | <c> |

The measured contrast factor for each reflection is an average of the contrast factors of each dislocation type ($\bar{C}^i$) weighted by the fraction of total dislocation density ($h_i$) represented by that type (Equation 4).

$$\overline{b^2 C_{hk.l}}^m = \sum_{i=1}^{3} h_i \bar{C}^i b_i^2 \qquad Equation\ 4$$

In hexagonal crystals, the average contrast factors for sub slip systems are given by Equation 5 [93],

$$\bar{C}_{hk.l} = \bar{C}_{hk.0}(1 + q_1 x + q_2 x^2) \qquad Equation\ 5$$

where $\bar{C}_{hk.0}$ is the average contrast factor for $hk.0$ reflections, $q_1$ and $q_2$ are parameters that depend on elastic properties, $x = \left(\frac{2}{3}\right)\left(\frac{l}{ga}\right)^2$, and $a$ is the lattice parameter. Values for $\bar{C}_{hk.0}$, $q_1$ and $q_2$ have been compiled for a variety of HCP materials in the literature [93]. It is clear from this equation that it is not possible to determine the dislocation densities of every sub slip system since peak broadening experiments yield 2 independent parameters ($q_1$ and $q_2$), as collected by the whole profile fitting procedure [94]. Rather, it is possible to determine the relative fractions of <a>, <c> and <c+a> dislocations, by using physically based assumptions on slip, as pointed out by Mathis et al. [66]. These measured values of $q_1^m$ and $q_2^m$ are related to the relative fraction of each Burgers vector ($h_i$) and tabulated values of $q_1$ and $q_2$ (Equations 6 and 7, respectively)

$$q_1^m = \frac{1}{P}\sum_{i=1}^{3} h_i \bar{C}_{hk.0} b_i^2 q_1^{(i)} \qquad Equation\ 6$$

$$q_2^m = \frac{1}{P}\sum_{i=1}^{3} h_i \bar{C}_{hk.0} b_i^2 q_2^{(i)} \qquad Equation\ 7$$

where $P = \sum_{i=1}^{3} h_i \bar{C}_{hk.0}^{i} b_i^2$.

The procedure for selecting the correct fractions of dislocation Burgers vectors and calculating densities is presented in [66] and summarized here. The number of possible dislocation types is reduced by determining the slip systems that are most likely to activate. All possible solutions, which must satisfy the criteria that $\sum_{i=1}^{3} h_i = 1$ and $h_i \geq 0$, create a matrix of solutions and are evaluated for <a>, <c> and <c+a> Burgers vectors to give a range of possible solutions. Dislocation contrast factors are calculated using an equation similar to Equation 4 over every sub slip system (i.e., edge and screw variations for each slip system), which is then used to calculate the total dislocation density in Equation 3.

*Dislocation density evolution during straining and post-test annealing*

The total dislocation density of sample of Mg is comprised of three major populations of dislocations: <a>, <c> and <c+a> as classified by their Burgers vectors. The rate of change in the total density is dependent on the generation and annihilation of these three populations which can be formalized by the Kocks-Mecking equation (Equation 8)[95]

$$\frac{\partial \rho_i}{\partial \gamma} = \left(k_1^i \sqrt{\rho_i} - k_2^i \rho_i\right) \qquad Equation\ 8$$

where the rate of dislocation generation for dislocation population $i$, $\frac{\partial \rho_i}{\partial \gamma}$, is influenced by the storage ($k_1^i\sqrt{\rho_i}$) and dynamic recovery ($k_2^i \rho_i$) of dislocations. $k_1^i$is a material constant and $k_2^i$ is a function of strain rate and temperature. A consequence of using ex-situ methods to interrogate the dislocation densities of high temperature deformed samples is that the effects of static

recovery must be accounted for. It is possible to extend the Kocks-Mecking equation to include the effects of static recovery using the chain rule (Equation 9)[96]

$$\frac{\partial \rho_i}{\partial \gamma}\frac{\partial \gamma}{\partial t} = (k_1^i\sqrt{\rho_i} - k_2^i\rho_i)\frac{\partial \gamma}{\partial t} - r_i \qquad Equation\ 9$$

where $\frac{\partial \gamma}{\partial t}$ is the applied shear strain rate and $r_i$ is the static recovery rate. The role of static recovery will be of interest for to potentially reconcile any discrepancies between ex-situ XLPA experimental results of the current study with: 1) in-situ observations from the literature and 2) the predicted mobile dislocation densities of the prior study [80]. An effective model for predicting the static recovery rate was reported by Kohnert and Capolungo [96] (Equation 10) for microstructures with randomly distributed dislocations

$$r_i = \frac{\kappa_1 D}{b}\rho^{\frac{3}{2}}\sqrt{1-\frac{\rho}{\rho_o}}\left[\exp\left(\left(\frac{\kappa_2 \mu b^4\sqrt{\rho}}{k_B T}\right)\left(\left(1-\frac{\rho}{\rho_o}\right)^{-\frac{1}{2}}-1\right)\right)-1\right] \qquad Equation\ 10$$

where $\kappa_1$ and $\kappa_2$ are constants of order unity, $\rho_o$ is the initial density and $\rho$ is the current density. The evolution of dislocation density over time was obtained by a forward finite difference method using a time step ($h$) of 0.01 seconds (Equation 11).

$$r_i = \frac{\partial \rho_s}{\partial t} = \frac{\rho_{i+1}-\rho_i}{h} \rightarrow \rho_{i+1} = \rho_i + h\frac{\partial \rho_s}{\partial t} \qquad Equation\ 11$$

The temperature dependence of the shear modulus, μ, was incorporated using the Varshni equation [97] (Equation 12) with fitted parameters of $\mu_0$ = 17.41 GPa, $D_0$ = 6.31 GPa and $T_0$ = 597.58 K using shear modulus data from Garlea, Radovic and Liaw [55] from temperature between room temperature and 450 °C.

$$\mu = \mu_0 - \frac{D_0}{\exp\left(\frac{T_0}{T}\right)-1} \qquad Equation\ 12$$

Values of $\kappa_1$ and $\kappa_2$ will be approximated by modeling the static recovery of ZK10 by comparing in-situ and ex-situ dislocation densities measurements. An attempt to predict the static recovery behavior of other Mg alloys will then be performed using these values to calculate the pre-recovery <a> dislocation density.

Equation 9 encapsulates the major dislocation interactions that influence the density evolution of each population. Mechanistically, these terms describe the result of glide and climb within the sample. As summarized in Beyerlein & Tomé [44], many mechanisms exist to describe the rate of generation, classified as those that generate loops such as Frank-Read sources or those that aid in the propagation of existing dislocation line length (e.g., cross slip). Dislocations which are attempting to glide are pinned at several locations along their length due to obstacles. It is assumed that the dominant obstacle is other dislocations, therefore the spacing between dislocations, $\sqrt{\rho_i}$, determines the rate of dislocation storage.

Dynamic recovery describes how quickly dislocations annihilate each other during deformation. The reduction of overall energy by removing two dislocations of line length $l$ provides the driving force for recovery ($\Delta G_{total} \sim -2\left(\frac{1}{2}\mu b^2\right) l$); non-conservative climb is one possible mechanism that allows dislocations to overcome obstacles and annihilate. By the same logic, the annihilation of dislocations in static recovery is also controlled by climb, as Peach-Koehler forces between the oppositely signed dislocations in close proximity to one another can provide the impetus to climb. If the observed densities of each dislocation type (<a>, <c> or <c+a>), or their fraction of the total density, change dramatically as a function of temperature, it suggests that the propensity for each dislocation type to climb may differ.

*Revisiting the importance of pipe diffusion in predicting the mobile dislocation density*

The aforementioned predictions of the mobile dislocation densities by Ritzo et al. [80] assumed that climb was mediated by vacancy diffusion through the lattice, which is valid when the dislocation densities are low. Under circumstances of higher dislocation densities (or lower temperatures), the effects of pipe diffusion cannot be ignored. Following Kohnert et al.[96], Equation 13 gives an estimate of the velocity ratio due to pipe and lattice diffusion-controlled climb

$$\frac{v_p}{v_l} \approx \rho b^2 \frac{D_p}{D_l} \qquad Equation\ 13$$

where $D_p$ and $D_l$ are the diffusivities of pipe and lattice diffusivities of vacancies. Using this expression, conditions under which the climb due to pipe diffusion exceeds that due to lattice diffusion can be estimated.

In addition to temperature, microstructure can also have an important role in diffusivity. Real microstructures are heterogeneous with densely packed regions of dislocations (cell walls) with sparse interiors. Thus, pipe diffusion may be active even under conditions where lattice diffusion is expected to dominate. The effect of pipe diffusion on the necessary dislocation density is demonstrated by calculating the strain rate due to climb ($\dot{\beta}$) (Equation 14) as a combination of strain accommodation in the grain interior ($\dot{\beta}_i$) and near boundary ($\dot{\beta}_b$) regions if it is assumed that each region abides by an Orowan expression.

$$\dot{\beta} = (1 - f_w)\dot{\beta}_i + f_w\dot{\beta}_w = (1 - f_w)\rho_i b v_l + f_w \rho_w b v_p \qquad Equation\ 14$$

The dislocation densities of the cell interior ($\rho_i$) and wall ($\rho_w$) relate to the total density ($\rho$) via Equation 15

$$\rho = (1 - f_w)\rho_i + f_w \rho_w \qquad Equation\ 15$$

where $f_w$ is the volume fraction of the sample occupied by the cell walls. Following the model of Mughrabi [28], the dislocation densities within the cells and in the walls are given by Equations 16 and 17.

$$\rho_i = \frac{f_w}{1 - f_w}\rho \qquad Equation\ 16$$

$$\rho_w = \frac{1 - f_w}{f_w}\rho \qquad Equation\ 17$$

It is assumed that lattice diffusion is controlling in the cell interior and pipe diffusion is controlling near the boundary and that $\rho_i < \rho < \rho_w$. The final expression is obtained by substituting Equations 13,16 and 17 into Equation 14 (Equation 18).

$$\dot{\beta} = f_w \rho b v_l + (1 - f_w)\rho b \left(\rho b^2 \frac{D_p}{D_l}\right) v_l \qquad Equation\ 18$$

Equation 18 will be used to test if pipe diffusion can explain any potential discrepancies between the predicted mobile dislocation densities and dislocation densities. VPSC simulations yielded suitable values for the climb strain rate, $\dot{\beta}$, and the threshold climb stress (within the climb velocity due to lattice diffusion [49]) and the total average density from XLPA measurements (after static recovery is accounted for) is used for $\rho$.

## 3- Results

*Initial texture measurements of AZ31B and ZK10*

Both AZ31B and ZK10 were predominantly basally textured, which is typical of rolled Mg alloys (Figure 1); however, the basal planes of ZK10 are tilted more strongly toward the rolling direction. It has been previously suggested that this texture component is the result of compression twinning or <c+a> slip [98]. A significant portion of basal planes in ZK10 also seems to have rotated into the plane of the sheet material (a signature of extension twinning as the <c> axis rotates 86° during twinning). Differences in initial texture can play in the selection of active slip modes and the subsequent multiplication and annihilation rates of dislocation populations.

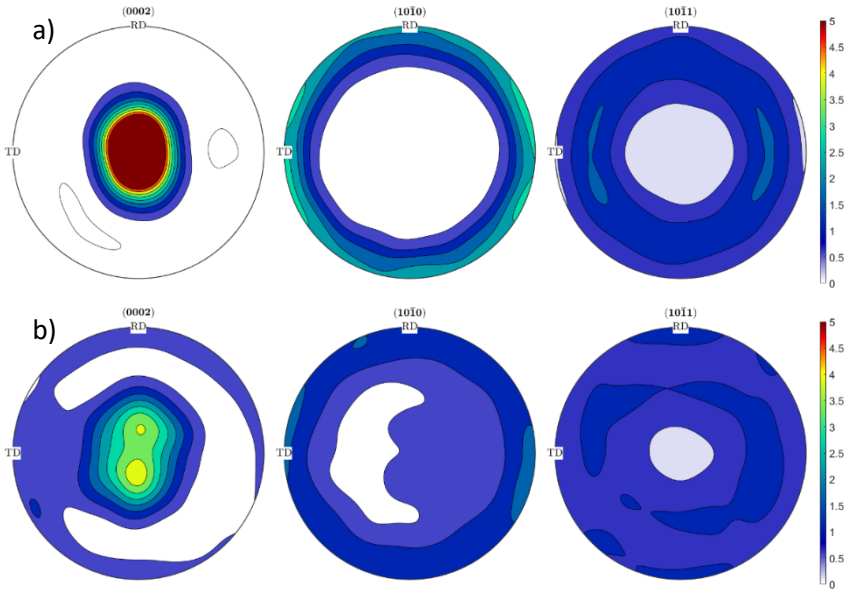


Figure 1: Initial textures for a) AZ31B and b) ZK10

*Dislocation density comparison via XLPA experiments*

The total densities of each dislocation type determined by XLPA are listed in Table 2. As expected, the densities of both alloys fell below the sensitivity limit of laboratory x-ray diffractometer-based XLPA ($<10^{13}$ 1/m$^2$) when in the annealed condition. In the deformed samples, the total dislocation density was found to decrease as the temperature increased. <a> dislocations were the dominant population for most conditions tested, consistent with understanding that basal and prism slip have the lowest critical resolved shear stresses (CRSSs) of any available glide mode in Mg alloys and should therefore lead to increased multiplication of <a> dislocations. At the highest temperature and lowest rate tested, <a> dislocations ceased to be the dominant population in AZ31B presumably due to increased annihilation. At higher temperatures, the velocity of climbing dislocations is increased due to more rapid lattice diffusion. As mentioned previously, these climb events can occur both during the test, as well as post-test due to static recovery.

Table 2: Total dislocation densities reported by Burgers vector in AZ31B and ZK10

| Deformation conditions | <a> Density [$10^{13}$ $m^{-2}$] | <c> Density [$10^{13}$ $m^{-2}$] | <c+a> Density [$10^{13}$ $m^{-2}$] | Total Density [$10^{13}$ $m^{-2}$] |
|---|---|---|---|---|
| **AZ31B** | | | | |
| **As-annealed** | <1 | <1 | <1 | <1 |
| **20 °C, $10^{-3}$ 1/s, TD** | 22.0 ± 3.2 | 0.0 ± 0.0 | 5.4 ± 0.8 | 27.0 ± 4.0 |
| **250 °C, $10^{-3}$ 1/s, TD** | 2.6 ± 0.6 | 0.6 ± 0.2 | 0.8 ± 0.2 | 4.0 ± 1.0 |
| **350 °C, $3\times10^{-4}$ 1/s,** | 0.3 ± 0.1 | 0.9 ± 0.3 | 1.8 ± 0.6 | 3.0 ± 1.0 |
| **ZK10** | | | | |
| **As-annealed** | <1 | <1 | <1 | <1 |
| **20 °C, $10^{-3}$ 1/s, TD** | 16.0 ± 3.0 | 1.1 ± 0.2 | 4.2 ± 0.8 | 21.2 ± 4.0 |
| **150 °C, $10^{-3}$ 1/s, TD** | 13.0 ± 3.3 | 0.8 ± 0.2 | 1.9 ± 0.5 | 15.9 ± 4.0 |
| **300 °C, $10^{-4}$ 1/s, RD** | 3.3 ± 0.7 | 0.05 ± 0.1 | 0.6 ± 0.1 | 4.4 ± 1.0 |

<c> dislocations were not present in significant numbers at room temperature in AZ31B, yet their density increased with temperature. Two possible explanations exist for this phenomenon: 1) the CRSS of prism <c> glide is highly temperature sensitive and 2) <c+a> dislocations may undergo thermally activated decomposition at higher temperatures, which can result in <c> dislocation formation [11], [42]. The latter is more likely as any strain accommodated by prism <c> slip can also be accommodated by easy basal <a> slip, as both slip modes are equally well oriented for in-plane tension, though Stohr and Poirier [99] and Edelin and Poirier [100] observed <c> dislocations to glide climb under c-axis compression of single crystals at high temperature.

AZ31B also had a surprising density of <c+a> dislocations (20% of the total density) despite <c+a> slip having a high CRSS at room temperature. However, it is clear that density of <c+a> dislocations decreased at elevated temperatures. Like <a> dislocations, <c+a> dislocations may climb, which may explain the decrease in density compared to room temperature. This possibility was not investigated in the previous study as it was assumed that the contribution of climbing non <a> dislocations to the strain rate was insignificant due to the abundance of <a> dislocations in Mg alloys (specifically AZ31B). This assumption was justified in the current study. Reduction of the <c+a> density can also be achieved by decomposition of <c+a> dislocations into <a> and <c> components. In summary, it appears that <a> dislocations more readily climb and annihilate than <c> and <c+a>, as their density decreases much more quickly in AZ31B at elevated temperatures.

In contrast, the total dislocation density in ZK10 was lower at room temperature and the decline in density was more gradual than in AZ31B (Figure 2). The more striking difference was in the dislocation populations present. The density of <a> dislocations (Figure 2b) in ZK10 does not decrease as rapidly as in AZ31B, though the evolution in the total density still mirrors the evolution of the <a> density, as they comprised the majority of all dislocations present in ZK10.

<c> dislocations are present during room temperature tension of ZK10, in contrast to AZ31B. This is consistent with the findings of Li et al.[40], who found that a significant density of <c> dislocations were present after room temperature tension of an extruded ZK60 sample, and Agnew and Duygulu [20], who found <c> dislocations to be very uncommon after tension in rolled AZ31B. The increase in <c> dislocation density in ZK10 at room temperature could potentially be caused by twinning transmutation of ½ <c+a> dislocations from <a> dislocations and their subsequent decomposition into <a> and <c> dislocations.

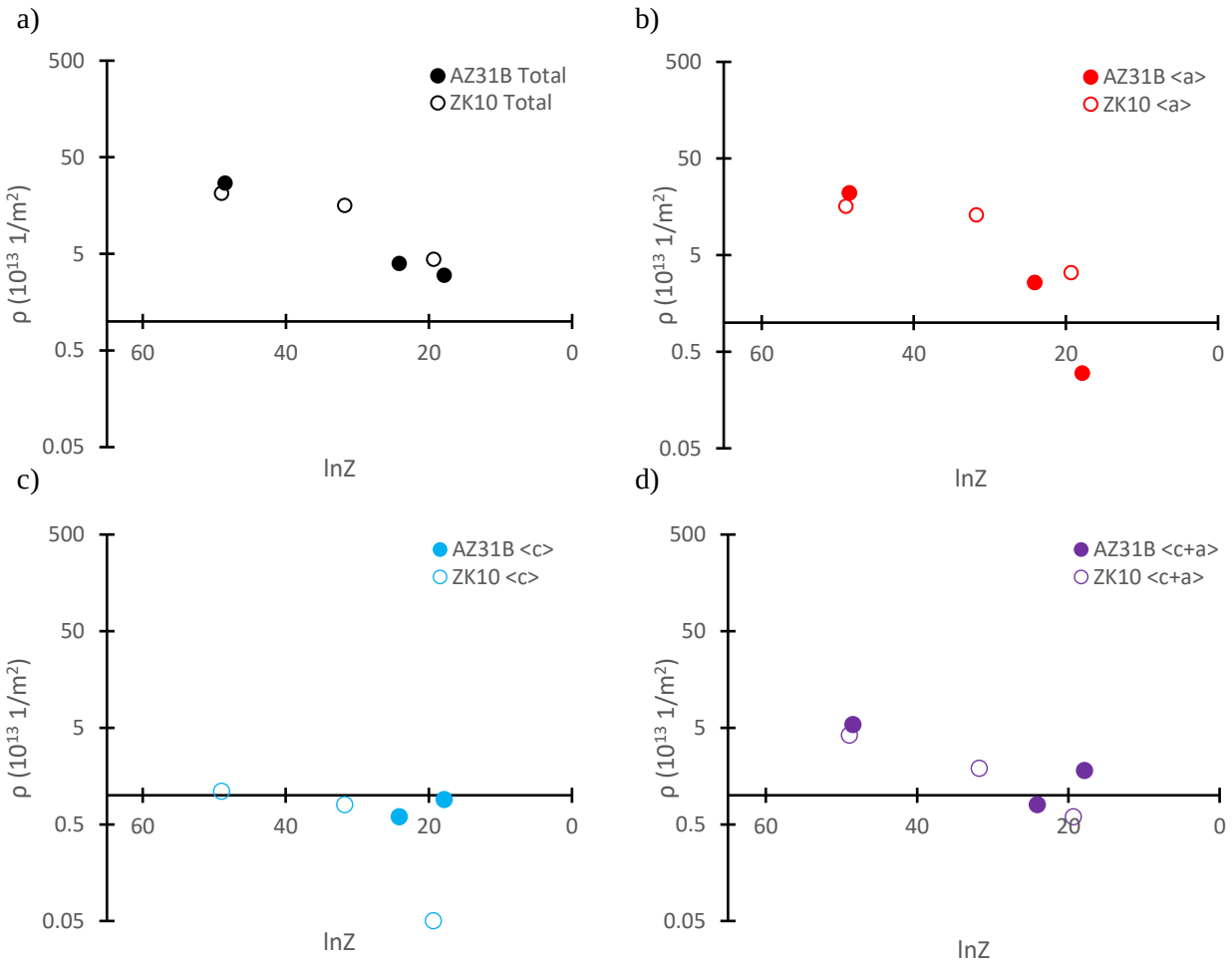


Figure 2: The a) total, b) <a>, c) <c> and d) <c+a> dislocation densities for AZ31B and ZK10. $Z = \dot{\varepsilon} \exp\left(\frac{Q}{RT}\right)$ where $\dot{\varepsilon}$ is the applied strain rate, $Q$ is the macroscopic activation energy for lattice diffusion, $R$ is the ideal gas constant and $T$ is the temperature

A sizable fraction of dislocations in ZK10 are <c+a> type at room temperature. The decline in <c+a> density was more rapid in ZK10 than AZ31B, which may suggest that <c+a> dislocations are more mobile in ZK10 and can participate in annihilation more readily than in AZ31B. The two possible explanations for these differences are initial texture and alloy chemistry. The former will influence the Hartley factor that resolves the applied stress onto the

climb mode and the latter will affect the energy barrier required for a dislocation to climb and annihilate. The relative contributions of each of these factors will be pursued further in the discussion.

*Comparing predicted mobile dislocation densities with XLPA densities*

Experimentally measured dislocation densities were compared to predictions of the necessary mobile, climbing densities required to match the texture evolution and strain anisotropy (Figure 3). It is clear that the predicted climbing dislocations densities are significantly higher than those experimentally observed (but within one order of magnitude). However, it must be noted that the densities measured by XLPA include all of the dislocations that were not annihilated during the test (upon activation of dynamic recovery) or post-test as the sample sits at temperature before being removed from the furnace (static recovery), though every attempt was made to remove the samples within 30 seconds of the end of testing. The XLPA densities thus underpredict the steady state density present during deformation. Several factors could contribute to the disparity between the XLPA (static recovery) and predicted climbing densities (pipe diffusion). Furthermore, the predicted mobile densities displayed in Figure 3 assume that lattice diffusion controls the climb velocity. This assumption may underestimate the velocity at lower temperatures where the dislocation density is higher. If the contributions of pipe diffusion are significant, then the necessary dislocation densities will decrease. This will also be visited in the discussion section.

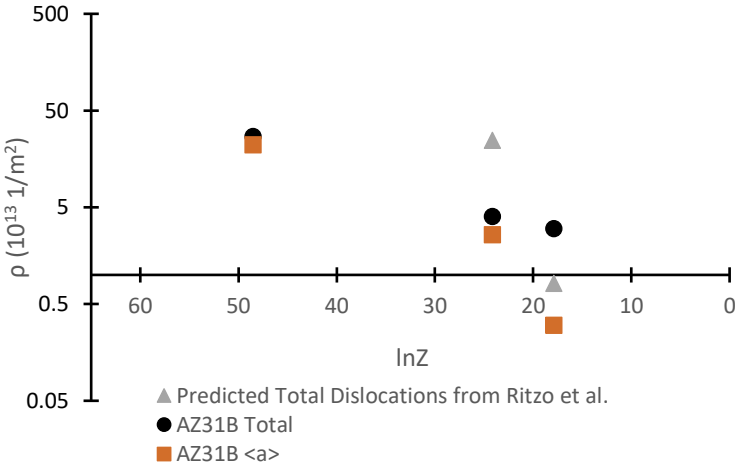


Figure 3: A comparison between the experimentally observed total and <a> dislocation densities with the predicted mobile density from Chapter 1. The mobile density was doubled to account for screw <a> dislocations which would be observed in XLPA, but do not contribute to climb.

The results of the current measurements suggest that alloy chemistry and texture may play a role in ex-situ populations of <a>, <c> and <c+a> dislocations. These results are compared to literature results of pure Mg measured ex-situ after tensile testing [66] and ZK10 measured during in-situ tension testing [67] (Table 3).

Table 3: Samples compared in the current study

| Sample | ex-situ or in-situ | Chemistry | Initial Texture | Source |
|---|---|---|---|---|
| Pure Mg | ex-situ | Mg | As-cast (Untextured) | Máthis et al. [66] |
| AZ31B | ex-situ | Mg – 3 wt% Al-1 Zn – 0.2 Mn | Strong basal | Current |
| ZK10 | ex-situ | Mg – 1 Zn – 0.5 Zr | Split basal | Current |
| ZK10 | in-situ | Mg – 1 Zn – 0.5 Zr | Strong basal | Ha et al. [67] |

The dislocation densities of the 4 samples listed in Table 3 are compared in Figure 4. The total dislocation densities of all samples are approximately the same at ambient temperature (high values of lnZ) and all densities decrease with increasing temperature and decreasing strain rate. However, the total density of the ZK10 sample tested in-situ is significantly higher than those tested ex-situ, regardless of texture or alloy chemistry. This offers evidence to the notion that static recovery may explain why the current XLPA measurements are so low. The fractions of each dislocation type were also calculated to show relative changes due to differences in multiplication and annihilation rates. All samples are overwhelmingly <a> type (<70% of all dislocations) after tension at ambient temperatures. The fraction of <a> dislocations in pure Mg and AZ31B decreases as deformation conditions approach the power law regime, while both samples of ZK10 have a consistent fraction of <a> dislocations. <c> dislocations make up a small proportion of the total density, but its fraction appears to increase in most samples tested, particularly AZ31B. <c+a> dislocations follow a similar trend as the <a> fraction, as their proportions are elevated in pure Mg and AZ31B at higher temperatures whereas they are constant in both ZK10 samples.

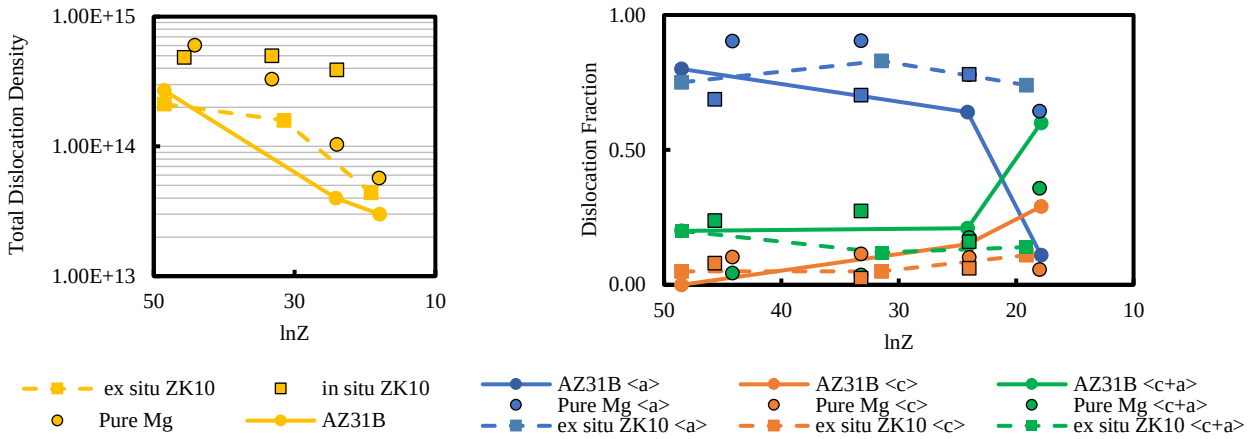


Figure 4: a) Total dislocation densities of pure Mg, AZ31B and ZK10, b) Dislocations categorized by fraction present. Lines represent data collected in current set of experiments, discrete circles were from [66] and discrete squares were taken from [67].

## 4- Discussion

*Understanding the propensity of dislocations to climb*

Changes in the fraction of an individual dislocation type can only occur due to a relevant adjustment in generation and annihilation rates at higher temperatures. Dislocation generation can occur via three main mechanisms: 1) dislocation multiplication due to strain accommodation through glide, 2) thermal decomposition reactions or 3) transmutation reactions due to twin boundary migration through preexisting dislocations [29]. For AZ31B, generation is likely due to multiplication since there are relatively few preexisting twin boundaries for transmutation to occur; thermal decomposition reactions are limited to <c+a> dislocations. Decomposition and transmutation reactions also reduce the density of specific types of dislocations (in the current situation, <c+a> and <a> dislocations, respectively). A more general method of dislocation reduction occurs from annihilation, which is the reaction of two dislocations with opposite Burgers vectors. Annihilation is assisted by dislocation climb to overcome obstacles. Insignificant levels of strain are accommodated in this case, as the contributions of each climbing dislocation cancel out. Dislocation density reduction due to strain accommodating climb and glide is assumed to be insignificant with respect to recovery since the associated glide will increase the dislocation density more than the incidental annihilation.

Annihilation is the likely mechanism to influence the fraction of dislocations for two reasons. First, the dislocation density of every type of the currently studied AZ31B (except <c> dislocations, which experienced a small increase) decreases with increasing temperature (Figure 2 and Table 2). The decreases in <a> and <c+a> density are much larger than the increase in <c> density (2.3 x $10^{14}$ 1/$m^2$ combined reduction in <a> and <c+a> density with a $10^{13}$ 1/$m^2$ increase in <c> density from room temperature to 350 °C). Other mechanisms for density reduction (transmutation and decomposition) result in the generation of <c> dislocations, which suggests

that most of the <a> and <c+a> dislocations no longer present were annihilated. Secondly, the fraction of <c+a> dislocations increases with temperature, suggesting that the reduction of <a> dislocations is faster than <c+a> dislocations. This is in agreement with previous VPSC simulations of AZ31B that suggested that the strain accommodation of climb increases with increasing temperature and decreasing strain rate [80]. These simulations assumed that only the climb of <a> dislocations (and therefore annihilation) was significant during deformation. The large reduction in <a> fraction also implies that <a> dislocations are more likely to annihilate than other types. This reasoning can also be applied to pure Mg.

ZK10 differs from AZ31B as twinning transmutation is a viable mechanism for dislocation generation since ZK series alloys have been observed to have large amounts of twin boundaries masquerading as grain boundaries [41]. Surprisingly, the transmutation of <a> dislocations into ½ <c+a> dislocations does not explain the trend in <a>, <c> and <c+a> fraction with temperature and strain rate. Significant numbers of transmutation reactions would decrease the amount of <a> dislocations and increase the amount of <c+a> dislocations. The number of <c> dislocations would also be expected to increase due to secondary decomposition reactions in <c+a> dislocations. However, the total density of dislocations decreases with increasing temperature as well as the density of each dislocation type (Table 2 and [67] for the ex-situ and in-situ ZK10 samples, respectively). Again, annihilation via climb can explain the reduction in dislocation densities; however, it is further suggested that the climb of all dislocation types (<a>, <c> and <c+a>) must occur to keep the relative amounts of <a>, <c> and <c+a> dislocations consistent. VPSC-CLIMB simulations of ZK10 have suggested that climb strain accommodation increases with increasing temperature. Unlike AZ31B, where the climb of non <a> dislocations was assumed to be insignificant, simulations representative of the highest temperature required significant climb (~10% of strain) of <c> dislocations to approach the low r-values determined experimentally (~0.7) (Chapter 3). This is in qualitative agreement with the XLPA results present here, as <c+a> climb has a straining direction intermediate of that <a> and <c> climb and therefore could be used to describe the reduction in r-value.

*The role of Burgers vector on climb mode selection during recovery*

It is apparent that recovery occurs at different rates between dislocation types in pure Mg and AZ31B (Figure 4). As these tests were performed ex-situ, it is impossible to separate the effects of dynamic and static recovery; however, the readiness of each dislocation type to undergo dynamic recovery can be inferred from its energetic barrier to climb. The climb of all dislocation types is mediated through the thermally activated nucleation and migration of jogs, which climb ahead of the whole dislocation line. Vacancy emission and absorption occur through these jogged regions and the velocity of a climbing dislocation under lattice diffusion is given by Equation 19 [101]

$$v \approx 2\pi \frac{D_l^{sd}}{x} \frac{\boldsymbol{k}:\boldsymbol{\sigma}\, a^3}{k_B T} \qquad Equation\ 19$$

where $D_l^{sd}$ is the self diffusivity, $\boldsymbol{k}$ is the Hartley tensor, $\boldsymbol{\sigma}$ is the applied stress tensor (during deformation) or the stress field imposed from another, nearby dislocation (during static

recovery), $a$ is the lattice parameter (3.21 Å) and $x$ is the jog separation distance (with an associated jog formation energy, $U_j$ - Equation 20).

$$x = a \exp\left(\frac{U_j}{k_B T}\right) \qquad Equation\ 20$$

While the self diffusivity is solely dependent on the atomic species present (assuming lattice diffusion), the jog spacing is not guaranteed to be independent of dislocation type. Very simply, the energy required to generate a dislocation segment of length $l$ is dependent on its Burgers vector length, given as $\sim\frac{1}{2}\mu b^2 l$. Without including the energy needed to climb the dislocation the distance of the jog height, it is clear that the jog spacing is likely different between <a> and <c+a> dislocations, which would affect their climb velocities. It is presently assumed that the jog formation energy is similar to that of a kink. Though the mechanisms controlling the cross-slip of screw dislocations and the climb of edge dislocations are distinct, they are both thermally activated processes at the relevant temperatures controlled by the nucleation of short dislocation segments that advance ahead of the whole dislocation line. The major difference is that kinks (in the case of cross-slip [77]) remain in the slip plane whereas jogs (during climb [101]) leave the slip plane. Following Caillard and Martin [101], the jog formation energy is given by Equation 21, assuming the Eshelby model for kink energy holds for jog formation,

$$U_j = 0.943 d (E_0 \Delta E)^{\frac{1}{2}} \qquad Equation\ 21$$

where $d$ is the height of the jog, $E_0$ is the energy required to form the kink (similar to the self energy of the dislocation ($\sim\frac{1}{2}\mu b^2$) per length) and $\Delta E$ is the energy needed for the dislocation to climb between low energy sites. For the Eshelby model, this is given by Equation 22 [101]

$$\Delta E = \frac{d b \sigma_c}{3.08} \qquad Equation\ 22$$

where the threshold stress needed to climb is used in place of the Peierls stress for glide.

Ratios of jog formation energies between different dislocation types can be formed from Equation 21 after substituting in Equations 22 (Equation 23).

$$\frac{U_{j,<a>}}{U_{j,<c+a>}} = \sqrt{\left(\frac{d_a b_a}{d_{c+a} b_{c+a}}\right)^3 \left(\frac{\sigma_{c,a}}{\sigma_{c,c+a}}\right)} \qquad Equation\ 23$$

Each dislocation type has an associated burgers vector, jog height and critical climb stress. The first two quantities are known from crystallography. The lengths of the Burgers vectors are known ($b_a = 3.21$ Å , $b_c = 5.21$ Å and $b_{c+a} = 6.11$ Å). For the <a> dislocation, the relevant spacing is ~c/2, as the dislocation must climb from the basal plane to the middle plane of atoms in the HCP unit cell (the $(0002)$ plane) to a stable lattice position. The climb distance for <c> and <c+a> dislocations is more complicated, but the interplanar spacing of the climb plane is a reasonable approximation, as a stable atomic position must exist. The spacing ($d$) of the prism

$((10\bar{1}0))$ and pyramidal II $((11\bar{2}2))$ planes is given by Equation 24 and found to be 2.78 and 1.37 Å, respectively.

$$\frac{1}{d_{hkil}^2} = \frac{4}{3}\left(\frac{h^2 + hk + k^2}{a^2}\right) + \frac{l^2}{c^2} \qquad Equation\ 24$$

Assuming that the climb stress for <c> and <c+a> dislocations are 1.6 and 2 times that of <a> dislocations (which is most likely a conservative estimate as this is simply the ratios of <c> and <c+a> burgers vectors to <a> dislocations), the energetic barrier for jog formation in <a> climb is ~33% of that in <c> dislocations and 70% of <c+a> climb. The nature of these differences is the larger interplanar spacing of the prism planes relative to the basal planes and the increased required stress needed to activate <c> and <c+a> climb.

This result is independent of accounting for pipe diffusion near the jog, as Equation 19 could be replaced by Equation 25 which is dependent on the formation energy of jog pairs (Equation 26)

$$v = \frac{4\pi}{ln\frac{\Delta x}{a}} \frac{D_l^{sd}}{X} \frac{k\sigma\Omega}{k_B T} \exp\left(-\frac{\Delta U_{sd}^{(l,p)}}{2k_B T}\right) \qquad Equation\ 25$$

where $\Delta x$ is the mean free path of a vacancy diffusing within a dislocation core, $X$ is the mean free path of a jog after nucleating from a pair and $\Delta U_{sd}^{(l,p)}$ is the energy difference between lattice and pipe self diffusion.

$$X = a \exp\left(\frac{U_{jp}^c}{2k_B T}\right) \qquad Equation\ 26$$

Here, the relevant energetic barrier is that which is required to nucleate a jog pair at the critical spacing. This is simply the energy to generate 2 jogs and the interaction between them (Equation 27). The form of the jog pair formation energy is identical to that of a single jog ($a\sqrt{\mu(h_a b_a)^3 \sigma_{c,a}}$), except that $a = \left(\frac{2(0.943)}{\sqrt{6.16}} - \left(\frac{1}{2\pi}\right)^{\frac{1}{2}}\right)$ for a jog pair and $a = \left(\frac{(0.943)}{\sqrt{6.16}}\right)$ for a single jog.

$$U_{jp}^c = 2U_j - (hb)^{\frac{3}{2}}\left(\frac{\mu\sigma_c}{2\pi}\right)^{\frac{1}{2}} \qquad Equation\ 27$$

The climb velocity is also dependent on the resolved stress on the dislocation, $\sigma_c = \boldsymbol{k}:\boldsymbol{\sigma}$. During deformation, the climb stress of <a> dislocations has been found to be ≤ 30 MPa within the power law regime (the exact value being dependent on the rate) [80]. The climb stresses of <c> and <c+a> dislocations were not investigated, but they were unnecessary to model the high temperature deformation of AZ31B, suggesting that they did not accommodate significant strain (≤5%). This suggests the resolved stress, $\sigma_c = \boldsymbol{k}:\boldsymbol{\sigma}$, needed to activate <c> and <c+a> climb is higher than that of <a> dislocation. The Hartley tensors of <c> and <c+a> dislocations, as

mentioned previously, are influenced by the initial texture of the alloy. In the rolled basal texture of AZ31B, the majority of grains have orientations similar to Figure 5 (where the c axis is parallel to the sheet normal direction). Basal <a> dislocations are most likely to be well oriented during in-plane tension since their Burgers vector can be aligned with the loading direction ($k = 1$), whereas <c> dislocations cannot climb under in-plane tension as the applied stress acts on the half plane. <c+a> climb represents an intermediate case where the Hartley factor is $0 \leq k \leq 1$. In contrast, ZK10 has a weaker split texture where the majority of <c> axes are tilted between ~25-30° along the rolling direction as well as orientations tilted at very large angles (~70-90°) away from the normal direction. Applying the same calculations as those devised in Chapter 2 to estimate the Schmid and Hartley tensors of as – rolled AZ31B results in average Hartley factors of 0.33, 0.42 and 0.23 for <a>, <c> and <c+a> dislocations respectively (compared to 0.55, 0.29 and 0.18 in AZ31B, respectively). The addition of these diverse orientations could open up opportunities for <c+a> and <c> climb to activate, which could explain the more consistent dislocation fractions observed in ZK10.

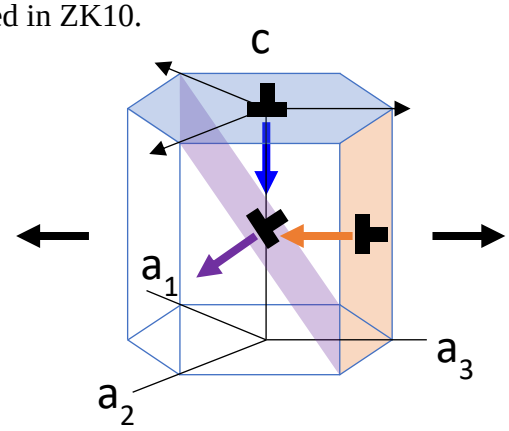


Figure 5: Climb directions of the most well aligned dislocations of the: <a> (blue arrow), <c> (orange arrow) and <c+a> (purple arrow) type under in-plane tension

*The role of alloy chemistry on climb mode selection*

In the absence of alloying effects, <c> and <c+a> climb are far less likely to occur as the formation of jogs in <c> and <c+a> dislocations seems more difficult. The previous methodology to estimate the jog formation energy was based on the assumption that climb can be treated analogously to cross slip [101]. The role of alloy chemistry can be interrogated by extending this proposal to include insights from past studies on solute effects on cross slip. Such a comparison ignores the fact that climb requires the diffusion of vacancies, but will serve to estimate the jog pair formation energy (Equation 27). Solute additions have been shown to have several effects on the ease of <a> cross slip (prism slip [77]). At low concentrations, solutes act as heterogeneous nucleation sites for kinks, leading to a lower energetic barrier and subsequent softening ([58], [102], [103]). At higher concentrations (> 0.5 at% for 500-600 K), the softening due to enhanced kink nucleation is overwhelmed by the increased resistance to kink migration (i.e., solute strengthening). Alloying additions of Al, Mn and Zn have been shown to harden the cross slip of <a> dislocations relative to pure Mg, with Al having particularly deleterious effects [72]. These effects also appear to be dislocation type dependent, following studies on the effect of alloying elements on <c+a> cross-slip barrier between pyramidal I and II planes ([12], [14],

[81]). The cross-slip barrier of <c+a> dislocations has also been found to be lower in ZK10 (represented as Mg-1 wt% Zn) than in AZ31B (represented as Mg-3Al-1Zn) [14]. If the treatment of climb using the principal equations derived for cross-slip remain appropriate, this suggests that all climb modes will be harder in AZ31B than in ZK10 due to higher solute content in the matrix. This may explain why only <a> dislocations appear to climb in AZ31B in contrast to ZK10 which appears to have approximately equal climb of <a>, <c> and <c+a> dislocations. If all climb modes are hardened by the presence of solutes equally, then only the softest mode will activate to accommodate strain which cannot be carried by glide. Conversely, if all climb modes are less hardened, each climb mode is more likely to activate in addition to more strain being accommodated by climb.

*Quantification of recovery and pipe diffusion in ex-situ XLPA*

From the above comparison between the studied samples and literature, it appears that alloy chemistry (and to a lesser extent, initial texture) has an important role in the activation of climb during high temperature deformation. However, it does not explain why experimental dislocation densities fall far below predicted mobile densities needed for climb to accommodate the deformation previously attributed to it. Therefore, two possible explanations remain: recovery and pipe diffusion. The role of static recovery in the discrepancy between in-situ and ex-situ ZK10 was tested by applying Equation 10 to the densities obtained by Ha et al. [67] and data interpolated between 2 datapoints measured ex-situ to obtain a reasonable estimate of the density at 250 °C (Table 2). The in-situ densities for 250 °C tests were taken as the initial densities ($\rho_o$) and values of $\kappa_1$ and $\kappa_2$ were fit to match the ex-situ densities obtained in the current study (Table 4). As there are many combinations of $\kappa_1$ and $\kappa_2$ which could explain the discrepancy between in-situ and ex-situ measurements, initial guesses were taken from Kohnert and Capolungo [96] ($\kappa_1 = 6$ and $\kappa_2 = 0.6$).

Table 4: Parameters employed in assessing the role of static recovery in ZK10

| | $\kappa_1$ | $\kappa_2$ | In-situ density ($10^{13}$ 1/m$^2$) | | Ex-situ density ($10^{13}$ 1/m$^2$) |
|---|---|---|---|---|---|
| 250 °C | | | Initial | Post recovery | |
| <a> | 3.77 | 0.37 | 31.0 | 5.5 | 5.5 |

It is clear that including static recovery can remove the disparity between the in-situ and ex-situ samples with parameters of order unity [96]. The values of $\kappa_1$ and $\kappa_2$ listed in Table 4 were used calculate the pre-static recovery density of AZ31B since the compositional differences between ZK10 and AZ31B are relatively minor (1 wt% Zn and 0.5% Zr vs 3% Al, 1% Zn and 0.3% Mn) as they are both dilute Mg alloys.

Static recovery was also estimated in AZ31B by Equation 10 by nonlinear optimization to find the initial <a> density that would result in the densities obtained through XLPA assuming a 5-minute post-test recovery period. As in ZK10, it is clear that static recovery can greatly decrease the <a> density at both 250 and 350 °C (Table 5) when compared to the densities

obtained through XLPA and the densities predicted in Ritzo et al. (multiplied by 2 to account for the presence of both edge and screw dislocations that would be observed in XLPA). In the lower temperature condition observed, static recovery significantly reduces the disparity between XLPA and predicted mobile densities, but cannot fully eliminate it; however, this is not true for the 350 °C sample, which had a density about 3 times of the minimum density under after a 5 minute anneal. This is in agreement with the understanding that lattice diffusion (and therefore climb assisted recovery) will be much more active at 350 °C than 250 °C.

In the previous calculation, the values of $\kappa_1$ and $\kappa_2$ were assumed to be independent of alloy chemistry, yet the veracity of this assumption is unknown as it has been suggested that climb may be alloy chemistry dependent, which could imply that recovery should also be dependent on solute content. This assumption was tested by a final thought experiment, which fit $\kappa_1$ and $\kappa_2$ to Equation 10, assuming that the initial, pre-static recovery density was twice the minimum density of climbing <a> dislocations predicted by [80]. As before, the values determined by Kohnert and Capolungo were used as initial guesses. Under these circumstances, it was found that the static recovery could explain the disparity between the predicted minimal number of climbing dislocations and those experimentally determined via XLPA at 250 °C using larger values of $\kappa_1 = 11.2$ and $\kappa_2 = 1.12$, respectively. At 350 °C, the minimum total climbing dislocation density predicted from VPSC results cannot be reached after a 5 minute post-test static recovery period. These calculations suggest that the disparity between the experimental densities measured by XLPA and those predicted previously could possibly be attributed to static recovery using reasonable values of $\kappa_1$ and $\kappa_2$, but more study must be done to rigorously understand the influence of alloy chemistry on recovery. In conclusion, these results suggest that dislocation density measurements of samples tested at high temperature should be performed in-situ to avoid the effects of static recovery from the sample resting at temperature post-test.

Table 5: Determining the role of static recovery in AZ31B of <a> dislocations

| T (°C) | Predicted total densities ($10^{13}$ 1/m$^2$) | XLPA densities ($10^{13}$ 1/m$^2$) | Predicted total densities after static recovery ($10^{13}$ 1/m$^2$) |
|---|---|---|---|
| Using $\kappa_1$ and $\kappa_2$ from ZK10 | | | |
| 250 | 71.5 | 2.6 ± 0.6 | 8.47 |
| 350 | 1.11 | 0.3 ± 0.1 | 0.32 |
| Using $\kappa_1$ and $\kappa_2$ fit from AZ31B data at 250 °C assuming the initial density is the total predicted density of climbing dislocations (11.23 and 1.123, respectively) | | | |
| 250 | 71.5 | 2.6 ± 0.6 | 2.55 |
| 350 | 1.11 | 0.3 ± 0.1 | 0.03 |

The calculations performed in this section assume that all dislocations are free to annihilate and ignores the potential role of geometrically necessary dislocations (GNDs) in slowing recovery, as GNDs cannot be annihilated due to the plastic strain gradient imposed on the crystal. Kohnert and Capolungo [96] developed a model to describe this phenomenon as well (Equation 24)

$$\frac{\partial \rho_s}{\partial t} = \frac{\kappa_1 D}{b}(\rho - \rho_{GND})^{\frac{3}{2}} \sqrt{\frac{1-\frac{\rho}{\rho_o}}{1-\frac{\rho_{GND}}{\rho_o}}} * \left[ \exp\left( \left( \frac{\kappa_2 \mu b^4 \sqrt{\rho - \rho_{GND}}}{k_B T} \right) \left( \left( 1 - \frac{\rho}{\rho_o} \right)^{-\frac{1}{2}} - 1 \right) \right) - 1 \right] \quad Equation\ 24$$

where $\kappa_1$ and $\kappa_2$ are constants of order unity, $\rho_o$ is the initial density, $\rho$ is the current density and $\rho_{GND}$ is the GND density. This is likely important near grain boundaries, where GNDs are known to congregate due to higher compatibility stresses [104]. The higher stresses near the boundaries have also been proposed to activate <c+a> slip, even at room temperature [17]. If the GND density for <c+a> dislocations comprises a large fraction of all <c+a> density, this may offer another explanation for why <c+a> dislocations appear more resistant to annihilation in the XLPA results with increasing temperature.

*Pipe diffusion calculations*

While it is possible that the static recovery could explain the lower than expected dislocation densities obtained by XLPA, it is worthwhile to investigate the role of pipe diffusion into the prediction of mobile dislocation densities due to uncertainties in the values of $\kappa_1$ and $\kappa_2$. The ratio of pipe to lattice controlled climb velocity using activation energies and pre-exponential factors from Frost and Ashby [27] for Mg was evaluated using Equation 13. Pipe diffusion is only important when the dislocation density is greater than $10^{14}$ 1/m$^2$. It is unlikely for the homogeneous dislocation distribution to attain this level of density at elevated temperatures (even when accounting for static recovery, the XLPA results suggest average dislocations densities of approximately $10^{13}$ -$10^{14}$ 1/m$^2$); however, most microstructures are heterogeneous and have regions of much higher local densities (i.e., subgrain boundaries). Therefore, pipe diffusion may provide an avenue to accommodate significant climb near these subgrain boundaries and reduce the need for such high climbing dislocation densities. Outside subgrain boundaries, pipe diffusion quickly becomes irrelevant with decreasing dislocation density (Figure 6).

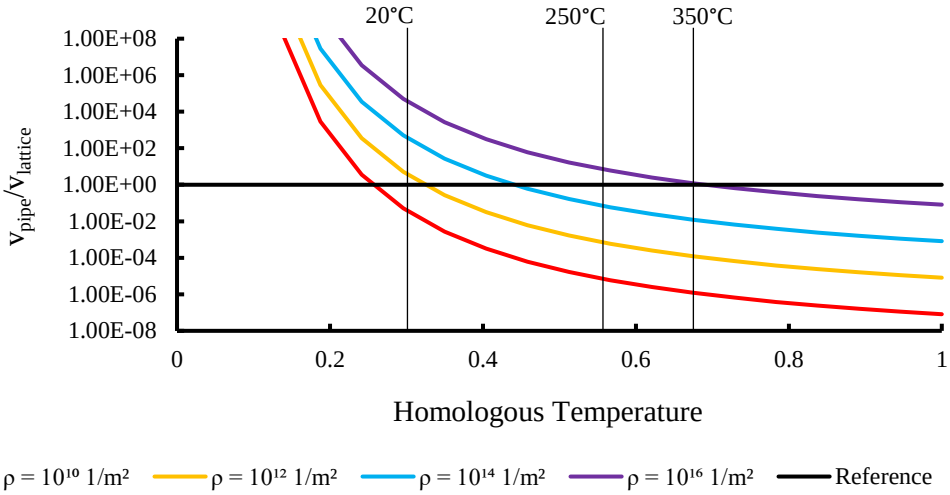


Figure 6: The effect of dislocation density on the ratio of pipe diffusion and lattice diffusion-controlled climb in Mg

The results of Equation 18 shown in Figure 7 demonstrate that the disparity between the VPSC-CLIMB predicted density and the XLPA density could not be explained by pipe diffusion. Simply put, at the temperatures of interest, pipe diffusion is not rapid enough to lead to reduced densities when the cell wall and interior densities are modeled using equations from Mughrabi [28]. On the whole, it appears that any benefit to including pipe diffusion is largely offset by the reduced pathways to transport vacancies ($\rho b^2$) relative to the bulk material.

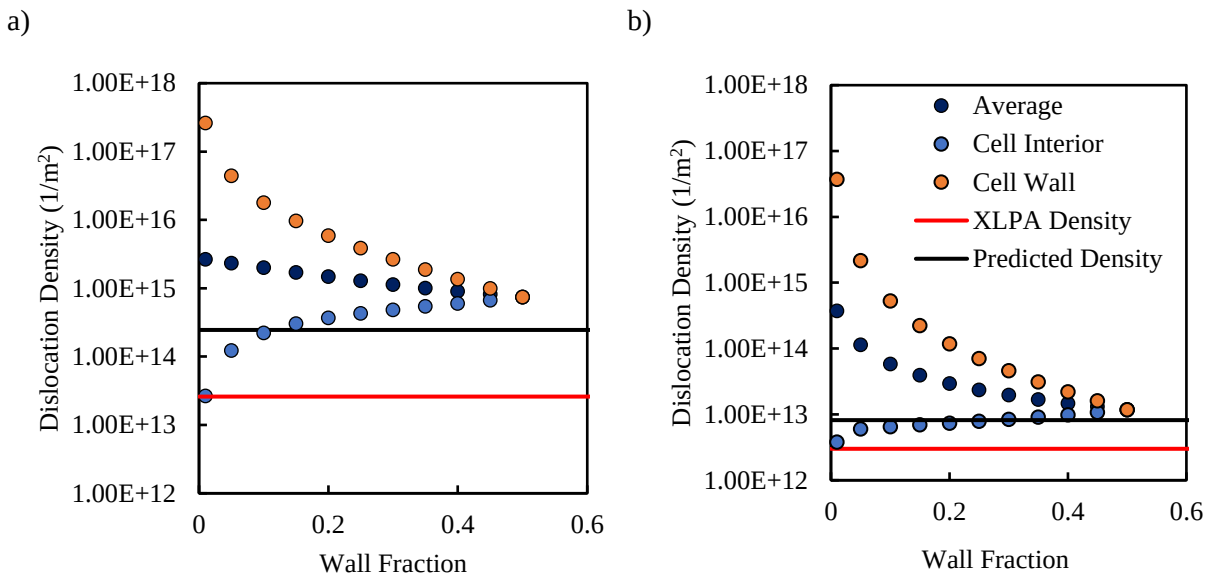


Figure 7: Required average dislocation densities needed to accommodate the deformation attributed to climb in [80] assuming a heterogeneous dislocation distribution as described in [28] at a) 250 °C and b) 350 °C. The densities in the cell wall and interior are plotted to show the relationship between the wall fraction and total dislocation density. The predicted densities are shown by solid black lines and the experimentally determined XLPA densities are in red.

## 5- Conclusions

- An overwhelming fraction of dislocations in X-ray diffraction line profile analysis (XLPA) were found to be <a> type. This was independent of initial texture and alloy chemistry.
- As the temperature of deformation is increased, the density of dislocations decreases.
    - The climb and annihilation of <a> dislocations appears to be favored in AZ31B as their density drops more rapidly than <c> and <c+a> with increasing temperature.
    - The same could not be said for ZK10, which had consistent ratios of <a>, <c> and <c+a> dislocations at all temperature observed.
- The differing evolution of <c> density between the two alloys was attributed to potential differences in dislocation-dislocation and dislocation-twin boundary reactions.
    - The <c> density increase with increasing temperature in AZ31B was attributed to thermally activated decomposition of <c+a> dislocations [42].
    - The initial <c> density in ZK10 was attributed to transmutation of <a> dislocations after being swept by migrating twin boundaries during annealing [29]
    - The <c> density decrease with increasing temperature in ZK10 was attributed to climb and annihilation.
- The increase in the fraction of <c+a> dislocations in AZ31B is possibly due to the difficulty of climb of <c+a> dislocations relative to <a> dislocations, as well as a possible effect of strain gradients associated with geometrically necessary dislocations in the vicinity of grain boundaries.

- Previously published *in-situ* XLPA measurements of ZK10 had higher total densities compared to ex-situ measurements of pure Mg, AZ31B, and ZK10, suggesting that the quantification of static recovery could be important in these measurements.
    - Alloy chemistry may play an important role in determining the activation of the various climb modes as the current ZK10 and in-situ ZK10 results had similar fractions of <a>, <c> and <c+a> dislocations.
- The <a> dislocation densities measured during ex-situ diffraction are about one order of magnitude lower than estimates of the mobile dislocation densities needed to accommodate the fraction of strain attributed to dislocation climb.
    - Static recovery is presented as a possible explanation and was able to fully explain discrepancies in the case of the highest temperatures considered (350 °C).
    - At lower temperatures, static recovery improved the fidelity between predicted mobile dislocation density and those measured by XLPA, but could not fully eliminate the disparity.
- Pipe diffusion was found to have little impact upon the results, due to the relatively high temperatures and relatively low dislocation densities involved.

# Chapter 5: Practical application of a climb-enabled Visco-Plastic Self Consistent crystal plasticity model through forming limit curve predictions


## Abstract

Ductility is highly path dependent and often quantified via forming limit curves (FLC). Here, the Marciniak – Kuczyński (M-K) method is employed with a climb-incorporated viscoplastic self-consistent (VPSC-CLIMB) model to investigate the role of climb under a variety stress straining conditions typical of sheet metal forming. It was found that climb can be a significant strain carrier outside of uniaxial tension within the power law regime and its inclusion led to higher formability when compared to glide only predictions of VPSC. Climb is naturally more rate sensitive than glide and its activation improves the macroscopic rate sensitivity, promoting more stable flow. Plastic instability occurs when the reduction in climb strain accommodation results in decreased rate sensitivity in the defect, leading to strain localization. Outside of the power law regime, strain accommodation via <c+a> slip appears to become more important, especially in nonuniaxial loading conditions where significant <c> axis strains must be accommodated.


## 1- Introduction

Magnesium and its alloys are coveted in engineering applications that require low weight and high bending resistance and flexural rigidity (i.e., the automotive and aerospace industries [2]). Due to its hexagonal closed packed structure (HCP), room temperature formability is often limited in comparison with cubic (face centered (FCC) or body centered (BCC)) metal alloys. It has already been demonstrated that it is more challenging for Mg to satisfy the Von Mises criterion for ductile failure [8] due to its insufficient slip modes at room temperature. The ductility of Mg has been found to increase dramatically with increasing temperature [19]. Two main factors are at work here: increased strain rate sensitivity (SRS) (which improves post uniform elongation) ([51], [69]) and lower applied stresses to initiate fracture. The former is a direct consequence of the mechanisms activated (Chapter 2). One possibility for the increased SRS is strain accommodation by climb due to its higher innate rate sensitivity ($m_c = 1/3$) with respect to glide ($m_g < 1/20$). A recent study by some of the co-authors highlighted the potential role of climb as a significant strain carrier during uniaxial tension in the power law regime [80]. From this previous study, it was clear that <a> climb was competitive with <c+a> slip, as they both can accommodate <c> axis strains; however, VPSC simulations showed that <c+a> slip gives rise to a sort of texture evolution that is not present in experimental observations. However, the strain path dependence on this competition is unclear, as climb is expected to be less active during in-plane equibiaxial stretching (having similar boundary conditions to through thickness compression) whereas <c+a> slip is more well-suited to accommodate such strain. Recent texture measurements of Bohlen et al. [37] of samples subjected to plane strain and equibiaxial

stretching were collected which poses an opportunity to investigate the strain path dependence of the competition between climb and <c+a> slip.

The ultimate goal of the aforementioned study by Bohlen et al. was to investigate the role of texture and alloy chemistry on Mg alloy sheet formability using forming limit diagrams (FLDs), as introduced by Keeler [30], and to describe the general, biaxial straining conditions with varying ratios of minor to major strain (known as the strain path) where an unstable neck forms in the sheet. The forming limit curve (FLC), which defines the strain conditions where failure occurs.The main features can be determined by probing 3 key strain paths: uniaxial straining (characteristic of *drawing* operations), plane strain (an intermediate condition which induces a minimum in formability) and equibiaxial *stretching*. Typically, these conditions, among others, are experimentally determined using a battery of limiting dome height tests using samples of varying geometries following Hasek [31]. The number of strain paths required make accurate quantifications of the FLD a very time consuming and costly endeavor for a single material. Understanding the constitutive behavior from ambient conditions to the power law regime is even more time consuming and costly, due to the equipment required and the multiple temperatures and strain rate conditions which must be taken into account.

The Marciniak-Kuczyński (M-K) method [32] is a common means of predicting a FLC and assumes that a defect is present in the material at the start of deformation (defined as a region of smaller thickness or lower strength relative to the bulk) and enforces equilibrium and compatibility between the defect and the bulk regions for a given strain path. An iterative approach is used to calculate the deformation within the defect until its strain rate is much higher relative to the bulk strain rate, leading to plastic instability. The M-K method requires a material yield description to calculate the unknown strain and stress components from the boundary conditions. A good review of the historically used yield descriptions can be found here [25], but crystal plasticity models are the preferred material yield descriptions as they can account for the effects and evolution in crystallographic texture, strength and strain anisotropy and distinct work hardening behaviors of the individual slip and twinning modes.

Neil & Agnew [25] implemented a viscoplastic self-consistent (VPSC) crystal plasticity model into the M-K framework to predict the forming limit of rolled AZ31B. Their results demonstrated that a more random texture had positive effects on the formability. However, several gaps exist in their initial work. Their VPSC model could not account for the effects of dislocation climb, which have been previously shown to accommodate significant amounts of strain under uniaxial tension [80]. Although their work incorporated the observed increases in strain rate sensitivity, the addition of climb would provide a more natural, mechanistic explanation for the increased rate sensitivity that occurs during high temperature deformation. In addition, their reported texture evolution shows an extraneous <c+a> texture component not observed experimentally in uniaxial tension from previous simulations [80] and experimental measurements performed in the intervening years ([36], [37]). Finally, additional experimental FLDs generated for Mg alloys within the power law regime provided an opportunity to investigate the effect of climb on other strain paths, which has not been studied previously.

The current study focuses on a comparison between glide-only predictions and novel climb-incorporating simulations with experimental results published by Bohlen et al. ([36], [37]) as well as lower temperatures by Li et al. [1]. The power law conditions from Bohlen et al. will be used to investigate the role of climb in formability within the power law regime. Interest in formability at lower temperatures, however, is both technological and scientific in nature. Forming Mg at lower temperatures and higher strain rates will reduce equipment costs and processing times in an industrial setting. In addition, lowering the temperature also provides an opportunity for exploring the transition between <c+a> slip controlled deformation and <a> climb accommodated flow.

The methods of simulating the FLDs are laid out in detail in the following section. The results of this comparison begin with formability estimates of uniaxial straining, plane strain and equibiaxial stretching strain paths to determine the role of climb strain accommodation in predicting the onset of plastic instability. The texture evolution of the bulk region of glide-only and climb-incorporating simulations provide insight into the role of boundary conditions on slip mode selection and mechanistic explanations for plastic instability. The results section concludes with a brief investigation into the effect of texture differences between the bulk and defect material on formability. A brief discussion follows of other possible thermally activated mechanisms, such as grain boundary sliding, which are not included in the simulations, but could impact the deformation behavior at high temperature is provided. The paper ends with a list of conclusions.

## 2- Methods and Materials

*FLD predictions using VPSC*

One common approach to predicting the forming limit curve at a specified temperature and rate is the Marciniak – Kuzcynski method, which uses a plastic instability criterion to predict the failure strain of the material (Figure 1).

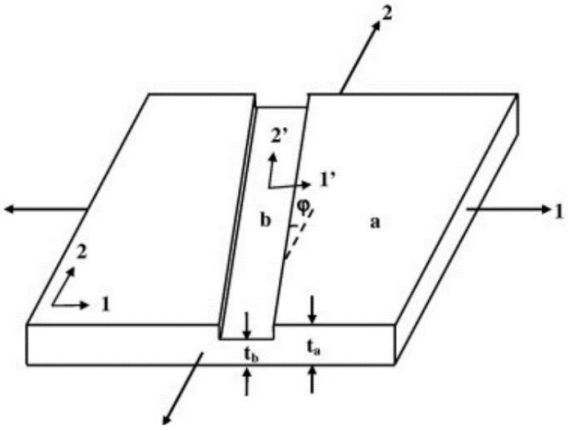


Figure 1: Diagram of the M-K method describing the deformation of the bulk material (a) and the defect material (b) when subjected to a biaxial strain path (the ratio of strain rates 1 and 2 are defined as ρ). The defect can be inclined toward the major straining direction by the angle ϕ. The size of the defect ($f$) is defined as the ratio of the defect and bulk thicknesses ($t_b$ and $t_a$, respectively). Taken from Neil & Agnew [25] following Hutchinson & Neale [105].

This method assumes that a defect of thickness $t_b$ is present at onset of plasticity and that the relative thinning rate between the defective and bulk material determines when the material fails, (a ratio of 20 is typically used to define plastic instability). During loading, the boundary conditions for the bulk material are defined by the applied strain path while those of the defect material are calculated by enforcing equilibrium and compatibility between the defect and the bulk material through Equations 10 - 12

$$\dot{\varepsilon}_{22}^{b} = \frac{\dot{\varepsilon}_{11}^{a} + \dot{\varepsilon}_{22}^{a}}{2} + \frac{\dot{\varepsilon}_{22}^{a} - \dot{\varepsilon}_{11}^{a}}{2}\cos(2\phi) + \frac{\dot{\gamma}_{12}^{a}}{2}\sin(2\phi) \qquad Equation\ 10$$

$$\sigma_{11}^{b} = \frac{1}{f}\left(\frac{\sigma_{11}^{a} + \sigma_{22}^{a}}{2} + \frac{\sigma_{11}^{a} + \sigma_{22}^{a}}{2}\cos(2\phi) + \tau_{12}^{a}\sin(2\phi)\right) \qquad Equation\ 11$$

$$\sigma_{12}^{b} = \frac{1}{f}\left(\frac{\sigma_{22}^{a} - \sigma_{11}^{a}}{2}sin(2\phi) + \tau_{12}^{a}\cos(2\phi)\right) \qquad Equation\ 12$$

where $\dot{\varepsilon}$ and $\dot{\gamma}$ represent the normal and shear components of the strain rate tensor and $\sigma$ and $\tau$ represent the normal and shear stress tensor components, respectively.

Volume is conserved during plastic deformation in both the bulk and defect (Equations 13 and 14), which generates additional boundary conditions.

$$\dot{\varepsilon}_{11}^{a} + \dot{\varepsilon}_{22}^{a} + \dot{\varepsilon}_{33}^{a} = 0 \rightarrow\ \dot{\varepsilon}_{33}^{a} = -(\dot{\varepsilon}_{11}^{a} + \dot{\varepsilon}_{22}^{a}) = -\dot{\varepsilon}_{11}^{a}(1+\rho) \qquad Equation\ 13$$

$$\dot{\varepsilon}_{11}^{b} + \dot{\varepsilon}_{22}^{b} + \dot{\varepsilon}_{33}^{b} = 0 \rightarrow\ \dot{\varepsilon}_{33}^{b} = -\left(\dot{\varepsilon}_{11}^{b} + \dot{\varepsilon}_{22}^{b}\right) \qquad Equation\ 14$$

where $\rho$ defines the strain path ($\rho = \frac{\dot{\varepsilon}_{22}^{a}}{\dot{\varepsilon}_{11}^{a}}$) and it is assumed that the material is a thin sheet and therefore, subject to plane stress ($\sigma_{33} = 0$, $\dot{\gamma}_{23} = \dot{\gamma}_{13} = 0$) in both the bulk and defect material. Following Hutchinson & Neale [105], the defect orientation can evolve via Equation 15

$$\tan(\phi) = \exp[(1-\rho)\,\varepsilon_{11}^{a}]\tan(\phi_0) \qquad Equation\ 15$$

where $\phi$ is the new orientation of the defect and $\phi_0$ is the initial orientation.

To ensure that the equivalent strain rate is nearly constant across all strain paths, the strain increment was scaled relative to that of uniaxial straining ($\rho = -0.5$) using the Von Mises equivalent strain (Equation 16). This is of particular importance in the climb incorporating simulations as the activity of climb is much more sensitive to rate than glide.

$$\varepsilon_{eq} = \frac{\left[(\varepsilon_{11}-\varepsilon_{22})^2 + (\varepsilon_{22}-\varepsilon_{33})^2 + (\varepsilon_{33}-\varepsilon_{11})^2 + \frac{3}{2}(\gamma_{12}^2+\gamma_{23}^2+\gamma_{31}^2)\right]^{\frac{1}{2}}}{(1+\nu)\sqrt{2}} \qquad Equation\ 16$$

Under conditions of plane stress and a general strain path, (i.e. $\dot{\varepsilon}_{22} = \rho\dot{\varepsilon}_{11}$ and $\dot{\varepsilon}_{33} = -(1+\rho)\dot{\varepsilon}_{11}$), Equation 16 becomes $\varepsilon_{eq} = \frac{\varepsilon_{11}}{(1+\nu)\sqrt{2}}[6+6\rho+6\rho^2]^{\frac{1}{2}}$ ($\nu$ is the Poisson's ratio). Assuming a strain increment for the uniaxial straining condition of $\Delta\varepsilon$, the strain increment under other loading conditions ($\Delta\varepsilon'$) is given by Equation 17.

$$\Delta\varepsilon' = \frac{\frac{[6+6\rho+6\rho^2]^{\frac{1}{2}}}{(1+\nu)\sqrt{2}}\varepsilon_{11}}{\frac{3}{2(1+\nu)}\varepsilon_{11}}\Delta\varepsilon \rightarrow [6+6\rho+6\rho^2]^{\frac{1}{2}}\left(\frac{\sqrt{2}}{3}\right)\Delta\varepsilon \qquad Equation\ 17$$

where $\frac{3}{2(1+\nu)}\varepsilon_{11}$ is the equivalent Von Mises strain under uniaxial straining ($\rho = -0.5$). $\Delta\varepsilon'$ is always greater than $\Delta\varepsilon$ since the minor straining direction in uniaxial straining is $-0.5\ \varepsilon_{11}$, the lower limit in the FLC. $\Delta\varepsilon'$ must be scaled by $\frac{3}{\sqrt{2}[6+6\rho+6\rho^2]^{\frac{1}{2}}}$ to achieve the same strain rate as in the uniaxial condition.

Analogous to the analyses by Neil & Agnew [25], the unknown components of the stress and strain tensors for the defect and bulk material were solved by employing a VPSC crystal plasticity model with the above boundary conditions incrementally with straining steps of ~0.003, which provided a balance of computational speed and solution stability. The time step was adjusted as a free parameter to enforce the applied strain rate of the test. The forming limit of each strain path is reached when plastic instability occurs. This version of the VPSC code was modified to allow dislocation climb as a possible slip mode ([23], [24]) and has already been shown potential as a significant contributor to strain accommodation at elevated temperatures (>200 °C) [80]. The initial textures of the experimental FLD samples - textures of rolled and

extruded AZ31B samples from Bohlen et al. [36] - were represented by the as-rolled and annealed AZ31B samples from Chapter 1 and the resultant texture from a uniaxial tension simulation where prism slip was activated to produce the symmetric nodes observed in the experimental texture.

a) b)

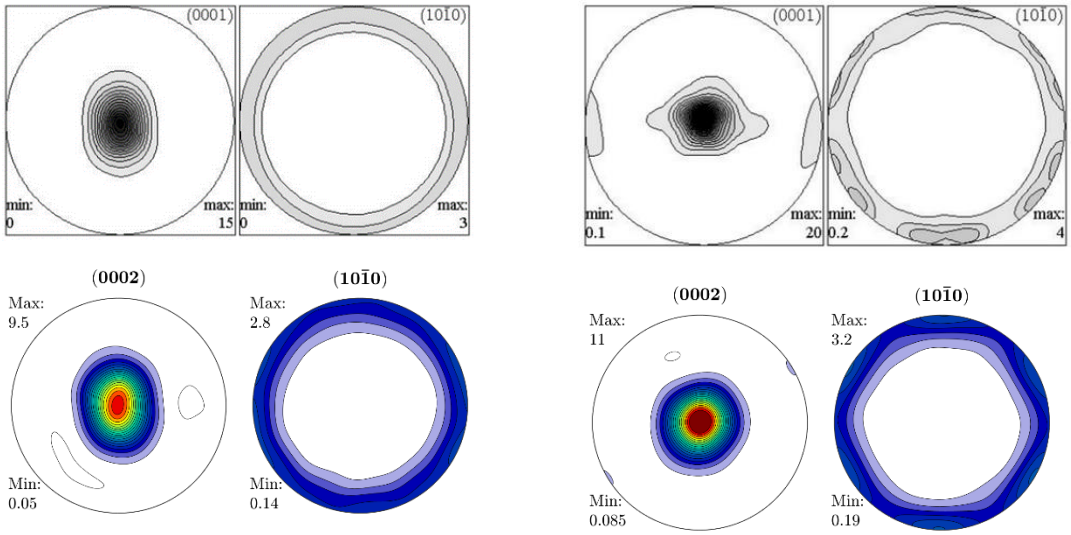


Figure 2: The initial a) as-rolled and b) extruded textures from Bohlen et al. [36] used during FLD prediction along with the textures used in the following simulations. Note that the texture representing an as-extruded sample has the six-fold symmetry on the nodes whereas the as-rolled texture does not.

*Estimating the strain rate of a limiting dome height test*

It is understood that the accurate assessments of the strain rate are imperative during incorporation of climb into modeling efforts due to its greatly increased strain rate sensitivity with respect to glide ($m_c = \frac{1}{3} > m_g \geq \frac{1}{20}$ at room temperature). Limiting dome height tests using a Hasek geometry [31] complicate estimations of the strain rate the material is experiencing as only the punch speed and displacement are typically reported. Additionally, the strain rate accelerates during constant punch velocity testing. This phenomenon is seen in strain path curves measured in Bohlen et al. [37] ,which demonstrate that the strain rate increases throughout the test. To that end, two different strain rates were used to bracket the true strain rate during experimental observations by Bohlen et al. ([36], [37]). The lower limit of strain rate was estimated by calculating the test time from the punch displacement and the specified punch speed. The estimated average rate for each strain path was then calculated by dividing the fracture strain by this time. The average of the 3 important strain paths (uniaxial straining, plane strain tension and biaxial stretching) was taken as the average strain rate of the test. The issue of an accelerating strain rate was handled by assuming that the upper limit would be the apparent strain rate of the punch (punch velocity divided by displacement), which was on average 2 to 3 times greater than the lower bound strain rate (Table 1).

Table 1: Average strain rates for each limiting dome height test

| | Uniaxial strain rate | Plane strain rate | Biaxial strain rate | Average strain rate |
|---|---|---|---|---|
| Lower Bound Strain Rate (1/s) | | | | |
| 200°C, 60 mm/min | 0.028 | 0.017 | 0.013 | 0.019 |
| 200°C, 6 mm/min | 0.002 | N/A | 0.002 | 0.002 |
| 250°C, 60 mm/min | 0.023 | 0.028 | 0.025 | 0.025 |
| Upper Bound Strain Rate (1/s) | | | | |
| 200°C, 60 mm/min | 0.051 | 0.065 | 0.066 | 0.061 |
| 200°C, 6 mm/min | 0.005 | 0.007 | 0.007 | 0.006 |
| 250°C, 60 mm/min | 0.050 | 0.055 | 0.050 | 0.052 |

*Determination of the critical resolved shear stresses and Voce hardening parameters*

Accurate estimations of the CRSSs and Voce hardening parameters are required to predict the forming limits via crystal plasticity modeling. The optimal CRSSs and climb stresses were determined using machine learning via genetic algorithm to best fit the experimental texture evolution and strain anisotropy in Chapter 1. Optimization was performed when climb was included and excluded to determine the effect of climb in the high temperature deformation. Resolved shear stresses (RSSs) in the current study were estimated from the results of Chapter 2 (Appendix B) which fit the RSSs and climb stresses to classical, thermally activated plasticity model using the temperatures and strain rates investigated in the FLC determination experiments of Bohlen et al. ([36], [37]). Voce hardening parameters were determined by fitting the predicted flow stresses at several temperatures to experimental stress-strain curves obtained in Chapter 1. Additional simulations performed in Chapter 2 allow for the investigation of formability in the transitional regime between ambient and power law deformation conditions to investigate the implications of lowering the forming temperature.

**2- Results**

*Comparison of the forming limit predictions with and without strain accommodation by climb*

Predictions using the M-K method were compared against the experimental observations of Bohlen et al. [36], [37] and Li et al. [74] (Figure 3). There is no clear trend between temperature, strain rate and experimental formability within the power law regime; however, other studies have shown that formability increases with temperature and decreasing strain rate ([1], [25]). Texture has a clear impact, as the formability of the extruded sample was

significantly lower than the as-rolled material for all strain paths. The present VPSC-based FLC predictions typically underpredict the experimental formability (i.e., they are conservative); however, there is a near universal increase in formability when significant strain accommodation occurs via climb, which has strong temperature and strain rate dependencies. At 200 °C, deformation at a lower strain rate (0.0025 1/s) demonstrates large increases in formability compared to glide-only simulations. In equibiaxial stretching, the formability is predicted to be lower than under plane strain conditions. This is likely due to strain hardening (which has previously been shown to increase formability [25]) which is reduced at the lower rate condition due to the inclusion of climb. It appears that strain hardening behavior must be incorporated in future studies to better describe the formability at elevated temperatures. Increasing the strain rate to 0.019 1/s shows identical formability between climb incorporating and glide-only simulations. In conditions with similar strain rates (200 °C at a rate of 0.019 1/s and 250 °C at a rate of 0.026 1/s), an increase in temperature led to a noticeable increase in plane strain and equibiaxial formability. Predicted formability in as-extruded samples (Figure 3d)) could not explain the reduced formability observed experimentally.

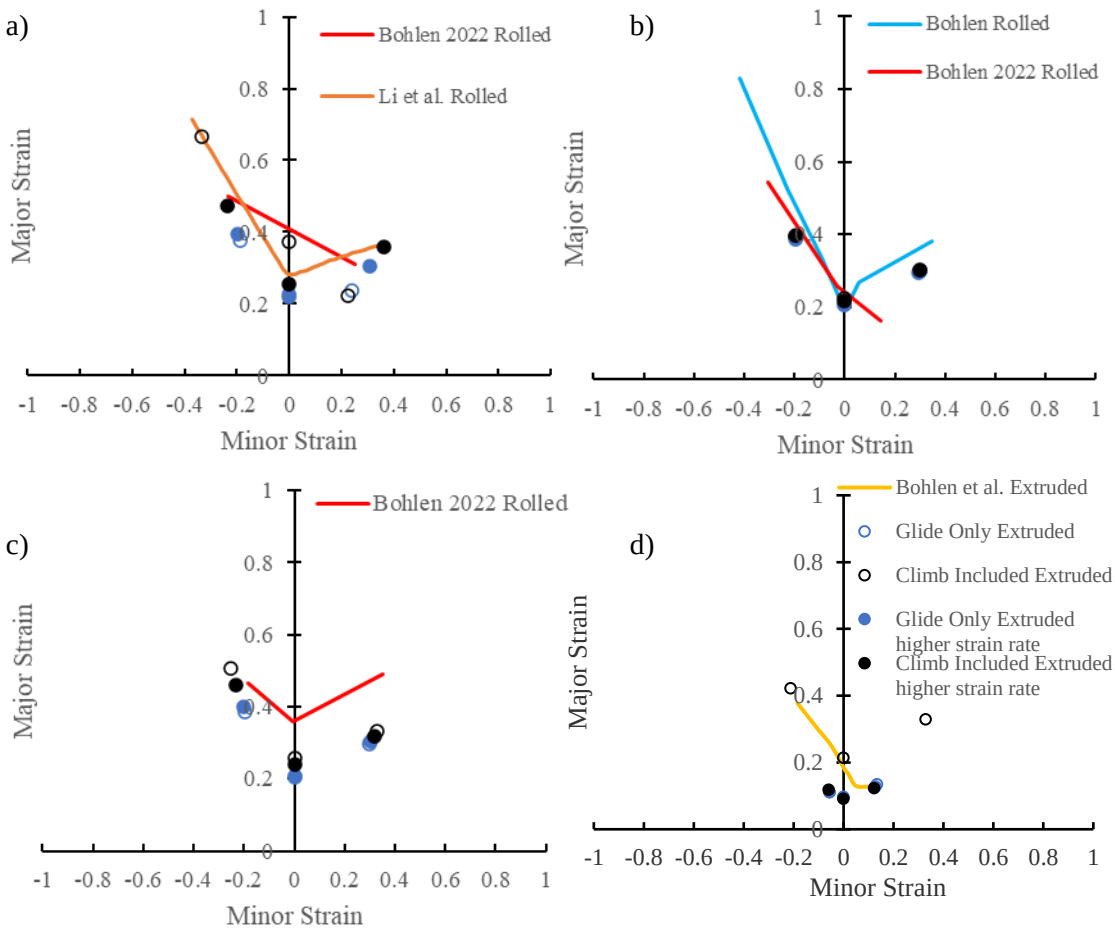


Figure 3: Experimental observations (Li et al. [1], Bohlen 2022 [106], Bohlen [36]) along with FLD-VPSC predictions with and without climb for 4 samples. a) Rolled AZ31B at 200 °C and 0.0025 1/s, b) Rolled AZ31B at 200 °C and 0.019 1/s, c) Rolled AZ31B at 250 °C and 0.025 1/s and d) Extruded AZ31B at 200 °C and 0.019 1/s.

*Investigating the texture evolution of bulk and defect regions during formability prediction*

As noted in previous studies ([23], [80], [107]), texture evolution can determine the active slip modes within the material. Due to the differing boundary conditions between the bulk and defective material (as noted in Equations 10 - 14), the texture evolution of each region was investigated at the predicted failure strain. It was found that the homogeneous texture evolution was strongly dependent on the strain path for both glide-only and climb-incorporated simulations; temperature and strain rate had weak effects (Figure 4). This is expected as all conditions investigated are of similar temperature and rate, falling in the power law breakdown regime (a region where elevated temperatures provide sufficient thermal energy for climb to occur, but outside the power law regime). Uniaxial straining conditions have texture evolution very similar to that of previous in-plane uniaxial tension ([20], [80]) while the characteristic signature of prism slip is absent during equibiaxial stretching. Similar texture evolutions between glide only and climb incorporating simulations suggests that the endpoint in texture evolution is

similar, but additional deformation is required when climb can accommodate strain, as it does not contribute to the texture evolution. This not only explains the similarities between glide only and climb incorporating simulations, but also why all conditions have the very similar texture evolution in both strain paths displayed in Figure 4, as well as the greatly reduced formability when extruded sheets are tested due to their stronger initial texture. Experimental texture evolutions observed by Bohlen et al. ([36], [37]) (Figure 5) suggest that <c+a> slip does not accommodate significant amounts of strain in agreement with both simulation sets, as there is no splitting of intensity in the (0002) pole figure. Relative slip activity (RSA) plots (Figure 6) show that in both glide-only and climb-incorporating simulations, prism and basal slip accommodate the majority of strain during uniaxial straining. In glide-only simulations, <c+a> slip accommodates significant strain, whereas climb incorporating simulations can also have contributions from climb. Most conditions in equibiaxial stretching cases, both glide-only and climb-incorporating simulations accommodate strain primarily through a combination of basal and <c+a> slip, which explains the similar texture evolution.

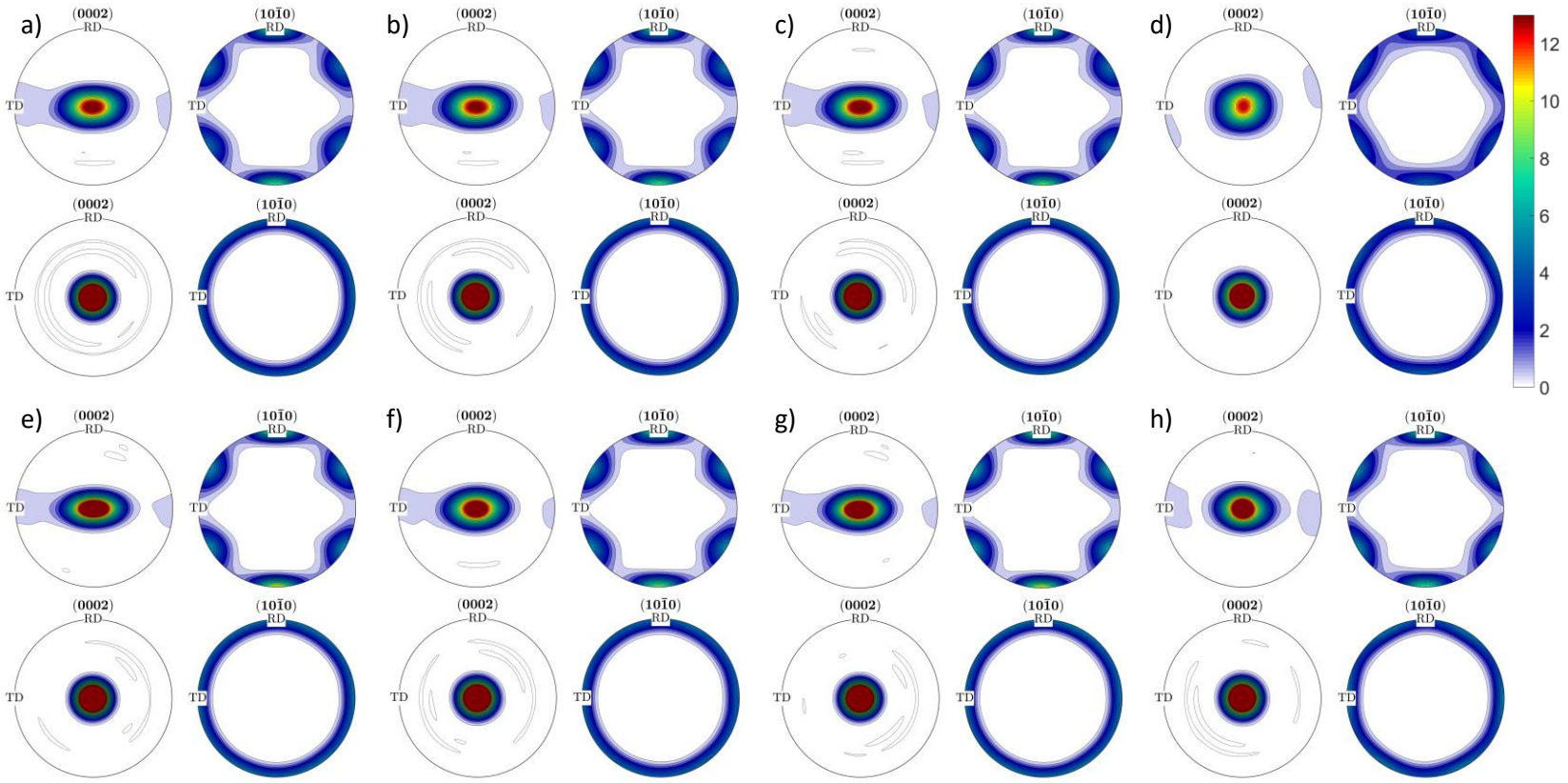


Figure 4: Bulk texture evolution for glide-only [a)-d)] and climb-incorporating [e)-h)] simulations for each condition: a)&e) 200 °C and 0.0025 1/s, b)&f) 200 °C and 0.019 1/s, c)&g) 250 °C and 0.026 1/s and d)&h) extruded AZ31B at 200 °C and 0.019 1/s. Top row – Uniaxial Strain, Bottom row – Biaxial Stretch

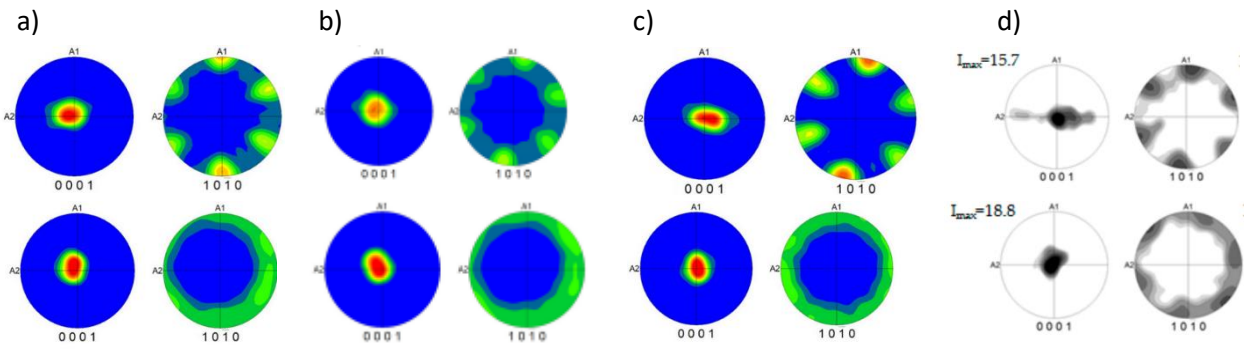


Figure 5: Experimental texture measurements of rolled AZ31B tested under a) 200 °C and 0.0025 1/s, b) 200 °C and 0.019 1/s, c) 250 °C and 0.026 1/s [37] and d) extruded AZ31B at 200 °C and 0.019 1/s [36]. Top row – Uniaxial Strain, Bottom row – Biaxial Stretch

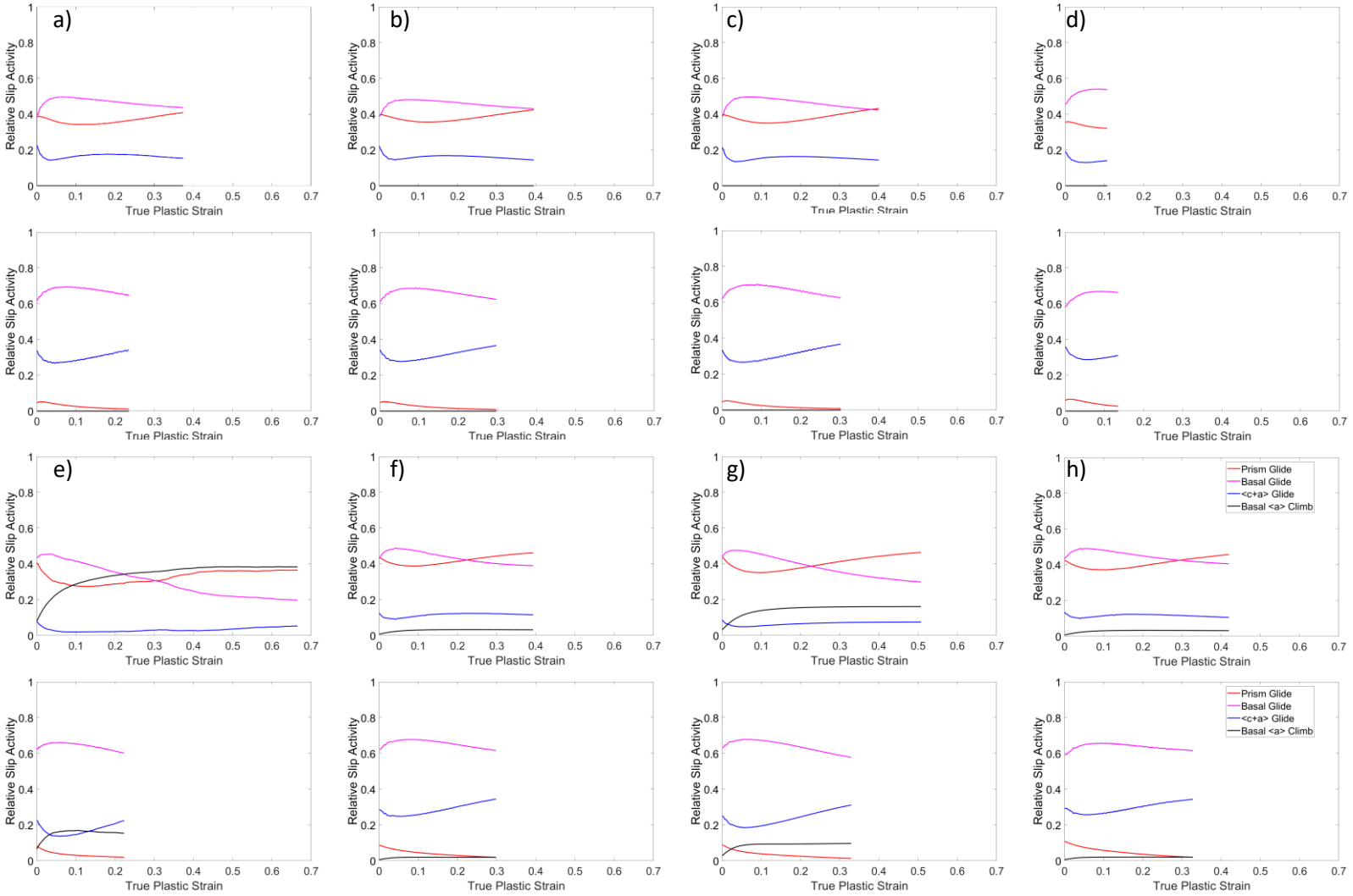


Figure 6: Relative slip activity plots for glide-only [a)-d)] and climb-incorporating [e)-h)] simulations of the bulk material for each condition: a)&e) 200 °C and 0.0025 1/s, b)&f) 200 °C and 0.019 1/s, c)&g) 250 °C and 0.026 1/s and d)&h) extruded AZ31B at 200 °C and 0.019 1/s. Top row – Uniaxial Strain, Bottom row – Biaxial Stretch

*Investigating deformation within the defect*

It is evident that the defect strain rate is always higher than in the bulk due to the higher applied stress associated with a reduction in cross sectional area, which suggests that climb strain accommodation in the defect will be more susceptible to deactivation. Figure 7 displays the texture evolution in the defect at the predicted failure strain for glide-only and climb-incorporating simulations. The texture evolution in the defective region in glide-only and climb incorporating simulations of rolled samples at 200 °C (Figures 7 a)-b)) are very similar (the rotation around ND in the uniaxial straining condition is a product of the defect inclining ~15-20° relative to the loading direction and is not indicative of dislocation motion). A slight intensity spreading along the rolling direction suggests that <c+a> may be active at 200 °C. The low texture intensity of the initially as-extruded sample is attributed to the low final strain level (~0.1 vs 0.3 for the other conditions tested). As in the bulk texture evolution, the texture at the failure strain in the defect is very similar for most samples, which suggests that texture may dictate the onset of plastic instability and that climb delays failure by slowing the texture evolution.

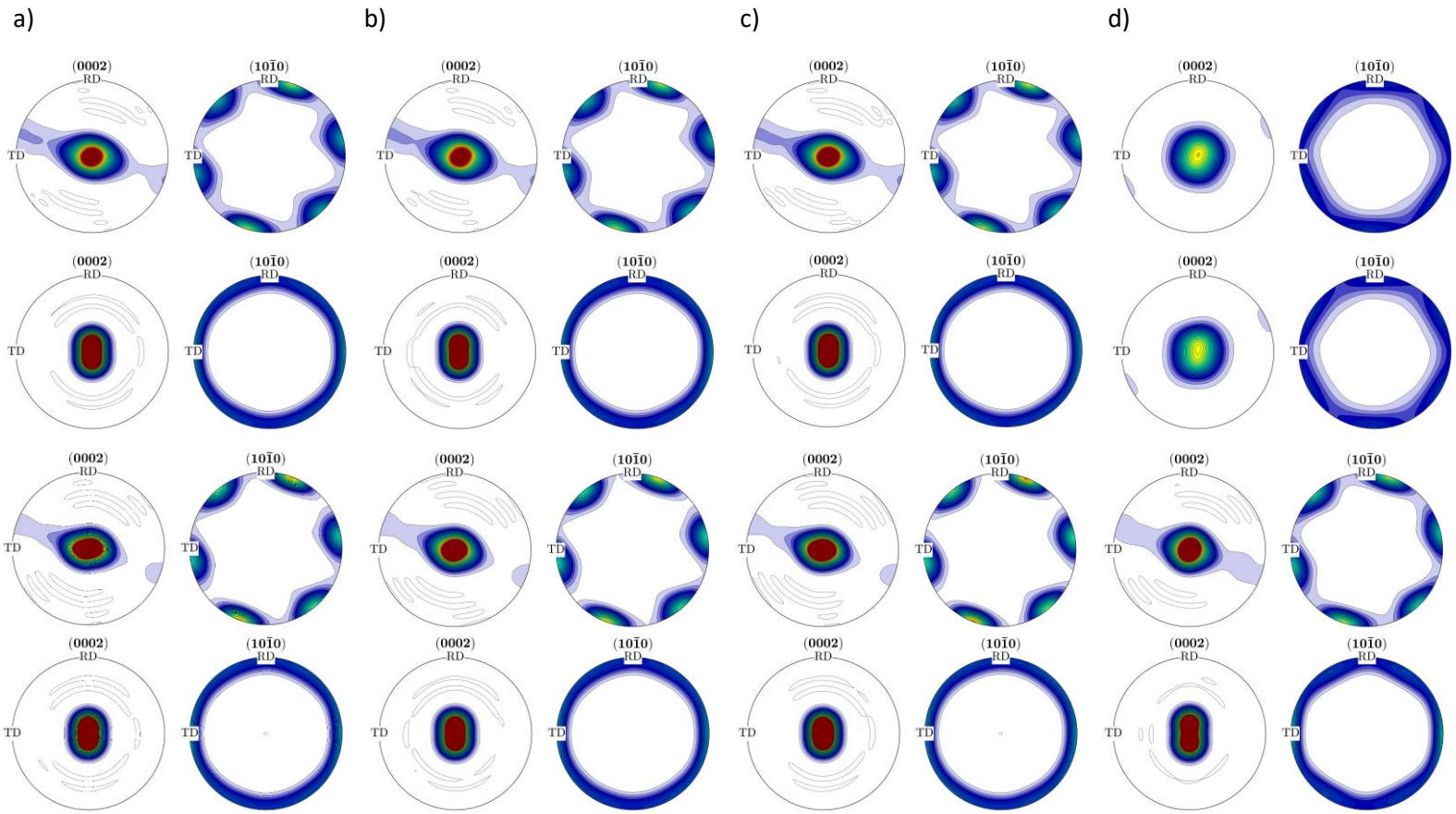


Figure 7: Defect texture evolution for glide-only [a)-d)] and climb-incorporating [e)-h)] simulations for each condition: a)&e) 200 °C and 0.0025 1/s, b)&f) 200 °C and 0.019 1/s, c)&g) 250 °C and 0.026 1/s and d)&h) extruded AZ31B at 200 °C and 0.019 1/s. Top row – Uniaxial Strain, Bottom row – Biaxial Stretch. The scale is identical to Figure 4.

RSA plots (Figure 8) for the defect again show that most of the strain is accommodated via prism and basal glide. Relative to the bulk material, that activation of <c+a> slip is more apparent at higher strain levels, particularly for equibiaxial stretching. When climb is excluded, failure is preceded by a noticeable drop in nonbasal strain accommodation (prism and <c+a>) in most conditions. Two possible explanations exist: slip mode hardening and texture evolution. From the fitting methodology of Chapter 2, it is clear that basal slip hardens significantly less than either of the nonbasal slip modes ($\tau_1^{basal} = 0.37$ ($\tau_0^{basal} = 10.8$) in comparison to $\tau_1^{prism} = 43.0$ ($\tau_0^{prism} = 48.5$) and $\tau_1^{<c+a>} = 38.5$ ($\tau_0^{<c+a>} = 52.2$) for 200 °C at a rate of 0.019 1/s). Thus, it becomes increasingly favorable for basal slip to be activated over the competing modes which harden more rapidly.

As mentioned previously, texture evolution (or lack thereof) may also give rise to more rapid (or delayed) onset of plastic instability. In the case of uniaxial straining, the average maximum Schmid factors in as-rolled and annealed AZ31B were found to be $\bar{m}_{basal} = 0.18$, $\bar{m}_{prism} = 0.44$ and $\bar{m}_{<c+a>} = 0.44$ (for the climb of <a> dislocations, $\bar{k}_{<a>} = 0.55$). As noted previously, strain accommodation via glide imposes shear strain onto the lattice, initiating texture evolution. As the lattice rotates, the Schmid factor decreases as the dislocation aligns with the applied stress, reducing the resolved shear stress. The reduction in Schmid factor effectively hardens the slip mode, as more stress must be applied to continue strain accommodation. This is particularly true in the 250 °C case, where a splitting in the basal pole figure is present to indicate the activation of <c+a> slip (Figure 7). When Schmid factors of the nonbasal slip modes are sufficiently reduced, it is possible that basal slip activates as it is the easy slip mode in Mg. Basal slip, however, cannot accommodate <c> axis strain (most of which lie approximately parallel to the sheet ND direction due to the initial texture) and therefore the material will fail if significant <c> strains are present. This is likely the case in rolled or extruded AZ31B where significant thinning of the sheet occurs during deformation. In addition, basal slip is known to have lower temperature and strain rate dependencies than non-basal mechanisms. As the test proceeds, the strain rate in the defect increases, hardening the non-basal mechanisms relative to basal slip. These processes also occur in climb-incorporating simulations where climb does not activate. In these instances, however, the initial strain accommodation via prism slip introduces an additional component to the texture, which delays the deactivation of <c+a> slip to later stages of deformation.

Climb activation forestalls plastic instability via increased rate sensitivity, as it has been noted previously that the SRS of climb is much higher than glide (1/5 – 1/3 vs > 1/100 – 1/10, respectively (Chapter 2) from room temperature to 350 °C ) and that increased macroscopic rate sensitivity leads to the formation of a stable neck (in this case, the defective region in the sheet) [69]. This is corroborated by the intimate relationship between climb strain accommodation and strain rate within the defect (Figure 8). Initially, climb accommodates a significant fraction of strain and the strain rate within the defect is marginally higher than in the bulk. Climb activation slows the texture evolution and stabilizes the defect region due to its higher rate sensitivity. Stable neck formation slows strain localization (i.e., the increased strain rate in the defect), which

allows for continued climb strain accommodation. At a critical strain level, the texture evolution due to nonbasal slip (in particular <c+a> slip, which rotates the <c> axes of the grains away from ND) begins to significantly reduce the Hartley factor for <a> dislocation climb. The ability of climb to accommodate strain, and therefore the macroscopic rate sensitivity, is reduced. This increase in the strain rate, also reduces the strain accommodation via climb as the vacancy diffusion rate required for climb begins to lag behind the strain rate in the defect. This begins a vicious cycle of increases in defect strain rate leading to a reduction in climb strain accommodation, which further reduces the macroscopic rate sensitivity. Note that strain accommodation by climb also slows the texture evolution, which helps to stabilize its activity by minimizing the reduction of the Hartley factor. Thus, the increased strain rate also increases the rate of texture evolution, which also reduces the amount of strain accommodation via climb. By these mechanisms, the thinning rate within the defect increases faster than that of the bulk and plastic instability occurs at a critical strain level.

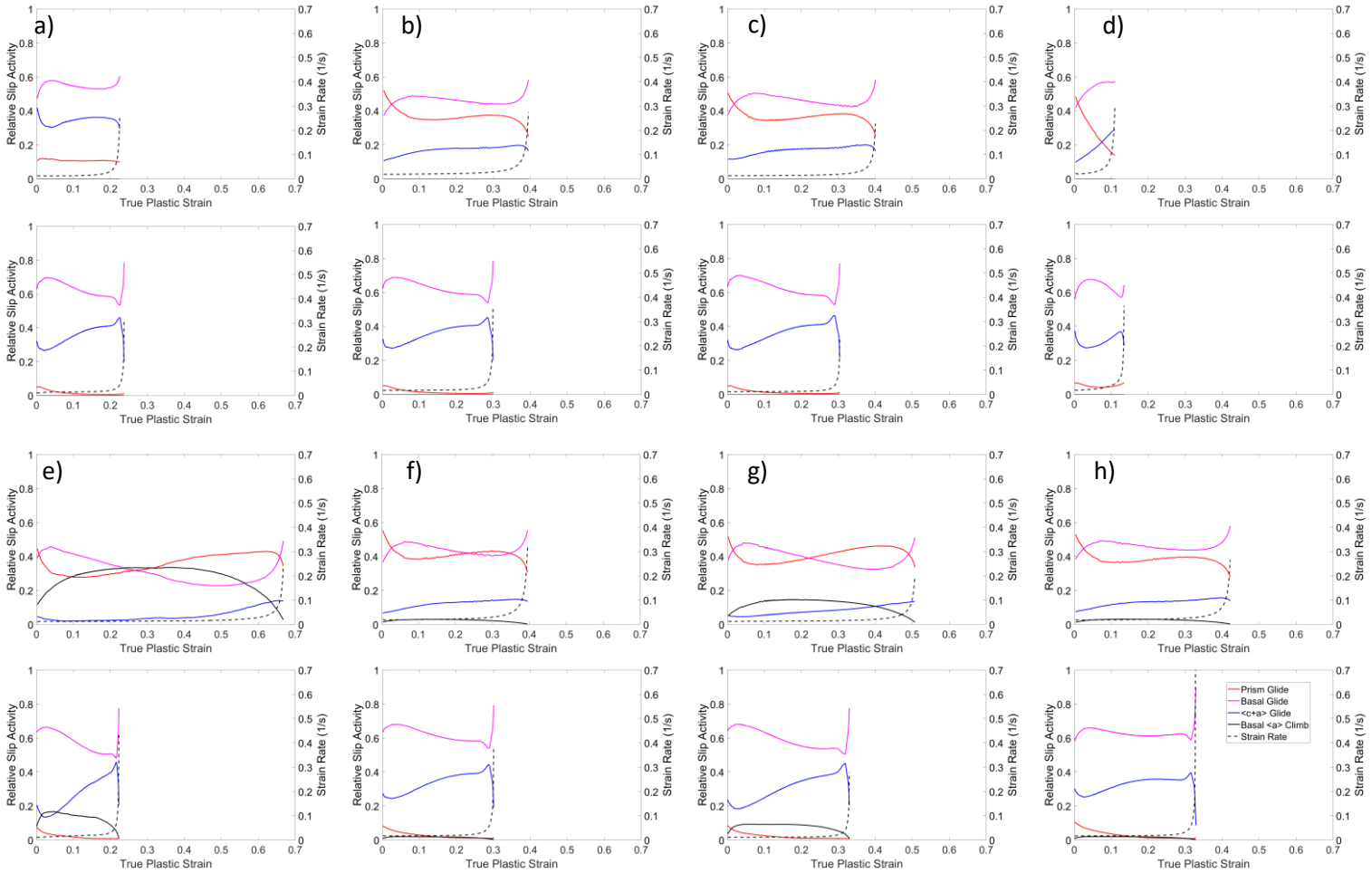


Figure 8: Relative slip activity plots for glide-only [a)-d)] and climb-incorporating [e)-h)] simulations of the defect for each condition: a)&e) 200 °C and 0.0025 1/s, b)&f) 200 °C and 0.019 1/s, c)&g) 250 °C and 0.026 1/s and d)&h) extruded AZ31B at 200 °C and 0.019 1/s. Top row – Uniaxial Strain, Bottom row – Biaxial Stretch

*Predicting the onset of plastic instability*

In both glide-only and climb-incorporating predictions, texture appears to play a significant role in material formability. Additional simulations were performed to separate the contributions of initial texture and texture evolution on formability. Figure 9 demonstrates the role of texture evolution in the defect and in the bulk material. When the defect texture cannot evolve, the formability is reduced in all loading conditions. If texture evolution is allowed in the bulk material, then the macroscopically imposed stresses must increase for the progressively less oriented slip modes to remain active. This requires the stresses to be higher in the defect; however, since texture evolution cannot occur in the defect, the minimum required stress needed for slip remains constant (not accounting for slip mode hardening). This results in an increased strain rate on the defect at lower strain levels and hastens the onset of plastic instability. The mechanism for the occurrence of plastic instability is identical to when texture evolution is allowed in the defect except that it occurs at lower strain levels. The notion that stalling texture evolution improves formability was tested by predicting the FLC without texture evolution in the bulk and defect. It was found that the uniaxial straining and equibiaxial stretching conditions had higher formability when texture evolution was excluded. Interestingly, the plane strain condition had reduced formability, which may be a result of the absence of texture evolution due to basal glide orienting the grains for <a> climb.

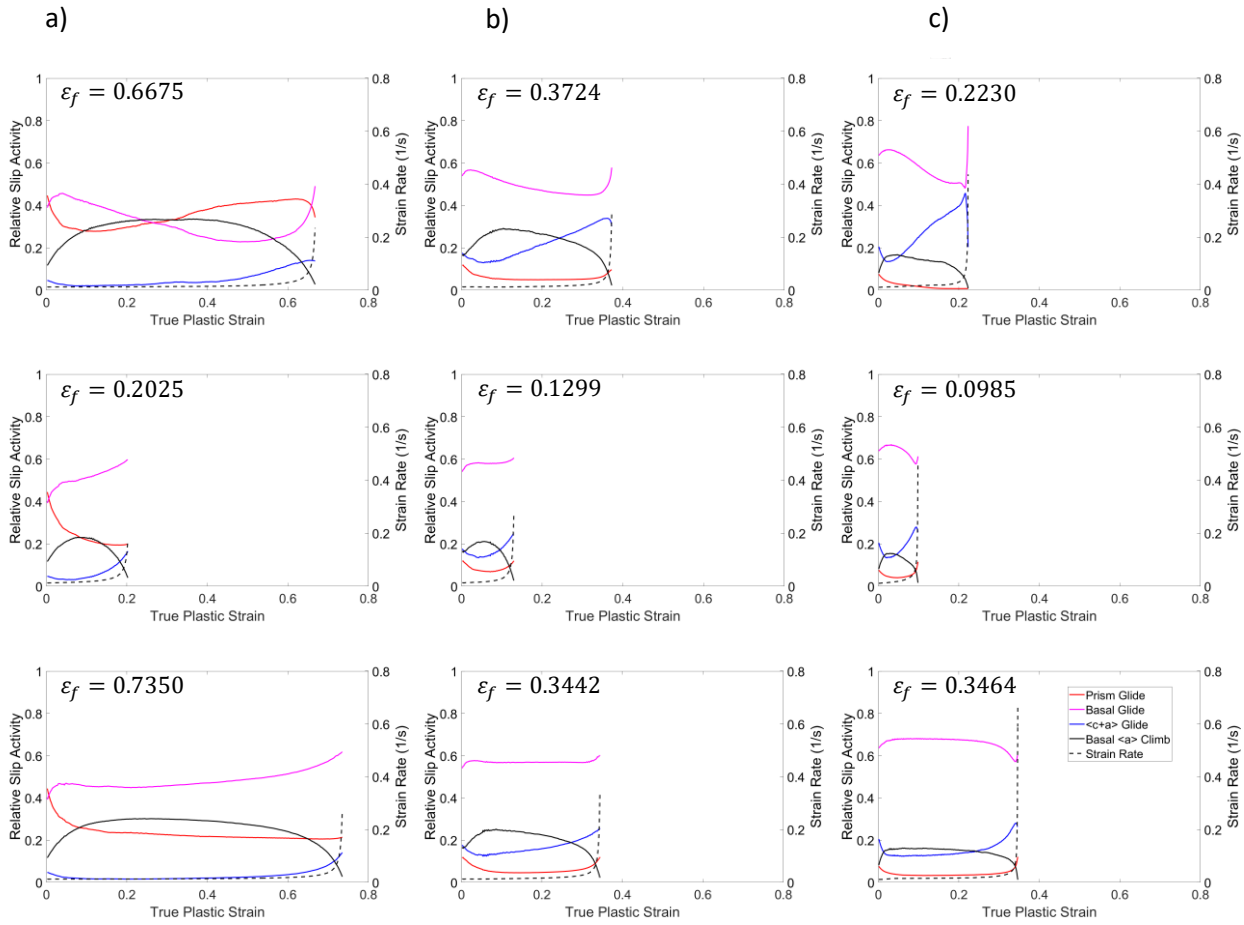


Figure 9: The RSA plots and forming limits of the 200 °C, 0.0025 1/s condition where texture evolution is present (top), absent in the defect (middle), absent in both the bulk and defect (bottom) for a) uniaxial straining, b) plane straining, c) biaxial stretching. Note that the decline in strain accommodation by climb coincides with a strong increase in strain rate.

Interesting phenomena are observed when the material of the bulk and defect are different. When the defective material is more strongly textured than the bulk material, plastic instability does not occur; in the converse case, the material immediately fails. Both instances are the direct result of geometric hardening due to texture evolution. In the former case, the bulk material requires less stress to deform since basal slip (the easy slip mode in Mg) will activate more frequently due to the absence of Schmid effects. This stress level is insufficient to activate significant strain in the defect, which is harder due to the presence of texture and would require more stress in order to either 1) activate basal slip which is poorly oriented in uniaxial straining ($m_b$ = 0.18) or 2) activate a better oriented, harder slip mode (e.g., prism slip or <c+a> slip ($m \approx$ 0.4)). Additionally, any strain that occurs in the defect will cause geometric hardening and increase the resistance to straining from the applied stress on the bulk material, leading to a situation where the defect material will not failure. Conversely, if the bulk material is more strongly textured than the defect, the imposed stresses on the defect will be much higher than

necessary to strain the randomly textured material, creating a very high strain rate and triggering plastic instability within the defect almost immediately.

The deformation of a completely random material results in a more isotropic, but lower, formability than a strongly textured sample. A sample with a strong rolling texture has a higher proportion of grains with <c> axes parallel to the sheet normal direction, which promotes climb during in-plane, uniaxial straining and <c+a> slip as the strain path (ρ) trends to unity. In contrast, a random texture is likely to have grains oriented such that climb is a plausible mechanism for all listed straining conditions (albeit fewer than that of a strongly textured material in uniaxial straining) (Figure 10). Since less strain is accommodated by climb, it is expected that the formability would be reduced.

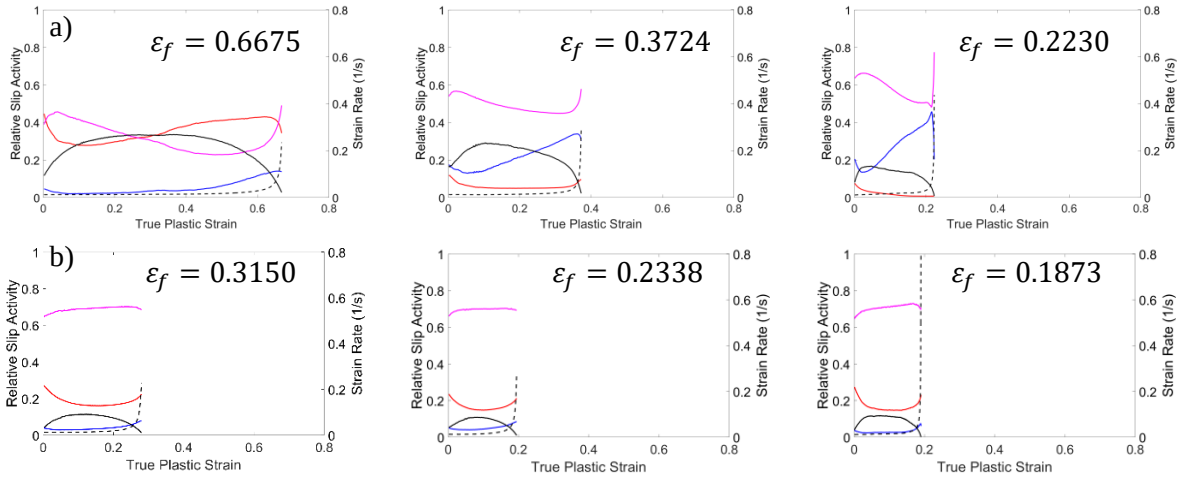


Figure 10: The active slip modes when the bulk and defect are a) strongly textured and b) randomly textured.

It is clear from these simulations that the increase in strain rate due to the smaller thickness in the defect relative to the bulk material reduces the climb activity as a result of relative differences in rate sensitivity between glide and climb. It is also clear that texture evolution in the defect introduces geometric hardening which slows the rate of the strain rate increase in the defect relative to the bulk material, maintaining the strain accommodation by climb to higher strain rates. This is desirable when the bulk sample is textured, so that the applied stress due to the boundary conditions does not trigger immediate plastic instability; however, textured materials have been observed to have lower formability, as texture evolution during deformation can result in the deactivation of major slip modes within the defect. Strain accommodation through climb increases the macroscopic rate sensitivity which allows for the creation of a stable neck, improving the post uniform elongation [69].

*Simulating formability within the transitional regime between ambient temperature deformation and the power law regime*

The prior sections suggest that climb may accommodate significant strain at conditions on the edge of power law conditions, but as noted previously, it is of technological importance to investigate lower temperatures and rates. Figure 11 displays the comparison between experimental and predicted formability at 150 °C and a rate of 0.001 1/s using a climb incorporating VPSC-CLIMB model. These levels of formability are decidedly lower than those performed at higher temperatures closer to the power law regime, suggesting that the active mechanisms may differ between these groups of simulations; these predictions underestimate the drawing limit and plane strain formability. Inspection of the texture evolution in both the bulk and defect regions (Figure 12) demonstrates that <c+a> slip accommodates a large amount of strain (splitting in the basal pole figure), unlike previous FLC predictions in the power law regime. Again, relative slip activity plots (Figure 13) show that plastic instability initiates in the defect due to an increase in strain rate. Unlike in the power law regime, plastic instability occurs due to reduction in activity of the most well-oriented slip mode and an increase in basal slip strain accommodation.

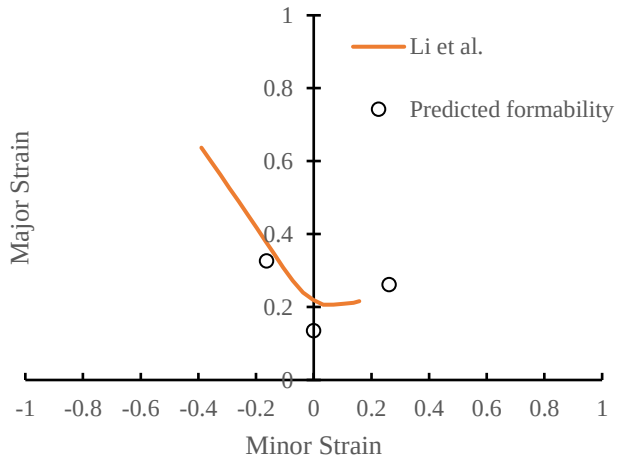


Figure 11: Formability comparison between experimental measurements [1] and predictions.

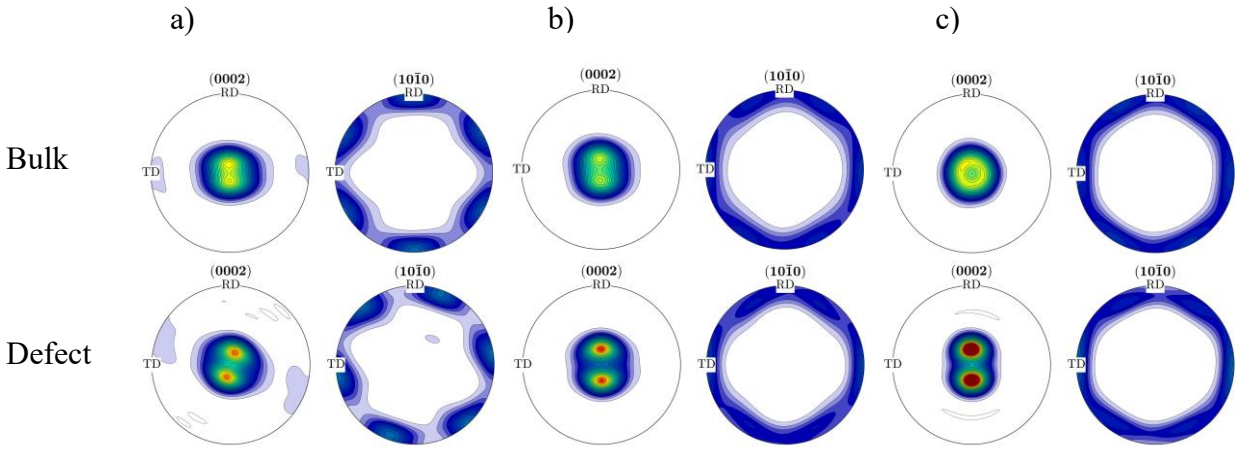


Figure 12: Texture evolution in the bulk and defect regions of FLC predictions at 150 °C and a rate of 0.001 1/s using GA optimized RSSs and climb stresses under a) uniaxial straining, b) plane strain and c) equibiaxial stretching.

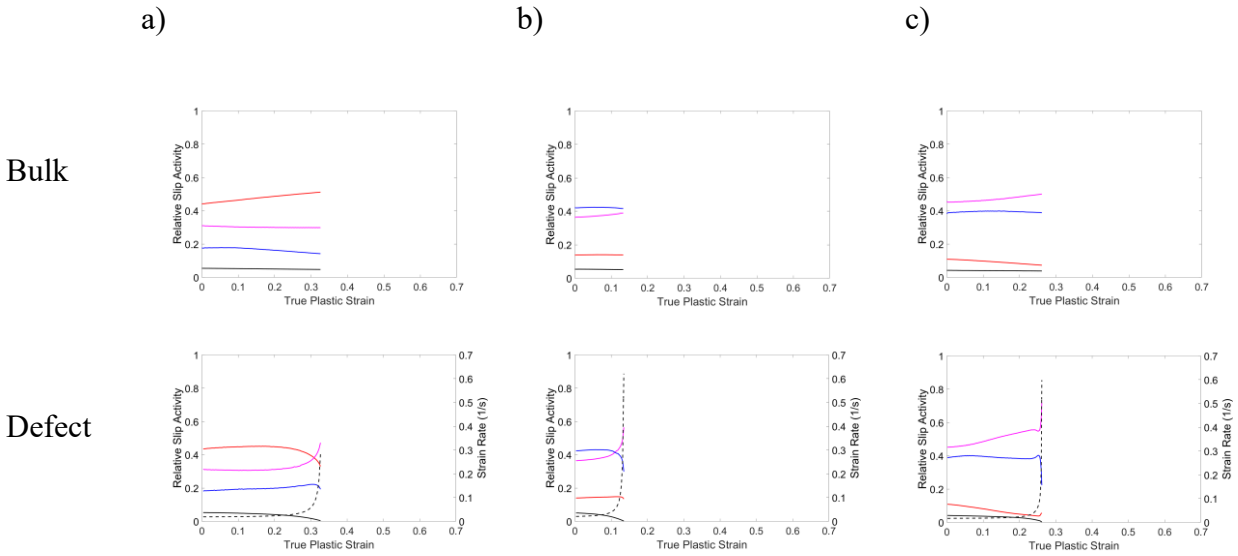


Figure 13: Relative slip activity plots in the bulk and defect regions of the FLC predictions at 150 °C for a) uniaxial straining, b) plane strain and c) equibiaxial stretching.

## 4- Discussion

*Comparison of experimental and predicted role of texture on formability*

The current simulations suggest that randomly textured samples should be less formable than strongly textured materials due to a decrease in climb strain accommodation caused by having fewer grains well oriented for <a> climb. However, this seems at odds with experimental predictions that randomly textured materials tend to have higher formability ([36], [37]), as well

as other results that demonstrate that stronger textures (e.g., as-extruded) result in lower formability (Figure 3). It is suggested here that the current methodology for calculating the climb stress is a conservative estimation and does not facilitate enough strain accommodation via climb to match this experimental observation. When <a> climb is softer, it can be activated in more grains with less regard to their orientation. In this case, the formability will be improved due to the weaker initial texture since plastic instability is controlled by the slowed texture evolution in the defect due to climb. Additional climb strain accommodation could also improve formability in Figure 3 and could explain the disparity between climb-incorporating simulations and experimental predictions.

*Alternative explanations for the high temperature formability increases*

The current work hypothesized that strain accommodation via climb could explain the improved formability at elevated temperatures and moderate strain rates, yet other thermally activated mechanisms (i.e., grain boundary sliding (GBS), diffusional flow) could be responsible. GBS has been proposed as a mechanism capable of accommodating significant strain during both low strain rates and quick plastic forming at comparable rates to those investigated ([51], [75], [108]), especially in ultrafine grained materials. Grain boundary sliding has been suggested as a mechanism which could lead reduced r-values [109] and can contribute randomization to the texture [110]. Simultaneous strain accommodation of via basal slip and grain boundary sliding has been proposed as an alternative mechanism for the slowed texture evolution [63]. However, GBS is more rate sensitive than climb (m = 1/3 - 1/2) depending on the accompanying mechanism [75], making it less likely to active at the rates employed in the current study than intragranular climb and glide. In addition, the motion of grain boundaries has previously been treated as non-crystallographic deformation [111] (i.e., no loading direction dependence on deformation). This is not evident in the experimental FLD results, which show that uniaxial straining typically yields much higher forming limits. Furthermore, some studies suggest that strain accommodation attributed to GBS may be explained by in terms of glide and climb motion, as expressed in this work. A recent study by Withers et al. [112] suggests that the majority of the grain boundary motion attributed to sliding is, in fact, intragranular dislocation motion in close proximity to the boundary, which aligns with the findings of the current study that a combination of intragranular glide and climb can describe the increases in formability. Even historical descriptions of GBS via the Ball-Hutchingson model suggest that the sliding of neighboring grains occurs via the climb and glide of disconnections – line defects with step height within the grain boundaries [113].

Dynamic recrystallization (DRX) could also potentially have a role in the increased formability as it is known to occur above 200 °C [19]. DRX is the process by which the new grains are nucleated from heavily deformed existing grains. It has been postulated that the removal of heavily deformed grains restores ductility, as the stress needed to continue deformation, and, consequently, the driving force for fracture, is lowered [114]. The reduction in stress is two-fold. First, DRX occurs due to the reduction in dislocation density, which is the driving force for the nucleation of new grains. The reduction in dislocation density also reduces the work hardening contribution to the flow stress. In addition, the nucleated grains do not have

an orientation relationship with the pre-existing grains ([63], [115]), randomizing the texture and contributing to a loss of hardening ([114], [116]). It has been hypothesized that the stalled texture evolution attributed to climb in this work is the result of texture randomization and basal glide to reform the initial as-rolled and annealed texture [63]. However, much like GBS, the activation of DRX is intrinsically linked to climb, as it is controlled by the annihilation (i.e., the climb and glide) of dislocations. Previous studies [117] have suggested as much from the operative mechanisms of DRX at increasing strain rates: single dislocation climb predominated by vacancy migration (0.001 1/s), diffusion and stress assisted climb of the leading dislocation in the array (0.01 1/s) and stress-controlled climb of the leading dislocations near pileups (1 1/s).

Nevertheless, several studies have pursued the implementation of DRX into VPSC simulations ([1], [63]), which yielded better fits of the flow stress, especially the characteristic softening that occurs at elevated temperatures, which this current work does not address. However, this is at the expense of texture evolution (Figure 14), particularly under RD tension. In this condition, the experimental texture evolution is very modest as characteristic of power law regime deformation. Both the initial and deformed experimental conditions have a split (0002) pole figure, which is not replicated in their simulations. Rather, a single peak in intensity is shown, representative of basal slip, which rotates the <c> axes (the normal to the (0001) plane) towards the sheet normal direction (ND). Additionally, the nodes on the $(10\bar{1}0)$ pole figure characteristic of prism slip are much more intense than those seen experimentally. The texture evolution under RD compression also follows suit, except that the texture is split further due to basal slip. The texture evolution under ND compression is more accurate since <c+a> slip is favored over other slip modes due to Schmid factors.

DRX-incorporating VPSC models [1] were recently used to predict the formability of rolled AZ31B and provide a convenient comparison to the simulations performed in the current work. The addition of DRX into FLC prediction resulted in improvements in the formability in all conditions, especially under uniaxial straining or equibiaxial stretching, which is likely attributable to the influence of DRX on the texture evolution. The predicted formability of DRX - incorporating FLC simulations (Figure 15) falls within the boundaries of the current climb – incorporating simulations, which suggests that the slowed texture evolution caused by both models controls the increases in texture evolution. However, the addition of DRX causes anomalous texture evolution through randomization (Figure 14) and suggests that the climb – incorporating model may better describe the kinematics of deformation within Mg alloys.

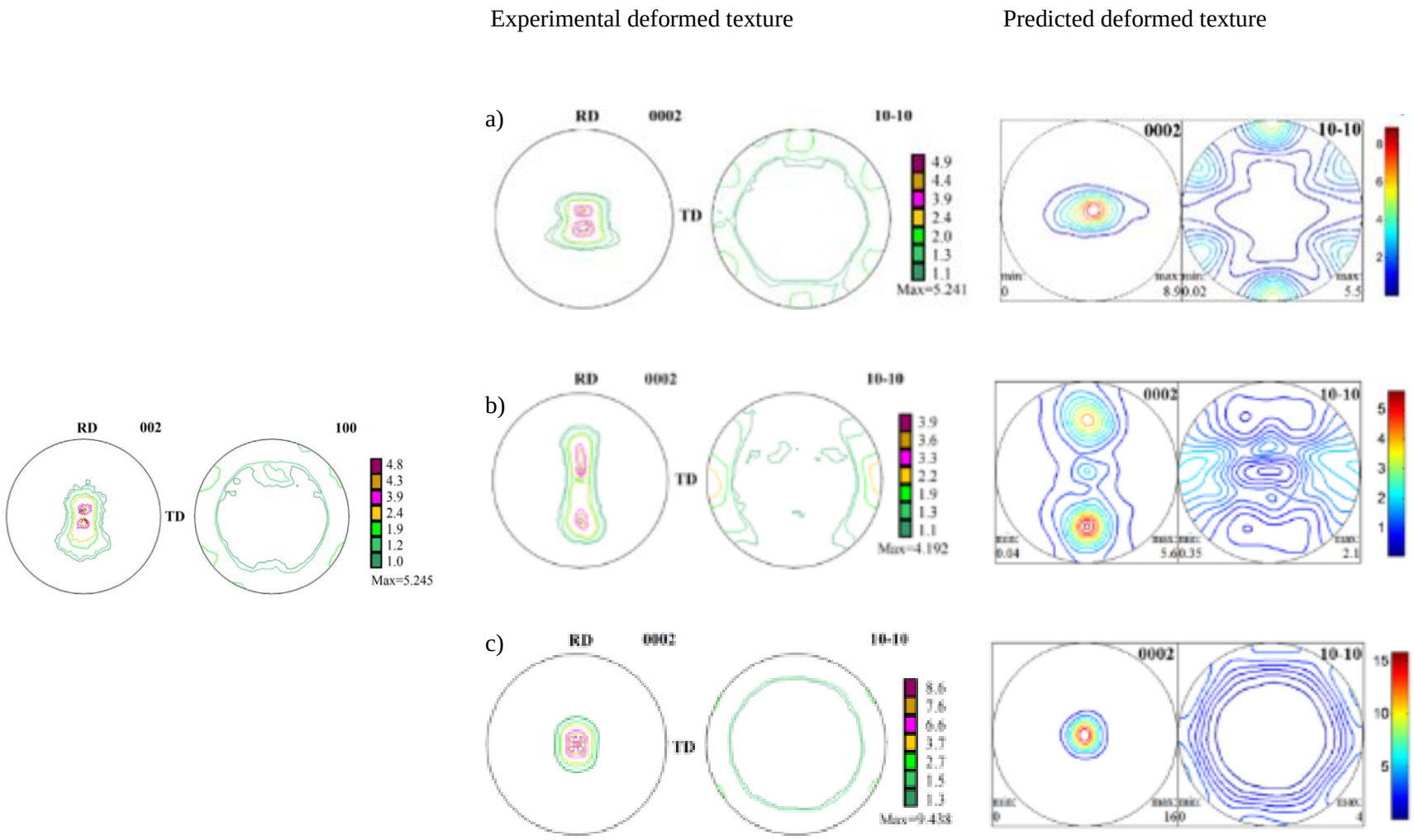


Figure 14: Predicted and experimental texture evolution at 200 °C and a rate of 0.0011/s (Zhou et al. [63]) under a) RD tension, b) RD compression and c) ND compression

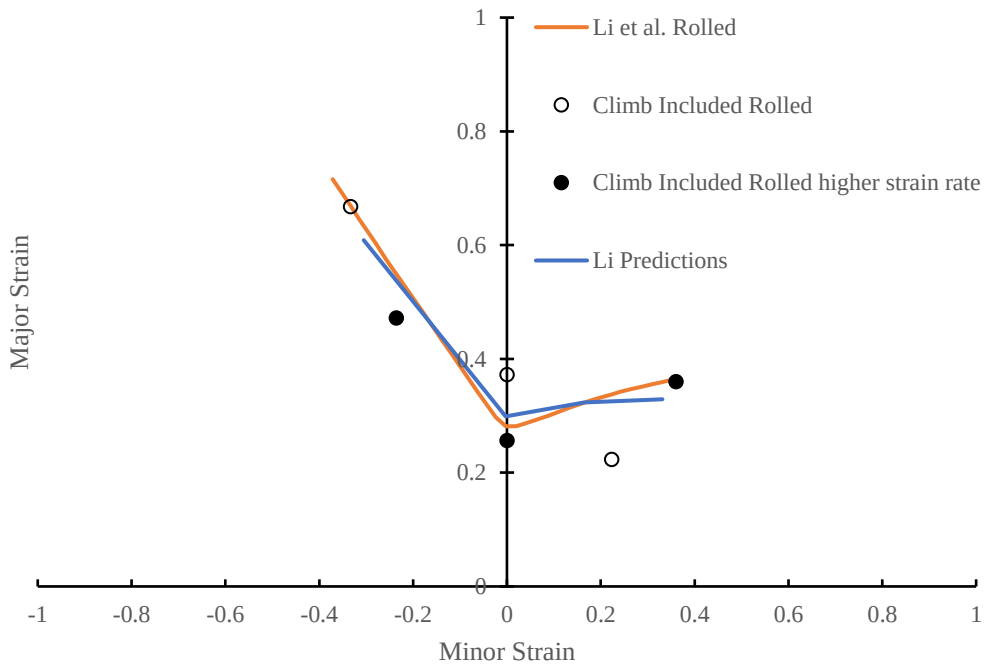


Figure 15: A comparison of DRX – incorporating [1] and climb – incorporating simulations against experimental measurements

## 5- Conclusions

- Simulations of sheet formability predict a general increase in the forming limits when the temperature is increased or the strain rate is decreased (within the range 200 < T < 250 °C and 0.001 < $\dot{\varepsilon}$ < 0.01 1/s), in agreement with experimental observations.
- The improved formability prediction correlates with an increase in the modeled incidence of dislocation climb-accommodated flow. As this climb accommodation induces a high strain rate sensitivity, which is in turn correlated with increases in formability, this forms a consistent chain of logic.
    - In one instance, the biaxial stretching condition, the predicted formability actually decreases with a decrease in strain rate. In this case, climb-accommodation appears competitive with <c+a> slip. It is speculated that a decrease in strain hardening may be responsible for this change. Careful consideration of strain hardening will have to be made during future work.
- Simulations of the sheet formability of distinctly textured (extruded) sheet material do not correlate with experimental observations, i.e., decreases in the strain rate do not lead to the increase in formability observed experimentally, and there is no presently available explanation these results.
    - Notably, dislocation climb-accommodated flow was not predicted in any of the simulations for this distinctly textured material.
- At lower temperatures, e.g., 150 °C, the strain accommodation and texture evolution at large strains typical of sheet forming limits are predicted to involve significant <c+a> slip, distinct from the higher temperature cases discussed above in which <c+a> slip was either inactive or only moderately active.
- This modeling effort does suggest that a transition from significant <c+a> slip at low temperatures (e.g., 150 °C) to significant <a> climb deformation at higher temperatures (e.g., 200 °C) may explain the marked transition in formability over the same temperature range. At this stage, the parameters which describe <c+a> slip and strain hardening require further refinement before more definitive statements can be made.

# Chapter 6: Conclusions and future works

The experiments and simulations performed in the body of work have improved our understanding of strain accommodation by climb in HCP materials and develop a new method of studying the high temperature deformation of non-cubic materials. The conventional role of <c+a> slip in power law creep was called into question as it cannot explain many of the experimentally observed changes in constitutive behavior past the onset of power law breakdown (e.g., the simultaneous reduction in strain anisotropy (r-value), increased strain rate sensitivity (SRS) and activation energy and the texture evolution). Matching the macroscopic, experimental measurements of texture evolution and r-value to predictions generated by climb incorporating, viscoplastic self-consistent (VPSC-CLIMB) crystal plasticity form the basis of a "bottom up" approach in which the fitting the kinematics of deformation (i.e., the strains accommodated by each slip mode) is favored due to the presence of a unique solution. Significant strain accommodation by climb was found to slow the texture evolution and reduce the r-value and coincided with increasing temperature and decreasing strain rate in agreement with the understanding of its vacancy diffusion control and significantly higher strain rate sensitivity (SRS) than glide.

Additional VPSC-CLIMB simulations at intermediate temperatures extended our understanding of climb into elevated temperatures outside the power law regime. While the genetic algorithm optimization was able to determine resolved shear stresses and climb stresses that described the texture evolution and strain anisotropy under these conditions, it is evident that <c+a> slip is currently unconstrained and likely accommodates some of the strain attributed to <a> climb. The assumption of independent climb strain accommodation suggested in the previous chapter was justified by modeling the macroscopic activation energy and strain rate sensitivity over a range of temperatures using an expression derived from an additive strain model where the total strain rate can be written as the sum of contributions from all active slip modes. This methodology demonstrated that strain accommodation via climb led to increased rate sensitivity and a plateau in activation energy in the power law regime with respect to glide only models.

The constitutive response of AZ31B was compared to another dilute Mg alloy, ZK10. Like AZ31B, ZK10 was found to be controlled by climb (the Garafalo-Sellars-Tegart model was fit with Q = 135 kJ/mol and n = 4.81). ZK10 had more subtle texture and strain anisotropy evolution than in AZ31B. GA optimization of CRSS and climb stress parameters for VSPC-CLIMB simulations determined that the room temperature deformation was controlled by basal slip and some prism slip, which explains the reduced strain anisotropy relative to AZ31B. <a> dislocation climb could possibly explain the evolution of the texture and r-value in the power law regime, but the more subtle texture evolution due to the weaker as-rolled and annealed texture in ZK10 made differentiating the effects of basal <a> glide and climb more difficult. At the highest temperatures investigated, the climb of <c> dislocations was necessary to predict the r-values, which were below unity.

X-ray line profile analysis (XLPA) interrogated two outstanding questions: 1) do the texture and alloy chemistry differences between AZ31B and ZK10 explain the activation of <c> climb in ZK10? and 2) are the densities needed for significant dislocation climb plausible? <a> dislocations are thought to be more likely to climb and annihilate than <c+a> and <c> dislocations in AZ31B, as their fraction of total dislocations and density decreased faster than the other dislocation types with increasing temperature after ex-situ analysis. Additionally, XLPA results suggested that climb is not restricted to <a> dislocations. This was particularly true in ZK10, as the fractions of all dislocations remained constant with increasing temperature, suggesting that the annihilation rates of each dislocation type are similar. Comparison with ZK10 and pure Mg data found in the literature suggested that alloy chemistry has a stronger role in facilitating non <a> climb modes. Mobile, climbing dislocation densities predicted using an lattice diffusion controlled Orowan expression were found to be plausible for every condition tested at elevated temperatures ($<10^{15}$ $1/m^2$); however, the required densities were significantly higher than those experimentally determined in XLPA. Accounting for the static recovery in the ex-situ XLPA samples greatly reduced the disparity between the measured <a> density and predicted density, particularly at 350 °C. The influence on pipe diffusion during deformation in the power law regime was found to have an insignificant effect at the conditions examined (250 °C, 0.001 1/s and 350 °C, 0.00028 1/s) when a heterogeneous (i.e., cell structure) microstructure is assumed.

The role of climb in high temperature deformation was extended in AZ31B by predicting forming limit curves (FLC), which are defined by uniaxial straining, plane strain and equibiaxial stretching. The formability was predicted to increase with temperature or decreasing rate within the power law regime ($200 < T < 250$ °C and $0.001 < \dot{\varepsilon} < 0.01$ 1/s). The incorporation of climb strain accommodation in this condition led to increased strain rate sensitivity (SRS) due to the higher SRS of climb relative to glide, which improves the formation of a stable neck during deformation. In these simulations, an increased strain rate in the defect causes plastic instability due to the reduction of strain accommodation via climb, which further reduces the SRS and increases the thinning rate in the sheet. At lower temperatures (150 °C), <c+a> slip was predicted to accommodate much more strain in all strain paths investigated, suggesting that a transition between <c+a> slip dominated deformation outside the power law regime and a regime where <a> climb accommodates significant strain exists.

Several avenues of future research are now available after the investigations performed in this body of work. Many relate to the modeling procedures of the original study. First, the modeling procedure emphasized deformation in the power law regime with a preliminary attempt to model room temperature deformation of Mg alloys, but the role of <c+a> slip was not rigorous investigated. A more comprehensive study using both in-plane deformation conditions and through-thickness compression would better constrain the activity of <c+a> slip may solve this disparity between current predictions and experimental results. In this regime where glide is expected to dominate the deformation behavior, additional constraints on the climb stress can be enforced to limit its strain accommodation. One such proposed addition would be to require the mobile density of climbing dislocations to be less than the estimated Taylor density at the specified temperature and rate. Slip mode hardening must also be implemented into GA-based

optimizations of VPSC-CLIMB simulation parameters using experimental flow stress data to avoid *ad hoc* adjustments to the resolved shear stresses as performed in the current work. Finally, an empirical description of the constitutive behavior (the MTS model and a steady state climb model) was employed to predict the RSSs of glide modes and the climb stresses of climb modes, respectively. While these attempts were unsuccessful at creating a holistic description of the constitutive behavior of Mg over a wide range of temperatures and strain rates, it did suggest that the implementation of a combined MTS - VPSC-CLIMB model could have merit and should be pursued with a steady state climb model to describe the evolution of the climb stress.

The role of initial texture was preliminarily explored in simulation by comparing the FLCs of AZ31B using the experimental as-rolled and annealed texture against formability predictions of as-extruded and randomly textured samples. The current simulations suggest that initial texture can have a strong impact on the activation of climb. Future studies should endeavor to elucidate the contribution of alloy chemistry to the strain accommodation of climb. Preliminary observations of AZ31B and ZK10 samples suggest that alloy chemistry may be important, as the climb of <c> dislocations was necessary to optimize the r-values of ZK10, but not AZ31B. In addition to chemistry effects, texture may also play an important role, as grains may be poorly oriented for <c> climb in a strong basal texture material. XLPA measurements also suggested that <a> dislocations may climb more easily than other types in AZ31B than in ZK10. However, these measurements were ex-situ and static recovery was shown to have a large effect on the posttest dislocation density. Future measurements should be performed in-situ to predict the climbing dislocation densities more accurately. It is also unclear whether the dislocations observed are statistically significant (SSDs) or geometrically necessary (GNDs). Future work should center on quantifying the GND populations of each dislocation type through electron backscatter diffraction (EBSD).

# Chapter 7: References


[1] Z. Li, G. Zhou, D. Li, M. K. Jain, Y. Peng, and P. Wu, "Forming limits of magnesium alloy AZ31B sheet at elevated temperatures," *Int J Plast*, vol. 135, Dec. 2020, doi: 10.1016/j.ijplas.2020.102822.

[2] M. K. Kulekci, "Magnesium and its alloys applications in automotive industry," *International Journal of Advanced Manufacturing Technology*, vol. 39, no. 9–10, pp. 851–865, 2008, doi: 10.1007/s00170-007-1279-2.

[3] M. Ashby, H. Shercliff, and D. Cebon, *Materials Engineering , Science , Processing and Design*, 3rd ed. Oxford, UK: Butterworth-Heinemann, 2014.

[4] D. S. Kumar, C. T. Sasanka, K. Ravindra, and K. N. S. Suman, "Magnesium and Its Alloys in Automotive Applications – A Review," *American Journal of Materials Science and Technology*, no. January, 2015, doi: 10.7726/ajmst.2015.1002.

[5] L. Gaines, R. Cuenca, F. Stodolsky, and S. Wu, "Potential Applications of Wrought Magnesium Alloys for Passenger Vehicles," *Automotive Technology Development Contractors' coordination meeting*, 1995.

[6] Ö. Ayer, "Effect of die parameters on the grain size, mechanical properties and fracture mechanism of extruded AZ31 magnesium alloys," *Materials Science and Engineering A*, vol. 793, Aug. 2020, doi: 10.1016/j.msea.2020.139887.

[7] H. Li, E. Hsu, J. Szpunar, H. Utsunomiya, and T. Sakai, "Deformation mechanism and texture and microstructure evolution during high-speed rolling of AZ31B Mg sheets," *J Mater Sci*, vol. 43, no. 22, pp. 7148–7156, Nov. 2008, doi: 10.1007/s10853-008-3021-3.

[8] R. V Mises, "Mechanik der plastischen Formänderung von Kristallen," *ZAMM - Journal of Applied Mathematics and Mechanics / Zeitschrift für Angewandte Mathematik und Mechanik*, vol. 8, no. 3, pp. 161–185, Jan. 1928, doi: https://doi.org/10.1002/zamm.19280080302.

[9] G. I. Taylor, "Taylor_1938.pdf," *Journal of the Institute of Metals*, vol. 62. pp. 307–324, 1938.

[10] D. Atwell and M. Barnett, "Extrusion Limits of Magnesium Alloys," *Metallurgical Material Transactions A*, vol. 38, pp. 3032–3041, 2007.

[11] S. R. Agnew, J. A. Horton, and M. H. Yoo, "Transmission electron microscopy investigation of 〈c + a〉 dislocations in Mg and α-solid solution Mg-Li alloys," *Metall Mater Trans A Phys Metall Mater Sci*, vol. 33, no. 3, pp. 851–858, 2002, doi: 10.1007/s11661-002-0154-x.

[12] S. R. Agnew, M. H. Yoo, and C. N. Tomé, "Application of texture simulation to understanding mechanical behavior of Mg and solid solution alloys containing Li or Y," *Acta Mater*, vol. 49, no. 20, pp. 4277–4289, 2001, doi: 10.1016/S1359-6454(01)00297-X.

[13] S. Ando, H. Rikihisa, M. Tsushida, and H. Kitahara, "Activities of non-basal slips in deformation of magnesium alloy single and poly crystals," *Materials Science Forum*, vol. 941 MSF, pp. 1242–1247, 2018, doi: 10.4028/www.scientific.net/MSF.941.1242.

[14] Z. Wu, R. Ahmad, B. Yin, S. Sandlöbes, and W. A. Curtin, "Mechanistic origin and prediction of enhanced ductility in magnesium alloys," *Science (1979)*, vol. 359, pp. 447–452, 2018, doi: 10.1017/s0368393100107606.

[15] Y. B. Chun and C. H. J. Davies, "Investigation of prism 〈a〉 slip in warm-rolled AZ31 alloy," *Metall Mater Trans A Phys Metall Mater Sci*, vol. 42, no. 13, pp. 4113–4125, 2011, doi: 10.1007/s11661-011-0800-2.

[16] T. Obara, H. Yoshinga, and S. Morozumi, "{11$\bar{2}$2}〈1123〉 Slip system in magnesium," *Acta Metallurgica*, vol. 21, no. 7, pp. 845–853, 1973, doi: 10.1016/0001-6160(73)90141-7.

[17] J. Koike *et al.*, "The activity of non-basal slip systems and dynamic recovery at room temperature in fine-grained AZ31B magnesium alloys," *Acta Mater*, vol. 51, no. 7, pp. 2055–2065, 2003, doi: 10.1016/S1359-6454(03)00005-3.

[18] H. Wang, P. D. Wu, and J. Wang, "Modeling inelastic behavior of magnesium alloys during cyclic loading-unloading," *Int J Plast*, vol. 47, pp. 49–64, 2013, doi: 10.1016/j.ijplas.2013.01.007.

[19] A. R. Antoniswamy, E. M. Taleff, L. G. Hector, and J. T. Carter, "Plastic deformation and ductility of magnesium AZ31B-H24 alloy sheet from 22 to 450°C," *Materials Science and Engineering A*, vol. 631, pp. 1–9, 2015, doi: 10.1016/j.msea.2015.02.018.

[20] S. R. Agnew and Ö. Duygulu, "Plastic anisotropy and the role of non-basal slip in magnesium alloy AZ31B," *Int J Plast*, vol. 21, no. 6, pp. 1161–1193, 2005, doi: 10.1016/j.ijplas.2004.05.018.

[21] N. Xia *et al.*, "Enhanced ductility of Mg–1Zn–0.2Zr alloy with dilute Ca addition achieved by activation of non-basal slip and twinning," *Materials Science and Engineering A*, vol. 813, no. 5988, p. 141128, 2021, doi: 10.1016/j.msea.2021.141128.

[22] J. Weertman, "Theory of steady-state creep based on dislocation climb," *J Appl Phys*, vol. 26, no. 10, pp. 1213–1217, 1955, doi: 10.1063/1.1721875.

[23] R. A. Lebensohn, C. S. Hartley, C. N. Tome, and O. Castelnau, "Modeling the mechanical response of polycrystals deforming by climb and glide," *Philosophical Magazine*, vol. 90, no. 5, pp. 567–583, 2010, doi: 10.1080/14786430903213320.

[24] R. A. Lebensohn, R. A. Holt, A. Caro, A. Alankar, and C. N. Tomé, "Improved constitutive description of single crystal viscoplastic deformation by dislocation climb," *Comptes Rendus - Mecanique*, vol. 340, no. 4–5, pp. 289–295, 2012, doi: 10.1016/j.crme.2012.02.011.

[25] C. John Neil and S. R. Agnew, "Crystal plasticity-based forming limit prediction for non-cubic metals: Application to Mg alloy AZ31B," *Int J Plast*, vol. 25, no. 3, pp. 379–398, 2009, doi: 10.1016/j.ijplas.2008.05.003.

[26] U. F. Kocks, A. S. Argon, and M. F. Ashby, "Thermodynamics and Kinetics of Slip," *Prog Mater Sci*, pp. 1–207, 1975.

[27] H. J. Frost and M. F. Ashby, *Deformation-mechanism Maps: The Plasticity and Creep of Metals and Ceramics*. Elsevier Science Limited, 1982. [Online]. Available: https://books.google.com/books?id=5PpDAQAAIAAJ

[28] H. Mughrabi, "A Two-parameter Description of Heterogeneous Dislocation Distributions in Deformed Metal Crystals*t," 1987.

[29] F. Wang and S. R. Agnew, “Dislocation transmutation by tension twinning in magnesium alloy AZ31,” *Int J Plast*, vol. 81, pp. 63–86, 2016, doi: 10.1016/j.ijplas.2016.01.012.

[30] S. P. Keeler, “Plastic instability and fracture in sheets stretched over rigid punches,” Massachusetts Institute of Technology, 1961. [Online]. Available: http://hdl.handle.net/1721.1/120282

[31] V. V. Hasek, “Investigation and Theoretical Description of Important Controlling Factors of the Forming Limit Diagram-I,” *Blech*, vol. 25, no. 5, pp. 213–220, May 1978.

[32] Z. Marciniak and K. Kuczyński, “Limit strains in the processes of stretch-forming sheet metal,” *Int J Mech Sci*, vol. 9, no. 9, pp. 609–620, 1967, doi: https://doi.org/10.1016/0020-7403(67)90066-5.

[33] F. Barlat, D. J. Lege, and J. C. Brem, “A six-component yield function for anisotropic materials,” *Int J Plast*, vol. 7, no. 7, pp. 693–712, 1991.

[34] W. F. Hosford, “A Generalized Isotropic Yield Criterion,” *J Appl Mech*, vol. 39, no. 2, pp. 607–609, Jun. 1972.

[35] R. Hill, “A theory of the yielding and plastic flow of anisotropic metals,” 1924. [Online]. Available: https://royalsocietypublishing.org/

[36] J. Bohlen *et al.*, “Processing effects on the formability of magnesium alloy sheets,” *Metals (Basel)*, vol. 8, no. 2, Feb. 2018, doi: 10.3390/met8020147.

[37] J. Bohlen, H. C. Trinh, K. Rätzke, S. Yi, and D. Letzig, “Recrystallization effects on the forming behaviour of magnesium alloy sheets with varied calcium concentration,” *Magnesium Technology*, pp. 87–94, 2020.

[38] J. Bohlen, M. R. Nürnberg, J. W. Senn, D. Letzig, and S. R. Agnew, “The texture and anisotropy of magnesium-zinc-rare earth alloy sheets,” *Acta Mater*, vol. 55, no. 6, pp. 2101–2112, 2007, doi: 10.1016/j.actamat.2006.11.013.

[39] B. C. Zhou, S. L. Shang, Y. Wang, and Z. K. Liu, “Diffusion coefficients of alloying elements in dilute Mg alloys: A comprehensive first-principles study,” *Acta Mater*, vol. 103, pp. 573–586, 2016, doi: 10.1016/j.actamat.2015.10.010.

[40] B. Li, E. Ma, and K. T. Ramesh, “Dislocation configurations in an extruded ZK60 magnesium alloy,” *Metallurgical and Materials Transactions A: Physical Metallurgy and Materials Scienceqqq*, vol. 39, no. 11, pp. 2607–2614, 2008, doi: 10.1007/s11661-008-9621-3.

[41] S. R. Agnew, C. Calhoun, and J. Bhattacharyya, Jishnu, “What is in a strain hardening ‘plateau’?,” *Magnesium Technology*, pp. 189–194, 2016.

[42] Z. Wu and W. A. Curtin, “The origins of high hardening and low ductility in magnesium,” *Nature*, vol. 526, no. 7571, pp. 62–67, Oct. 2015, doi: 10.1038/nature15364.

[43] M. E. Kassner, *Fundamentals of Creep in Metals and Alloys*, 2nd ed. Waltham, MA: Butterworth Heinemann, 2009.

[44] I. J. Beyerlein and C. N. Tomé, “A dislocation-based constitutive law for pure Zr including temperature effects,” *Int J Plast*, vol. 24, no. 5, pp. 867–895, 2008, doi: 10.1016/j.ijplas.2007.07.017.

[45] P. S. Follansbee, *Fundamentals of strength : principles, experiment, and applications of an internal state variable constitutive formulation*. 2014.

[46] S. Mandal, B. T. Gockel, S. Balachandran, D. Banerjee, and A. D. Rollett, “Simulation of plastic deformation in Ti-5553 alloy using a self-consistent viscoplastic model,” *Int J Plast*, vol. 94, pp. 57–73, Jul. 2017, doi: 10.1016/j.ijplas.2017.02.008.

[47] S. Zhu, M. Zhao, J. Mao, and S. Y. Liang, “Study on Hot Deformation Behavior and Texture Evolution of Aluminum Alloy 7075 Based on Visco-Plastic Self-Consistent Model,” *Metals (Basel)*, vol. 12, no. 10, Oct. 2022, doi: 10.3390/met12101648.

[48] E. Orowan, “Problems of plastic gliding,” 1940.

[49] W. Wen, A. Kohnert, M. Arul Kumar, L. Capolungo, and C. N. Tomé, “Mechanism-based modeling of thermal and irradiation creep behavior: An application to ferritic/martensitic HT9 steel,” *Int J Plast*, vol. 126, no. November 2019, 2020, doi: 10.1016/j.ijplas.2019.11.012.

[50] H. Mughrabi, “The α-factor in the Taylor flow-stress law in monotonic, cyclic and quasi-stationary deformations: Dependence on slip mode, dislocation arrangement and density,” *Curr Opin Solid State Mater Sci*, vol. 20, no. 6, pp. 411–420, 2016, doi: 10.1016/j.cossms.2016.07.001.

[51] F. K. Abu-Farha and M. K. Khraisheh, “Analysis of superplastic deformation of AZ31 magnesium alloy,” *Adv Eng Mater*, vol. 9, no. 9, pp. 777–783, 2007, doi: 10.1002/adem.200700155.

[52] C. Zener and J. H. Hollomon, “Effect of strain rate upon plastic flow of steel,” *J Appl Phys*, vol. 15, no. 1, pp. 22–32, 1944, doi: 10.1063/1.1707363.

[53] D. Sherby, J. L. Lytton, and J. E. DORNt, “ACTIVATION ENERGIES FOR CREEP OF HIGH-PURITY ALUMINUM*,” 1957.

[54] R. P. Carreker and W. R. Hibbard, “TENSILE DEFORMATION OF HIGH-PURITY COPPER AS A FUNCTION OF TEMPERATURE, STRAIN RATE, AND GRAIN SIZE*.”

[55] E. Garlea, M. Radovic, and P. K. Liaw, “High-Temperature Dependency of Elastic Mechanical Behavior of Two Wrough Magnesium Alloys AZ31B and ZK60A studied by Resonant Ultrasound Spectroscopy,” pp. 1–24, 2019.

[56] M. A. Shabana, J. J. Bhattacharyya, M. Niewczas, and S. R. Agnew, “Exploring stress equivalence for solid solution strengthened Mg alloy polycrystals,” *Materials Science and Engineering A*, vol. 816, Jun. 2021, doi: 10.1016/j.msea.2021.141252.

[57] G. P. M. Leyson and W. A. Curtin, “Solute strengthening at high temperatures,” *Model Simul Mat Sci Eng*, vol. 24, no. 6, Jul. 2016, doi: 10.1088/0965-0393/24/6/065005.

[58] J. A. Yasi, L. G. Hector, and D. R. Trinkle, “Prediction of thermal cross-slip stress in magnesium alloys from direct first-principles data,” *Acta Mater*, vol. 59, no. 14, pp. 5652–5660, Aug. 2011, doi: 10.1016/j.actamat.2011.05.040.

[59] A. Couret and D. Caillard, “An in situ study of prismatic glide in magnesium-I. The rate controlling mechanism,” *Acta Metallurgica*, vol. 33, no. 8, pp. 1447–1454, 1985, doi: 10.1016/0001-6160(85)90045-8.

[60] A. Akhtar and E. Teghtsoonian, “Solid solution strengthening of magnesium single crystals-I alloying behaviour in basal slip,” *Acta Metallurgica*, vol. 17, no. 11, pp. 1339–1349, 1969, doi: 10.1016/0001-6160(69)90151-5.

[61] P. W. Flynn, J. E. D. J. Mote, and J. E. Dorn, “On the thermally activated mechanism of prismatic slip magnesium single crystals,” *Transactions of the Metallurgical Society of AIME*, vol. 221, no. 6, pp. 1148–1154, Jan. 1961.

[62] J. J. Bhattacharyya, F. Wang, P. D. Wu, W. R. Whittington, H. El Kadiri, and S. R. Agnew, “Demonstration of alloying, thermal activation, and latent hardening effects on quasi-static and dynamic polycrystal plasticity of Mg alloy, WE43-T5, plate,” *Int J Plast*, vol. 81, pp. 123–151, Jun. 2016, doi: 10.1016/j.ijplas.2016.01.005.

[63] G. Zhou, Z. Li, D. Li, Y. Peng, H. Wang, and P. Wu, “Misorientation development in continuous dynamic recrystallization of AZ31B alloy sheet and polycrystal plasticity simulation,” *Materials Science and Engineering A*, vol. 730, pp. 438–456, Jul. 2018, doi: 10.1016/j.msea.2018.05.095.

[64] J. Weertman, “Theory of steady-state creep based on dislocation climb,” *J Appl Phys*, vol. 26, no. 10, pp. 1213–1217, 1955, doi: 10.1063/1.1721875.

[65] J. E. Dorn, “SOME FUNDAMENTAL EXPERIMENTS ON HIGH TEMPERATURE CREEP,” Pergamon Press Ltd, 1954.

[66] K. Máthis, K. Nyilas, A. Axt, I. Dragomir-Cernatescu, T. Ungár, and P. Lukáč, “The evolution of non-basal dislocations as a function of deformation temperature in pure magnesium determined by X-ray diffraction,” *Acta Mater*, vol. 52, no. 10, pp. 2889–2894, 2004, doi: 10.1016/j.actamat.2004.02.034.

[67] C. Ha *et al.*, “Influence of Nd or Ca addition on the dislocation activity and texture changes of Mg–Zn alloy sheets under uniaxial tensile loading,” *Materials Science and Engineering A*, vol. 761, no. April, p. 138053, 2019, doi: 10.1016/j.msea.2019.138053.

[68] J. J. Bhattacharyya, S. R. Agnew, and G. Muralidharan, “Texture enhancement during grain growth of magnesium alloy AZ31B,” *Acta Mater*, vol. 86, pp. 80–94, 2015, doi: 10.1016/j.actamat.2014.12.009.

[69] A. K. Ghosh, “Tensile instability and necking in materials with strain hardening and strain-rate hardening,” *Acta Metallurgica*, vol. 25, no. 12, pp. 1413–1424, 1977, doi: 10.1016/0001-6160(77)90072-4.

[70] A. Chapuis and Q. Liu, “Modeling strain rate sensitivity and high temperature deformation of Mg-3Al-1Zn alloy,” *Journal of Magnesium and Alloys*, vol. 7, no. 3, pp. 433–443, Sep. 2019, doi: 10.1016/j.jma.2019.04.004.

[71] M. Knezevic, M. Zecevic, I. J. Beyerlein, and R. A. Lebensohn, “A numerical procedure enabling accurate descriptions of strain rate-sensitive flow of polycrystals within crystal visco-plasticity theory,” *Comput Methods Appl Mech Eng*, vol. 308, pp. 468–482, 2016, doi: 10.1016/j.cma.2016.05.025.

[72] J. A. Yasi, L. G. Hector, and D. R. Trinkle, “Prediction of thermal cross-slip stress in magnesium alloys from a geometric interaction model,” *Acta Mater*, vol. 60, no. 5, pp. 2350–2358, Mar. 2012, doi: 10.1016/j.actamat.2012.01.004.

[73] Y. Zhao, L. S. Toth, R. Massion, and W. Skrotzki, “Role of Grain Boundary Sliding in Texture Evolution for Nanoplasticity,” *Adv Eng Mater*, vol. 1700212, pp. 1–9, 2017, doi: 10.1002/adem.201700212.

[74] Z. Li *et al.*, “Crystal plasticity based modeling of grain boundary sliding in magnesium alloy AZ31B sheet,” *Transactions of Nonferrous Metals Society of China (English Edition)*, vol. 31, no. 1, pp. 138–155, Jan. 2021, doi: 10.1016/S1003-6326(20)65483-8.

[75] T. G. Langdon, “Grain boundary sliding revisited: Developments in sliding over four decades,” *J Mater Sci*, vol. 41, no. 3, pp. 597–609, 2006, doi: 10.1007/s10853-006-6476-0.

[76] J. Bonneville and B. Escaig, “CROSS-SLIPPING PROCESS AND THE STRESS-ORIENTATION DEPENDENCE IN PURE COPPER.”

[77] A. Couret, D. Caillard, W. Püschl, and G. Schoeck, “Prismatic glide in divalent h.c.p. metals,” *Philosophical Magazine A*, vol. 63, no. 5, pp. 1045–1057, May 1991, doi: 10.1080/01418619108213936.

[78] H. Wang, B. Raeisinia, P. D. Wu, S. R. Agnew, and C. N. Tomé, “Evaluation of self-consistent polycrystal plasticity models for magnesium alloy AZ31B sheet,” *Int J Solids Struct*, vol. 47, no. 21, pp. 2905–2917, 2010, doi: 10.1016/j.ijsolstr.2010.06.016.

[79] H. Wang, P. D. Wu, J. Wang, and C. N. Tomé, “A crystal plasticity model for hexagonal close packed (HCP) crystals including twinning and de-twinning mechanisms,” *Int J Plast*, vol. 49, pp. 36–52, 2013, doi: 10.1016/j.ijplas.2013.02.016.

[80] M. A. Ritzo, R. A. Lebensohn, L. Capolungo, and S. R. Agnew, “Accounting for the effect of dislocation climb-mediated flow on the anisotropy and texture evolution of Mg alloy, AZ31B,” *Materials Science and Engineering A*, vol. 839, Apr. 2022, doi: 10.1016/j.msea.2021.142581.

[81] S. Ando, N. Harada, M. Tsushida, H. Kitahara, and H. Tonda, “Temperature Dependence of Deformation Behavior in Magnesium and Magnesium Alloy Single Crystals,” *Key Eng Mater*, vol. 345–346, pp. 101–104, 2007, doi: 10.4028/www.scientific.net/kem.345-346.101.

[82] S. Ando, A. Kodera, K. Fukushima, M. Tsushida, and H. Kitahara, “Tensile deformation of magnesium and magnesium alloy single crystals,” *Materials Science Forum*, vol. 783–786, pp. 341–345, 2014, doi: 10.4028/www.scientific.net/msf.783-786.341.

[83] F. Bachmann, R. Hielscher, and H. Schaeben, “Texture analysis with MTEX- Free and open source software toolbox,” *Solid State Phenomena*, vol. 160, pp. 63–68, 2010, doi: 10.4028/www.scientific.net/SSP.160.63.

[84] L. Yi *et al.*, “Warm deformation and strain-hardening behaviors of fine-grained ZK60 alloy sheet,” *Mater Res Express*, vol. 6, no. 12, pp. 0–9, 2019, doi: 10.1088/2053-1591/ab3ed5.

[85] W. G. Feather *et al.*, “Mechanical response, twinning, and texture evolution of WE43 magnesium-rare earth alloy as a function of strain rate: Experiments and multi-level crystal plasticity modeling,” *Int J Plast*, vol. 120, pp. 180–204, Sep. 2019, doi: 10.1016/j.ijplas.2019.04.019.

[86] L. Jiang, J. J. Jonas, A. A. Luo, A. K. Sachdev, and S. Godet, “Twinning-induced softening in polycrystalline AM30 Mg alloy at moderate temperatures,” *Scr Mater*, vol. 54, no. 5, pp. 771–775, 2006, doi: 10.1016/j.scriptamat.2005.11.029.

[87] B. (Brent) Fultz and J. M. Howe, *Transmission electron microscopy and diffractometry of materials*. Springer, 2008.

[88] W. Pantleon, “Resolving the geometrically necessary dislocation content by conventional electron backscattering diffraction,” *Scr Mater*, vol. 58, no. 11, pp. 994–997, Jun. 2008, doi: 10.1016/j.scriptamat.2008.01.050.

[89] J. Jiang, T. Ben Britton, and A. J. Wilkinson, “The orientation and strain dependence of dislocation structure evolution in monotonically deformed polycrystalline copper,” *Int J Plast*, vol. 69, pp. 102–117, 2015, doi: 10.1016/j.ijplas.2015.02.005.

[90] F. J. Polesak, C. E. Dreyer, T. J. Shultz, and S. R. Agnew, “Blind study of the effect of processing history on the constitutive behaviour of alloy AZ31B,” *Magnesium Technology*, pp. 491–496, 2009.

[91] G. Ribárik, J. Gubicza, and T. Ungár, “Correlation between strength and microstructure of ball-milled Al-Mg alloys determined by X-ray diffraction,” *Materials Science and Engineering A*, vol. 387–389, no. 1-2 SPEC. ISS., pp. 343–347, Dec. 2004, doi: 10.1016/j.msea.2004.01.089.

[92] T. Ungár, J. Gubicza, G. Ribárik, and A. Borbély, “Crystallite size distribution and dislocation structure determined by diffraction profile analysis: Principles and practical application to cubic and hexagonal crystals,” *J Appl Crystallogr*, vol. 34, no. 3, pp. 298–310, 2001, doi: 10.1107/S0021889801003715.

[93] I. C. Dragomir and T. Ungár, “Contrast factors of dislocations in the hexagonal crystal system,” *J Appl Crystallogr*, vol. 35, no. 5, pp. 556–564, Oct. 2002, doi: 10.1107/S0021889802009536.

[94] G. Ribárik, T. Ungár, and J. Gubicza, “MWP-fit: A program for multiple whole-profile fitting of diffraction peak profiles by ab initio theoretical functions,” *J Appl Crystallogr*, vol. 34, no. 5, pp. 669–676, Oct. 2001, doi: 10.1107/S0021889801011451.

[95] U. F. Kocks and H. Mecking, “Physics and phenomenology of strain hardening: The FCC case,” *Prog Mater Sci*, vol. 48, no. 3, pp. 171–273, 2003, doi: 10.1016/S0079-6425(02)00003-8.

[96] A. A. Kohnert and L. Capolungo, “The kinetics of static recovery by dislocation climb,” *NPJ Comput Mater*, vol. 8, no. 1, Dec. 2022, doi: 10.1038/s41524-022-00790-y.

[97] Y. P. Varshni, “Temperature Dependence of the Elastic Constants,” *Phys Rev B*, vol. 2, no. 10, pp. 3952–3958, 1970.

[98] S. Sandlöbes, S. Zaefferer, I. Schestakow, S. Yi, and R. Gonzalez-Martinez, “On the role of non-basal deformation mechanisms for the ductility of Mg and Mg-Y alloys,” *Acta Mater*, vol. 59, no. 2, pp. 429–439, 2011, doi: 10.1016/j.actamat.2010.08.031.

[99] J. F. Stohr and J. P. Poirier, “Etude en microscopie electronique du glissement pyramidal {1122} 〈1123〉 dans le magnesium,” *The Philosophical Magazine: A Journal of Theoretical Experimental and Applied Physics*, vol. 25, no. 6, pp. 1313–1329, Jun. 1972, doi: 10.1080/14786437208223856.

[100] G. Edelin and J. P. Poirier, “Etude de la montée des dislocations au moyen d’expériences de fluage par diffusion dans le magnésium,” *Philosophical Magazine*, vol. 28, no. 6, pp. 1211–1223, Dec. 1973, doi: 10.1080/14786437308227995.

[101] D. Caillard and J. L. Martin, *Thermally Activated Mechanisms in Crystal Plasticity*. Pergamon, 2003.

[102] N. Stanford and M. R. Barnett, “Solute strengthening of prismatic slip, basal slip and {10$\bar{1}$2} twinning in Mg and Mg-Zn binary alloys,” *Int J Plast*, vol. 47, pp. 165–181, 2013, doi: 10.1016/j.ijplas.2013.01.012.

[103] A. Akhtar and E. Teghtsoonian, “Solid solution strengthening of magnesium single crystals-ii the effect of solute on the ease of prismatic slip,” *Acta Metallurgica*, vol. 17, no. 11, pp. 1351–1356, 1969, doi: 10.1016/0001-6160(69)90152-7.

[104] A. Arsenlis and D. M. Parks, “Crystallographic aspects of geometrically-necessary and statistically-stored dislocation density,” *Acta Mater*, vol. 47, no. 5, pp. 1597–1611, 1999, doi: 10.1016/S1359-6454(99)00020-8.

[105] J. W. Hutchinson and K. W. Neale, “Sheet necking-II. Time-independent behavior,” *Mechanics of Sheet Metal Forming: Material Behavior and Deformation Analysis*, pp. 127–153, 1978.

[106] J. Bohlen, H. C. Trinh, K. Rätzke, S. Yi, and D. Letzig, “Recrystallization effects on the forming behaviour of magnesium alloy sheets with varied calcium concentration.”

[107] H. Wang, D. Li, Y. Peng, and P. D. Wu, “Numerical study of inelastic behavior of magnesium alloy sheets during cyclic loading-unloading,” *J Phys Conf Ser*, vol. 1063, no. 1, 2018, doi: 10.1088/1742-6596/1063/1/012050.

[108] M.-A. Kulas, W. P. Green, E. M. Taleff, P. E. Krajewski, and T. R. Mcnelley, “Deformation mechanisms in superplastic AA5083 materials,” *Metallurgical and Materials Transactions A*, vol. 36, pp. 1249–1261, 2005.

[109] M. R. Barnett, A. Ghaderi, I. Sabirov, and B. Hutchinson, “Role of grain boundary sliding in the anisotropy of magnesium alloys,” *Scr Mater*, vol. 61, no. 3, pp. 277–280, 2009, doi: 10.1016/j.scriptamat.2009.04.001.

[110] T. R. Jin, Z. and Bieler, “Superplasticity in Advanced Materials,” *Japan Society for Research on Superplasiticity*, p. 587, 1991.

[111] A. Staroselsky and L. Anand, “A constitutive model for hcp materials deforming by slip and twinning: Application to magnesium alloy AZ31B,” *Int J Plast*, vol. 19, no. 10, pp. 1843–1864, 2003, doi: 10.1016/S0749-6419(03)00039-1.

[112] B. Yavuzyegit *et al.*, “Mapping Plastic Deformation Mechanisms in AZ31 Magnesium Alloy at the Nanoscale.” [Online]. Available: https://ssrn.com/abstract=4198880

[113] A. Ball and M. M. Hutchison, “Superplasticity in the Aluminium–Zinc Eutectoid,” *Metal Science Journal*, vol. 3, no. 1, pp. 1–7, Jan. 1969, doi: 10.1179/msc.1969.3.1.1.

[114] T. Al-Samman and G. Gottstein, “Dynamic recrystallization during high temperature deformation of magnesium,” *Materials Science and Engineering A*, vol. 490, no. 1–2, pp. 411–420, 2008, doi: 10.1016/j.msea.2008.02.004.

[115] J. W. Senn, “Texture Randomization of Magnesium-Y/Nd Alloys during Recrystallization,” 2008.

[116] B. Srinivasarao, N. v. Dudamell, and M. T. Pérez-Prado, “Texture analysis of the effect of non-basal slip systems on the dynamic recrystallization of the Mg alloy AZ31,” *Mater Charact*, vol. 75, pp. 101–107, 2013, doi: 10.1016/j.matchar.2012.10.002.

[117] Z. Y. Liu, T. T. Huang, W. J. Liu, and S. Kang, “Dislocation mechanism for dynamic recrystallization in twin-roll casting Mg-5.51Zn-0.49Zr magnesium alloy during hot compression at different strain rates,” *Transactions of Nonferrous Metals Society of China (English Edition)*, vol. 26, no. 2, pp. 378–389, 2016, doi: 10.1016/S1003-6326(16)64126-2.